

Article

The Role of Nanoparticle Shapes and Structures in Material Characterisation of Polyvinyl Alcohol (PVA) Bionanocomposite Films

Mohanad Mousa ^{1,2} and Yu Dong ^{1,*}

¹ School of Civil and Mechanical Engineering, Curtin University, GPO Box U1987, Perth 6845, Australia; mohanadmousa616@yahoo.com

² Shatrah Technical Institute, Southern Technical University, Basra 61001, Iraq

* Correspondence: Y.Dong@curtin.edu.au; Tel.: +61-8-9266-9055

Received: 13 November 2019; Accepted: 15 January 2020; Published: 25 January 2020

Abstract: Three different types of nanoparticles, 1D Cloisite 30B clay nanoplatelets, 2D halloysite nanotubes (HNTs), and 3D nanobamboo charcoals (NBCs) were employed to investigate the impact of nanoparticle shapes and structures on the material performance of polyvinyl alcohol (PVA) bionanocomposite films in terms of their mechanical and thermal properties, morphological structures, and nanomechanical behaviour. The overall results revealed the superior reinforcement efficiency of NBCs to Cloisite 30B clays and HNTs, owing to their typical porous structures to actively interact with PVA matrices in the combined formation of strong mechanical and hydrogen bondings. Three-dimensional NBCs also achieved better nanoparticle dispersibility when compared with 1D Cloisite 30B clays and 2D HNTs along with higher thermal stability, which was attributed to their larger interfacial regions when characterised for the nanomechanical behaviour of corresponding bionanocomposite films. Our study offers an insightful guidance to the appropriate selection of nanoparticles as effective reinforcements and the further sophisticated design of bionanocomposite materials.

Keywords: polyvinyl alcohol (PVA); bionanocomposites; nanomechanical behaviour; thin films

1. Introduction

Nanoparticles in spheroidal, platelet-like, and tubular shapes as effective nanofillers have attracted materials engineers and researchers in the field of nanocomposite materials in the past few decades [1,2]. The incorporation of different nanoparticles into continuous polymer matrices has been proven to significantly alter the properties of virgin polymers, resulting in a novel-class system of polymer nanocomposites with superior properties and excellent functionalities [1,2]. In general, when embedded with a small fraction of nanoparticles being less than 10 wt %, the optical [3], mechanical [4], thermal [5], electronic [6], and antimicrobial [7] properties of polymer nanocomposites can be remarkably enhanced while maintaining some features of net polymer systems such as low density and easy processibility [2]. Such polymer nanocomposites possess a wide range of applications including medical devices, aerospace engineering, and automotive components [1]. For instance, nanocomposites reinforced with some polymeric and inorganic nanofillers such as chitosan nanoparticles and silver nanoparticles have been proven to be effective for antimicrobial treatment in dentistry [8] or for bone tissue regeneration [9]. Other studies [10,11] demonstrated that polymer nanocomposites, as exemplified by polypropylene (PP)/clay nanocomposites, have real automotive industrial potential to result in significant property improvement with only minor increasing cost if a deeper understanding of their structure–property relationship can be achieved.

The effective reinforcing mechanism is based on the fundamental concept that the chain mobility of polymeric molecules is restricted by rigid nanofillers according to the matrix–particle interfacial interactions in polymer nanocomposites [2,12]. The specific areas associated with matrix–filler interactions are known as interfacial regions with completely distinct properties from those of nanoparticles and polymer matrices individually. More importantly, the material performance of polymer nanocomposites primarily depends on the volume of interfacial regions and interfacial properties [12] in relation to critical nanofiller parameters such as nanoparticle shapes and structures.

In addition to a major concern of nanoparticle structures, nanoparticle shapes are also equally important when matrix–filler interaction is considered in polymer nanocomposites, which can be classified into three popular shapes, namely 1D platelet-like nanoparticles such as montmorillonite (MMT) clays and nanoplatelet graphene sheets, 2D tubular nanoparticles such as HNTs and carbon nanotubes (CNTs), as well as 3D spherical nanoparticles such as diamond nanoparticles and nanosilica particles and fractal-like or irregular near circular-like nanoparticles such as NBCs. In a nanocomposite system, the alteration of nanoparticle shapes means that the contact areas inevitably vary between polymer matrices and nanoparticles to effectively control the volume of their interfacial regions [12]. Most previous studies [13,14] were based on theoretical or numerical modelling approaches such as atomistic and coarse-grained molecular dynamic (MD) simulations for evaluating the matrix–filler bonding effect. Nonetheless, current computational capability and the environment may be mostly restricted to the context of single and two-particle systems by neglecting the effect of actual nanoparticle structures and shapes induced in different material processing techniques [15].

The main objective and novelty of this study lie in holistically assessing the influence of different dimensional nanoparticle shapes, structures, and contents on the effective reinforcement mechanism of PVA bionanocomposites reinforced with 1D Cloisite 30B clays, 2D HNTs, and 3D NBCs, respectively. The selection of PVA as a base polymer arises from its good biodegradability and water solubility to replace conventional petroleum-based polymers for generating much less marine plastic wastes [16]. Our study demonstrated that 3D NBCs could act as relatively new and superior carbon-based nanofillers to clay-based Cloisite 30B and HNTs for the best material performance of nanocomposites. This highlighted their great benefit to be more competitive nanoreinforcements in the manufacture of composite materials, as well as future potential to electronics, material packaging, and biomedical applications.

2. Materials and Methods

2.1. Materials

PVA (material type: MFCD00081922), as a popular water-soluble biopolymer, was purchased from Sigma Aldrich Pty. Ltd., Castle Hill, NSW, Australia with the molecular weight of 89,000–98,000 g/mol and the degree of hydrolysis of 99.0%–99.8%. Three different types of nanoparticles used in this study comprised Cloisite 30B clays, HNTs, and NBCs. In between, NBCs were directly purchased from US Research Nanomaterials, Inc. Co., Houston, TX, USA (molecular weight: 12.01 g/mol, particle density: 0.43 g/cm³, and particle size <69.43 nm [4]). Moreover, Cloisite 30B clays with methyl, tallow, bis-2-hydroxyethyl, quaternary ammonium were supplied by Southern Clay Products, Gonzales, LA, USA while HNT powders, donated by Imerys Tableware Limited, Auckland, New Zealand, have particle dimensions of 120–140 nm in outer diameter, 15–100 nm in inner diameter, and 0.3–1.5 µm in length [17].

2.2. Fabrication of PVA Bionanocomposite Films

All PVA bionanocomposite films reinforced with Cloisite 30B clays, HNTs, and NBCs were prepared using solution casting according to the fabrication procedure mentioned in our previous work [4]. Initially, 5 wt %/v PVA aqueous solution was prepared by mixing 10 g PVA into 190 mL deionised water under vigorous magnetic stirring at 400 rpm and 90 °C for 3 h until PVA was completely dissolved. Aqueous suspensions of all nanoparticles were achieved by mechanical mixing

filler powders in deionised water with a rotor speed of 405 rpm at 40 °C for 2 h, which was followed by the ultrasonication (Model ELMA Ti-H-5, Elma Schmidbauer GmbH, Singen, Germany) at 25 kHz and 40 °C with a power intensity of 70% for 1 h. Subsequently, nanoparticle contents of 0, 3, 5 and 10 wt % were obtained by controlling PVA amounts used in each material formulation. Then, such aqueous suspensions were gradually added in a dropwise manner into PVA solutions and simultaneously subjected to mechanical mixing at 405 rpm and 40 °C for 2 h. Afterwards, their mixtures were stirred at 400 rpm and 90 °C for 1 h prior to the sonication for 30 min to achieve uniform nanoparticle dispersion. Finally, 20 mL prepared solution was poured on a glass Petri dish and allowed to dry in an air-circulating oven at 40 °C for 48 h. Subsequently, different types of PVA bionanocomposite films were stored in a silica gel-containing desiccator prior to material testing.

2.3. Characterisation Methods

In this study, nanomechanical properties of PVA bionanocomposite films were quantitatively assessed in peak force quantitative nanomechanical mapping (PFQNM) [12] via atomic force microscopy (AFM) based on a Bruker Dimension Fastscan AFM system (Bruker Corporation, Karlsruhe, Germany). A Tapping Mode Etched Silicon Probe (TESPA) was employed with the nominal spring constant of 40 N/m and tip radius of 8 nm. The image scan rate was controlled at 2 Hz with 256 × 256 digital pixel resolution. In order to remove unwanted noise, bow and tilt features from the vertical scanner (Z) and AFM topographic images were first-order flattened via the *Flatten* command with the aid of Bruker Nanoscope 1.5 software (Bruker Corporation, Karlsruhe, Germany).

Fourier transform infrared (FTIR) spectrometry (PerkinElmer Spectrum 100 FTIR spectrometer, PerkinElmer, Waltham, MA, USA) was utilised to characterise the chemical bonding effects of PVA, nanoparticles as well as PVA bionanocomposites in a wavenumber range of 650–4000 cm⁻¹ with a resolution of 4 cm⁻¹ according to an attenuated total reflectance (ATR) method.

Additionally, X-ray diffraction (XRD) analysis was carried out using a Bruker D8 Advanced Diffractometer (Bruker Corporation, Karlsruhe, Germany). The X-ray source was Ni-filtered Cu-K α radiation (wavelength $\lambda = 0.1541$ nm) carried out at the accelerating voltage and current of 40 kV and 40 mA, respectively. X-ray spectra were recorded in a 2θ range of 10–50° at the scan rate of 0.015°/s.

A universal testing machine (Lloyd EZ50, Lloyd Instruments Ltd., West Sussex, UK) was employed at room temperature at the crosshead speed of 10 mm/min (gauge length: 50 mm) in order to measure the tensile properties of neat PVA and PVA bionanocomposite films according to ASTM D882-02. For each material batch, six specimens were tested with the mean values and standard deviations being calculated accordingly. Moreover, the tensile toughness was also determined based on tensile energy to break (TEB) with reference to ASTM D882-02.

The fracture morphology for tensile testing specimens was evaluated with the aid of a field emission scanning electron microscope (FE-SEM, Zeiss NEON 40 EsB Cross Beam, Carl Zeiss Microscopy GmbH, Jena, Germany) at an accelerating voltage of 5 kV after being coated with platinum (layer thickness: 5 nm).

The thermal properties of PVA bionanocomposite films were examined using a combined measurement system based on thermal gravimetric analysis (TGA) and differential scanning calorimetry (DSC) (1 STAR^e system, Mettler-Toledo, Columbus, OH, USA) from 35 to 700 °C at a scan rate of 10 °C/min and a flow rate of 25 mL/min under argon atmosphere. The degree of crystallinity χ_c of PVA matrices within PVA bionanocomposites was calculated as follows:

$$\chi_c (\%) = \frac{\Delta H_m}{w\Delta H_m^O} \times 100\% \quad (1)$$

where ΔH_m is the measured melting enthalpy according to DSC data. $\Delta H_m^O = 138.6$ J/g [5] is the enthalpy of fully crystalline PVA, and w is the weight fraction of PVA matrices in corresponding PVA bionanocomposites.

3. Results and Discussion

3.1. Nanoparticle Shape and Size

The morphological structures of as-received nanoparticles of Cloisite 30B clays, HNTs, and NBCs are illustrated in Figure 1. All nanoparticles powders show high irregularities in size and material morphology. However, HNTs are most likely to possess cylindrical shapes with transparent central areas running longitudinally along such cylindrical structures, as illustrated in Figure 1a,b. The outer diameters and lumen diameters of HNTs, as typical tubular nanoparticles in hollow and open-end structures, were found to be in range of 20–115 and 5–30 nm, respectively. Whereas, the lengths of HNTs vary from 50 nm to 1.5 μm . On the other hand, the morphological structures of Cloisite 30B clays were detected using an AFM tapping mode from diluted clay suspension when deposited onto the mica substrate, as revealed in Figure 1c,d. It is evident that Cloisite 30B clays possess platelet-like structures with an average particle diameter of approximately 100.75 ± 6.5 nm by measuring 925 clay particles, while their thickness varies from 1.69 to 5.9 nm, which is exemplified by a cross-sectional analysis for a typical section (A2–B2) illustrated in Figure 1d. These results suggest that clay platelet-like layered structures can consist of single platelets (thickness: ~ 1 nm) [18] as well as stacked layered platelets, signifying the combination of clay exfoliation and intercalation. NBC sizes were determined previously to be 69.43 nm by average [4], as shown in Figure 1e,f, which can be considered as 3D anisotropic nanoparticles as opposed to 1D platelet-like clays and 2D HNTs.

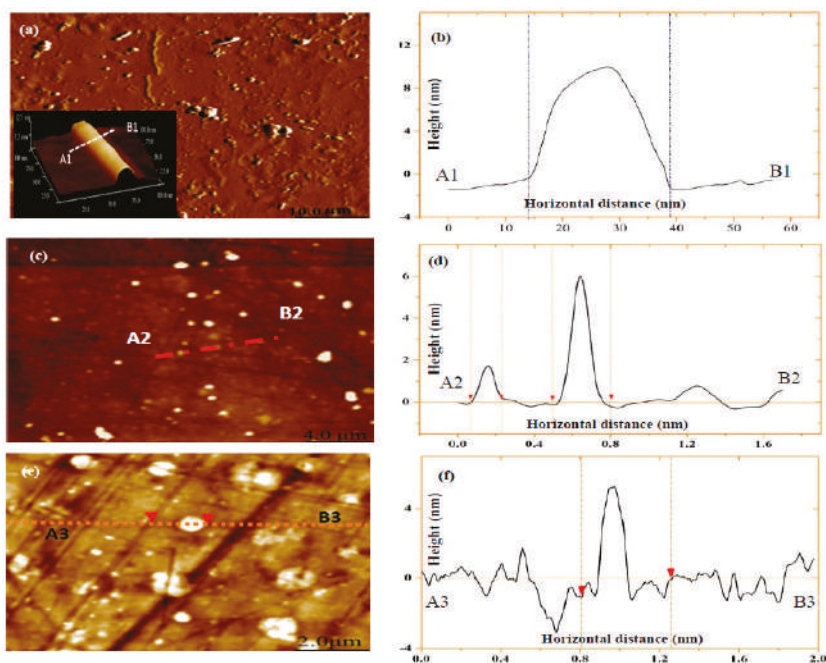


Figure 1. Atomic force microscopy (AFM) characterisation of different nanoparticles: AFM images of (a) HNTs, (c) Cloisite 30B clays, and (e) NBCs deposited on mica substrate in aqueous solutions, and height profiles of (b) HNTs, (d) Cloisite 30B clays, and (f) NBCs at typical cut sections A1–B1, A2–B2, and A3–B3, respectively.

3.2. Chemical Bonding Effect

FTIR was employed to evaluate functional groups in PVA matrices and nanoparticles as well as their associated chemical bonding effects. As-received HNTs exhibit two Al₂OH stretching bands assigned to 3691.5 and 3621 cm⁻¹ in Figure 2a, resulting from OH bending in connection with two Al atoms along with other band features of inorganic aluminosilicate structures of halloysite [19]. Furthermore, FTIR peaks observed at 1004 and 906 cm⁻¹ are associated with Si–O–Si and Al–OH stretchings, respectively. In comparison, as-received Cloisite 30B clays have an existing peak at 3629.6 cm⁻¹ corresponding to Si–OH and Al–OH stretchings in Figure 2b. The broad band at 3405 cm⁻¹ is assigned to OH groups in relation to interlayer water, while two typical bands at 2924.6 and 2853.5 cm⁻¹ are related to –CH₂ asymmetric and symmetric stretchings, respectively [20,21]. Moreover, FTIR peaks at 1647 and 1123.3 cm⁻¹ can be due to the deformation vibration of interlayer water and Si–O bending accordingly, as opposed to an assigned band at 1470 cm⁻¹ arising from –CH₂ bending [20]. The NBC results presented in Figure 2c confirm the absence of –OH groups in their FTIR spectra, which infers much lower moisture and alcohol contents obtained in NBCs. Additionally, FTIR peaks at 2417.5 and 1567.4 m⁻¹ reveal the existence of C≡H stretching [22] and C=C vibration in an aromatic system [23], respectively. On the other hand, the peak spectrum at 1696 cm⁻¹ was assigned to the C=O band primarily for ionisable carboxyl groups as an indicator of surface hydrophilicity [24].

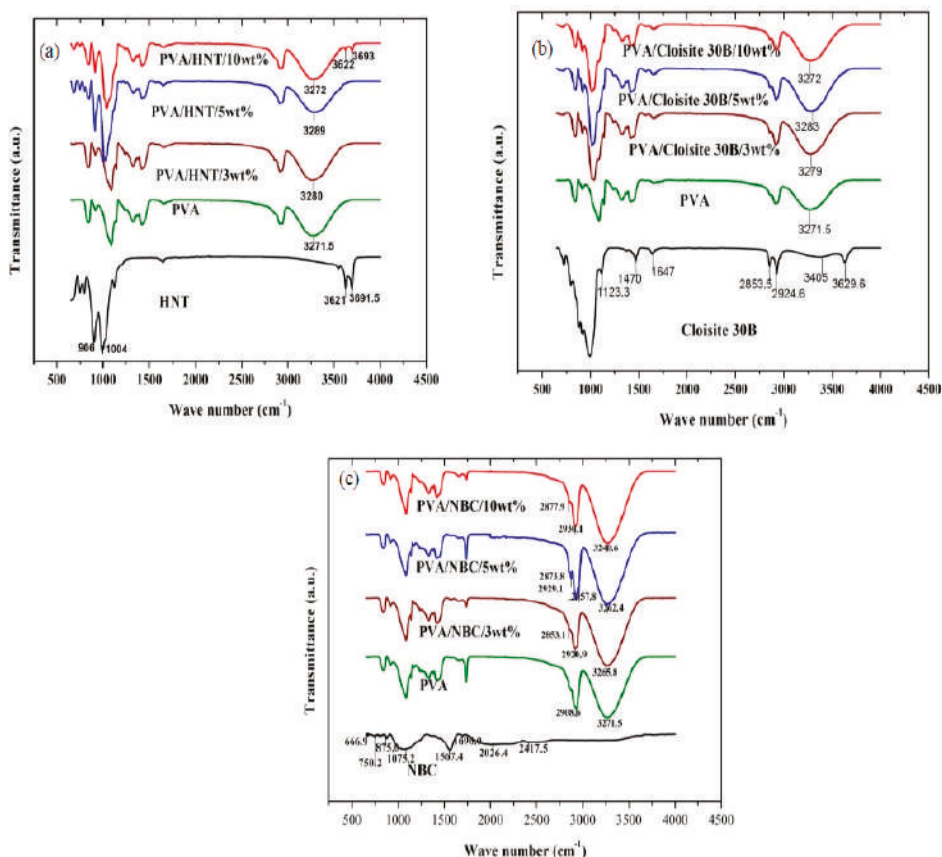


Figure 2. FTIR spectra for chemical interactions of polyvinyl alcohol (PVA) bionanocomposite films reinforced with (a) HNTs, (b) Cloisite 30B clays, and (c) NBCs.

In the case of bionanocomposite systems, the FTIR spectra of PVA/HNT bionanocomposites and PVA/Cloisite 30B clay bionanocomposites are also illustrated in Figure 2a,b, respectively. The FTIR peak located at 3271.5 cm^{-1} associated with O–H stretching shifts to higher wavenumbers at 3280 and 3289 cm^{-1} , as well as 3279 and 3283 cm^{-1} with the inclusion of HNTs and Cloisite 30B clays at the nanoparticle contents of 3 and 5 wt %, respectively. Such a finding was attributed to the strengthening effect of hydrogen bonds between –OH groups from PVA molecules and those located on clay surfaces such as silanol groups (–SiOH), which is in good agreement with previous investigations on PVA/organomodified Cloisite Na^+ (OMMT) nanocomposites [21], poly (ϵ -caprolactone) (PCL)/Cloisite 30B clay nanocomposites [25], and PVA/chitosan (CS)/HNT nanocomposites [26]. However, when the HNT content increases up to 10 wt %, two Al_2OH stretchings appear for embedded HNTs in bionanocomposite films due to typical HNT agglomeration [27]. As for PVA/NBC bionanocomposite films, increasing the NBC content from 0 to 10 wt % leads to the band-peak shift to a lower wavenumber at 3240.6 cm^{-1} owing to large amounts of hydroxyl groups in PVA molecules [4] as well as strong filler–matrix bonding. As a result, hydrogen bonds are generated to be intertwined at PVA/NBC interfaces with a broad O–H band. Such a variation associated with –OH stretching vibration proves the formation of hydrogen bonds, which is in good accordance in PVA/graphene nanocomposites [27] and PVA/bamboo charcoal (BC) nanocomposites [5]. The aforementioned results fail to show existing new bands in PVA films with the inclusion of both HNTs and Cloisite 30B clays. On the contrary, the addition of 3 and 5 wt % NBCs within PVA matrices in bionanocomposite films gives rise to a new band in relation to $-\text{CH}_2$ -asymmetric and symmetric stretchings [4]. Such a finding can be ascribed to typical NBC porous structures enabling absorbing molecular chains of hydrophilic polymers such as PVA with the combined mechanical and chemical bondings. More consistently, the incorporation of HNTs and Cloisite 30B clays in PVA bionanocomposites shifts the hydroxyl peaks of PVA to relatively high wavenumbers compared to the addition of NBCs [4]. Such results indicate that the numbers of hydrogen bonding generated in PVA/HNT bionanocomposites and PVA/Cloisite 30B clay bionanocomposites are higher when compared with those detected in PVA/NBC bionanocomposites, owing to different chemical structures of nanofillers. Since NBCs do not possess –OH peaks, most hydrogen bonding formed in bionanocomposites can arise from hydroxyl groups of PVA molecules. Whereas, existing –OH peaks detected in HNTs and Cloisite 30B clays in PVA bionanocomposites are believed to further facilitate the formation of more hydrogen bonds within PVA matrices.

3.3. XRD Patterns

XRD analysis is a very useful material characterisation method to evaluate the crystalline structures of polymers and composites as well as to determine d -spacing values between clay interlayers. By monitoring the position and intensity of basal reflections from distributed silicate layers, nanocomposite structures (i.e., intercalated or exfoliated) as well as clay aggregated structures can be identified accordingly [28,29]. The XRD patterns of HNTs and corresponding nanocomposites are presented in Figure 3a. HNT patterns possess three major peaks of (001), (020)/(110), and (002) located at $2\theta = 11.9^\circ$, 20° , and 24.9° , leading to d -spacing values of 0.74, 0.44, and 0.37 nm, respectively. The relevant peak taking place at $2\theta = 24.9^\circ$ is attributed to the presence of silica in the form of cristobalite and quartz [30]. After the incorporation of HNTs into PVA matrices in nanocomposite systems, the XRD characteristic peak at $2\theta = 11.9^\circ$ appears to be very weak at the low HNT content of 3 wt %. Similar XRD peaks have been detected at $2\theta = 12.5^\circ$ and 12.6° with slight peak shift at relatively high HNT contents of 5 and 10 wt %, respectively. Overall, decreasing the HNT content significantly reduces the intensity of XRD peaks for all PVA/HNT nanocomposites, which may be due to uniform HNT dispersion at the low HNT content levels. Such a phenomenon suggests that the disappearance or intensity reduction of XRD peaks at low HNT contents results from uniform HNT dispersion in a more randomly oriented manner. On the other hand, the reappearance of XRD peaks at higher HNT contents is indicative of possible HNT agglomeration.

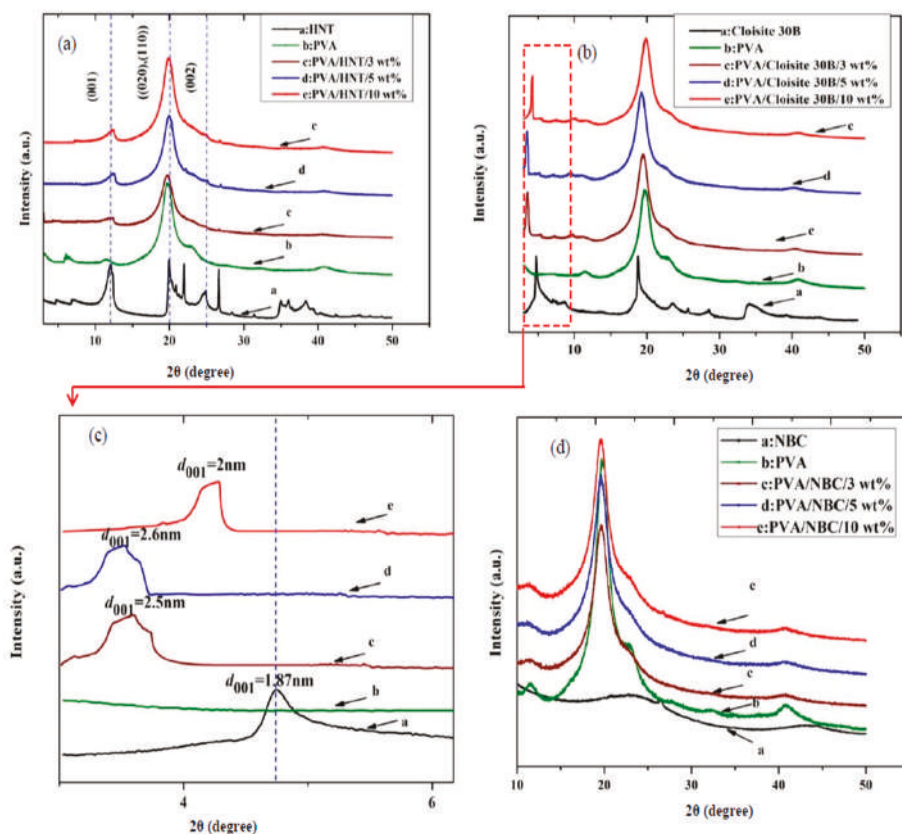


Figure 3. XRD patterns for PVA bionanocomposites reinforced with (a) HNTs, (b,c) Cloisite 30B clays with both wide and small diffraction angles, respectively, and (d) NBCs.

The XRD patterns of Cloisite 30B clays reveal the diffraction peak at $2\theta = 4.72^\circ$ corresponding to the d -spacing value of 1.87 nm, as shown in Figure 3b,c. The (001) diffraction peak shifted to lower angles, as evidenced by the d -spacing values of 2.5, 2.6, and 2 nm for PVA/Cloisite 30B nanocomposites at the clay contents of 3, 5 and 10 wt %, respectively. This phenomenon clearly arises from the diffusion of polymeric chains inside clay interlayers to induce clay intercalation in agreement with PVA/Na⁺ MMT nanocomposites [21] and PLA/Cloisite 30B nanocomposites [31]. The XRD peak for PVA alone appears at $2\theta = 19.7^\circ$, which is associated with the total (101) crystalline atactic formation of PVA molecular chains [32] to slightly shift to lower diffraction angles when increasing the clay content in PVA bionanocomposites. The occurrence of PVA molecular chains at the (101) crystalline plane suggests that PVA matrices evolve towards crystalline structures under more constraints. A similar behaviour was also reported in PVA/clay nanocomposites [32,33], which is ascribed to the strong chemical interactions between nanofillers and polymer matrices. The aforementioned results indicate that Cloisite 30B clays are successfully intercalated and/or exfoliated by PVA molecular chains, and HNTs are homogeneously dispersed at their low contents within continuous PVA matrices, which is attributed to active interactions between PVA matrices and clay nanoparticles due to strong hydrogen bonding taking place between carboxyl groups of PVA molecules and hydroxyl groups in the interlayer areas of Cloisite 30B clays or on the surface edges of HNTs [28].

In comparison, the XRD patterns of NBCs demonstrate two broad XRD peaks, as depicted in Figure 3d. The broad peaks located at $2\theta = 22.9^\circ$ are associated with the sharp peaks of graphite assigned to the (002) diffraction plane [34]. Besides, the second broad peak detected at $2\theta = 43.6^\circ$ characterises 2D in-plane symmetry (101) along with graphene layers. Moreover, XRD patterns of PVA/NBC bionanocomposites only show the diffraction angles from PVA, as illustrated in Figure 3d, which is consistent with the previous finding [35] in PVA/5 wt % graphene oxide (GO) nanocomposites with a clear disappearance sign of GO diffraction peaks in regular and periodic structures, leading to individually exfoliated GOs in PVA matrices.

3.4. Topographic Surface Morphology and Roughness

To assess nanofiller dispersion within PVA matrices, 3D height mapping images of PVA and PVA bionanocomposites are exhibited in Figure 4. As illustrated in Figure 4b, HNT nanoparticles are separated from one another with better HNT dispersion in PVA bionanocomposites reinforced with 3 wt % HNTs, as opposed to typical clay agglomeration and clustering issues beyond the 3 wt % HNTs shown in Figure 4c,d. An excessive amount of HNTs results in decreasing intraparticle spacing along with the higher intramolecular bonding of HNTs, leading to particle agglomeration [36]. Besides, the average root mean square (R_q) value as an indicator of the surface roughness of PVA bionanocomposites has been reported to be 2.4 ± 0.13 nm at the HNT content of 3 wt % when compared with 1.9 ± 0.17 nm for neat PVA, as shown in Figure 4a. It is suggested that the smooth surfaces of PVA/HNT bionanocomposites remain with the incorporation of HNTs at relatively low HNT contents, owing to their uniform dispersion. Such a finding is consistent with PVA/HNT hydrogels mentioned elsewhere [37]. At the low HNT content of 3 wt %, the smooth surfaces of PVA/HNT bionanocomposites can also be ascribed to the combination of strong interactions and good compatibility between HNTs and PVA matrices. Nonetheless, increasing the HNT content up to 5 and 10 wt % leads to much higher surface roughness (i.e., $R_q = 4.54 \pm 0.18$ and 13.1 ± 0.23 nm, respectively) due to the presence of prevalent HNT aggregates [38].

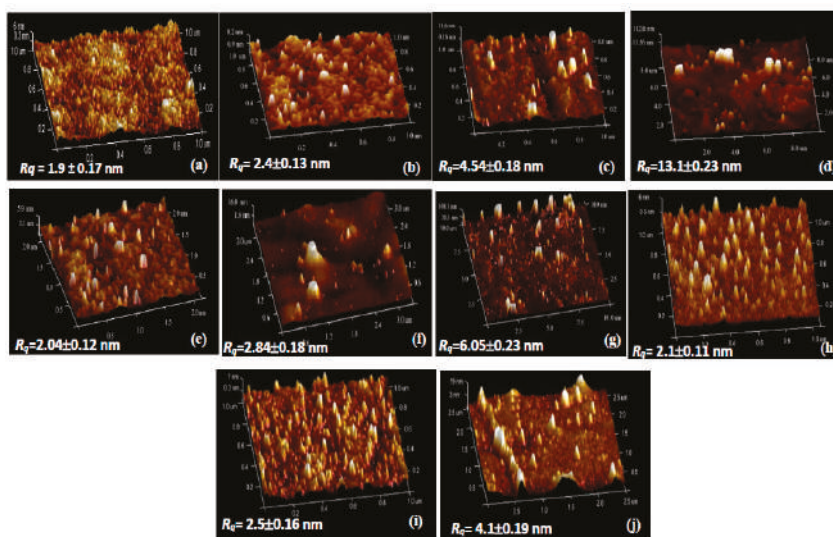


Figure 4. 3D AFM height mapping images of (a) PVA and PVA bionanocomposites reinforced with (b) 3 wt % HNTs, (c) 5 wt % HNTs, (d) 10 wt % HNTs, (e) 3 wt % Cloisite 30B clays, (f) 5 wt % Cloisite 30B clays, (g) 10 wt % Cloisite 30B clays, (h) 3 wt % NBCs, (i) 5 wt % NBCs, and (j) 10 wt % NBCs.

On the other hand, PVA/Cloisite 30B clay bionanocomposites and PVA/NBC bionanocomposites reveal different dispersibilities as opposed to PVA/HNT bionanocomposites. When nanofiller contents are below 10 wt %, spiky nanoparticles appear to be separated from one another, resulting in the homogeneous dispersion of Cloisite 30B clays and NBCs within PVA matrices, as shown in Figure 4e,f, as well as Figure 4h,i accordingly. In particular, as the nanofiller content increases from 3 to 5 wt %, R_q values increase moderately from 2.04 ± 0.12 to 2.84 ± 0.18 nm for PVA/Cloisite 30B clay bionanocomposites, as well as from 2.1 ± 0.11 to 2.5 ± 0.16 nm for PVA/NBC bionanocomposite in contrast with 1.9 ± 0.17 nm for neat PVA. This finding suggests that the smooth surfaces for PVA bionanocomposites are evident at the low nanofiller contents of Cloisite 30B clays and NBCs, which is in good agreement with previous studies of PVA/nanocellulose composite films [39]. On the contrary, the inclusion of 10 wt % Cloisite 30B clays and NBCs in PVA bionanocomposites consistently gives rise to increasing R_q values up to 6.05 ± 0.23 and 4.1 ± 0.19 nm, respectively, which are also far higher than that of neat PVA at 1.9 ± 0.17 nm. Such results indicate that the presence of aggregated Cloisite 30B clays and NBCs results in a much higher surface roughness on PVA surfaces, as expected. In comparison, the R_q value of 4.1 ± 0.19 nm for PVA/NBC bionanocomposites appears to be relatively low as compared with those of other PVA nanocomposites reinforced with carbon-based fillers such as PVA/reduced graphene oxide (rGO) nanocomposites with a R_q value of 4.6 ± 0.55 nm based on deposition layers [40].

Notwithstanding that the same manufacturing process condition and nanofiller contents have been utilised for preparing PVA bionanocomposite films, different nanoparticle types play an important role in changing the degree of surface roughness. Overall, with increasing the nanofiller content, the surface roughness of PVA bionanocomposites in this study is enhanced to a different extent, as evidenced by increasing the maximum relative change of surface roughness up to 589.4%, 218.4%, and 115.8%, respectively with the inclusion of HNTs, Cloisite 30B clays, and NBCs at the same filler content of 10 wt % shown in Figure 5. Such results suggest that NBCs may have better ability to be dispersed uniformly in PVA matrices as opposed to HNTs and Cloisite 30B clays due to their least increasing level in surface roughness, especially when beyond 5 wt % in filler content. Whereas, the effect of different nanoparticle shapes and sizes on the surface roughness of PVA bionanocomposites becomes less pronounced at low filler contents below 3 wt %.

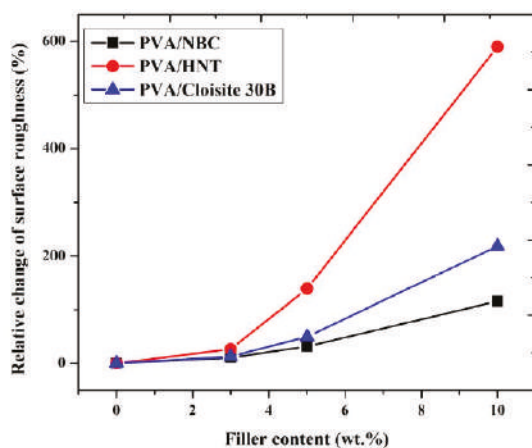


Figure 5. Relative change of surface roughness in terms of filler content in different PVA bionanocomposites.

3.5. Aspect Ratios of Embedded Nanofillers in PVA Bionanocomposites

The aspect ratio of nanofillers is regarded as one of key factors in reinforcement efficiency and mechanical performance of nanocomposites, which is generally defined as the ratio between the

largest dimensions over the smallest dimension of nanofillers. According to this fundamental concept, the largest dimension of nanofillers can be represented by the lengths of tubular HNTs and platelet-like Cloisite 30B clays or the diameters of NBCs, while the smallest dimension is represented by the diameter of HNTs or thickness of Cloisite 30B clays and NBCs [28].

For instance, it is well known that when nanoclays are uniformly dispersed within polymer matrices, the formation of their exfoliated or intercalated structures leads to the improvement of the mechanical performance of nanocomposites to different extent, which is totally different from agglomerated nanoclays, resulting in the deterioration of their mechanical properties [1].

To investigate the degree of clay-exfoliated structures in detail, the height profiles of clay platelets relative to those of PVA matrices have been determined (Figure S1 in the Supporting Information). The thickness of 3 wt % Cloisite 30B clays within PVA matrices in bionanocomposites appears to be in range of 0.85–1.43 nm, suggesting typical exfoliated clay structures in dispersion. MMT clays are well known to be exfoliated when their thickness is similar to that of individual clay platelets (i.e., ~1 nm) [18]. Gaume et al. [33] and other groups [41,42] also detected intercalated and exfoliated structures of MMT clays in the thickness range of 1.3–5 nm.

The surface roughness mentioned earlier can be associated with nanofiller shapes and sizes since HNTs and Cloisite 30B clays may possess relatively high aspect ratios when compared with those of NBCs despite an existing ‘nanofiller waviness’ issue. HNTs and Cloisite 30B clays with high aspect ratios inevitably undergo considerable wavy nanofiller formation, thus undermining their homogeneous dispersion within polymer matrices [28]. Moreover, ultrasonication, as an effective fine nanoparticle dispersion technique in this study, also enables potentially damaging nanofiller structures particularly by applying high-power intensity or using a longer sonication time [43]. As such, the specific sizes/dimensions of nanofillers may vary to different extent, which are required to be determined for embedded HNTs, Cloisite 30B clays, and NBCs in PVA bionanocomposites to calculate their actual aspect ratios, as evidenced in Figure 6. The relevant frequency distribution of nanofiller dimensions are presented in Figures S2–S4 in Supporting Information as the reference. It is clearly revealed that the aspect ratios of nanofillers increase from 5.91 to 10.60 for HNTs in Figure 6a–c, as well as 5.75 to 8.17 for NBCs in Figure 6g–i with increasing the nanofiller content from 3 to 10 wt %. In contrast, the aspect ratios of Cloisite 30B clays decrease from 22.70, 12.38 to 13.46 when increasing the clay contents from 3, 5 to 10 wt % accordingly, despite their overall highest aspect ratios among all the nanofillers, as shown in Figure 6d–f. Such findings imply that the majority of Cloisite 30B clays tend to form exfoliated or intercalated clay structures with relatively high aspect ratios. However, the decrease in the aspect ratios of Cloisite 30B clays can be associated with more severe clay aggregation. It is very convincing that the aspect ratios of nanofillers can be greatly influenced by nanofiller shapes, and apparently 3D NBC nanoparticles have relatively low aspect ratios when compared with 1D platelet-like Cloisite 30B clays [28].

Overall, the aspect ratio may play a significant role in mechanical performance of nanocomposites when nanofiller shapes or structures are only considered within polymer matrices. However, for different types of nanofillers, several other factors such as the number of particles per unit volume, interphase modulus, interphase volume, and surface area, as well as the ratio of interphase volume per nanoparticle volume should also be taken into account for their overall material properties.

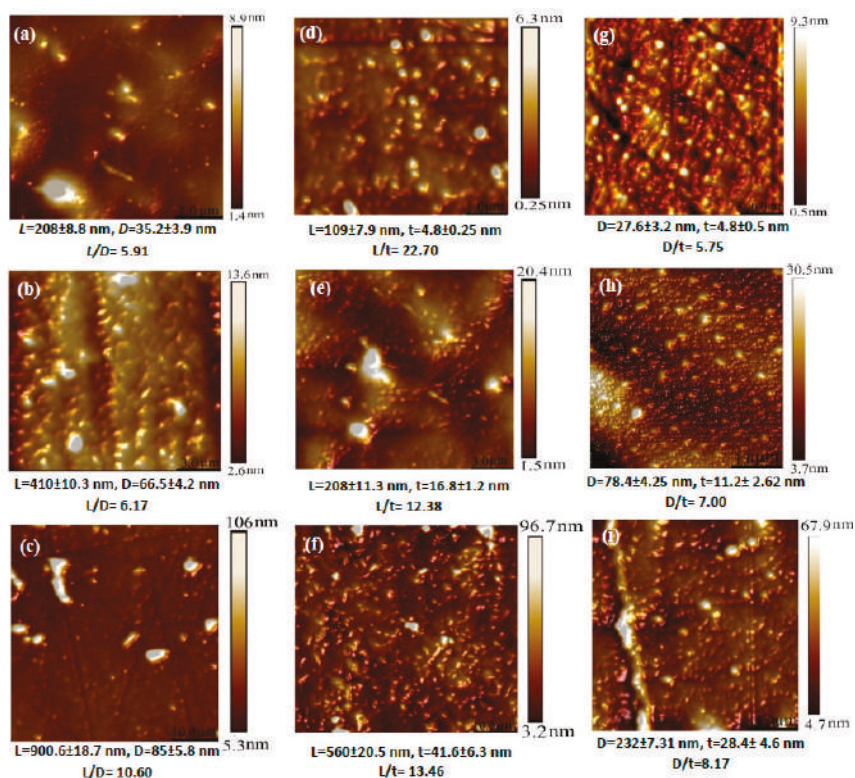


Figure 6. AFM topographic images of PVA bionanocomposites associated with aspect ratios of embedded fillers: (a) 3 wt % HNTs, (b) 5 wt % HNTs, (c) 10 wt % HNTs, (d) 3 wt % Cloisite 30B clays (e) 5 wt % Cloisite 30B clays, (f) 10 wt % Cloisite 30B clays, (g) 3 wt % NBCs (h) 5 wt % NBCs, and (i) 10 wt % NBCs.

3.6. Mechanical Properties

Figure 7 displayed the mechanical properties of PVA bionanocomposites reinforced with HNTs, Cloisite 30B clays, and NBCs at different nanofiller contents. Overall, the tensile moduli of such bionanocomposites increase significantly in a monotonic manner with the increasing nanofiller content, as shown in Figure 7a. The addition of only 3 wt % HNTs, Cloisite 30B clays, and NBCs result in increasing the tensile moduli by 40%, 52%, and 70.67% as opposed to that of neat PVA at 2.08 GPa, which is in good accordance with the previous results obtained in PVA/starch/ glycerol (GL)/HNT nanocomposites [44] and PVA/chitosan/HNT nanocomposites [45]. More remarkably, the maximum increases in tensile modulus are achieved by 61.5%, 84.1%, and 123% with the addition of 10 wt % HNTs, Cloisite 30B clays, and NBCs, respectively when compared with that of neat PVA. This phenomenon usually takes place for most polymers filled with more rigid inorganic nanoparticles, as the reinforcements lead to much stiffer nanocomposite materials [46]. In particular, NBCs induce more reinforcement efficiency as nanofillers when compared with Cloisite 30B clays and HNTs. This can be clearly seen from the overall relatively high tensile moduli of PVA/NBC bionanocomposites, arising from much closer interactions between PVA matrices and NBCs via the formation of mechanical and hydrogen bonds owing to highly porous structures of NBCs. On the other hand, a different trend for the tensile strengths of PVA/NBC bionanocomposites is clearly revealed from those of PVA/Cloisite 30B clay bionanocomposites and PVA/HNT bionanocomposites, as shown in Figure 7b. The tensile

strength of PVA/HNT nanocomposites is improved by 23% with the addition of 3 wt % HNTs relative to that of neat PVA at 70.32 MPa. Nonetheless, a drastic strength-decreasing tendency takes place with the strength reductions of 3.2% and 13.9% when embedded with 5 and 10 wt % HNTs accordingly. Such results indicate that the enhancement of tensile strengths for PVA/HNT nanocomposites depends on effective stress transfer from PVA matrices to HNTs, resulting from homogeneous HNT dispersion within PVA matrices. On the contrary, increasing the HNT content inevitably causes noticeable particle aggregation with more stress concentration sites around HNT agglomerates as a result of potential crack initiation to deteriorate the mechanical performance of bionanocomposites. With respect to PVA/Cloisite 30B clay bionanocomposites, their tensile strengths are increased by 18.8% and 28.4% with the incorporation of 3 and 5 wt % Cloisite 30B clays, respectively. This finding is ascribed to more uniform clay dispersion as well as the formation of stronger matrix–filler network structures, resulting from increasing hydrogen bonding between these constituents due to larger clay surface areas [47,48]. When the Cloisite 30B clay content increases up to 10 wt %, the tensile strength of PVA/Cloisite 30B clay bionanocomposites is decreased by 5.16% as opposed to that of neat PVA. This phenomenon suggests that the aggregation of nanofillers at high clay content levels can undermine the tensile strengths of bionanocomposites. On the contrary, the tensile strengths of PVA/NBC bionanocomposites have the initial improvement up to 147.94 MPa (by a maximum level of 110.4%) when the NBC content increases from 0 to 3 wt %. Beyond 3 wt % NBCs, the tensile strengths of such bionanocomposites tend to decline until they reach the lowest strength levels of 96.34 MPa at the NBC content of 10 wt %. However, such lowest strength levels are still better than that of neat PVA. Overall, both tensile moduli and tensile strengths of PVA/NBC bionanocomposites are consistently superior to those of PVA/HNT bionanocomposites and PVA/Cloisite 30B bionanocomposites to confirm the most effective reinforcement efficiency of NBCs among all three different nanofillers.

The elongation at break and tensile toughness of PVA/Cloisite 30B clay bionanocomposites and PVA/NBC bionanocomposites were continuously decreased, especially beyond the nanofiller content of 3 wt %, as shown in Figure 7c,d. The maximum decreasing levels by approximately 59.5% and 58% in elongation at break have been detected for PVA bionanocomposites reinforced with 10 wt % Cloisite 30B clays and NBCs, respectively. This finding can be associated with the stiffening effect from filler reinforcements of NBCs and Cloisite 30B clays to restrict the mobility of PVA molecular chains, thus resulting in the overall flexibility reduction in bionanocomposite films [49]. As for PVA/HNT bionanocomposites, elongation at break and tensile toughness are increased by 12.7% and 16.9% with the incorporation of 3 wt % HNTs. Beyond that, they both remarkably diminish until maximum reductions of 50% and 45.3% take place at the HNT content of 10 wt %, respectively, as opposed to those of PVA. The former finding can be explained by good particle–matrix interactions with more uniform particle dispersion at low HNT contents. Whereas, the latter result can be associated with typical particle agglomeration at high HNT contents up to 10 wt % with the disappearance of the ‘nano effect’ of HNTs, since most HNT aggregates become less favourable microfillers with poor particle dispersion. As such, those HNT aggregates act as typical defects with high stress concentration prone to crack initiation towards mechanical failure, thus leading to poor material toughness [36].

In this study, the incorporation of three different nanofillers (i.e., HNTs, Cloisite 30B clays, and NBCs) has successfully enhanced the mechanical properties of PVA bionanocomposite films. According to our results, the highest increasing level among PVA/HNT bionanocomposites and PVA/NBC bionanocomposites can be achieved at the filler content of 3 wt %, as opposed to the optimum content of 5 wt % for PVA/Cloisite 30B clay bionanocomposites. Nonetheless, such an increasing rate achieved in PVA bionanocomposites using three types of nanofillers appears to be quite different, which is associated with various nanofiller features in terms of their structures and geometries, as well as the degree of compatibility between nanofillers and polymer matrices. With respect to nanofiller shape, it is well known that NBCs are regarded as 3D nanofillers as opposed to 2D nanofillers for HNTs and 1D nanofillers for Cloisite 30B clays. Different nanofiller shapes thereby influence the overall interfacial areas between fillers and polymer matrices, which plays a key

role in the improvement of tensile strengths of nanocomposites with different levels of filler–matrix interactions. The second aspect is related to the structures, particularly the location of hydroxyl groups for nanofiller structures and amounts of hydroxyl groups within nanofillers. In the case of NBCs, hydroxyl groups are located inside their pores, which tend to more closely interact with PVA from a 3D point of view. As for HNTs, the majority of hydroxyl groups are constrained in inner tubes between layers, which makes the matrix–HNT interaction limited to the inner tubes of HNTs only. Moreover, in the case of Cloisite 30B clays, hydroxyl groups are located between layered structures, which means that the interactions between polymer matrices and platelet-like clays are limited to small highly constrained interlayer areas. The highest tensile moduli and tensile strength of bionanocomposite films have been achieved with the incorporation of NBCs relative to that of PVA. Several reasons can explain the above-mentioned results in relation to the mechanical properties of bionanocomposites. First, 3D nanofiller shape of NBCs can be generated at low nanofiller contents and in small particle sizes with relatively large interfacial areas, as compared with 2D HNTs and 1D Cloisite 30B clays. Liu and Brinson [2] investigated the effect of nanofiller geometry on the reinforcing efficiency of nanocomposites, which shows that at a low nanofiller content with the random nanofiller orientation, the transverse modulus of nanoparticle-based nanocomposites significantly exceeded those of nanotube-based nanocomposites, as well as nanoplatelet-based nanocomposites. Schadler et al. [50] reported that in the case of a nanocomposite system, with the incorporation of nanoparticles and nanotubes having a nanofiller diameter of 10 nm at the volume fraction of 10 vol%, the volume fraction of interfacial polymers was about 30% in the case of nanoparticle-based nanocomposites as opposed to only 10% for nanotube-based nanocomposites. The second reason in relation to the high mechanical performance of PVA/NBC bionanocomposites can be ascribed to the chemical structures of nanofillers in terms of the amounts and locations of hydroxyl groups in order to control the nanofiller dispersion within bionanocomposites, thus reflecting upon the bonding between polymer matrices and nanofillers. Pakzad et al. [51] indicated that the number and nature of hydrogen bonds had a substantial effect on the mechanical properties of nanocomposites. In the case of PVA/3 wt % NBC bionanocomposites, NBCs have highly porous structures with a large amount of hydroxyl groups located inside these pores when NBCs are uniformly dispersed. As confirmed by the FTIR and XRD results, polymeric chains enter these pores and form both hydrogen and mechanical bondings. Such two bonding types can be particularly recognised for NBCs as compared to Cloisite 30B clays and HNTs, thus significantly reflecting upon the enhanced mechanical properties of nanocomposites [4,5]. In case of PVA/5 wt % Cloisite 30B clay bionanocomposites in comparison to PVA/5 wt % HNT bionanocomposites, the strong adhesion of clays in polymer matrices associated with uniform clay dispersion leads to the strong interfacial bonding between nanoclays and polymer matrices, which thus significantly contributes to the improvement of mechanical properties of bionanocomposites.

The dispersion state of nanofillers can also influence the mechanical properties of PVA bionanocomposites. As mentioned earlier, NBCs have a better dispersion state than Cloisite 30B clays and HNTs. The incorporation of NBCs within PVA matrices yields smoother bionanocomposite films with higher tensile strength when compared with those of PVA/HNT bionanocomposites and PVA/Cloisite 30B clay bionanocomposites. The better dispersion state of NBCs improves their interaction with PVA matrices, thus leading to the higher tensile strengths of PVA/NBC bionanocomposites. On the contrary, increasing the nanofiller content appears to induce higher surface roughness as well as lower tensile strengths of nanocomposites, which indicates that nanofiller agglomeration apparently has detrimental effect on the improvement of tensile strength. This is particularly the case for PVA/HNT bionanocomposites due to the poor HNT dispersion state. On the contrary, PVA/3 wt % HNT bionanocomposites yield much higher elongation at break and fracture toughness as opposed to those of neat PVA, which are different from PVA/3 wt % NBC bionanocomposites and PVA/5 wt % Cloisite 30B clay bionanocomposites with corresponding lower values. Such results can be clearly explained by two major reasons. The first reason is ascribed to the number of nanoparticles depending on the volume and volume fraction of nanoparticles in bionanocomposites. At the same volume fraction,

the number of NBCs is significantly larger than those of tubular HNTs or platelet-like Cloisite 30B clays. As such, this finding results in increasing the number of available reinforcements for improving the matrix rigidity and then decreasing the fracture toughness [43,52]. The second reason is related to the mechanism of fracture toughness, including the pre-crack effect for the fracture of nanocomposites. In general, crack deflection and crack pinning are most well-known mechanisms resulting in an increase in fracture energy [53], and consequently an increase in fracture toughness of nanocomposites. In both mechanisms mentioned earlier, the crack growth path can increase as long as those cracks reach nanofiller regions and the reinforcement shape highly affects the amount of crack deviation from their initial path. Since HNTs have larger lateral dimensions in comparison with NBCs, the cracks tend to pass over longer distances in PVA bionanocomposites reinforced with HNTs. Moreover, crack bridging is also well recognised as a fracture mechanism in nanocomposites reinforced with nanoparticles with a high aspect ratio [43]. An ideal situation in this mechanism occurs when nanotube fillers are still embedded in matrices while aligned in a perpendicular direction to crack faces. Consequently, PVA/HNT bionanocomposites achieve less reduction in fracture toughness when compared with the PVA/Cloisite 30B bionanocomposites and PVA/NBC bionanocomposites in Figure 7d.

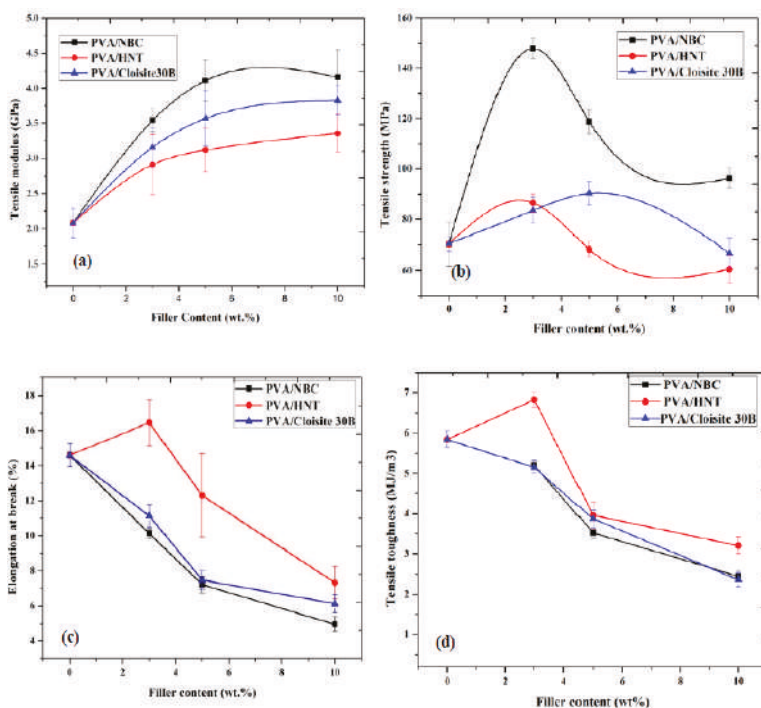


Figure 7. Mechanical properties of PVA bionanocomposites at different filler contents: (a) tensile modulus, (b) tensile strength, (c) elongation at break, and (d) tensile toughness.

3.7. Fracture Morphology

Figure 8 shows typical SEM micrographs of cross-sectional fracture surfaces for PVA, PVA/HNT bionanocomposites, PVA/Cloisite 30B clay bionanocomposites, and PVA/NBC bionanocomposites. It can be clearly seen in Figure 8b,e that PVA bionanocomposites reinforced with 3 wt % of HNTs and Cloisite 30B clays reveal much rougher fractured surfaces when compared with that of neat PVA films, as illustrated in Figure 8a. Moreover, 3 wt % HNTs or Cloisite 30B clays are distributed uniformly within PVA matrices. The good dispersion of both nanoparticles and the strong interaction between clay

particles and polymer matrices clearly contribute to the reinforcing effect, as reflected by the increase in both tensile strength and elastic modulus. Nevertheless, in both PVA/HNT bionanocomposite and PVA/Cloisite 30B clay bionanocomposite systems, uniform multi-layered structures have not been achieved similar to those detected in PVA/3 wt % NBC bionanocomposites, as illustrated in Figure 8h. Such results are indicative of high NBC dispersability as compared with those of HNTs and Cloisite 30B clays, resulting in the highest mechanical performance. Meanwhile, at the HNT content of 5 wt %, particle–particle interactions are more favourable than their particle–matrix counterparts, as evidenced by more filler agglomeration in the presence of debonding and microvoid effects depicted in Figure 8c. Such defects in nanocomposite systems give rise to the decreasing tensile strengths of PVA/HNT bionanocomposites. However, as for PVA/5 wt % Cloisite 30B clay bionanocomposites, the clay dispersion appears to be still relatively uniform with the presence of small particle agglomeration shown in Figure 8f. With increasing the nanofiller contents of HNTs and Cloisite 30B clays from 5 to 10 wt %, the fracture surfaces of bionanocomposites films are altered from ductile characteristic to more brittle behaviour, as illustrated in Figure 8d,g, respectively. Similar phenomena are also found in PVA/NBC bionanocomposites according to Figure 8j. As is well known, decreasing surface roughness reveals that the failure mode of PVA bionanocomposite films can be quite different by changing from ductile to brittle fracture [54], which is consistent with the reduced mechanical properties of bionanocomposite films in this study.

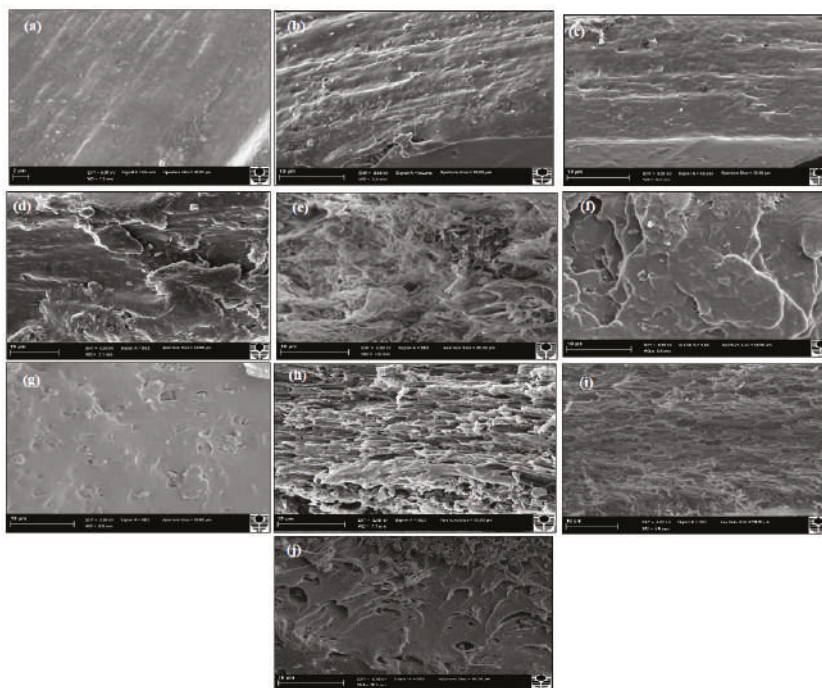


Figure 8. SEM micrographs of tensile fracture surfaces: (a) PVA, (b) PVA/3 wt % HNT bionanocomposites, (c) PVA/5 wt % HNT bionanocomposites, (d) PVA/10 wt % HNT bionanocomposites, (e) PVA/3 wt % Cloisite 30B clay bionanocomposites, (f) PVA/5 wt % Cloisite 30B bionanocomposites, (g) PVA/10 wt % Cloisite 30B clay bionanocomposites, (h) PVA/3 wt % NBC bionanocomposites, (i) PVA/5 wt % NBC bionanocomposites and (j) PVA/10 wt % NBC bionanocomposites. Note that Figure 8a shows the SEM micrograph with a scale bar of 2 μm while the rest of micrographs are labelled with a scale bar of 10 μm .

3.8. Thermal Properties

PVA is a water-soluble semicrystalline polymer, in which high physical interchain and intrachain interactions exist because of the typical hydrogen bonding between hydroxyl groups. The inclusion of nanoclays with hydroxyl groups can alter the intramolecular and intermolecular interactions of PVA molecular chains. This may affect both the crystallisation behaviour and physical structures of PVA. Similar observations can be found in previous studies dealing with PVA/HNT bionanocomposites [46,55].

Figure 9 shows the DSC results of PVA/HNT bionanocomposites, PVA/Cloisite 30B clay bionanocomposites, and PVA/NBC bionanocomposites. The summarised data of these thermal characteristics are reported in Table S1 in Supporting Information. For PVA/HNT bionanocomposites, it is clearly seen that the glass transition temperature T_g of PVA becomes unchanged with the addition of HNTs in bionanocomposite films, implying that HNTs do not play an important role in inhibiting the chain mobility of PVA molecules. Qiu and Netravali [46] also reported a similar result in T_g with the incorporation of HNTs into PVA. Such a finding might be related to the reduction in the entanglements and interactions of PLA polymeric chains with HNT inclusions. The relatively unchanged T_g in PVA/HNT bionanocomposites, as compared to that of neat PVA, may arise from different nanofiller geometries. The diameters of HNTs are at a nanoscaled level as opposed to submicron- or microsized tubular lengths that considerably exceed the typical gyration radii of polymeric chains [4]. As a result, HNTs cannot be completely wrapped by PVA molecular chains leading to many voids surrounding HNT particles. On the contrary, the high T_g values for all PVA/Cloisite 30B clay bionanocomposites are evident, as opposed to that of neat PVA. With the incorporation of 3, 5 and 10 wt % Cloisite 30B clays, the T_g values of such PVA bionanocomposites are moderately enhanced up to 67.5, 70.2 and 71.8 °C, respectively when compared with that of neat PVA at 65.19 °C. This phenomenon can be attributed to the confinement of polymeric chains by intercalated clay structures to prevent their segmental motions [1], which has also been recorded in PVA/MMT nanocomposites [56,57], PVA/bentonite nanocomposites [58], as well as PVA/starch/MMT nanocomposites [59]. In the case of PVA/NBC bionanocomposites, the T_g increases monotonically up to 75.06 °C with increasing the NBC content from 0 to 10 wt % accordingly. The incorporation of rigid NBC particles can restrict the chain mobility of PVA matrices so that higher T_g values are required for the phase transformation of nanocomposites from a glassy state to a rubbery state. This finding is well known for many types of nanofillers such as nanoclays, GOs, CNTs, HNTs, etc. [1]. Overall, the T_g values of PVA bionanocomposite films with the incorporation of NBCs and Cloisite 30B clays are much higher than those of PVA/HNT bionanocomposites. Such results indicate that NBCs and Cloisite 30B clays can restrict PVA chains more efficiently, as evidenced by the enhanced mechanical properties of corresponding bionanocomposite films. According to previous studies [60,61], the phenomenon of increasing T_g is primarily associated with the reduction in polymeric chain mobility by incorporating inorganic nanofillers. The incorporation of nanoparticles into polymer matrices can change the distribution of chain segments, which is most likely due to a change in the chain packing density in the vicinity of nanofiller surfaces. It should be noted that filler geometry may play a critical role to influence T_g . NBCs and Cloisite 30B clays have different nanofiller shapes to render the absorption of polymeric chains with entangled structures on their surfaces when nanofiller diameters are comparable to the gyration radii of polymeric chains. As such, it leads to increasing the packing density for polymeric chains and restricting their chain mobility as a result of higher T_g values. However, the incorporation of HNTs into PVA matrices has a minor impact on increasing T_g instead, which is consistent with the previous work [55]. Although the diameter of HNTs is on the nanometer scale, their length turns to be submicron- or microsized, which becomes considerably higher than the typical gyration radii of polymeric chains. As a consequence, it is very difficult for polymeric chains to cover entire HNT structures. Moreover, the presence of microvoids along HNT lengths could offer free sites for the segments of polymeric chains, resulting in an insignificant increase of T_g [55].

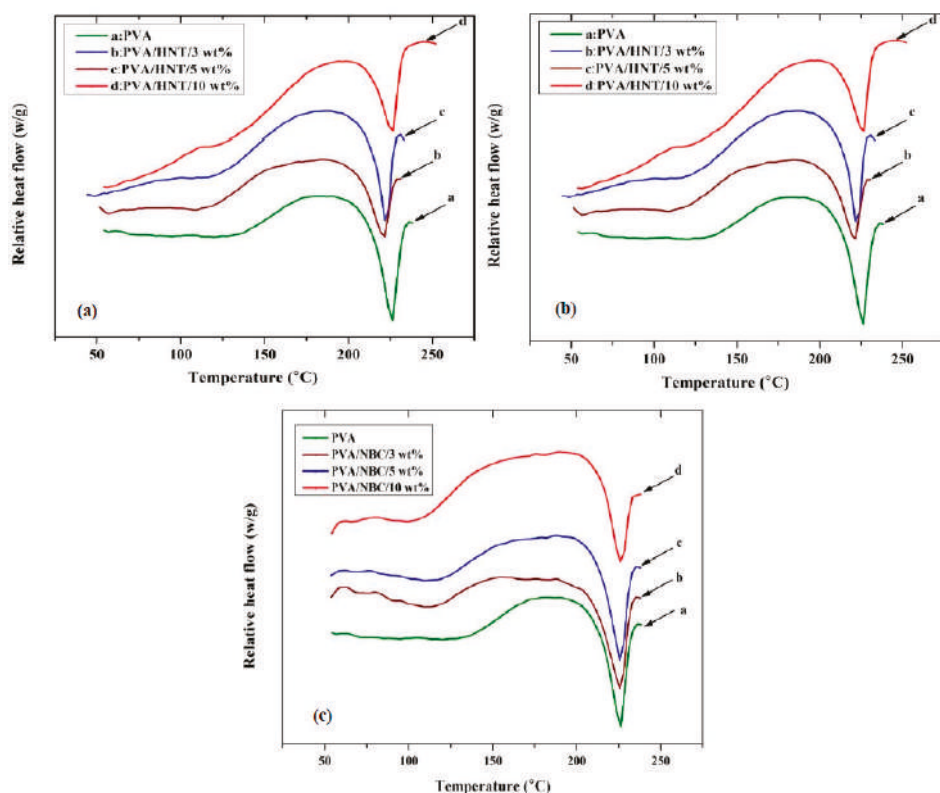


Figure 9. Differential scanning calorimetry (DSC) thermograms of PVA bionanocomposites reinforced with (a) HNTs, (b) Cloisite 30B clays, and (c) NBCs. The curves are shifted vertically for clarity.

The degree of crystallinity (χ_c) of PVA slightly increases from 36.65% for neat PVA to 38.2% and 37.2%, 40% for corresponding bionanocomposites with the incorporation of 5 wt % HNTs and Cloisite 30B clays and 10 wt % of NBCs, respectively. This suggests that such nanofillers have minor effect on the crystalline phases of PVA matrices in bionanocomposites. On the other hand, the melting temperature T_m of PVA bionanocomposites virtually has no change with the addition of Cloisite 30B clays and NBCs, as evidenced by the given T_m ranges of 220.44–221.62 °C and 221–225 °C, respectively when compared with that of neat PVA at 222.91 °C. However, PVA/HNT bionanocomposites possess a moderate increase in T_m up to 226.67 °C with the inclusion of 10 wt % HNTs. A similar phenomenon has also been noticed in PHBV/HNT nanocomposites [28] with their T_m values being increased from 169 to 173 °C when incorporated with 5 wt % HNTs. Based on their XRD results, thicker and more oriented HNT/PHBV structures could be formed, leading to higher melting temperatures.

The thermal decomposition behaviours of PVA/HNT bionanocomposites, PVA/Cloisite 30B clay bionanocomposites, and PVA/NBC bionanocomposites have been evaluated using thermogravimetric analysis (TGA) with the corresponding results being presented in Figures 10 and 11, as well as Table S1 in Supporting Information. The relevant results for both systems reveal the existence of three major degradation steps according to previous studies [21]. Initially, the first degradation takes place at 107 °C owing to the breakage of hydrogen bonds, impurities, and monomers of vinyl alcohol. Then, the second degradation occurring at 274 °C involves a dehydration reaction on PVA molecular chains, the degradation of main backbones, as well as the decomposition of organic clays. This process is accompanied by a drastic mass change caused by the removal of organic compounds such as

CO₂ and the long molecular chains of alkyl derivatives. Finally, the third degradation step appears at a temperature level below 429 °C with more complexity including the further degradation of polyene residues to yield the carbon and hydrocarbon. The incorporation of HNTs, Cloisite 30B clays, and NBCs can increase the thermal stability of PVA by reducing the weight loss and increasing the decomposition temperatures, as presented in Figures 10 and 11. As for PVA/HNT bionanocomposites, the decomposition temperature at 5% weight loss $T_{5\%}$ increases from 200.2 °C for PVA to 265.3, 268.1, and 270.2 °C for PVA bionanocomposites reinforced with 3, 5 and 10 wt % HNTs, respectively. Such a finding suggests that HNTs work as an effective barrier material to heat and mass transfer. Moreover, the intrinsic hollow tubular structures of HNTs can produce the traps for volatile particles, thus improving the thermal stability by delaying the mass transfer during a decomposition process. Moreover, as clearly seen from the derivative thermogravimetry (DTG) curves in Figure 11a, the maximum decomposition temperature T_d of PVA shifts to a higher temperature level, which means that the dehydration process is hindered, resulting from strong interactions between PVA matrices and HNTs, as well as an important role of HNTs as good barrier materials to increase the thermal resistance of PVA bionanocomposites. Furthermore, the second DTG peaks of PVA/HNT bionanocomposites reinforced with 5 and 10 wt % HNTs are much wider than that of neat PVA in the presence of main and side peaks as compared to the single DTG peak for PVA at the same step. This signifies that a single peak for PVA can be attributed to the eliminated reaction while the side and main peaks of PVA/HNT bionanocomposites correspond to the eliminated reaction as well as the overlap of continual elimination and chain-scission reaction with the requirement of more energy to accrue at high temperatures [60].

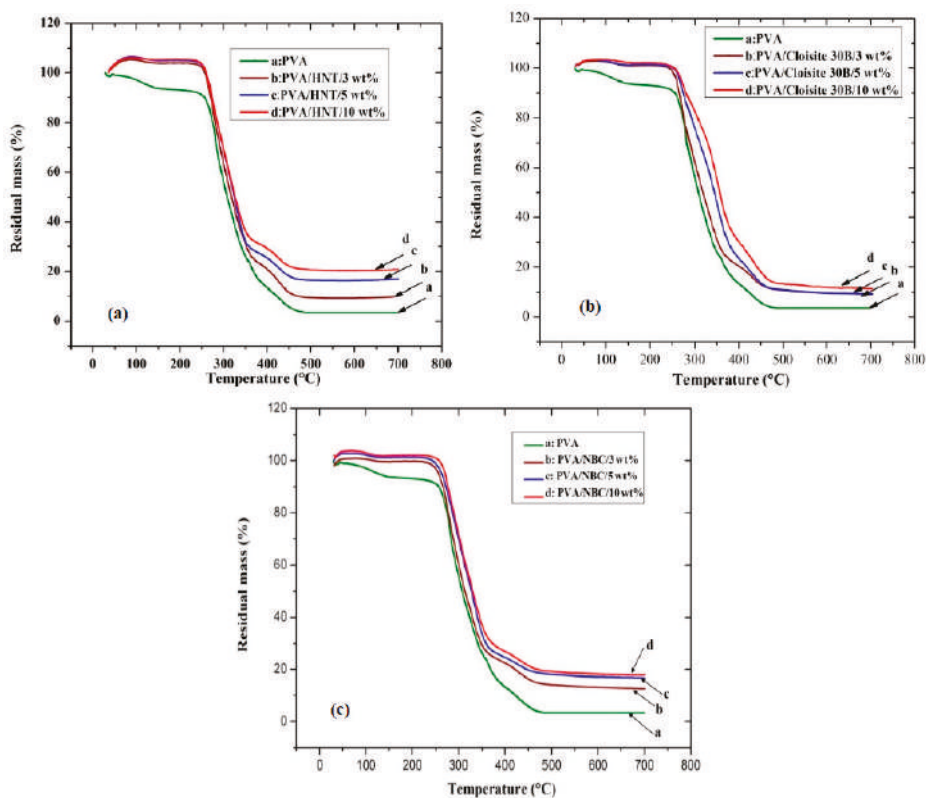


Figure 10. TGA curves for PVA bionanocomposites reinforced with (a) HNTs, (b) Cloisite 30B clays, and (c) NBCs.

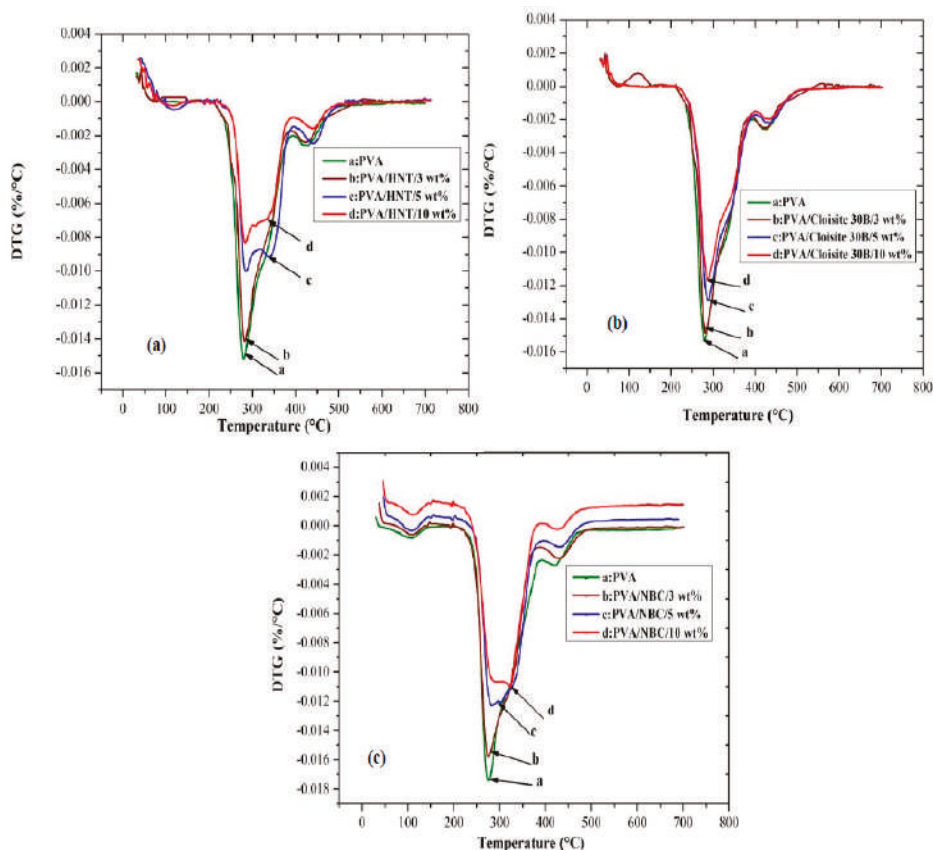


Figure 11. DTG curves for PVA bionanocomposites reinforced with (a) HNTs, (b) Cloisite 30B clays, and (c) NBCs.

On the other hand, in the case of PVA/Cloisite 30B clay bionanocomposites, with increasing the clay content, the thermal stability of bionanocomposites improves as compared to that of PVA, which is evidently demonstrated from consistently high $T_{5\%}$, $T_{80\%}$, and T_d values shown in Figure 10b. For instance, the $T_{80\%}$ of PVA increases from 363.5 to 407 °C with the inclusion of 5 wt % Cloisite 30B clays. Such a result is in good agreement with previous studies of PVA/MMT nanocomposites [21,62]. Moreover, the shift in the decomposition temperatures T_d for PVA/Cloisite 30B bionanocomposites depicted in Figure 11b suggests the hindrance of a dehydration process. Such a finding in thermal stability is associated with the presence of nanolayers acting as the barriers to maximise the heat insulation and minimise the permeability of volatile degradation products in the materials. This increase is also attributed to the decrease in oxygen permeability related to good clay dispersion in PVA matrices.

Moreover, the thermal stabilities of PVA/NBC bionanocomposites are improved significantly relative to that of PVA, as evidenced by consistently higher $T_{5\%}$, $T_{80\%}$, and T_d values, as shown in Figure 10c. The degree of thermal stability of bionanocomposites is even more pronounced when incorporated with NBCs in relation to $T_{5\%}$ and $T_{80\%}$. The $T_{5\%}$ of PVA/3 wt % NBC bionanocomposites was determined to be 256.3 °C, and it increases to 262.95 °C with the incorporation of 5 wt % NBCs, which is relatively similar to that of PVA/5 wt % Cloisite 30B bionanocomposites at 261.1 °C. On the other hand, the $T_{5\%}$ of PVA/3 wt % HNT bionanocomposites appears to be determined at 265.29 °C,

which is significantly higher as compared with PVA bionanocomposites reinforced with NBCs and Cloisite 30B clays. On the contrary, the $T_{80\%}$ of PVA/3 wt % NBC bionanocomposites has been found to be 390.67 °C and reaches 440.28 °C with the inclusion of 5 wt % NBCs, which is significantly higher than those of PVA bionanocomposites reinforced with HNTs and Cloisite 30B clays. This result infers that the maximum thermal stability is achieved in the presence of NBCs as compared with HNTs and Cloisite 30B clays. As opposed to other nanofillers, the better NBC dispersion within PVA matrices takes place along with the higher barrier towards the thermal degradation. Therefore, such a barrier effect can counterbalance the degradation drawback with the further improvement of thermal stability [5].

The shift of maximum decomposition temperatures for the first and second degradation steps T_d and T_d' in Figure 11c also means the obstruction of the dehydration process, which can result from the interaction between the hydroxyl groups of PVA and the hydroxyl groups on NBCs, as confirmed from our previous FTIR results. Furthermore, the mass loss process occurring in the second DTG peaks suggests that the thermal decomposition of PVA bionanocomposites requires more reaction activation energy with the higher reaction order [63]. This finding may be attributed to the existence of NBCs working as effective barrier materials to limit the exothermicity of pyrolysis reaction with the better thermal resistance of PVA bionanocomposites. The wider DTG peaks of PVA/NBC bionanocomposites beyond 3 wt % NBCs at the second decomposition step demonstrates a similar trend to those of the corresponding PVA/HNT bionanocomposites along with the same dual-peak effect, as mentioned elsewhere [63].

4. Conclusions

PVA bionanocomposites reinforced with Cloisite 30B clays, HNTs, and NBCs have been successfully prepared and characterised. The following conclusions can be drawn.

The properties of PVA/HNT bionanocomposites are remarkably affected when embedding HNTs, which primarily depend on the HNT content. Nanofiller dispersion can lead to various morphological structures resulting in enhanced mechanical properties at different levels for such bionanocomposites. In particular, the incorporation of 3 wt % HNTs has improved mechanical properties, while increasing the HNT content beyond that causes the decreases in tensile strength, elongation at break, and tensile toughness of PVA/HNT bionanocomposites, which is possibly associated with the typical filler–matrix debonding effect. Moreover, the thermal properties of PVA/HNT bionanocomposites in terms of the degree of crystallinity, melting temperature, and thermal stability are enhanced with increasing the HNT content as opposed to those of neat PVA films.

The morphological structures of PVA/Cloisite 30B clay bionanocomposites demonstrate uniform clay dispersion within PVA matrices in combined clay exfoliated and intercalated structures, which are in agreement with those obtained from XRD results. The tensile strengths and Young's moduli of PVA/Cloisite 30B clay bionanocomposite films are increased considerably with increasing the clay content up to 5 wt % amid decreasing elongation at break and fracture toughness. The thermal properties of PVA/Cloisite 30B clay bionanocomposites are improved compared to those of neat PVA films due to the strong hydrogen-bonding interactions between PVA matrices and nanofillers.

The effect of different nanofiller shapes and structures on the properties of PVA/NBC bionanocomposite films reveals that the maximum tensile strength and tensile modulus can be achieved with the incorporation of NBCs. This can be related to the large amount of interphase resulting from a high degree of filler dispersion in the case of PVA/NBC bionanocomposites relative to those reinforced with HNTs and Cloisite 30B clays. Moreover, the thermal stability of PVA/NBC bionanocomposites is remarkably enhanced with the inclusion of NBCs in contrast to those incorporated with HNTs and Cloisite 30B clays. This can be ascribed to the uniform dispersion of NBCs to generate more efficient interfacial regions as opposed to other nanofillers.

Supplementary Materials: The following are available online at <http://www.mdpi.com/2073-4360/12/2/264/s1>, Figure S1: Characterisations of PVA/ 3wt% Cloisite 30B clay bionanocomposites: (a) height mapping image and (b) height profiles on cut-line sections AS_1 - BS_1 and AS_2 - BS_2 , Figure S2: Frequency distributions of dimensions of

HNTs embedded within PVA/HNT bionanocomposites at different HNT contents: (a) and (b) for HNT length and diameter (3 wt% HNTs), (c) and (d) for HNT length and diameter (5 wt% HNTs), as well as (e) and (f) for HNT length and diameter (10 wt% HNTs), Figure S3: Frequency distributions of dimensions of Cloisite 30B clays embedded within PVA/Cloisite 30B clay bionanocomposites at different clay contents: (a) and (b) for clay length and thickness (3 wt% Cloisite 30B clays), (c) and (d) for clay length and thickness (5 wt% Cloisite 30B clays), as well as (e) and (f) for length and thickness (10 wt% Cloisite 30B clays), Figure S4: Frequency distributions of dimensions of NBCs embedded within PVA/NBC bionanocomposites at different NBC contents: (a) and (b) for NBC thickness and diameter (3 wt% NBCs), (c) and (d) for NBC thickness and diameter (5 wt% NBCs), as well as (e) and (f) for NBC thickness and diameter (10 wt% NBCs), Table S1: Thermal properties of PVA bionanocomposite films.

Author Contributions: M.M. did the experimental work and the characterisation of material samples, M.M. and Y.D. analysed the data, jointly prepared, and approved the final research manuscript. All authors have read and agreed to the published version of the manuscript.

Funding: This research is financially supported by the Higher Committee for Education Development (HCED) in Iraq through a scholarship awarded to M.M to study at Curtin University, Australia.

Conflicts of Interest: The authors declare no conflict of interest.

References

1. Mousa, M.H.; Dong, Y.; Davies, I.J. Recent advances in bionanocomposites: Preparation, properties, and applications. *Int. J. Polym. Mater. Polym. Biomater.* **2016**, *65*, 225–254. [[CrossRef](#)]
2. Liu, H.; Brinson, L.C. Reinforcing efficiency of nanoparticles: A simple comparison for polymer nanocomposites. *Compos. Sci. Technol.* **2008**, *68*, 1502–1512. [[CrossRef](#)]
3. Dung, M.X.; Choi, J.-K.; Jeong, H.-D. Newly synthesized silicon quantum dot–polystyrene nanocomposite having thermally robust positive charge trapping. *ACS Appl. Mater. Interfaces* **2013**, *5*, 2400–2409. [[CrossRef](#)] [[PubMed](#)]
4. Mousa, M.; Dong, Y. Strong poly (vinyl alcohol) (PVA)/bamboo charcoal (BC) nanocomposite films with particle size effect. *ACS Sustain. Chem. Eng.* **2017**, *6*, 467–479. [[CrossRef](#)]
5. Mousa, M.; Dong, Y.; Davies, I.J. Eco-friendly polyvinyl alcohol (PVA)/bamboo charcoal (BC) nanocomposites with superior mechanical and thermal properties. *Adv. Compos. Mater.* **2018**, *27*, 499–509. [[CrossRef](#)]
6. Maliakal, A.; Katz, H.; Cotts, P.M.; Subramoney, S.; Mirau, P. Inorganic oxide core, polymer shell nanocomposite as a high K gate dielectric for flexible electronics applications. *JACS* **2005**, *127*, 14655–14662. [[CrossRef](#)]
7. Bogdanović, U.; Vodnik, V.; Mitrić, M.; Dimitrijević, S.; Skapin, S.D.; Zunic, V.; Budimir, M.; Stoiljkovic, M. Nanomaterial with high antimicrobial efficacy-copper/polyaniline nanocomposite. *ACS Appl. Mater. Interfaces* **2015**, *7*, 1955–1966. [[CrossRef](#)]
8. Makvandi, P.; Gu, J.T.; Zare, E.N.; Ashtari, B.; Moeini, A.; Tay, F.R.; Niu, L. Polymeric and inorganic nanoscopic antimicrobial fillers in dentistry. *Acta Biomater.* **2020**, *101*, 69–101. [[CrossRef](#)]
9. Makvandi, P.; Ali, G.W.; Sala, F.D.; Abdel-Fattah, W.I.; Borzacchiello, A. Hyaluronic acid/corn silk extract based injectable nanocomposite: A biomimetic antibacterial scaffold for bone tissue regeneration. *Mater. Sci. Eng. C* **2020**, *107*, 110195. [[CrossRef](#)]
10. Garcés, J.M.; Moll, D.J.; Bicerano, J.; Fibiger, R.; McLeod, D.G. Polymeric nanocomposites for automotive applications. *Adv. Mater.* **2000**, *12*, 1835–1839. [[CrossRef](#)]
11. Naskar, A.K.; Keum, J.K.; Boeman, R.G. Polymer matrix nanocomposites for automotive structural components. *Nat. Nanotechnol.* **2016**, *11*, 1026–1030. [[CrossRef](#)] [[PubMed](#)]
12. Mousa, M.; Dong, Y. Novel three-dimensional interphase characterisation of polymer nanocomposites using nanoscaled topography. *Nanotechnology* **2018**, *29*, 385701. [[CrossRef](#)] [[PubMed](#)]
13. Komarov, P.; Mikhailov, I.; Chiu, Y.T.; Chen, S.M.; Khalatur, P. Molecular dynamics study of interface structure in composites comprising surface-modified SiO₂ nanoparticles and a polyimide matrix. *Macromol. Theory Simul.* **2013**, *22*, 187–197. [[CrossRef](#)]
14. Meng, D.; Kumar, S.K.; Lane, J.M.D.; Grest, G.S. Effective interactions between grafted nanoparticles in a polymer matrix. *Soft Matter* **2012**, *8*, 5002–5010. [[CrossRef](#)]
15. Ganesan, V.; Jayaraman, A. Theory and simulation studies of effective interactions, phase behavior and morphology in polymer nanocomposites. *Soft Matter* **2014**, *10*, 13–38. [[CrossRef](#)]

16. Wierckx, N.; Narancic, T.; Eberlein, C.; Wei, R.; Drzyzga, O.; Magnin, A.; Ballerstedt, H.; Kenny, S.T.; Pollet, E.; Avérous, L.; et al. Plastic biodegradation: Challenges and opportunities. In *Consequences of Microbial Interactions with Hydrocarbons, Oils, and Lipids: Biodegradation and Bioremediation*; Steffan, R., Ed.; Springer: Cham, Switzerland, 2019; pp. 1–29.
17. Haroosh, H.J.M. Investigating Novel Biopolymeric Nanostructures for Drug Delivery. Ph.D. Thesis, Curtin University, Perth, Australia, 2014.
18. Ploehn, H.J.; Liu, C. Quantitative analysis of montmorillonite platelet size by atomic force microscopy. *Ind. Eng. Chem. Res.* **2006**, *45*, 7025–7034. [[CrossRef](#)]
19. Aloui, H.; Khwaldia, K.; Hamdi, M.; Fortunati, E.; Kenny, J.M.; Buonocore, G.G.; Lavorgna, M. Synergistic effect of halloysite and cellulose nanocrystals on the functional properties of PVA based nanocomposites. *ACS Sustain. Chem. Eng.* **2016**, *4*, 794–800. [[CrossRef](#)]
20. Ramadan, A.R.; Esawi, A.M.; Gawad, A.A. Effect of ball milling on the structure of Na⁺-montmorillonite and organo-montmorillonite (Cloisite 30B). *Appl. Clay Sci.* **2010**, *47*, 196–202. [[CrossRef](#)]
21. Mallakpour, S.; Shahangi, V. Bio-modification of Cloisite Na⁺ with chiral L-leucine and preparation of new poly (vinyl alcohol)/organo-nanoclay bionanocomposite films. *Synth. React. Inorg. Met. Org. Nano Met. Chem.* **2013**, *43*, 966–971. [[CrossRef](#)]
22. Fu, D.; Zhang, Y.; Lv, F.; Chu, P.K.; Shang, J. Removal of organic materials from TNT red water by bamboo charcoal adsorption. *Chem. Eng. J.* **2012**, *193*, 39–49. [[CrossRef](#)]
23. She, B.; Tao, X.; Huang, T.; Lu, G.; Zhou, Z.; Guo, C.; Dang, Z. Effects of nano bamboo charcoal on PAHs-degrading strain *Sphingomonas* sp. GY2B. *Ecotoxicol. Environ. Saf.* **2016**, *125*, 35–42. [[CrossRef](#)] [[PubMed](#)]
24. Lorenzoni, M.; Evangelio, L.; Verhaeghe, S.; Nicolet, C.; Navarro, C.; Pérez-Murano, F. Assessing the local nanomechanical properties of self-assembled block copolymer thin films by peak force tapping. *Langmuir* **2015**, *31*, 11630–11638. [[CrossRef](#)] [[PubMed](#)]
25. Babu, S.S.; Mathew, S.; Kalarikkal, N.; Thomas, S. Antimicrobial, antibiofilm, and microbial barrier properties of poly (ϵ -caprolactone)/cloisite 30B thin films. *Biotech* **2016**, *6*, 249. [[CrossRef](#)] [[PubMed](#)]
26. Huang, D.; Wang, W.; Kang, Y.; Wang, A. A chitosan/poly (vinyl alcohol) nanocomposite film reinforced with natural halloysite nanotubes. *Polym. Compos.* **2012**, *33*, 1693–1699. [[CrossRef](#)]
27. Abdullah, Z.W.; Dong, Y.; Davies, I.J.; Barbhuiya, S. PVA, PVA blends, and their nanocomposites for biodegradable packaging application. *Polym. Plast. Technol. Eng.* **2017**, *56*, 1307–1344. [[CrossRef](#)]
28. Carli, L.N.; Crespo, J.S.; Mauler, R.S. PHBV nanocomposites based on organomodified montmorillonite and halloysite: The effect of clay type on the morphology and thermal and mechanical properties. *Compos. Part A Appl. Sci. Manuf.* **2011**, *42*, 1601–1608. [[CrossRef](#)]
29. Ray, S.S.; Okamoto, M. Polymer/layered silicate nanocomposites: A review from preparation to processing. *Prog. Polym. Sci.* **2003**, *28*, 1539–1641.
30. Swapna, V.; Suresh, K.; Saranya, V.; Rahana, M.; Stephen, R. Thermal properties of poly (vinyl alcohol)(PVA)/halloysite nanotubes reinforced nanocomposites. *Inter. J. Plast. Technol.* **2015**, *19*, 124–136.
31. Rhim, J.-W.; Hong, S.-I.; Ha, C.-S. Tensile, water vapor barrier and antimicrobial properties of PLA/nanoclay composite films. *LWT-Food Sci. Technol.* **2009**, *42*, 612–617. [[CrossRef](#)]
32. Strawhecker, K.; Manias, E. Structure and properties of poly (vinyl alcohol)/Na⁺ montmorillonite nanocomposites. *Chem. Mater.* **2000**, *12*, 2943–2949. [[CrossRef](#)]
33. Gaume, J.; Taviot-Gueho, C.; Cros, S.; Rivaton, A.; Therias, S.; Gardette, J.-L. Optimization of PVA clay nanocomposite for ultra-barrier multilayer encapsulation of organic solar cells. *Sol. Energy Mater. Sol. Cells* **2012**, *99*, 240–249. [[CrossRef](#)]
34. Li, R.S.; Li, X.; Deng, Q.; Li, D. Three kinds of charcoal powder reinforced ultra-high molecular weight polyethylene composites with excellent mechanical and electrical properties. *Mater. Des.* **2015**, *85*, 54–59. [[CrossRef](#)]
35. Liang, J.; Huang, Y.; Zhang, L.; Wang, Y.; Ma, Y.; Guo, T.; Chen, Y. Molecular-level dispersion of graphene into poly (vinyl alcohol) and effective reinforcement of their nanocomposites. *Adv. Funct. Mater.* **2009**, *19*, 2297–2302. [[CrossRef](#)]
36. Cheng, Z.L.; Qin, X.X.; Liu, Z.; Qin, D.Z. Electrospinning preparation and mechanical properties of PVA/HNTs composite nanofibers. *Polym. Adv. Technol.* **2017**, *28*, 768–774. [[CrossRef](#)]

37. Azmi, S.; Razak, S.I.A.; Abdul Kadir, M.R.; Iqbal, N.; Hassan, R.; Nayan, N.H.M.; Abdul Wahab, A.H.; Shaharuddin, S. Reinforcement of poly (vinyl alcohol) hydrogel with halloysite nanotubes as potential biomedical materials. *Soft Mater* **2017**, *15*, 45–54. [[CrossRef](#)]
38. Ormanci-Acar, T.; Celebi, F.; Keskin, B.; Mutlu-Salmanli, O.; Agtas, M.; Turken, T.; Tufani, A.; Imer, D.Y.; Ince, G.O.; Demir, T.U.; et al. Fabrication and characterization of temperature and pH resistant thin film nanocomposite membranes embedded with halloysite nanotubes for dye rejection. *Desalination* **2018**, *429*, 20–32. [[CrossRef](#)]
39. Hakalahti, M.; Mautner, A.; Johansson, L.-S.; Hanninen, T.; Setälä, H.; Kontturi, E.; Bismarck, A.; Tammelin, T. Direct interfacial modification of nanocellulose films for thermoresponsive membrane templates. *ACS Appl. Mater. Interfaces* **2016**, *8*, 2923–2927. [[CrossRef](#)]
40. Humood, M.; Qin, S.; Song, Y.; Polychronopoulou, K.; Zhang, Y.; Grunlan, J.C.; Polycarpou, A.A. Influence of graphene reduction and polymer cross-linking on improving the interfacial properties of multilayer thin films. *ACS Appl. Mater. Interfaces* **2016**, *9*, 1107–1118. [[CrossRef](#)]
41. Carrado, K.A.; Thiyagarajan, P.; Elder, D.L. Polyvinyl alcohol-clay complexes formed by direct synthesis. *Clays Clay Miner.* **1996**, *44*, 506–514. [[CrossRef](#)]
42. Theng, B.K.G. Clay–polymer interactions: Summary and perspectives. *Clays Clay Miner.* **1982**, *30*, 1–10. [[CrossRef](#)]
43. Alishahi, E.; Shadlou, S.; Doagou, R.S.; Ayatollahi, M.R. Effects of carbon nanoreinforcements of different shapes on the mechanical properties of epoxy-based nanocomposites. *Macromol. Mater. Eng.* **2013**, *298*, 670–678. [[CrossRef](#)]
44. Abdullah, Z.W.; Dong, Y. Preparation and characterisation of poly (vinyl) alcohol (PVA)/starch (ST)/halloysite nanotube (HNT) nanocomposite films as renewable materials. *J. Mater. Sci.* **2018**, *53*, 3455–3469. [[CrossRef](#)]
45. Khoo, W.; Ismail, H.; Ariffin, A. Tensile, swelling, and oxidative degradation properties of crosslinked polyvinyl alcohol/chitosan/halloysite nanotube composites. *Inter. J. Polym. Mater. Polym. Biomater.* **2013**, *62*, 390–396. [[CrossRef](#)]
46. Qiu, K.; Netravali, A.N. Halloysite nanotube reinforced biodegradable nanocomposites using noncrosslinked and malonic acid crosslinked polyvinyl alcohol. *Polym. Compos.* **2013**, *34*, 799–809. [[CrossRef](#)]
47. Sapalidis, A.A.; Katsaros, F.K.; Kanellopoulos, N.K. PVA/montmorillonite nanocomposites: Development and properties. In *Nanocomposites and Polymers with Analytical Methods*; Cuppoletti, J., Ed.; InTechOpen: London, UK, 2011; pp. 29–50.
48. Asad, M.; Saba, N.; Asiri, A.M.; Jawaid, M.; Indarti, E.; Wanrosli, W. Preparation and characterization of nanocomposite films from oil palm pulp nanocellulose/poly (Vinyl alcohol) by casting method. *Carbohydr. Polym.* **2018**, *191*, 103–111. [[CrossRef](#)]
49. Raheel, M.; Yao, K.; Gong, J.; Chen, X.-C.; Liu, D.-T.; Lin, Y.C.; Cui, D.M.; Siddiq, M.; Tang, T. Poly (vinyl alcohol)/GO-MMT nanocomposites: Preparation, structure and properties. *Chin. J. Polym. Sci.* **2015**, *33*, 329–338. [[CrossRef](#)]
50. Schadler, L.; Brinson, L.; Sawyer, W. Polymer nanocomposites: A small part of the story. *JOM* **2007**, *59*, 53–60. [[CrossRef](#)]
51. Pakzad, A.; Simonsen, J.; Yassar, R.S. Gradient of nanomechanical properties in the interphase of cellulose nanocrystal composites. *Compos. Sci. Technol.* **2012**, *72*, 314–319. [[CrossRef](#)]
52. Santos, K.; Castel, C.D.; Liberman, S.; Oviedo, M.; Mauler, R. Polyolefin-based nanocomposite: The effects of processing aids. *J. Appl. Polym. Sci.* **2011**, *119*, 1567–1575. [[CrossRef](#)]
53. Wetzels, B.; Rosso, P.; Haupt, F.; Friedrich, K. Epoxy nanocomposites—fracture and toughening mechanisms. *Eng. Fract. Mech.* **2006**, *73*, 2375–2398. [[CrossRef](#)]
54. Li, Y.; Yang, T.; Yu, T.; Zheng, L.; Liao, K. Synergistic effect of hybrid carbon nanotube–graphene oxide as a nanofiller in enhancing the mechanical properties of PVA composites. *J. Mater. Chem.* **2011**, *21*, 10844–10851. [[CrossRef](#)]
55. Liu, M.; Guo, B.; Du, M.; Jia, D. Drying induced aggregation of halloysite nanotubes in polyvinyl alcohol/halloysite nanotubes solution and its effect on properties of composite film. *Appl. Phys. A* **2007**, *88*, 391–395. [[CrossRef](#)]
56. Yu, Y.-H.; Lin, C.Y.; Yeh, J.M.; Lin, W.H. Preparation and properties of poly(vinyl alcohol)-clay nanocomposite materials. *Polymer* **2003**, *44*, 3553–3560. [[CrossRef](#)]

57. Sirousazar, M.; Kokabi, M.; Hassan, Z.M.; Bahramian, A.R. Polyvinyl alcohol/Na-montmorillonite nanocomposite hydrogels prepared by freezing-thawing method: Structural, mechanical, thermal, and swelling properties. *J. Macromol. Sci Part B* **2012**, *51*, 1335–1350. [[CrossRef](#)]
58. Jose, T.; George, S.C.; Maria, H.J.; Wilson, R.; Thomas, S. Effect of bentonite clay on the mechanical, thermal, and pervaporation performance of the poly(vinyl alcohol) nanocomposite membranes. *Ind. Eng. Chem. Res.* **2014**, *53*, 16820–16831. [[CrossRef](#)]
59. Ali, S.S.; Tang, X.; Alavi, S.; Faubion, J. Structure and physical properties of starch/poly vinyl alcohol/sodium montmorillonite nanocomposite films. *J. Agric. Food Chem.* **2011**, *59*, 12384–12395. [[CrossRef](#)] [[PubMed](#)]
60. Nakane, K.; Yamashita, T.; Iwakura, K.; Suzuki, F. Properties and structure of poly (vinyl alcohol)/silica composites. *J. Appl. Polym. Sci.* **1999**, *74*, 133–138. [[CrossRef](#)]
61. Mbhele, Z.; Salemane, M.; Van Sittert, C.; Nedeljković, J.; Djoković, V.; Luyt, A. Fabrication and characterization of silver–polyvinyl alcohol nanocomposites. *Chem. Mater.* **2003**, *15*, 5019–5024. [[CrossRef](#)]
62. Mondal, D.; Mollick, M.M.R.; Bhowmick, B.; Maity, D.; Bain, M.K.; Rana, D.; Mukhopadhyay, A.; Dana, K.; Chattopadhyay, D. Effect of poly (vinyl pyrrolidone) on the morphology and physical properties of poly (vinyl alcohol)/sodium montmorillonite nanocomposite films. *Prog. Nat. Sci. Mater. Int.* **2013**, *23*, 579–587. [[CrossRef](#)]
63. Peng, Z.; Kong, L.X. A thermal degradation mechanism of polyvinyl alcohol/silica nanocomposites. *Polym. Degrad. Stab.* **2007**, *92*, 1061–1071. [[CrossRef](#)]



© 2020 by the authors. Licensee MDPI, Basel, Switzerland. This article is an open access article distributed under the terms and conditions of the Creative Commons Attribution (CC BY) license (<http://creativecommons.org/licenses/by/4.0/>).

Article

Application of Adaptive Neuro-Fuzzy Inference System in Flammability Parameter Prediction

Rhoda Afriyie Mensah ¹, Jie Xiao ¹, Oisik Das ², Lin Jiang ^{1,*}, Qiang Xu ^{1,*} and Mohammed Okoe Alhassan ¹

¹ School of Mechanical Engineering, Nanjing University of Science and Technology, Nanjing 210094, China; ramensah@gmail.com (R.A.M.); xiaojieblue@163.com (J.X.); mohaokoe2020@yahoo.com (M.O.A.)

² The Division of Material Science, Department of Engineering Sciences and Mathematics, Luleå University of Technology, Luleå 97187, Sweden; oisik.das@ltu.se

* Correspondence: ljiang@njust.edu.cn (L.J.); xuqiang@njust.edu.cn (Q.X.); Tel.: +86-125-84317023 (Q.X.)

Received: 12 December 2019; Accepted: 1 January 2020; Published: 5 January 2020

Abstract: The fire behavior of materials is usually modeled on the basis of fire physics and material composition. However, significant strides have been made recently in applying soft computing methods such as artificial intelligence in flammability studies. In this paper, multiple linear regression (MLR) was employed to test the degree of non-linearities in flammability parameter modeling by assessing the linear relationship between sample mass, heating rate, heat release capacity (HRC) and total heat release (THR). Adaptive neuro-fuzzy inference system (ANFIS) was then adopted to predict the HRC and THR of the extruded polystyrene measured from microscale combustion calorimetry experiments. The ANFIS models presented excellent predictions, showing very low mean training and testing errors as well as reasonable agreements between experimental and predicted datasets. Hence, it can be inferred that ANFIS can handle the non-linearities in flammability modeling, making it apt as a modeling technique for accurate and effective flammability assessments.

Keywords: flammability; heat release rate; microscale combustion calorimetry; multiple linear regression; adaptive neuro-fuzzy inference system

1. Introduction

Material flammability analysis is carried out using flammability characteristics obtained from fire experiments. Fire experiments are grouped into small-scale, bench-scale and full-scale experiments depending on the size of sample required. In reality, full-scale fire experiments provide the best estimates of material flammability since they imitate actual fire scenarios. However, due to the high cost, operational and technical challenges, small-scale experiments have been adopted for flammability evaluations. To validate the accuracy of small-scale experiments, correlation analysis conducted between the different scales of experiments shows feasible relationships in the test results [1–4].

Microscale combustion calorimetry (MCC) is a small-scale fire experiment operated on the principles of oxygen consumption calorimetry. MCC has received significant attention in recent years and remains the most commonly cited fire experiment for polymer flammability assessments due to the wealth of data measured from it [5,6]. Amongst the data is the heat release capacity (HRC), a flammability parameter and material property measured exclusively from the 'Method A' [6] of MCC. HRC integrates thermal stability and combustion properties, hence rendering it the best predictor of a materials response to fire. HRC is defined as the ratio of the maximum value of the specific heat release rate to the average heating rate of a sample [5–9]. The total heat released (THR) is a measure from the total heat released when a sample undergoes a complete combustion in an oxygen atmosphere. THR is also a flammability property calculated from the results measured from the Method A procedure [7,9,10]. Several chemistry-based models, such as inverse modeling, quantitative structure-property relationship

(QSPR), quantitative structure-activity relationship (QSAR) and additive molar group contribution methods, have been developed over the years to estimate these important fire safety parameters (HRC and THR). Although effective, some disadvantages, like large prediction errors, have been identified in the traditional modeling approaches and need to be addressed.

Until now, correlation analysis and statistical prediction models have been appropriate analytical tools in material flammability [11]. The significance of the prediction models lies in the employment of robust techniques and strategies for the accurate estimation of flammability parameters, whereas correlation analysis assesses the relationship between the predicted or measured parameters. Statistical analysis is mostly empirical, devoid of the chemical compositions and physical structure of the material under consideration [12]. It is imperative to note that fire experiments are demanding, expensive and time consuming. Similarly, traditional flammability parameter predictions involve sophisticated fire modeling and calibration, requiring a great deal of expertise and computing power. It is, therefore, quite convenient for researchers to opt for these system theoretical models as opposed to conceptual models. Statistical models in recent times largely embrace the artificial neural network (ANN) due to its ability to capture complex nonlinearities in a system when compared to linear regression methods. ANN mimics the operation of the human brain by processing information available to the input layers to achieve a desirable output.

Generalized regression and the ANN's feed-forward back propagation methods have been applied in flammability studies to predict peak heat release rate, heat release capacity, total heat released, etc., with a high level of accuracy [13,14]. Deviation of the predicted results from the actual or experimental results was seen to be low when compared with classical methods including quantity structure activity/property relationships. Alternative methods, such as the group method of data handling neural network, also enhanced the predictability of the aforementioned methods, as reported by Mensah et al. [15]. It is well-known that the overall performance of these models highly depends on physical variables such as the network architecture, transfer and activation functions. Despite their simple implementation, the iterative process employed to obtain optimal variables for the prediction makes them quite cumbersome.

Adaptive neuro-fuzzy inference system (ANFIS) was developed in the 1990's on the principles of the Takagi-Sugeno fuzzy inference system [16]. This method has been applied in several research areas with an excellent degree of accuracy; however, it has not been applied in flammability studies. It is a hybrid analytical method, i.e., it combines the merits of the neural network and theories of fuzzy logic systems in its operation [17]. Each concept plays an important role in achieving the required result. While neural networks control the representation of information and the physical architecture, fuzzy logic systems imitate human reasoning and increase the model's ability to manage uncertainty within the system [17]. ANFIS basically learns the features of a given data and alters the system parameters to suit the required error criterion of the system in order to generate an output. It utilizes less computing power with shorter training times and, therefore, serves as a suitable method for the prediction of flammability parameters [18,19].

In the current study, an MCC experiment was conducted with extruded polystyrene samples at heating rates ranging from 0.1 to 3.5 K s⁻¹. This research explored the applicability of ANFIS in the prediction of HRC and THR derived from the experiment. The degree of accuracy was determined by comparing the root mean squared error (RMSE) criterion, the coefficient of correlation and the coefficient of determination. A comparative analysis was carried out with multiple linear regression and the feed-forward back propagation neural network to show the efficacy, accuracy and superiority of ANFIS. The modeling results obtained from this research will help validate the robustness of ANFIS and its continual usage in future flammability assessments.

2. Experimental Methods

2.1. Material

The flammability of pure extruded polystyrene (XPS) obtained from Zhengbang New Building Material Co. Ltd. located at Zaozhuang, China was studied. The samples were cut from large boards of XPS into milligram sizes for the experiments. The Mettler AX-205 Analytical Semi Micro Balance Delta Range from Hamilton company in Reno, NV, US. The instrument has a readability of 0.01 mg and a weighing range of 81 g was used to weigh the samples. The material properties are listed in Table 1 [5,11].

Table 1. Properties of XPS.

Property	Value
Thermal conductivity/Wm ⁻¹ K ⁻¹	0.1316
Thermal diffusivity/m ² s ⁻¹	0.4201
Specific heat capacity/kJ g ⁻¹ K ⁻¹	1.34
LOI %	19.3
Density, ρ/kg m ⁻³	52.6
Density of molten material, ρ/kg m ⁻³	828

2.2. Microscale Combustion Calorimetry (MCC)

The MCC experiment took place at the VTT Technical research center of Finland in MCC-2 equipment from Govmark (Farmingdale, NY, US) Limited. According to standards in ASTM D7309-13 [20], the experimental procedure applied was in line with Method A. Milligram samples taken from extruded polystyrene boards were weighed and prepared for the MCC experiment. Samples of mass ranging from 1 to 4 mg were heated at a temperature of 75 to 600 °C in a pyrolyzer under heating rates ranging from 0.1 to 3.5 K s⁻¹. The volatile pyrolysis products were removed from the pyrolyzer by nitrogen gas and were oxidized with excess oxygen at 900 °C in a tubular combustion furnace. Oxygen consumption calorimetry was applied for calculating the heat release rate from the volumetric flow rate and the oxygen concentration of the gases that flowed out of the combustor [6,13,14,20]. The samples were tested in three replicates and an average of the measured results was recorded. The samples were labelled as xps_1_0.1 representing the first sample tested under 0.1 K s⁻¹, and so on. The heat release temperature, time to heat release and heat release rate were measured and recorded. HRC was obtained by dividing the specific heat release rate by the corresponding heating rate. Additionally, THR was calculated from the area under the specific heat release rate against time plots at a given heating rate.

2.3. Adaptive Neuro-Fuzzy Inference System (ANFIS)

The artificial neural network has a unique quality of learning the input and output datasets for the system and reproducing accurate values to match the data. Fuzzy logic, on the other hand, has the capability of interpreting, organizing, representing and also adding an element of reasoning to an applied data. A Fuzzy Inference System (FIS) is made up of four distinct components, namely a fuzzifier, fuzzy rules, inference engine and a de-fuzzifier [17]. With a given input dataset, the output of an FIS is determined by building the fuzzy rules, fuzzifying the inputs with the membership functions, developing a rule strength and finding its consequences. The consequences are then put together to obtain an output distribution, which is then further de-fuzzified. There are two types of FIS, the Mamdani and Sugeno types. The Mamdani type FIS requires the use of fuzzy rules to link fuzzy set to outputs, which are de-fuzzified to produce scalar variables. The Sugeno FIS is quite similar to the Mamdani type, however, no output distribution or output membership function is included in the system. Instead, to obtain the output, the inputs are multiplied by a constant and the results are added [21].

A combination of ANN and FIS, therefore, employs the architecture of ANN with its learning ability and integrates fuzzy reasoning to add logic and the prior knowledge effect. With this method, ANN accurately learns the membership functions of a fuzzy logic system in order to build the input data of the model, which is organized as fuzzy IF-THEN rules by the FIS. This hybridization is carried out to ensure the optimization of the parameters used in developing the FIS with an application of a learning algorithm for input-output mapping. The architecture of a typical ANFIS structure that has two input variables with five layers is presented in Figure 1 [21]. It must be noted that the squares and circles in Figure 1 represent adaptive nodes and fixed nodes, respectively.

The first layer has four adaptive nodes showing the premise parameters A_1, A_2, B_1, B_2 . The fuzzy IF-THEN rules for Figure 1 are described below.

Rule 1: If x is A_1 and y is B_1 , then

$$f_1 = p_1x + q_1y + r_1. \tag{1}$$

Rule 2: If x is A_2 and y is B_2 , then

$$f_2 = p_2x + q_2y + r_2 \tag{2}$$

where p_i, q_i, r_i are the consequent parameters and $i = 1, 2$. The first layer has two inputs x and y representing the heating rate and sample mass, respectively, with one output (either HRC or THR). The values in each input variable are changed to a membership value using the assigned membership functions. The membership function usually applied for ANFIS is the generalized bell function. The output of Layer 1, which is also the fuzzy membership value, is denoted as O_i , representing the value for any i th node in layer j . The operations in the adaptive nodes are shown in Equations (1) and (2).

$$O_{1,i} = \mu_{A_i}(x), \quad i = 1, 2 \tag{3}$$

$$O_{1,i} = \mu_{B_{i-2}}(y), \quad i = 3, 4 \tag{4}$$

From Equations (1) and (2), $O_{1,i}$ represents the membership function (generalized bell function, triangular function or Gaussian function) of the fuzzy set A_1, A_2, B_1, B_2 , which also shows the connection between the input set x and y and the fuzzy set. The variables A_i and B_{i-2} are all parameters in the i th node of layer j .

$$\mu_{A_i}(x) = \left\{ 1 + \left[\frac{(x - c_i)}{a_i^2} \right]^{b_i} \right\}^{-1} \tag{5}$$

The membership functions can be expressed in mathematical forms as Equations (4)–(7).

$$\begin{aligned} \text{Triangular: } \mu_x(a) &= \frac{(a-x)}{(y-x)}, x \leq a \leq y \\ &= \frac{(z-a)}{(z-y)}, y \leq a \leq z \\ &= 0 \end{aligned} \tag{6}$$

$$\text{Gaussian: } \mu_x(a) = \frac{1}{1 + \left(\frac{a-z}{x}\right)^2} \tag{7}$$

Bell shaped:

$$\mu_{X_i}(a) = \frac{1}{1 + \left(\frac{a-z_i}{x_i}\right)^{2x_i}}, \quad i = 1, 2, \dots \tag{8}$$

$$\mu_{Y_j}(b) = \frac{1}{1 + \left(\frac{b-z_j}{y_j}\right)^{2y_j}}, \quad j = 1, 2, \dots \tag{9}$$

Altering the consequent parameters of the membership function will subsequently produce a different membership function and ensures the flexibility in defining membership functions.

Layer 2 contains fixed nodes that operate on multiplication rules. In Layer 2, the product of the various input signals is obtained to generate rule-firing strengths. This operation is presented in Equation (8).

$$O_{2,i} = \omega_i = \mu_{A_i}(x) \times \mu_{B_i}(x), i = 1, 2 \tag{10}$$

Normalization of the firing strengths attained in the second layer takes place in Layer 3. The ratio of the firing strength of the *i*th rule to the sum of rules in the model is assessed at this point. The mathematical expression of the normalization process is shown in Equation (9) [22–25].

$$O_{3,i} = \bar{\omega}_i = \frac{\omega_i}{\omega_1 + \omega_2}, i = 1, 2 \tag{11}$$

The rules for the outputs are computed in the fourth layer. The consequent parameters are adjusted until an optimal value is obtained with minimal errors. This layer is made up of adaptive nodes, which helps in calculating the total output of the developed model. The output of Layer 3, $\bar{\omega}_i$, is multiplied by a parameter set $\{a_i, b_i, c_i\}$ to get the output of Layer 4 [26].

$$O_{4,i} = \bar{\omega}_i f_i = \bar{\omega}_i(p_i x + q_i y + r_i) \tag{12}$$

Lastly, the various outputs in Layer 4 are added up to obtain the final output of the ANFIS model. Layer 5 has one fixed node with a summation function operation [17].

$$O_{5,i} = \sum_i \bar{\omega}_i f_i \tag{13}$$

The neuro-fuzzy app designer in Matlab provides a very simple platform for ANFIS predictions. After loading the training and test data, the app trains the data to shape the membership functions and generates fuzzy rules for the calculation of the output data. The language recognition and reasoning aspect is handled by the fuzzy logic part of the app.

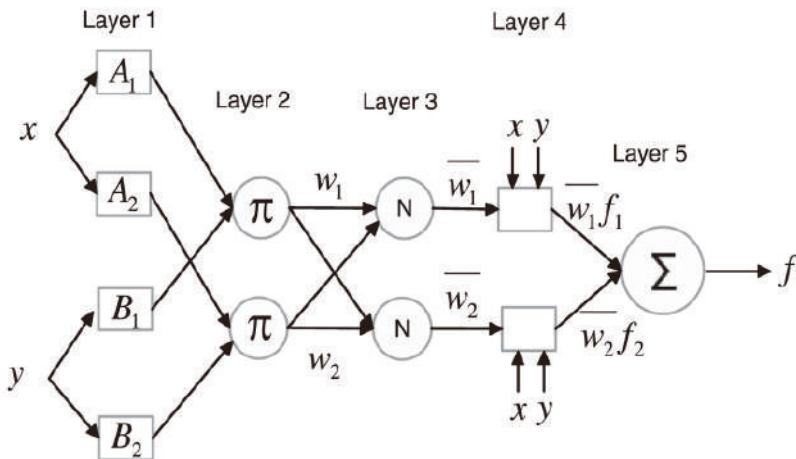


Figure 1. Structure of Adaptive Neuro Fuzzy Inference System.

2.4. Multiple Linear Regression (MLR)

Regression analysis is used to evaluate the cause-effect relationship among variables in a given dataset with the aim of developing prediction equations. Multiple linear regression is a statistical method applied to describe how several explanatory variables define a corresponding dependent variable. MLR basically models the linear relationship between dependent and independent variables [27]. MLR fits a linear equation of the form shown in Equation (12) to the observed data. The coefficients in the fitted equation show the effect of or the changes in the dependent variable when the independent variables change by one unit, while the constant attached (ϵ) shows the value of the dependent variable if all the other variables are zero.

$$y_i = \beta_0 + \beta_1 x_{i1} + \beta_2 x_{i2} + \dots + \beta_p x_{ip} + \epsilon \quad (14)$$

where for any $i = n$ observations, y_i is the dependent variable (HRC and THR), x_i represents the independent variable (sample mass and heating rate) and the y-intercepts are denoted by β_0 and β_p , representing the slope coefficients of x_i . Lastly, the error obtained during the modeling process is represented by ϵ . The degree of linearity is evaluated using the coefficient of determination, while the error term accounts for the variation or the difference between the predicted and actual variables. To ascertain the suitability of conducting MLR on a specific dataset, various tests such as the linearity, normality, missing value test and extreme value test are conducted [28,29].

2.5. Model Implementation

ANFIS prediction technique was applied to estimate the heat release capacity and total heat released of extruded polystyrene samples. The Sugeno method was used since it is known to display faster convergence and better accuracy than the Mamdani method [15]. A trial and error method was used to select the optimal membership function for the model. The membership function that presented the least root mean squared error was chosen. The other variables such as the optimization method (hybrid or back propagation), method of generating FIS (sub-clustering or grid partition), the number of membership functions within a hidden layer, the types of composition function and interference were selected based on the minimum error approach. The MCC experimental data, divided into training and testing sets, were used as input data in the neuro-fuzzy designer app built in MATLAB (R2018a). The computer used for the training has the following specifications: 64-bit operating system and a 4 GB memory with an i3-4005U CPU @ 1.70 GHz processor. The suitable structure for the model was selected depending on the data size and application. The necessary parameters were selected and the model was trained to evaluate the learning ability and determine the structural parameters (consequence and premise) with an optimization algorithm. The hybrid optimization algorithm is an integration of the gradient descent and the least squares method [21]. The outputs of the various nodes are forward propagated until it reaches the fourth layer. The consequent parameters in this section are determined by the least-squares method. The errors attained are back propagated, and the premise parameters are altered and adjusted using the gradient descent algorithm. The error factor in ANFIS is defined as presented in Equation (13).

$$E = \sum_{k=1}^n (f_k - f'_k)^2 \quad (15)$$

Basically, the hybrid method employs different algorithms for each of the training parts, hence, eliminating the local minima convergence and increasing the performance of the model. The overall performance was assessed using the test patterns in the Neuro-Fuzzy Designer app [21].

3. Results and Discussion

3.1. MCC Experimental Results

The specific heat release rate of XPS measured during the MCC experiment is plotted against temperature in Figure 2. The figure affirms the relationship between HRR, heating rate and temperature at peak HRR (pTemp), which is that the heat release rate and the corresponding heat release temperature increases with the increasing heating rate. Figures 3 and 4 also show the variation of HRC with respect to sample mass and heating rate. On average, 1.5 mg samples had the highest HRC values compared to the other masses. More distinct lines at lower heating rates are shown in Figure 4, which are the HRC values versus the inverse of heating rate [11,14,30–32].

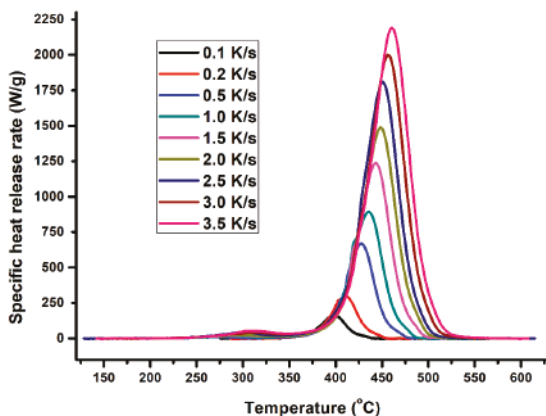


Figure 2. Plot of specific heat release rate versus temperature.

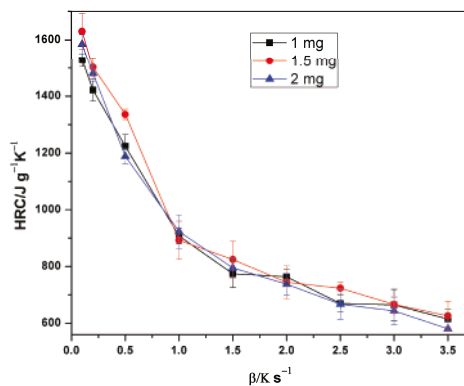


Figure 3. Plot of Heat Release Capacity versus heating rate for different sample masses.

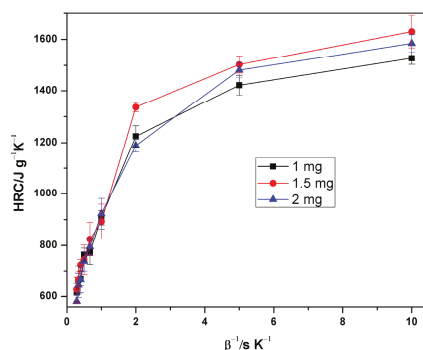


Figure 4. Plot of HRC versus inverse of heating rate for different sample masses.

3.2. Statistical Analysis

To determine the regression equation using multiple regression analysis, HRC and THR were selected as the independent variables with heating rate and sample mass being the dependent variables. The descriptive statistics of the input data are listed in Table 2. The analysis of variance showing the influence of HRC and THR on heating rate and sample mass in this regression analysis is presented in Tables 3 and 4. It is clearly seen that the dependent variables have a greater significance in the estimation of HRC than THR. The test statistic of HRC has an F-value of 53.85, which is larger than the critical value $F_{0.05, 2, 25} = 3.385$. This analysis signifies that there is a significant statistical difference in the means of the variables. However, the F-value for THR is quite smaller than the critical value; hence, the null hypothesis for equal population means cannot be rejected.

Table 2. Descriptive statistics of experimental data.

	N	Mean	SD	Sum	Min	Max
HRC/J g ⁻¹ K ⁻¹	28	966.64571	349.69697	27,066.08	580.4	1630
THR/kj g ⁻¹	28	32.10357	1.29257	898.9	28.6	34.6
Heating rate	28	1.56786	1.1757	43.9	0.1	3.5
Mass	28	1.49607	0.41362	41.89	0.93	2.11

Table 3. Analysis of variance for HRC.

	DF	Sum of Squares	Mean Square	F Value	Prob > F
Model	2	2.68×10^6	1.34×10^6	53.85	8.68×10^{-10}
Error	25	622,061.52	24,882.46		
Total	27	3.31×10^6			

Table 4. Analysis of variance for Total Heat Release.

	DF	Sum of Squares	Mean Square	F Value	Prob > F
Model	2	3.20	1.60	0.95	0.39
Error	25	41.91	1.68		
Total	27	45.11			

In Table 5, the multiple linear regression model summarized for HRC and THR are presented. It can be seen that the adjusted R-square for HRC is higher than THR. HRC has a linear relationship with sample mass and heating rate, while THR is almost constant throughout the range of heating rates applied. It should be noted that to get a very accurate prediction of these flammability parameters,

especially for THR, a method that can handle non-linear modeling could be used. Hence, the next section applies ANFIS networks in the prediction of HRC and THR.

Table 5. Summary of regression analysis.

HRC/J g ⁻¹ K ⁻¹			THR/kJ g ⁻¹		
Variable	Value	Std. Error	Variable	Value	Std. Error
Constant	1392.82	120.32	Constant	31.42	0.99
Heating rate	-267.94	25.82	Heating rate	0.29	0.22
Sample mass	-4.07	73.4	Sample mass	0.16	0.61
Adjusted R ²		0.8	Adjusted R ²		0.033

3.3. ANFIS Network Prediction Results

The present study employed ANFIS networks to model the relationship between sample mass, heating rate, heat release capacity and total heat release rate measured from the MCC experiment. To develop the ANFIS model, the hold-out data splitting technique was adopted. Twenty-four randomly selected data-points out of the 28 experimental data were used for training, while the remaining 4 represented the test data for the model. For improved accuracy, the test data covered the entire range of the available dataset. Table 6 shows the datasets used for developing the models [14].

Table 6. Training and testing datasets.

	$\beta/K\ s^{-1}$	Mass/m	THR/kJ g ⁻¹	HRC/J g ⁻¹ K ⁻¹
Training Set	0.1	1.00	29.3 ± 0.9	1528 ± 23.5
	0.1	1.98	31.6 ± 0.7	1585 ± 33.3
	0.2	2.02	30.9 ± 0.3	1481.5 ± 28.5
	0.5	0.93	32.9 ± 0.5	1224.2 ± 39
	0.5	1.38	34.5 ± 1.8	1336.0 ± 18.2
	1.0	0.99	31.1 ± 0.7	907.1 ± 40.8
	1.0	1.52	31.9 ± 0.5	892.3 ± 67.3
	1.0	2.03	32.7 ± 0.3	922.6 ± 59.3
	1.5	1.02	33.2 ± 0.8	774.7 ± 27.5
	1.5	1.99	32.1 ± 0.9	795.0 ± 33.4
	1.5	1.45	32.2 ± 0.5	824.3 ± 65.1
	2.0	0.99	33.3 ± 1.3	763.8 ± 49.3
	2.0	1.48	34.6 ± 0.7	744.2 ± 57.8
	2.0	1.99	32.1 ± 0.7	737.4 ± 37.4
	2.5	1.07	32.7 ± 0.5	669.8 ± 28.6
	2.5	1.53	32.5 ± 0.8	723.6 ± 21.3
	2.5	2.11	33.0 ± 0.6	667.28 ± 53.2
	3.0	0.97	32.6 ± 0.5	664.6 ± 55.2
	3.0	1.49	32.6 ± 5.5	666.6 ± 30.2
	3.0	2.08	32.8 ± 2.5	643.7 ± 47.2
3.5	1.02	32.3 ± 1.6	615.1 ± 35.8	
3.5	1.41	31.1 ± 0.5	626.3 ± 50.9	
3.5	1.94	32.5 ± 0.9	580.4 ± 26.7	
Testing Test	0.1	1.46	32.4 ± 0.07	1630.0 ± 62.4
	0.2	1.06	28.6 ± 3.0	1422.0 ± 28.3
	0.2	1.52	31.0 ± 1.5	1503.0 ± 33.8
	0.5	1.96	31.5 ± 2.8	1188.8 ± 25.7

The membership function for the model was selected by trial and error, and the hybrid learning algorithm was adopted for the training process. The model structure for HRC and THR, as illustrated in Figure 5, consists of two inputs, three membership functions for each input and one output.

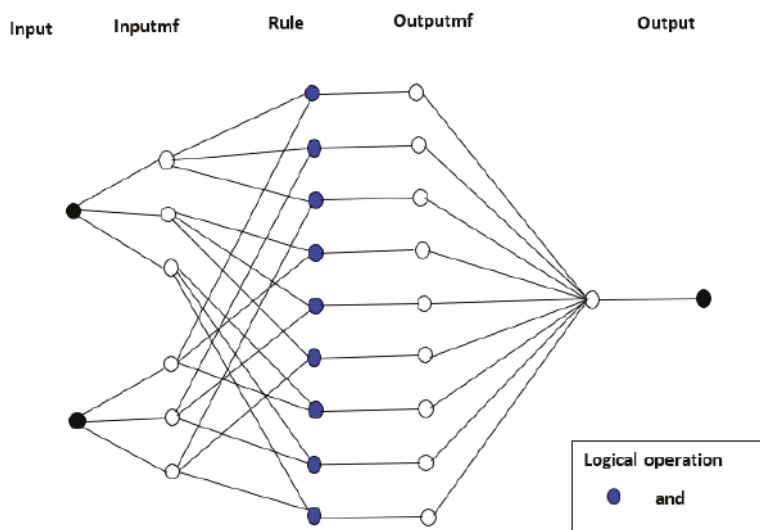


Figure 5. ANFIS model structure.

Three logical operators—*and*, *or* and *not*—are adopted in ANFIS applications. However, depending on the fuzzy logic rules extracted, any of the operators can be used to suit the structure of input data. In this research, only the ‘*and*’ logical operator was utilized.

The neurons in Layer 3 consist of fuzzy rules, the conditions of each rule and the consequences. The fuzzy IF-THEN rules generated for the membership functions from the input data of the developed models are detailed from 1–10. These conditional statements describe how the outputs were formulated according to the three membership functions applied.

1. If (input1 is in1mf1) and (input2 is in2mf1), then (output is out1mf1) (1).
2. If (input1 is in1mf1) and (input2 is in2mf2), then (output is out1mf2) (1).
3. If (input1 is in1mf1) and (input2 is in2mf3), then (output is out1mf3) (1).
4. If (input1 is in1mf2) and (input2 is in2mf1), then (output is out1mf4) (1).
5. If (input1 is in1mf2) and (input2 is in2mf2), then (output is out1mf5) (1).
6. If (input1 is in1mf2) and (input2 is in2mf3), then (output is out1mf6) (1).
7. If (input1 is in1mf3) and (input2 is in2mf1), then (output is out1mf7) (1).
8. If (input1 is in1mf3) and (input2 is in2mf2), then (output is out1mf8) (1).
9. If (input1 is in1mf3) and (input2 is in2mf3), then (output is out1mf9) (1).

The models were trained using 100 iterations. The modeling parameters for the developed ANFIS network after the training process are as listed in Table 7.

Table 7. Specifications for ANFIS model.

Variable	HRC/J g ⁻¹ K ⁻¹	THR/kJ g ⁻¹
	Value	Value
Number of nodes	53	35
Number of linear parameters	24	9
Number of nonlinear parameters	32	12
Total number of parameters	56	21
Number of training data pairs	24	24
Number of checking data pairs	0	0
Number of fuzzy rules	9	9

Plots of experimental data against predicted data from the HRC ANFIS model during training and testing are illustrated in Figures 6–8. From the simulation, the minimal training Root Mean Squared Error (RMSE) was 0.0224, while the average testing error obtained was 0.625. It is quite clearly seen that the predicted data show a close proximity to the experimental data. A surface plot demonstrating the relationship between the predicted HRC, sample mass and heating rate is presented in Figure 8. The shape of the curve is similar to the one illustrated in Figure 3; hence, the plots from the ANFIS model show that the model has a high predictive ability.

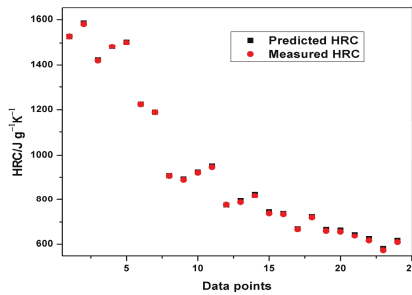


Figure 6. Plot of predicted and measured HRC for training.

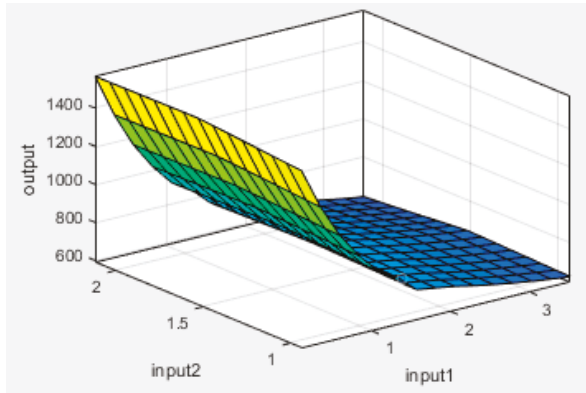


Figure 7. Surface plot of output (HRC), input2 (sample mass) and input1 (heating rate).

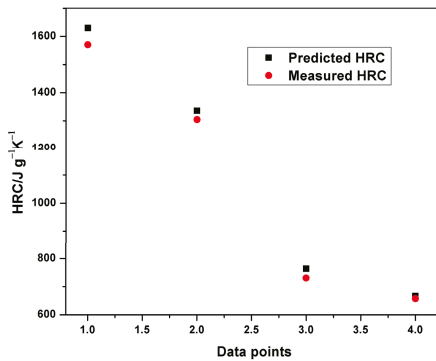


Figure 8. Plot of predicted and measured HRC for testing.

Similarly, plots of experimental and predicted THR datasets were obtained from the Neuro-Fuzzy Designer app. The minimum average training and testing RMSE for THR were 0.00781 and 0.9395, respectively.

Table 8 indicates the performance of ANFIS models in estimating THR and HRC from the MCC experiment. The basic attributes considered are the adjusted R-squared and the root mean squared errors. It is quite obvious from Table 8 that the RMSEs in all the predictions are less than one, indicating an excellent performance. Although, the training of THR outperformed the other models in terms of prediction errors, no obvious differences can be observed. The learning ability of the developed THR model was more accurate than the generalization one, as shown in the training and testing plots (Figures 9–11). Furthermore, the training of the THR model was better than the HRC model, while the test results of HRC outperformed THR. In general, the predictions were in good agreement and fitted the experimental data accurately. Considering the R^2 values obtained, one notable conclusion can be made: the model predicted HRC better than THR since both training and testing of HRC had the best results. This is due to the fact that HRC has a direct and significant statistical relationship with the input parameters, whereas THR is almost constant at any given heating rate and sample mass, thus presenting an uneven statistical distribution. It should also be noted that the test results are an indication of the excellent ability of the developed models to predict data beyond the limits of the training range.

Table 8. Performance of ANFIS models.

Statistical Indicator	HRC		THR	
	Training	Testing	Training	Testing
R^2	0.99994	0.99904	0.99315	0.9148
RMSE	0.0224	0.625	0.00781	0.9395

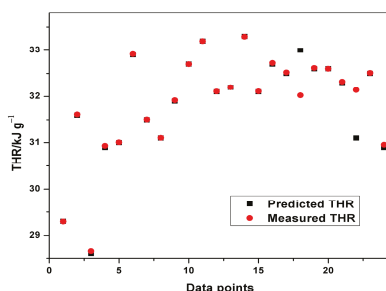


Figure 9. Plot of predicted and measured THR for training.

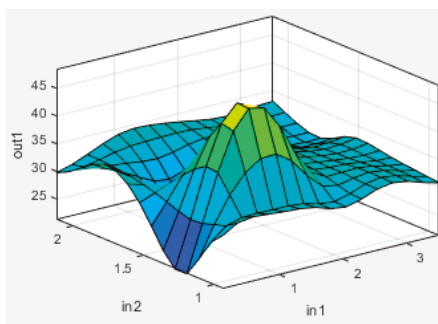


Figure 10. Surface plot of out1 (THR), in2 (sample mass) and in1 (heating rate).

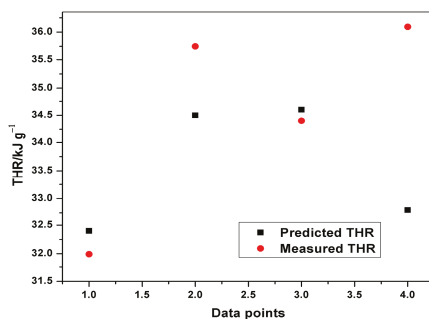


Figure 11. Plot of predicted and measured THR for testing.

The average training and testing errors in the present study have been compared with the results obtained from prediction of HRC and THR with the feed-forward back propagation neural network (FFBPNN) by Mensah et al. [14]. Table 9 shows the RMSE obtained from both the models. Similarly, Figures 12–15 give a visual representation of the variations in the predicted data from the ANFIS and FFBPNN models.

Table 9. Error comparison from ANFIS and Feed Forward Back Propagation Neural Network models.

Model	HRC			THR		
	Training	Testing	Training Time (s)	Training	Testing	Training Time (s)
ANFIS	0.0224	0.625	7.8	0.00781	0.9395	7.35
FFBPNN	0.382	0.980	13.3	0.457	1.048	12.26

Although the results from both ANFIS and FFBPNN models are seemingly good, the comparison in Table 9 indicates the presence of significant differences in the attainable prediction errors as well as the training time. From the table, the ANFIS models attained very low average errors in all cases (both training and testing). The high errors presented in the ANN models could be attributed to the limited amount of data used for the simulation. The results further affirm the superiority and accuracy in the application of ANFIS over ANN.

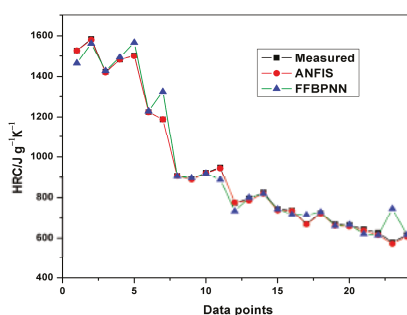


Figure 12. Comparison of HRC training results.

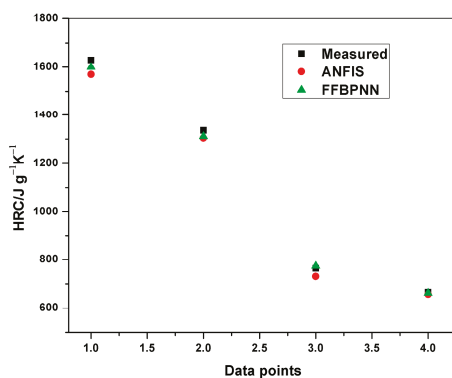


Figure 13. Comparison of HRC testing results.

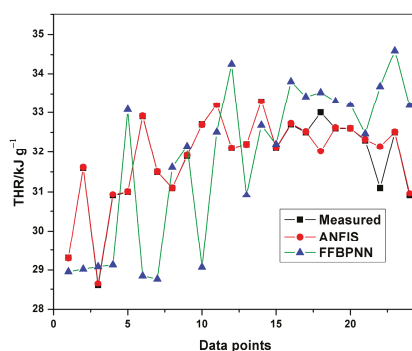


Figure 14. Comparison of THR training results.

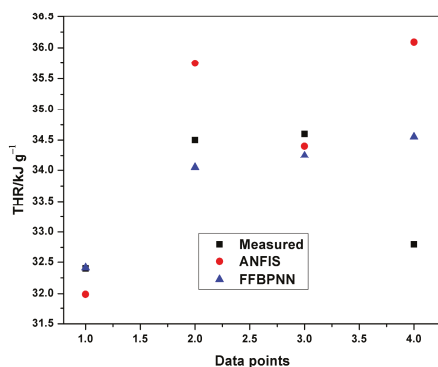


Figure 15. Comparison of THR testing results.

The combination of fuzzy reasoning and artificial neural networks optimizes and improves the learning and generalization capabilities of models. The ability of the system to tackle non-linearities in datasets is also greatly enhanced. This improvement can be observed in the application of ANFIS in flammability studies covered in the present study. The insignificant RMSE values obtained show that ANFIS is suitable for predicting HRC and THR from MCC experiments. With sufficient training, testing data and the right selection of input parameters, this modeling method can be accurately extended to a double scale analysis, such as the prediction of cone calorimeter test data from MCC test results.

4. Conclusions

The adaptive neuro-fuzzy inference system is an artificial intelligence-based computing predictive technique that combines fuzzy inference and the artificial neural network. The method has been applied in various research areas for predicting an output from various input variables. An attempt has been made in the present study to predict HRC and THR measured from the Method A procedure of the MCC experiment. This was done after realizing the degree of non-linearities in flammability parameter modeling using multiple linear regression. While developing the ANFIS models, sample mass and heating rate were used as input variables. The training and testing datasets consisted of 24 and 4 data points, respectively. The research showed that ANFIS has a great potential in flammability simulations and assessments and can, therefore, be used accurately and reliably in flammability studies.

Author Contributions: Conceptualization, R.A.M. and M.O.A.; methodology, R.A.M., M.O.A. and J.X.; software, R.A.M.; validation, O.D., L.J. and Q.X.; formal analysis, R.A.M.; investigation, R.A.M.; resources, O.D., L.J. and Q.X.; data curation, O.D., L.J. and Q.X.; writing—original draft preparation, R.A.M.; writing—review and editing, O.D., L.J., R.A.M.; visualization, O.D., L.J., R.A.M.; supervision, L.J.; project administration, L.J.; funding acquisition, O.D., L.J. and Q.X. All authors have read and agreed to the published version of the manuscript.

Acknowledgments: The authors would like to thank the National Natural Science Foundation of China (NSFC, Grant 51776098), the joint project of NSFC and STINT (51911530151, China side, and CH2018-7733, Sweden side), and NSFC (Grant 51706219). Oisik Das expresses his gratitude to *Bio4Energy*.

Conflicts of Interest: The authors declare no conflict of interest.

References

1. Lyon, R.E.; Richard, W. *A Microscale Combustion Calorimeter*; Federal Aviation Administration Washington DC Office of Aviation Research: Washington, DC, USA, 2002; No. DOT/FAA/AR-01/117.
2. Hostikka, S.; Matala, A. Pyrolysis Model for Predicting the Heat Release Rate of Birch Wood. *Combust. Sci. Technol.* **2017**, *189*, 1373–1393. [[CrossRef](#)]
3. Lyon, R.E.; Walters, R.N.; Stoliarov, S.I. Screening flame retardants for plastics using microscale combustion calorimetry. *Polym. Eng. Sci.* **2007**, *47*, 1501–1510. [[CrossRef](#)]
4. Schartel, B.K.; Pawlowski, H.; Richard, E.L. Pyrolysis combustion flow calorimeter: A tool to assess flame retarded PC/ABS materials. *Thermochim. Acta* **2007**, *462*, 1–14. [[CrossRef](#)]
5. Xu, Q.; Jin, C.; Majlingova, A.; Restas, A. Discuss the heat release capacity of polymer derived from microscale combustion calorimeter. *J. Therm. Anal. Calorim.* **2018**, *133*, 649–657. [[CrossRef](#)]
6. *Standard Test Method for Determining Flammability Characteristics of Plastics and Other Solid Materials Using Microscale Combustion Calorimetry*; ASTM D7309; American Society for Testing and Materials: West Conshohocken, PA, USA, 2013.
7. Keshavarz, M.H.; Dashtizadeh, A.; Motamedoshariati, H.; Soury, H. A simple model for reliable prediction of the specific heat release capacity of polymers as an important characteristic of their flammability. *J. Therm. Anal. Calorim.* **2017**, *128*, 417–426. [[CrossRef](#)]
8. Yang, C.Q.; He, Q. Textile heat release properties measured by microscale combustion calorimetry: Experimental repeatability. *Fire Mater.* **2012**, *36*, 127–137. [[CrossRef](#)]
9. Lyon, R.E.; Walters, R.N. Heat release capacity. In Proceedings of the Fire and Materials Conference, San Francisco, CA, USA, 22 January 2001; pp. 285–300.
10. Lyon, R.E.; Walters, R.N. Thermal analysis of polymer flammability. *Bridg. Centuries Sampe's Mater. Process. Technol.* **2000**, *24*, 1721–1729.
11. Mensah, R.A.; Xu, Q.; Asante-Okyere, S.; Jin, C.; Bentum-Micah, G. Correlation analysis of cone calorimetry and microscale combustion calorimetry experiments. *J. Therm. Anal. Calorim.* **2018**, *136*, 589–599. [[CrossRef](#)]
12. Yilmaz, I.; Kaynar, O. Multiple regression, ANN (RBF, MLP) and ANFIS models for prediction of swell potential of clayey soils. *Expert Syst. Appl.* **2011**, *38*, 5958–5966. [[CrossRef](#)]
13. Asante-Okyere, S.; Xu, Q.; Mensah, R.A.; Jin, C.; Ziggah, Y.Y. Generalized regression and feed forward back propagation neural networks in modelling flammability characteristics of polymethyl methacrylate (PMMA). *Thermochim. Acta* **2018**, *667*, 79–92. [[CrossRef](#)]

14. Mensah, R.A.; Jiang, L.; Xu, Q.; Asante-Okyere, S.; Jin, C. Comparative evaluation of the predictability of neural network methods on the flammability characteristics of extruded polystyrene from microscale combustion calorimetry. *J. Therm. Anal. Calorim.* **2019**, *138*, 3055–3064. [[CrossRef](#)]
15. Jang, J.S. ANFIS: Adaptive-network-based fuzzy inference system. *IEEE Trans. Syst. Man Cybern.* **1993**, *23*, 665–685. [[CrossRef](#)]
16. Sharma, M. Artificial neural network fuzzy inference system (ANFIS) for brain tumor detection. *arXiv* **2012**, arXiv:1212.0059.
17. Atuahene, S.; Bao, Y.; Ziggah, Y.; Gyan, P.; Li, F. Short-Term Electric Power Forecasting Using Dual-Stage Hierarchical Wavelet-Particle Swarm Optimization-Adaptive Neuro-Fuzzy Inference System PSO-ANFIS Approach Based on Climate Change. *Energies* **2018**, *11*, 2822. [[CrossRef](#)]
18. Sihag, P.; Tiwari, N.K.; Ranjan, S. Prediction of unsaturated hydraulic conductivity using adaptive neuro-fuzzy inference system (ANFIS). *ISH J. Hydraul. Eng.* **2019**, *25*, 132–142. [[CrossRef](#)]
19. Emiroğlu, M.; Beycioğlu, A.; Yildiz, S. ANFIS and statistical based approach to prediction the peak pressure load of concrete pipes including glass fiber. *Expert Syst. Appl.* **2012**, *39*, 2877–2883. [[CrossRef](#)]
20. Lyon, R.E.; Walters, R.N. Pyrolysis combustion flow calorimetry. *J. Anal. Appl. Pyrolysis* **2004**, *71*, 27–46. [[CrossRef](#)]
21. Hadi, A.A.; Wang, S. A Novel Approach for Microgrid Protection Based upon Combined ANFIS and Hilbert Space-Based Power Setting. *Energies* **2016**, *9*, 1042. [[CrossRef](#)]
22. Lee, C.C. Fuzzy logic in control systems: Fuzzy logic controller. *IEEE Trans. Syst. Man Cybern.* **1990**, *20*, 404–418. [[CrossRef](#)]
23. Kisi, O.; Haktanir, T.; Ardiclioglu, M.; Ozturk, O.; Yalcin, E.; Uludag, S. Adaptive neuro-fuzzy computing technique for suspended sediment estimation. *Adv. Eng. Softw.* **2009**, *40*, 438–444. [[CrossRef](#)]
24. Zarandi, M.H.F.; Türksen, I.B.; Sobhani, J.; Ramezaniannpour, A.A. Fuzzy polynomial neural networks for approximation of the compressive strength of concrete. *Appl. Soft Comput.* **2008**, *8*, 488–498. [[CrossRef](#)]
25. Takagi, T.; Sugeno, M. Fuzzy identification of systems and its applications to modeling and control. *IEEE Trans. Syst. Man Cybern.* **1985**, *1*, 116–132. [[CrossRef](#)]
26. Al-Sulaiman, M.A. Applying of an adaptive neuro fuzzy inference system for prediction of unsaturated soil hydraulic conductivity. *Biosci. Biotechnol. Res. Asia* **2015**, *12*, 2261–2272. [[CrossRef](#)]
27. Pal, M.; Bharati, P. Introduction to Correlation and Linear Regression Analysis. In *Applications of Regression Techniques*; Springer: Singapore, 2019; pp. 1–18.
28. Liu, D.; Xu, Z.; Fan, C. Predictive analysis of fire frequency based on daily temperatures. *Nat. Hazards* **2019**, *97*, 1175–1189. [[CrossRef](#)]
29. Zhang, Y.; Shen, L.; Ren, Y.; Wang, J.; Liu, Z.; Yan, H. How fire safety management attended during the urbanization process in China? *J. Clean. Prod.* **2019**, *236*, 117686. [[CrossRef](#)]
30. An, W.; Jiang, L.; Sun, J.; Liew, K.M. Correlation analysis of sample thickness, heat flux, and cone calorimetry test data of polystyrene foam. *J. Therm. Anal. Calorim.* **2015**, *119*, 229–238. [[CrossRef](#)]
31. Fan, C.L.; Zhang, S.; Jiao, Z.; Yang, M.; Li, M.; Liu, X. Smoke spread characteristics inside a tunnel with natural ventilation under a strong environmental wind. *Tunn. Undergr. Space Technol.* **2018**, *82*, 99–110. [[CrossRef](#)]
32. Gao, X.; Jiang, L.; Xu, Q. Experimental and theoretical study on thermal kinetics and reactive mechanism of nitrocellulose pyrolysis by traditional multi kinetics and modeling reconstruction. *J. Hazard. Mater.* **2019**, 121645, in press. [[CrossRef](#)]



Article

Development of Coffee Biochar Filler for the Production of Electrical Conductive Reinforced Plastic

Mauro Giorcelli * and Mattia Bartoli

Politecnico di Torino, C.so Duca degli Abruzzi 24, 10129 Torino, Italy; mattia.bartoli@polito.it

* Correspondence: mauro.giorcelli@polito.it; Tel.: +39-0110-904-327

Received: 15 October 2019; Accepted: 18 November 2019; Published: 21 November 2019

Abstract: In this work we focused our attention on an innovative use of food residual biomasses. In particular, we produced biochar from coffee waste and used it as filler in epoxy resin composites with the aim to increase their electrical properties. Electrical conductivity was studied for the biochar and biochar-based composite in function of pressure applied. The results obtained were compared with carbon black and carbon black composites. We demonstrated that, even if the coffee biochar had less conductivity compared with carbon black in powder form, it created composites with better conductivity in comparison with carbon black composites. In addition, composite mechanical properties were tested and they generally improved with respect to neat epoxy resin.

Keywords: electrical properties; mechanical properties; recycling; epoxy resin

1. Introduction

Anthropogenic waste stream management is one of the main unresolved problems of industrialized societies [1,2]. In the food waste sector, coffee residuals could be considered not only a waste material but a resource. Recently Christoph Sanger [3] reported that worldwide coffee production was 159.7 million of bags in crop year 2017/18 (about 9.6 MTONs), with a mean of 5 kg/capita per year in traditional markets (Germany, Italy, France, USA and Japan) and an increasing consumption in emerging markets (South Korea, Russia, Turkey and China). The coffee waste stream becomes a relevant problem not only after consumption but also during the wet processing of coffee beans when 1 ton of fresh berries results in only about 400 kg of wet waste pulp. Several solutions have been proposed to solve the problem of waste coffee biochar, such as the production of biogas [4] and flavours [5], use as filler in ceramics [6] or as absorbent for the removal of basic dyes from aqueous solutions [7]. Coffee wastes have been also used as feedstock for pyrolytic conversion producing hydrogen-rich gas [8] and fuel-quality biochar [9]. Biochar has been used not only as solid fuel but also as high performance material [10,11], as a flame retardant additive [12,13], for electrochemical [14] and energy storage applications [15] and for production of composites [16–19].

Traditionally, in the realm of carbon fillers in polymer composites, carbon black (CB) plays the main role especially in the automotive field with an estimated consumption of 8.1 MTON/year according to data released by the International CB association [20]. CB has been used for producing conductive composites [21] but, as recently reported by Quosai et al. [22], coffee-based biochar also shows remarkably conductive properties. Furthermore, coffee biochar production has an indisputable advantage if compared with CB. Coffee biochar production uses a food waste stream while oil-based feedstock is required for CB production. This decreases the environmental impact of the production process [23–25].

Among different polymers, in this work we focused our attention on epoxy resins doped with these two carbon fillers. As is well known, epoxy resin is a thermoset polymer widely applied in the field of coatings [26], adhesives [27], casting [28], potting [29], composites [30], laminates [31] and encapsulation

of semiconductor devices [32]. Epoxy resins are used intensively because of their peculiar properties such as high strength, good stiffness, good thermal stability and excellent heat, moisture and chemical resistance [33,34]. Another, unneglectable advantage of epoxy resin is the possibility of being dispersed into the cross-linked polymeric matrix additives, such as micro-encapsulated amines [35,36], that could be realised after material failure promoting the self-healing process of the epoxy composite [37].

In the field of composites materials, production of conductive reinforced plastic materials has attracted an increasing interest in the last few decades [38,39]. Large-scale application fields deserve particular attention. For example conductive epoxy resin has a large-scale application in the field of coatings and adhesives [40]. In these large-scale applications, filler cost is a crucial issue. Epoxy resins have been used as a polymeric host for plenty of carbonaceous materials for the production of conductive reinforced materials [41–44], but the cost of carbon filler has to be taken into account. High-cost carbon fillers such as carbon nanotubes and graphene are problematic for large-scale applications. These carbon fillers induce an increment of its electrical and mechanical properties in the host polymer matrix [45–48] but are not a suitable choice for industrial scale production. This is mainly due to the high-cost, up to 300 k\$/kg [49], and the problem of low productivity of the plants is well known [50]. Thus, low cost carbon fillers which are not derived from fossil fuels, such as CB, are a topic of relevant interest.

In this study, we investigated the use of biochar derived from pyrolytic conversion of the coffee waste stream, such as low cost carbon fillers derived by recycling materials. Results were compared with CB-based composites. Mechanical properties were also investigated for full composite characterization.

2. Materials and Methods

2.1. Carbonaceous Materials Preparation and Characterization

Exhausted coffee powder was selected as a real case study. It was collected from Bar Katia (Turin, Italy) supplied by Vergnano (Arabica mixture). Coffee was collected and dried at 105 °C for 72 h. Coffee samples (100 g) were pyrolyzed using a vertical furnace and a quartz reactor, heating rate of 15 °C/min and kept at the final temperature (400, 600, 800 and 1000 °C) for 30 min in an argon atmosphere. Samples were named as C400, C600, C800 and C1000 respectively. Biochar was grinded using a mechanical mixer (Savatec BB90E) for 10 min in order to decrease the particle size. Commercial CB (VULCAN® 9 N115) was used to compare with coffee biochar.

Ash contents of coffee and carbon-based materials (biochars and CB) were evaluated using a static furnace set at 550 or 800 °C respectively for 6 h.

All samples were investigated from morphological point of view using a field emission scanning electrical microscopy (FE-SEM, Zeis SupraTM 40, Oberkochen, Germany). The microscope was equipped with an energy dispersive X-ray detector (EDX, Oxford Inca Energy 450, Oberkochen, Germany) that was used to explore the carbon composition of biochars.

Particle size distribution of carbon fillers was evaluated using a laser granulometry (Fritsch Analysette 22, Idar-Oberstein, Germany) after a dispersion in ethanol and sonication in an ultrasonic bath for 10 min.

Coffee, biochars and CB were analysed through FT-IR (Nicolet 5700, Thermoscientific, Waltham, US) on attenuated total reflectance (ATR) mode (Smartorbit, Thermoscientific) in the range from 500 to 4000 cm^{-1} .

Biochars and CB were analysed through Raman spectroscopy using Renishaw® Ramanscope InVia (H43662 model, Gloucestershire, UK).

2.2. Composites Preparation

Biochar, derived from coffee, and commercial CB containing epoxy composites were produced using a two component bis-phenol A (BPA) diglycidyl resin (CORES epoxy resin, LPL). Carbonaceous filler (15 wt. %) were dispersed into epoxy monomer using a tip ultrasonicator apparatus (Sonics Vibra-cell) for 15 min. After the addition of the curing agent, the mixture was ultrasonicated for another 2 min

and left into the moulds for 16 h at room temperature. A final thermal curing was performed using a ventilated oven (I.S.C.O. Srl “The scientific manufacturer”) at 70 °C for 6 h.

2.3. Electrical Characterization

The measurement set-up was derived from Gabhi et al. [51] and is sketched in Figure 1a for fillers and Figure 1b for composites. The instrument was composed of two solid copper cylinders, 30 mm in diameter and 5 cm in length, encapsulated in a hollow Plexiglas cylinder with a nominal inner diameter of 30 mm in the case of filler electrical characterization. In this configuration, the inner diameter was slightly higher so that it was possible to force the copper rods inside the Plexiglas cavity and the upper rod could slide inside the cylinder during the measurement. This arrangement created an internal chamber between the two cylinders, where the carbon powder could be inserted. In the case of composites, the Plexiglas cylinder was removed and the sample was positioned between the aligned copper cylinders. The electrical resistance of the powders or composites was measured at increasing loads (up to 1500 bar) applied by a hydraulic press (Specac Atlas Manual Hydraulic Press 15T). Electrically insulating sheets were placed between the conductive cylinders and the load surfaces in order to ensure that the electrical signal passed through the sample. The resistance of the carbon fillers was measured using an Agilent 34401A multimeter.

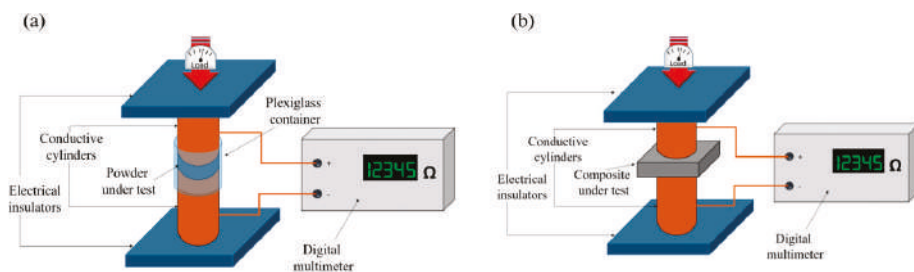


Figure 1. Sketch of measurement set-up for conductivity study of (a) carbon fillers and (b) composite.

2.4. Composites Mechanical Characterization

Carbonaceous materials containing composites were produced as dog-bone shaped according to the ASTM 638 procedure. Samples were tested using a mechanical stress test (MTS) machine (MTS Q-test10) in tensile test mode until break point. Data were analysed using a self-developed software compiled using Matlab.

2.5. Data Analysis

Statistical analysis used were based on t-tests with a significance level of 0.05 ($p < 0.05$) were carried out using Excel™ software (Microsoft Corp.) and the “data analysis” tool.

3. Results

3.1. Carbonaceous Materials Characterization

Pyrolysis of spent grounds coffee proceeded according to the mechanism reported by Setter et al. [52]. The main mechanisms that occurred during the degradative processes were those related with decomposition of the small lignin fraction [53] and the most abundant polysaccharides (i.e., cellulose and hemicellulose) [54] with the formation of bio-oils rich in anhydrosugars, furans and acetic acid with trace of aromatics [55–57].

Ash content of feedstock and carbonaceous materials were preliminary investigated and summarized in Figure 2.

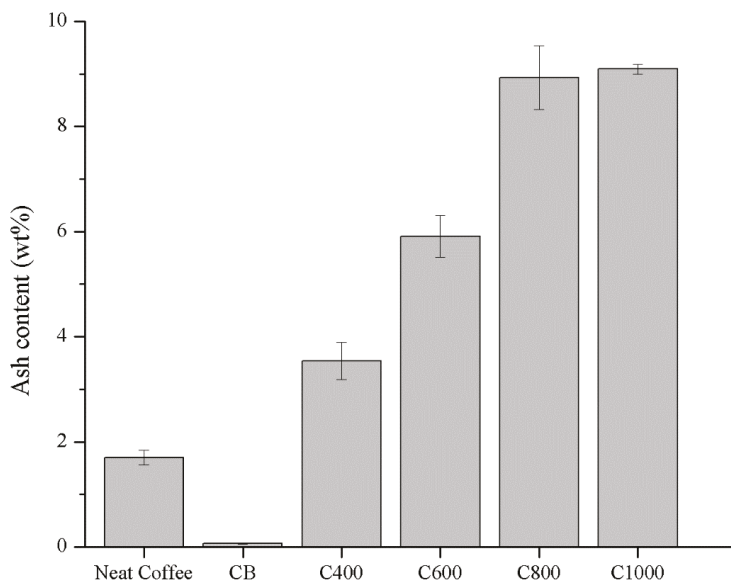


Figure 2. Ash contents of neat coffee, carbon black (CB) and coffee biochar samples heated at 400, 600, 800 and 1000 °C (C400, C600, C800 and C1000 respectively). Columns marked with different letters were significantly different ($p < 0.05$).

The ash content of neat coffee was 1.70 ± 0.14 wt. % and it increased with temperature increments reaching a value around 9 wt. % in the case of C800 (8.92 ± 0.61 wt. %) and C1000 (9.09 ± 0.09 wt. %). As expected, CB showed a very low ash content (0.07 ± 0.01 wt. %) according to Medalia et al. [58] mainly as oxides. Ash content increment at higher temperatures was imputable to advance pyrolytic degradation of the organic matrix leading to the concentration of inorganic residue [59] that did not undergo any temperature induced degradation.

The effect of pyrolytic temperature on biochar morphology was studied using FE-SEM as shown in Figure 3. Neat coffee displayed flaked collapsed structures (Figure 3a, b) that was retained by C400 after pyrolysis at 400 °C (Figure 3e,f). With the increase of temperature to 600 °C lead to the formation of porous structures with average diameters close to 30 μm separated by carbon lamellae with a thickness around 1 μm (Figure 3g,h). At 800 °C, the biochar recovered lost the structure due to the massive release of volatile organic matters during the overall pyrolytic process that induced the collapse of carbonaceous structures together with an improved grindability [60]. At 1000 °C, the increased temperature allowed the massive formation of carbon–carbon bonds that promoted the stabilization of the porous architecture with nanoscale lamellae structures. CB showed a typical highly aggregate spherule-based shape with average diameter of single particles around 50 nm.

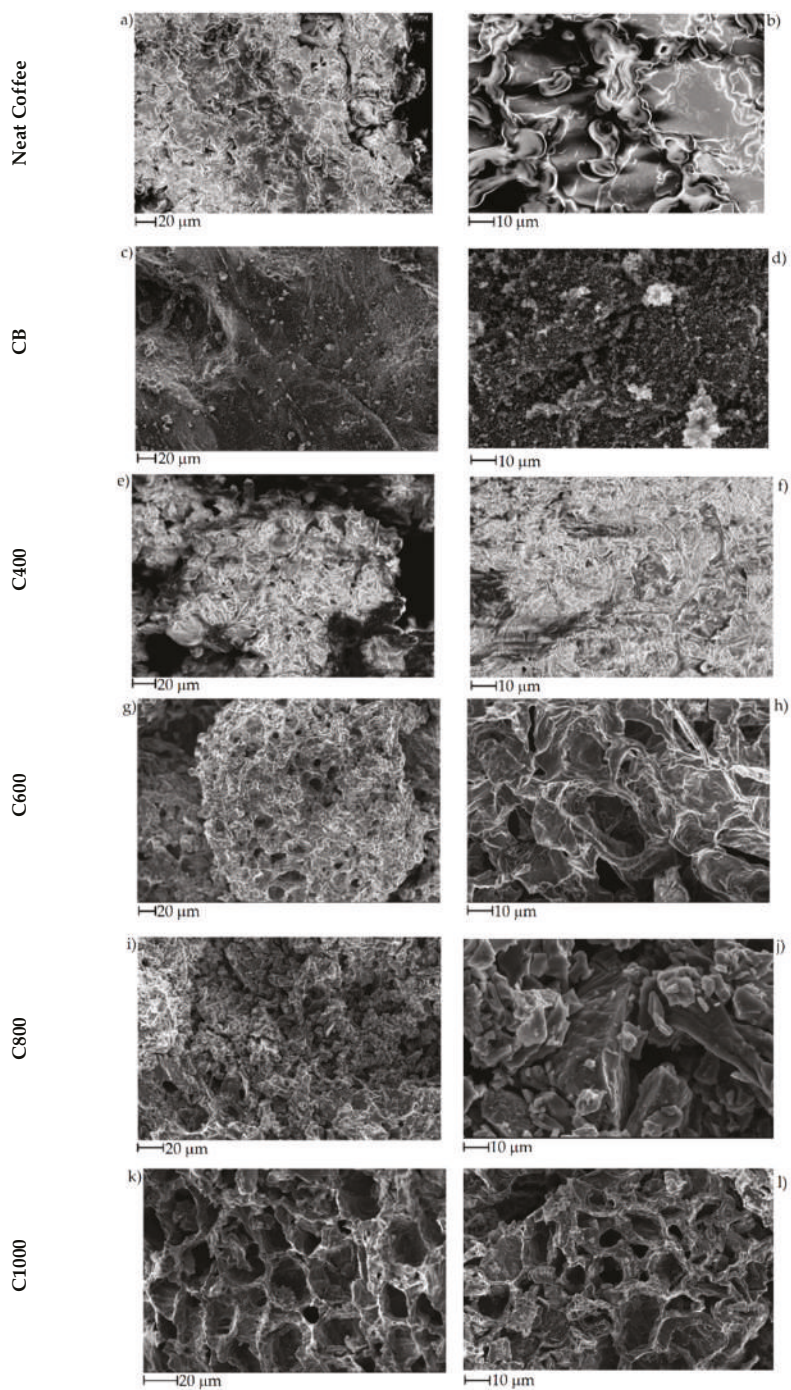


Figure 3. FE-SEM captures of (a,b) neat coffee, (c,d) CB, (e,f) C400, (g,h) C600, (i,j) C800 and (k,l) C1000.

Organic component of significant carbonaceous materials was also analysed using both FT-IR and Raman spectrometry techniques. Among carbonaceous materials, we reported neat coffee, C1000 and CB. Results are shown in Figure 4.

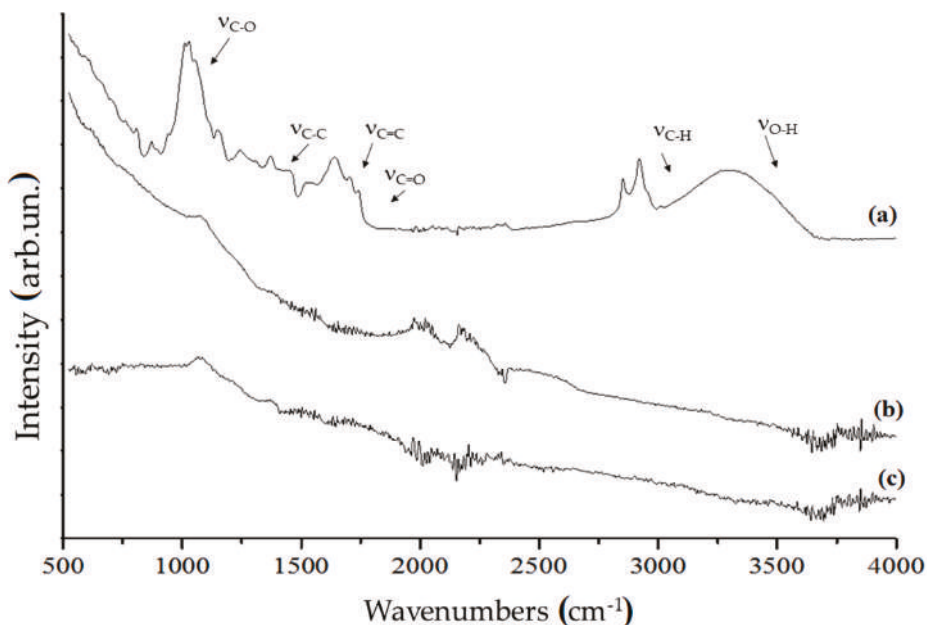


Figure 4. FT-IR spectra (ATR mode) of (a) neat coffee, (b) coffee biochar produced at 1000 °C and (c) CB in the range of 500–4000 cm^{-1} .

The FT-IR spectrum of neat coffee showed the broad band of $\nu_{\text{O-H}}$ (3300–3500 cm^{-1}), the bands of saturated $\nu_{\text{C-H}}$ (2850–2950 cm^{-1}), $\nu_{\text{C=O}}$ (1710–1741 cm^{-1}) due to the carboxylic functionalities, $\nu_{\text{C=C}}$ (1540–1638 cm^{-1}) due to the presence of aromatic structures, saturated and unsaturated $\delta_{\text{C-H}}$ (1370–1440 cm^{-1}), saturated $\nu_{\text{C-C}}$ (1243 cm^{-1}), $\nu_{\text{C-O}}$ (1030–1148 cm^{-1}) and out-of-plane $\delta_{\text{O-H}}$ below 700 cm^{-1} . Those bands clearly identified a lignocellulosic derived matrix with massive presence of polysaccharides and aromatics. C1000 did not show any of the characteristic bands of organic matrix but show an envelope of bands below 1800 cm^{-1} due to carbon skeletal movements. Contrary, CB showed low bands intensity below 1000 cm^{-1} due the lower variety of carbon structure embedded into particles.

Raman spectra normalized on G peak are shown in Figure 5. Coffee biochars had the typical profiles of amorphous materials [61] in contrast to CB which was more graphitic. The graphitic structure for CB could be observed by the deep gorge between D and G peaks and their shaped structure. An increase of $I_{\text{D}}/I_{\text{G}}$ ratio was evident for biochars moving from a pyrolytic temperature of 400 to 1000 °C. This increase of $I_{\text{D}}/I_{\text{G}}$ ratio could be ascribed to the progressively loss of residual functional groups with the increase of temperature. This observation was also supported by the decrease of fluorescence [62]. Due to the loss of less intense parts of these weak interactions, biochar underwent an appreciable disorganization together with aromatic structure formation, in particular up to 600 °C, without the completion of a proper graphitization process that occurs at higher temperature [63].

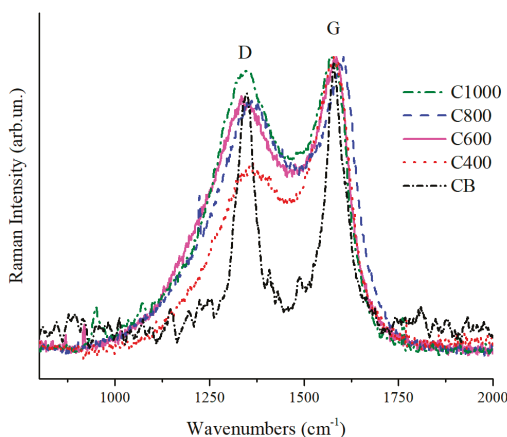


Figure 5. Magnification of Raman spectra in the range from 800 to 2000 cm^{-1} of C400, C600, C800, C1000 and CB.

The evolution of biochar structures due to temperature increment could be monitored through Raman according to Ferrari et al. [61]. Accordingly, the D peaks (Figure 5) showed wave numbers close to 1350 cm^{-1} that is typical of transition from amorphous carbon to nanocrystalline graphite. At the same time the biochar G peaks showed wavenumbers close to 1580 cm^{-1} with exception of C1000. This last showed a G peak at 1600 cm^{-1} due the high amount of nanocrystalline domains not yet rearranged in the ordered structure [64].

The above mentioned consideration was also supported by EDX analysis that showed the carbon content that significantly increased from C400 to C600–C1000 while oxygen content decreased. Carbon content of C600–C1000 were not significantly different from CB even if CB showed a more ordered structure. This support the hypothesis that the driving force of the biochar enhanced conductivity is the reorganization of nanocrystalline domains and not merely the carbon content, shown in Figure 6. Traces of Mg, P, K and Ca were also detected.

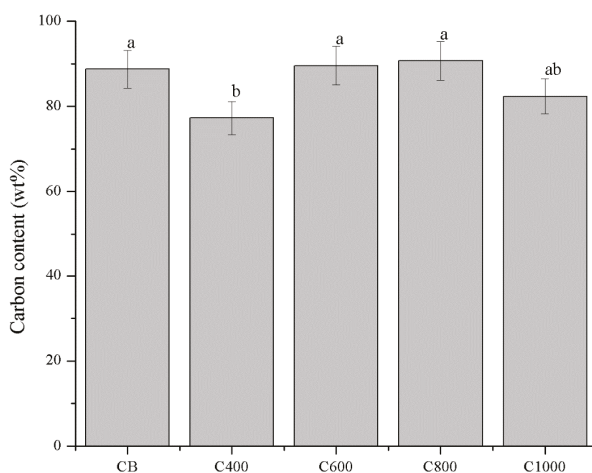


Figure 6. Carbon content of biochars and CB. Evaluated through energy dispersive X-ray (EDX) analysis. Error values were reported as 5% of the detected values according with Laskin et al. [65]. Columns marked with different letters are significantly different ($p < 0.05$).

3.2. Composites Characterization

3.2.1. Electrical Characterization of Carbonaceous Filler and Composites

The set-up shown in Figure 1a was used for biochar powders electrical characterization. Around 3 g of carbonaceous powder, which creates a few millimetres distance between copper cylinders was positioned in the chamber. After the closure of the chamber a pressure was applied with the aim of compacting the powder. The pressure range was from 0 to 1500 bar (step of 250 bar). For each step the stabilized value of resistivity was registered such as the distance between the copper cylinders. The same procedure was repeated for composites of few millimetre thickness. Carbonaceous powders and composites decreased their resistance value during compression until they reached a plateau when high pressure was reached. The decreasing of resistance value could be correlated with the decreasing of space between carbon particles as sketched in Figure 7. In the case of powders, the void among particles collapsed with a production of compact carbon agglomerate as shown in Figure 7a. In the case of composites, Figure 7b shows the mechanism where the polymer chains flow let the carbon particles situate.

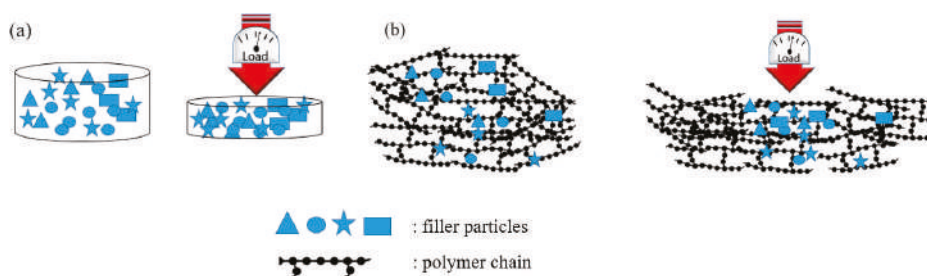


Figure 7. Behaviour of (a) powders and (b) composites during compression.

The resistance value, R , with the value of surface S and distance l between copper surfaces were used in Ohm law ($\sigma = l/RS$) to evaluate the conductivity σ . The conductivity value of carbon powder and composites were evaluated following this procedure:

- (1) A starting value of conductivity was evaluated without any sample in order to measure the value of resistance of the system. This value was subtracted to the resistance value read with samples.
- (2) The same quantity of carbon powders (CB and biochar) were positioned between copper cylinders and kept by the Plexiglas hollow cylinder. The measurement was repeated several times in order to have a reliable value.
- (3) Composites were positioned between copper cylinders, in this case the Plexiglas hollow cylinder was not necessary and the value of conductivity was measured in different sample portions.

Preliminary results are shown in Figure 8 showing the conductivity of the biochar powders (red line) and percolation curves of related composites.

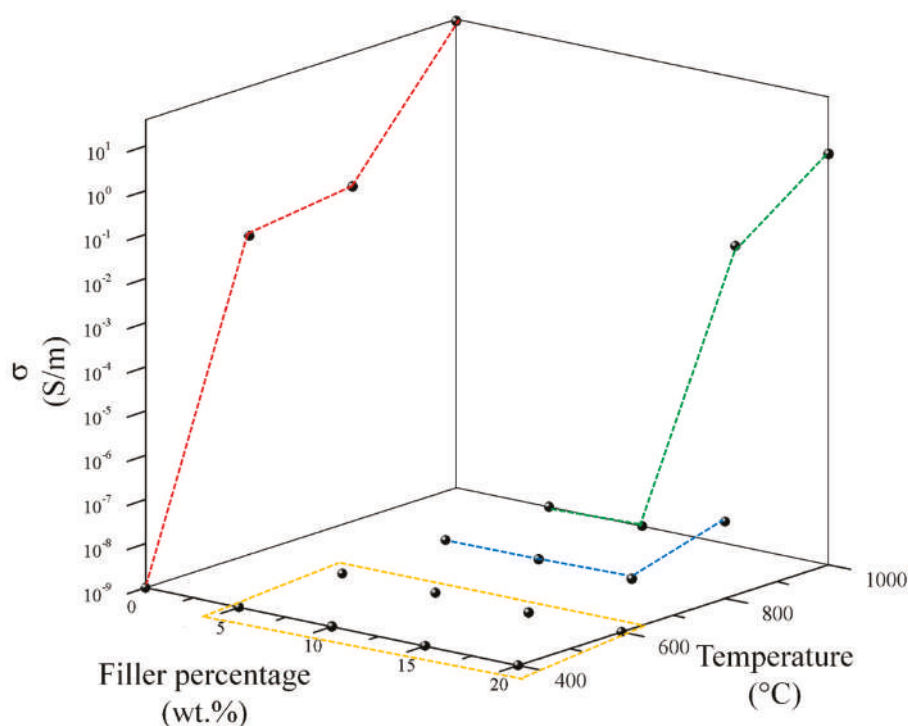


Figure 8. Trends of composites conductivity as function of filler percentage. Red line represents the biochar conductivity trends while yellow, blue and green show respectively the percolation curves of composites containing C400–C600, C800 and C1000.

C400 did not show an appreciable conductivity while an increment of pyrolytic temperature up to 600 °C induced a conductivity of up to 0.02 S/m. Further increments of processing temperature up to 800 and 1000 °C led to a conductivity of up to 0.04 and 35.96 S/m. This remarkable increment of conductivity between 800 and 1000 °C was due the enlargement of aromatic region formed as consequence of high temperature carbonization [64]. This deeply affected the electrical behaviour of related composites. Consequently, C400 and C600 containing composites were not conductive for all the range of filler percentage investigated. CB composites were not conductive until the filler concentration of 15 wt. % reaching a conductivity of 5.4×10^{-8} S/m with a filler loading of 20 wt. %. C1000 composites showed the best performances showing a detectable electrical conductivity with a 15 wt. % of filler and reaching a conductivity of 2.02 S/m with a filler loading of 20 wt. %.

Accordingly, with these data, electrical properties of C1000 and C1000 containing composites were studied under a wide range of static pressures comparing with the related CB and CB composites as shown in Figure 9.

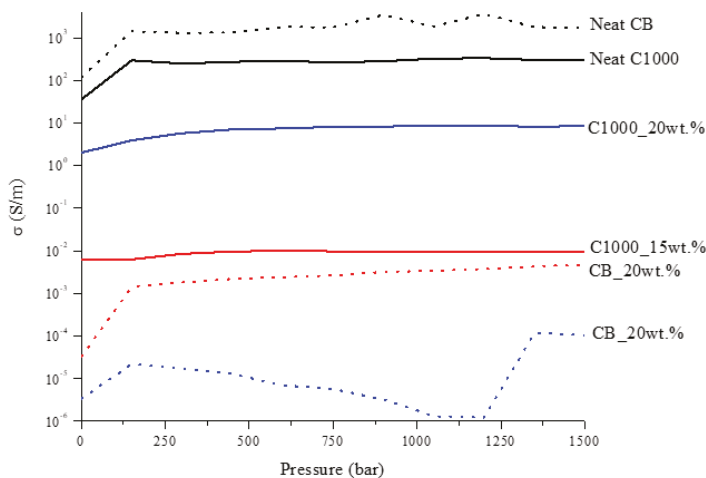


Figure 9. Trends of CB and C1000 powders and related composites conductivity as a function of pressure applied.

CB powder reached a conductivity around 1700 S/m while in the same conditions C1000 reached a conductivity of 300 S/m. Composites containing of CB and C1000 were conductive but the results showed a different trend compared with the relative powders. CB 15 wt. % reached the value of 4×10^{-3} S/m and its conductive value showed an influence of applied pressure in the first compression movement. C1000 15 wt. % reached to 10^{-2} S/m, with an increment around one order of magnitude if compared with CB 15 wt. %. This difference was more relevant for a filler concentration of 20 wt. %. In this case, the conductivity of CB-based composites dropped down to 10^{-5} – 10^{-4} S/m in contrast to C1000 which reached ~ 10 S/m. The high conductive value for coffee biochar could be due to more uniform filler dispersion inside epoxy resin. Dispersion of the filler inside the epoxy matrix was investigated through FE-SEM (Figure 10) after samples were cryo-fractured using liquid nitrogen and compared to composites with a filler loading of 15 wt. % due to the similarity of conductivity. CB containing composites showed a dark and clear area (Figure 10a) with different compositions. The clear ones were rich in CB aggregates (Figure 10b,c) while the darkest were poor (Figure 10d). C1000 containing composites showed smooth surfaces with holes (Figure 10e) due the expulsion of embedded C1000 particles during the fracturing (Figure 10e) as clearly shown in Figure 10g. Particles size analysis (Figure 11) showed clearly that C1000 was composed by two particle populations, one around 100 μm and one around 20 μm . Considering the average size of C1000 particles into the composites was reasonable it was assumed that the bigger ones underwent a disruption during the ultrasonication forming small sized well-dispersed particles. CB particles size showed also that it would be more appropriate speaking of CB aggregates instead of single particles [66]. Aggregates could be justified also from Figure 10c where the CB single particles were less than 100 nm but they created agglomerates that also the particle size analysis (Figure 11) was not able to detect.

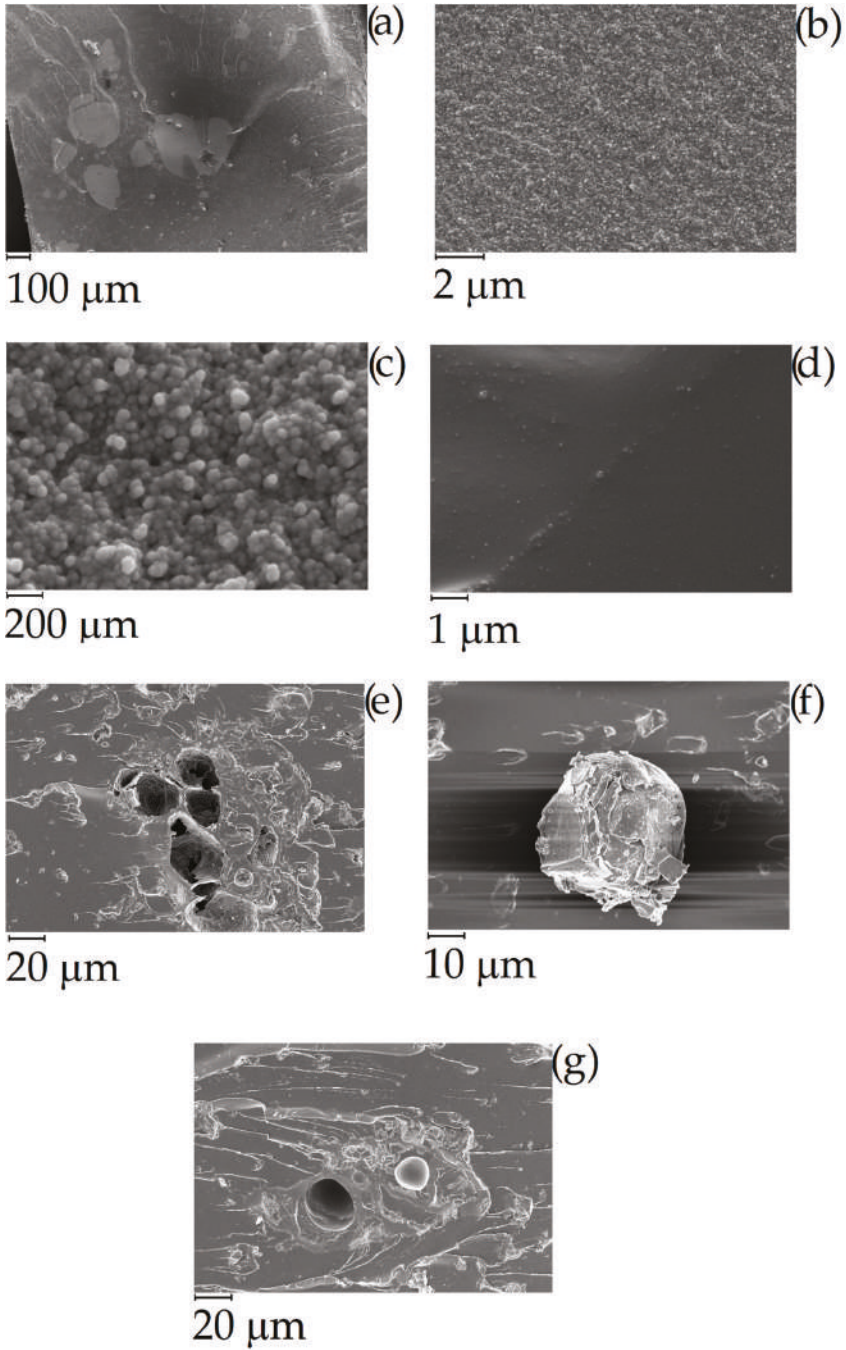


Figure 10. Field emission scanning electrical microscopy (FESEM) of cryo-fractured (a–d) CB and (e–g) C1000 containing composites with a filler loading of 15 wt. %.

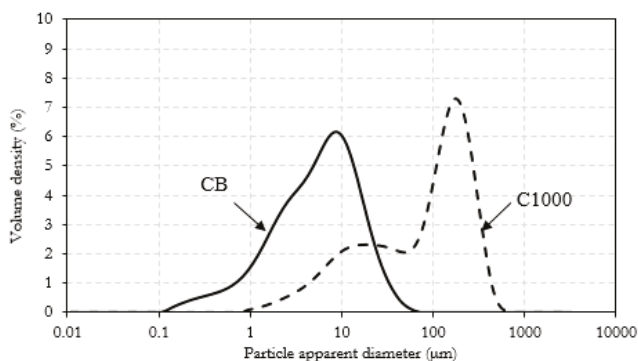


Figure 11. Particle size distribution for CB and C1000.

3.2.2. Composites Mechanical Characterization

With the aim of confirming mechanical consistence of samples, a stress–strain curve was investigated for composites of 15 wt. % for CB and C1000 compared with neat resin. Mechanical tests on dog-bones shaped samples are summarized in the Figure 12.

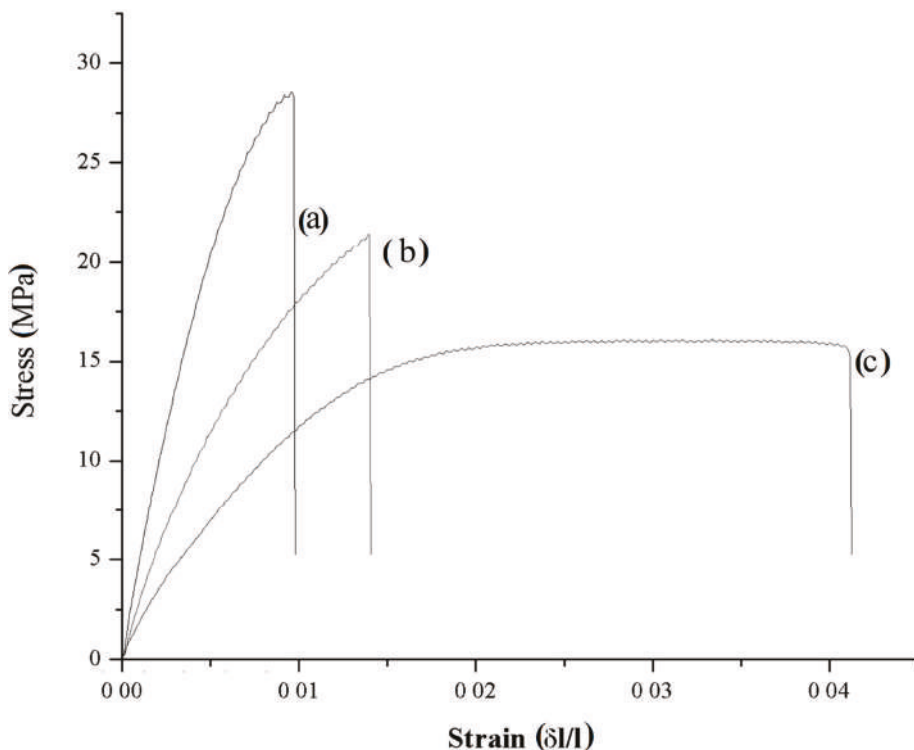


Figure 12. Stress–strain curves of composites containing 15 wt. % of (a) C1000, (b) CB and (c) neat resin.

According to data report in Figure 13, maximum elongation of neat resin ($3.50\% \pm 0.64\%$) was the highest compared with those of C1000 and CB containing composites ($1.16\% \pm 0.09\%$ and 1.63%

$\pm 0.08\%$ respectively). Neat resin showed also a remarkably higher toughness ($0.48 \pm 0.03 \text{ MJ/m}^3$) compared with composites that showed values not significantly different from each other close to 0.18 MJ/m^3 . Young's modulus (YM) showed a significant difference between C1000-based composites ($3258 \pm 273 \text{ MPa}$) and CB ones ($1940 \pm 163 \text{ MPa}$). These last values were quite close to those of neat resin ($1510 \pm 160 \text{ MPa}$) and a similar trend was observed with ultimate tensile strength with values of CB composites not significantly different from those of neat resin (both close to 19 MPa) and higher values for biochar-based composites (up to $24.9 \pm 1.5 \text{ MPa}$).

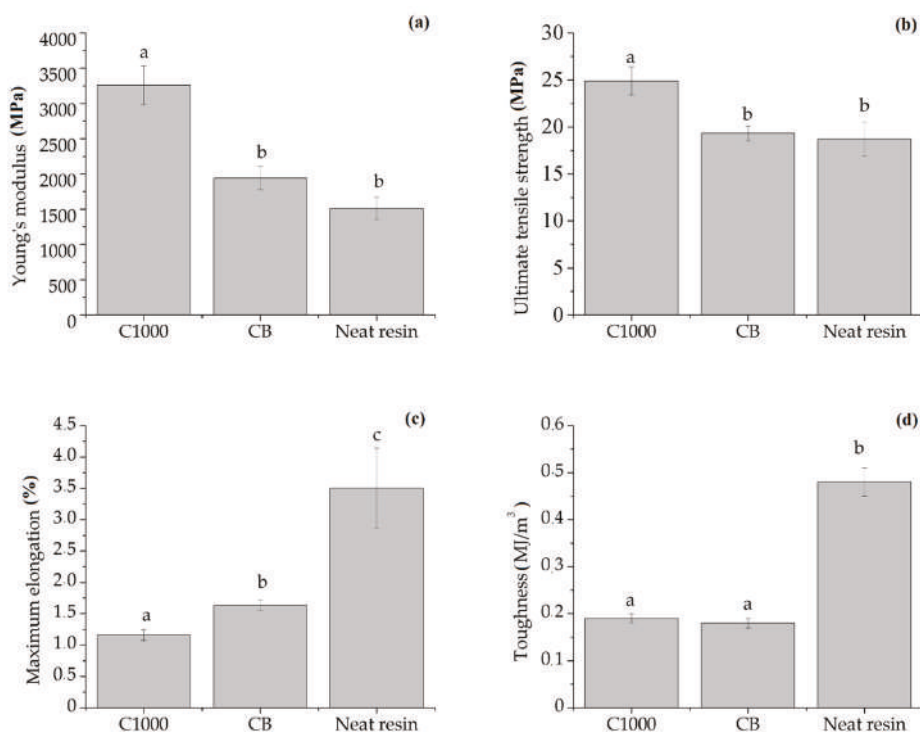


Figure 13. Summary of (a) ultimate tensile strength, (b) Young's modulus, (c) toughness and (d) maximum elongation of neat resin, biochar and carbon-based composites. Columns marked with same letters were not significantly different ($p < 0.05$).

Composites behaviour observed during the mechanical tests enlightened the different interaction between different carbonaceous filler with epoxy matrix with magnification of filler–resin interaction, and in the case of biochar-based composites with an increase brittleness and a reduced elongation.

As reported by Chodak et al. [39] about CB containing poly(propylene) composites, the formation of a diffuse particles network is detrimental for the mechanical properties. The same behaviour was observed in the production of CB-based composites which presented a decrement of Ultimate tensile strength compared with CB1000 ones. CB1000 were very close to the percolation threshold (Figure 7) and this induced a very relevant decrement of maximum elongation. Working below the percolation threshold allowed the preservation of some of the appealing properties of a brittle resin (i.e., high Young's modulus and ultimate tensile strength) together with the magnification of electrical conductivity.

4. Conclusions

The coffee waste stream was efficiently used as feedstock for pyrolytic conversion at different temperatures. The effect of process temperature on the properties of biochar was investigated and it was observed that further increments of temperature improved the porous stability and conductivity of the material. This phenomenon was probably due to both the formation of new C–C bonds and to the rearrangement of graphitic and quasi-graphitic domains formed during pyrolysis as shown by Raman characterization.

The most relevant result of this study was that even if neat biochar produced at 1000 °C showed less conductivity with respect to CB when it was dispersed in composite, the electrical properties of a composite containing coffee biochar were some orders of magnitude higher than composites containing CB. In the case of 20 wt. % of C1000, composites showed four orders of magnitudes more than composites containing 20 wt. % of CB. This could be ascribed to the uniform dispersion of coffee biochar, in contrast to CB which creates agglomerations. These agglomerations induced a non-uniform composite structure in the CB containing composites. Mechanical properties of composites with coffee biochar were verified and they were not compromised with respect to composites containing C1000, showing better UTS and YM. Both materials were more brittle than neat resin but C1000 showed some of the properties of high performances resins. Mechanical properties also showed a direct correlation with filler dispersion. Where the filler dispersion was uniform, the mechanical performances were improved.

A new era could be at the door for carbon fillers in polymer composites. Considering the sustainability of coffee biochar production, the results reported show how biomass-derived carbon could be a sound replacement for oil-derived carbon fillers such as CB.

Author Contributions: Conceptualization, M.G.; methodology M.G., M.B.; formal analysis M.G., M.B.; investigation M.G., M.B.; resources, M.G.; data curation, M.G., M.B.; writing—original draft preparation, M.G., M.B.; writing—review and editing, M.G., M.B.; supervision, M.G.

Funding: MODCOMP project (grant 685844, European H2020 program).

Acknowledgments: The authors acknowledge Andrea Marchisio for particle size analysis, Salvatore Guastella for FE-SEM and EDX analysis, Massimo Rovere for Raman spectra, Carlo Rosso for mechanical tests and Alberto Tagliaferro for fruitful discussions.

Conflicts of Interest: The authors declare no conflict of interest.

References

1. Girotto, F.; Alibardi, L.; Cossu, R. Food waste generation and industrial uses: A review. *Waste Manag.* **2015**, *45*, 32–41. [[CrossRef](#)]
2. Burkhard, R.; Deletic, A.; Craig, A. Techniques for water and wastewater management: A review of techniques and their integration in planning. *Urban Water* **2000**, *2*, 197–221. [[CrossRef](#)]
3. Sängler, C. Value Addition in the Coffee Sector. In Proceedings of the 10th Multi-Year Expert Meeting on Commodities and Development, Geneva, Switzerland, 25–26 April 2018.
4. Battista, F.; Fino, D.; Mancini, G. Optimization of biogas production from coffee production waste. *Bioresour. Technol.* **2016**, *200*, 884–890. [[CrossRef](#)] [[PubMed](#)]
5. Kusch, S.; Udenigwe, C.C.; Gottardo, M.; Micolucci, F.; Cavinato, C. First-and second-generation valorisation of wastes and residues occurring in the food supply chain. In Proceedings of the 5th International Symposium on Energy from Biomass and Waste, Venice, Italy, 17–20 November 2014.
6. Sena da Fonseca, B.; Vilão, A.; Galhano, C.; Simão, J. Reusing coffee waste in manufacture of ceramics for construction. *Adv. Appl. Ceram.* **2014**, *113*, 159–166. [[CrossRef](#)]
7. Lafi, R.; ben Fradj, A.; Hafiane, A.; Hameed, B. Coffee waste as potential adsorbent for the removal of basic dyes from aqueous solution. *Korean J. Chem. Eng.* **2014**, *31*, 2198–2206. [[CrossRef](#)]
8. Dominguez, A.; Menéndez, J.; Fernandez, Y.; Pis, J.; Nabais, J.V.; Carrott, P.; Carrott, M.R. Conventional and microwave induced pyrolysis of coffee hulls for the production of a hydrogen rich fuel gas. *J. Anal. Appl. Pyrol.* **2007**, *79*, 128–135. [[CrossRef](#)]

9. Tsai, W.-T.; Liu, S.-C.; Hsieh, C.-H. Preparation and fuel properties of biochars from the pyrolysis of exhausted coffee residue. *J. Anal. Appl. Pyrol.* **2012**, *93*, 63–67. [[CrossRef](#)]
10. Qian, K.; Kumar, A.; Zhang, H.; Bellmer, D.; Huhnke, R. Recent advances in utilization of biochar. *Renew. Sustain. Energy Rev.* **2015**, *42*, 1055–1064. [[CrossRef](#)]
11. Ok, Y.S.; Chang, S.X.; Gao, B.; Chung, H.-J. SMART biochar technology—A shifting paradigm towards advanced materials and healthcare research. *Environ. Technol. Innov.* **2015**, *4*, 206–209. [[CrossRef](#)]
12. Das, O.; Kim, N.K.; Hedenqvist, M.S.; Bhattacharyya, D.; Johansson, E.; Xu, Q.; Holder, S. Naturally-occurring bromophenol to develop fire retardant gluten biopolymers. *J. Clean. Prod.* **2019**, 118552. [[CrossRef](#)]
13. Das, O.; Kim, N.K.; Sarmah, A.K.; Bhattacharyya, D. Development of waste based biochar/wool hybrid biocomposites: Flammability characteristics and mechanical properties. *J. Clean. Prod.* **2017**, *144*, 79–89. [[CrossRef](#)]
14. Ziegler, D.; Palmero, P.; Giorcelli, M.; Tagliaferro, A.; Tulliani, J.-M. Biochars as Innovative Humidity Sensing Materials. *Chemosensors* **2017**, *5*, 35. [[CrossRef](#)]
15. Jiang, J.; Zhang, L.; Wang, X.; Holm, N.; Rajagopalan, K.; Chen, F.; Ma, S. Highly ordered macroporous woody biochar with ultra-high carbon content as supercapacitor electrodes. *Electrochim. Acta* **2013**, *113*, 481–489. [[CrossRef](#)]
16. Khan, A.; Jagdale, P.; Rovere, M.; Nogués, M.; Rosso, C.; Tagliaferro, A. Carbon from waste source: An eco-friendly way for strengthening polymer composites. *Compos. Part B Eng.* **2018**, *132*, 87–96. [[CrossRef](#)]
17. Arrigo, R.; Jagdale, P.; Bartoli, M.; Tagliaferro, A.; Malucelli, G. Structure–Property Relationships in Polyethylene-Based Composites Filled with Biochar Derived from Waste Coffee Grounds. *Polymers* **2019**, *11*, 1336. [[CrossRef](#)] [[PubMed](#)]
18. Bartoli, M.; Giorcelli, M.; Rosso, C.; Rovere, M.; Jagdale, P.; Tagliaferro, A. Influence of Commercial Biochar Fillers on Brittleness/Ductility of Epoxy Resin Composites. *Appl. Sci.* **2019**, *9*, 3109. [[CrossRef](#)]
19. Das, O.; Kim, N.K.; Hedenqvist, M.S.; Lin, R.J.; Sarmah, A.K.; Bhattacharyya, D. An attempt to find a suitable biomass for biochar-based polypropylene biocomposites. *Environ. Manag.* **2018**, *62*, 403–413. [[CrossRef](#)]
20. Association, I.C.B. What is Carbon Black? Available online: <http://www.carbon-black.org/> (accessed on 19 November 2019).
21. Tchoudakov, R.; Breuer, O.; Narkis, M.; Siegmann, A. Conductive polymer blends with low carbon black loading: Polypropylene/polyamide. *Polym. Eng. Sci.* **1996**, *36*, 1336–1346. [[CrossRef](#)]
22. Quosai, P.; Anstey, A.; Mohanty, A.K.; Misra, M. Characterization of biocarbon generated by high- and low-temperature pyrolysis of soy hulls and coffee chaff: For polymer composite applications. *R. Soc. Open Sci.* **2018**, *5*, 171970. [[CrossRef](#)]
23. Field, J.L.; Keske, C.M.; Birch, G.L.; DeFoort, M.W.; Cotrufo, M.F. Distributed biochar and bioenergy coproduction: A regionally specific case study of environmental benefits and economic impacts. *Gcb Bioenergy* **2013**, *5*, 177–191. [[CrossRef](#)]
24. Dutta, B.; Raghavan, V. A life cycle assessment of environmental and economic balance of biochar systems in Quebec. *Int. J. Energy Environ. Eng.* **2014**, *5*, 106. [[CrossRef](#)]
25. Roberts, K.G.; Gloy, B.A.; Joseph, S.; Scott, N.R.; Lehmann, J. Life cycle assessment of biochar systems: Estimating the energetic, economic, and climate change potential. *Environ. Sci. Technol.* **2009**, *44*, 827–833. [[CrossRef](#)] [[PubMed](#)]
26. Liang-Hsing, L.; Lin, Y.-j.; Lin, Y.-s.; Hwang, K.-Y.; Yi-Sern, W. Reactive Epoxy Compounds and Method for Producing the Same, Core-Shell Type Epoxy Resin Particles, Waterborne Epoxy Resin Composition, and Coating Composition Containing the Reactive Epoxy Compounds. U.S. Patent Application 20190055397, 21 February 2019.
27. Ahmadi, Z. Nanostructured epoxy adhesives: A review. *Prog. Org. Coat.* **2019**, *135*, 449–453. [[CrossRef](#)]
28. Liao, J.; Zhang, D.; Wu, X.; Luo, H.; Zhou, K.; Su, B. Preparation of high strength zirconia by epoxy gel-casting using hydantion epoxy resin as a gelling agent. *Mater. Sci. Eng. C* **2019**, *96*, 280–285. [[CrossRef](#)] [[PubMed](#)]
29. Lall, P.; Dornala, K.; Deep, J.; Lowe, R. Measurement and Prediction of Interface Crack Growth at the PCB-Epoxy Interfaces Under High-G Mechanical Shock. In Proceedings of the 2018 17th IEEE Intersociety Conference on Thermal and Thermomechanical Phenomena in Electronic Systems (ITherm), San Diego, CA, USA, 29 May–1 June 2018; pp. 1097–1105.
30. Rana, S.; Alagirusamy, R.; Joshi, M. A review on carbon epoxy nanocomposites. *J. Reinf. Plast. Compos.* **2009**, *28*, 461–487. [[CrossRef](#)]

31. Sela, N.; Ishai, O. Interlaminar fracture toughness and toughening of laminated composite materials: A review. *Composites* **1989**, *20*, 423–435. [[CrossRef](#)]
32. Enhua, H.; Kaichang, K.; Lixin, C. Research Progress on Encapsulating Materials of Epoxy Resin. *Chem. Ind. Eng. Progress* **2003**, *22*, 1057–1060.
33. Jin, F.-L.; Li, X.; Park, S.-J. Synthesis and application of epoxy resins: A review. *J. Ind. Eng. Chem.* **2015**, *29*, 1–11. [[CrossRef](#)]
34. Rafique, I.; Kausar, A.; Anwar, Z.; Muhammad, B. Exploration of epoxy resins, hardening systems, and epoxy/carbon nanotube composite designed for high performance materials: A review. *Polymer Plast. Technol. Eng.* **2016**, *55*, 312–333. [[CrossRef](#)]
35. McIlroy, D.A.; Blaiszik, B.J.; Caruso, M.M.; White, S.R.; Moore, J.S.; Sottos, N.R. Microencapsulation of a Reactive Liquid-Phase Amine for Self-Healing Epoxy Composites. *Macromolecules* **2010**, *43*, 1855–1859. [[CrossRef](#)]
36. Yin, T.; Rong, M.Z.; Zhang, M.Q.; Yang, G.C. Self-healing epoxy composites—Preparation and effect of the healant consisting of microencapsulated epoxy and latent curing agent. *Comp. Sci. Technol.* **2007**, *67*, 201–212. [[CrossRef](#)]
37. Neisiany, R.E.; Khorasani, S.N.; Lee, J.K.Y.; Ramakrishna, S. Encapsulation of epoxy and amine curing agent in PAN nanofibers by coaxial electrospinning for self-healing purposes. *RSC Advances* **2016**, *6*, 70056–70063. [[CrossRef](#)]
38. Sundstrom, D.W.; Chen, S.Y. Thermal conductivity of reinforced plastics. *J. Compos. Mater.* **1970**, *4*, 113–117. [[CrossRef](#)]
39. Amarasekera, J. Conductive plastics for electrical and electronic applications. *Reinf. Plast.* **2005**, *49*, 38–41. [[CrossRef](#)]
40. Kinloch, A. Toughening epoxy adhesives to meet today's challenges. *MRS Bull.* **2003**, *28*, 445–448. [[CrossRef](#)]
41. Chatterjee, S.; Wang, J.; Kuo, W.; Tai, N.; Salzmann, C.; Li, W.-L.; Hollertz, R.; Nüesch, F.; Chu, B. Mechanical reinforcement and thermal conductivity in expanded graphene nanoplatelets reinforced epoxy composites. *Chem. Phys. Lett.* **2012**, *531*, 6–10. [[CrossRef](#)]
42. Gojny, F.H.; Wichmann, M.H.; Fiedler, B.; Kinloch, I.A.; Bauhofer, W.; Windle, A.H.; Schulte, K. Evaluation and identification of electrical and thermal conduction mechanisms in carbon nanotube/epoxy composites. *Polymer* **2006**, *47*, 2036–2045. [[CrossRef](#)]
43. El-Tantawy, F.; Kamada, K.; Ohnabe, H. In situ network structure, electrical and thermal properties of conductive epoxy resin–carbon black composites for electrical heater applications. *Mater. Lett.* **2002**, *56*, 112–126. [[CrossRef](#)]
44. Chekanov, Y.; Ohnogi, R.; Asai, S.; Sumita, M. Electrical properties of epoxy resin filled with carbon fibers. *J. Mater. Sci.* **1999**, *34*, 5589–5592. [[CrossRef](#)]
45. Wajid, A.S.; Ahmed, H.T.; Das, S.; Irin, F.; Jankowski, A.F.; Green, M.J. High-Performance Pristine Graphene/Epoxy Composites with Enhanced Mechanical and Electrical Properties. *Macromol. Mater. Eng.* **2013**, *298*, 339–347. [[CrossRef](#)]
46. Wang, F.; Drzal, L.T.; Qin, Y.; Huang, Z. Mechanical properties and thermal conductivity of graphene nanoplatelet/epoxy composites. *J. Mater. Sci.* **2015**, *50*, 1082–1093. [[CrossRef](#)]
47. Gojny, F.H.; Wichmann, M.H.; Fiedler, B.; Schulte, K. Influence of different carbon nanotubes on the mechanical properties of epoxy matrix composites—A comparative study. *Compos. Sci. Technol.* **2005**, *65*, 2300–2313. [[CrossRef](#)]
48. Sandler, J.; Shaffer, M.; Prasse, T.; Bauhofer, W.; Schulte, K.; Windle, A. Development of a dispersion process for carbon nanotubes in an epoxy matrix and the resulting electrical properties. *Polymer* **1999**, *40*, 5967–5971. [[CrossRef](#)]
49. Tubes, C. Welcome to Cheap Tubes. Available online: <https://www.cheaptubes.com/> (accessed on 9 October 2019).
50. Smail, F.; Boies, A.; Windle, A. Direct spinning of CNT fibres: Past, present and future scale up. *Carbon* **2019**, *152*, 218–232. [[CrossRef](#)]
51. Gabhi, R.S.; Kirk, D.W.; Jia, C.Q. Preliminary investigation of electrical conductivity of monolithic biochar. *Carbon* **2017**, *116*, 435–442. [[CrossRef](#)]
52. Setter, C.; Silva, F.T.M.; Assis, M.R.; Ataíde, C.H.; Trugilho, P.F.; Oliveira, T.J.P. Slow pyrolysis of coffee husk briquettes: Characterization of the solid and liquid fractions. *Fuel* **2020**, *261*, 116420. [[CrossRef](#)]

53. Carrier, M.; Loppinet-Serani, A.; Denux, D.; Lasnier, J.-M.; Ham-Pichavant, F.; Cansell, F.; Aymonier, C. Thermogravimetric analysis as a new method to determine the lignocellulosic composition of biomass. *Biomass Bioenergy* **2011**, *35*, 298–307. [[CrossRef](#)]
54. Mishra, R.K.; Mohanty, K. Pyrolysis kinetics and thermal behavior of waste sawdust biomass using thermogravimetric analysis. *Bioresour. Technol.* **2018**, *251*, 63–74. [[CrossRef](#)]
55. Bartoli, M.; Rosi, L.; Giovannelli, A.; Frediani, P.; Frediani, M. Pyrolysis of α -cellulose using a multimode microwave oven. *J. Anal. Appl. Pyrol.* **2016**, *120*, 284–296. [[CrossRef](#)]
56. Lin, Y.-C.; Cho, J.; Tompsett, G.A.; Westmoreland, P.R.; Huber, G.W. Kinetics and mechanism of cellulose pyrolysis. *J. Phys. Chem. C* **2009**, *113*, 20097–20107. [[CrossRef](#)]
57. Collard, F.-X.; Blin, J. A review on pyrolysis of biomass constituents: Mechanisms and composition of the products obtained from the conversion of cellulose, hemicelluloses and lignin. *Renew. Sustain. Energy Rev.* **2014**, *38*, 594–608. [[CrossRef](#)]
58. Medalia, A.I.; Rivin, D. Particulate carbon and other components of soot and carbon black. *Carbon* **1982**, *20*, 481–492. [[CrossRef](#)]
59. Kambo, H.S.; Dutta, A. A comparative review of biochar and hydrochar in terms of production, physico-chemical properties and applications. *Renew. Sustain. Energy Rev.* **2015**, *45*, 359–378. [[CrossRef](#)]
60. Weber, K.; Quicker, P. Properties of biochar. *Fuel* **2018**, *217*, 240–261. [[CrossRef](#)]
61. Ferrari, A.C.; Robertson, J. Interpretation of Raman spectra of disordered and amorphous carbon. *Phys. Rev. B* **2000**, *61*, 14095. [[CrossRef](#)]
62. Bishui, B. On the Origin of Fluorescence in Diamond. *Indian J. Phys.* **1950**, *24*, 441–460.
63. Oberlin, A. Carbonization and graphitization. *Carbon* **1984**, *22*, 521–541. [[CrossRef](#)]
64. De Fonton, S.; Oberlin, A.; Inagaki, M. Characterization by electron microscopy of carbon phases (intermediate turbostratic phase and graphite) in hard carbons when heat-treated under pressure. *J. Mater. Sci.* **1980**, *15*, 909–917. [[CrossRef](#)]
65. Laskin, A.; Cowin, J.P. Automated single-particle SEM/EDX analysis of submicrometer particles down to 0.1 μm . *Anal. Chem.* **2001**, *73*, 1023–1029. [[CrossRef](#)]
66. Schueler, R.; Petermann, J.; Schulte, K.; Wentzel, H.P. Agglomeration and electrical percolation behavior of carbon black dispersed in epoxy resin. *J. Appl. Polym. Sci.* **1997**, *63*, 1741–1746. [[CrossRef](#)]



© 2019 by the authors. Licensee MDPI, Basel, Switzerland. This article is an open access article distributed under the terms and conditions of the Creative Commons Attribution (CC BY) license (<http://creativecommons.org/licenses/by/4.0/>).

Article

Durability Analysis of Formaldehyde/Solid Urban Waste Blends

Francesca Ferrari, Raffaella Striani, Paolo Visconti, Carola Esposito Corcione * and Antonio Greco

Department of Engineering for Innovation, University of Salento, 73100 Lecce, Italy;
francesca.ferrari@unisalento.it (F.F.); raffaella.striani@unisalento.it (R.S.); paolo.visconti@unisalento.it (P.V.);
antonio.greco@unisalento.it (A.G.)

* Correspondence: carola.corcione@unisalento.it; Tel.: +39-0832-297326

Received: 28 October 2019; Accepted: 5 November 2019; Published: 8 November 2019

Abstract: Following the innovative research activity carried out in the framework of the POIROT (Italian acronym of dOmotoc Platform for Inertization and tRaceability of Organic wasTe) Project, this work aims to optimize the composition of the blends between the organic fraction of municipal solid waste (OFMSW) and formaldehyde-based resins, in order to improve the durability properties. To this aim, in this work, commercial urea-formaldehyde and melamine-formaldehyde powder polymers have been proposed for the inertization of the OFMSW, according to the previous optimized OFMSW-transformation process. A preliminary study about the mechanical properties of the composite panels produced with the different resins was carried out by evaluating compressive, flexural, and tensile performances of the panels. Artificial weathering by cyclic (heating–cooling) and boiling tests were carried out and the mechanical properties were evaluated in order to assess the resistance of the panels to water and humidity. The melamine-formaldehyde based resin had the best performances also when subjected to the weathering tests and despite the higher content of resin in the composites, the panels produced with melamine-formaldehyde have the lowest values of release of formaldehyde minimizing their potential hazard level.

Keywords: solid urban waste; formaldehyde; durability

1. Introduction

In the last decade, municipal solid waste management has grown to be one of the main challenges of modern smart cities in the world. Any solution to improve the environmental sustainability represents a welcome candidate that can improve the quality of life for the population. In our previous research [1–3], we reported on the design and realization of an innovative prototype platform able to produce inertized and valorized panels, starting from the organic fraction of the municipal solid waste (OFMSW). The platform is managed by Arduino-based electronic sections for controlling process parameters and integrated with user recognition and a product traceability system based on radio frequency identification (RFID) technology. The POIROT (Italian acronym of dOmotoc Platform for Inertization and tRaceability of Organic wasTe) prototype machinery implements a transformation process, constituted by different sequential steps for transforming the organic wastes into a fully inert material. In particular, the main purposes of the transformation process are:

To transform the organic material into bricks, which are inert from a bacteriological point of view and, thus, storable for a long time without any problems in domestic environments;

To modify the composition of the produced inert material by adding specific additives, for giving it appropriate physical and mechanical characteristics, aimed at targeting the specific application of the products, for efficient reuse and recycling;

To label by means of a RFID tag and to properly identify the products for allocating them into storage centers so that they can be recovered and then reutilized in a targeted manner, thanks to the possibility of identification and traceability given by the RFID technology.

Among the other thermos-setting resins, such as epoxy and polyurethane, urea-formaldehyde (UF) systems were previously selected for inertization of OFMSW [1,2], due to their distinct advantages, such as high crosslinking, water solubility, high strength, cost effectiveness, and rapid curing performance [4]. For its own specific characteristics formaldehyde is, in fact, employed for a wide range of applications. The large diffusion of formaldehyde-based materials is due to the high chemical activity and relative cheapness that allows the employment of formaldehyde in several industrial realities. The high bactericidal action is exploited in the medical sector for the conservation of biological material or for sterilizing and disinfecting in pharmacology. Formaldehyde is used in chemical synthesis in the production of detergents, soaps, shampoos, and other cosmetic products as well as for the manufacturing of building materials, such as plywood lacquers, coatings, or glues. Outside of industrial processes, it is also well known that formaldehyde exists naturally in some vegetables and fruits [5]. For instance, pears (38.7–60 mg/kg), grapes (22.4 mg/kg), potatoes (19.5 mg/kg), bananas (16.3 mg/kg), bulb vegetables (11.0 mg/kg), apples (6.3–22.3 mg/kg), carrots (6.7–10.0 mg/kg), and watermelons (9.2 mg/kg) are the aliments that contain the most amount of formaldehyde. Formaldehyde is also employed as a feed hygiene substance in feed for animals [6–8]. The food industry widely uses formaldehyde like food preservatives (identified as E240) especially in smoked food products [9]. The use of formaldehyde as a preservative for food is still an open issue in Europe [7,10], although concentrations equal to 2.5 g/kg are permitted in the United States [9,11]. On one side, people are exposed to small amounts of formaldehyde by eating food, on the other side, the greatest damage occurs by inhalation. Nowadays, automobile and aircraft exhaust emissions, natural gas, fossil fuels, waste incineration, and oil refineries are the major man-made sources of formaldehyde [12]. Formaldehyde is normally present in both indoor [13] and outdoor air [14]. Building materials can be significant emission sources of volatile organic compounds (VOCs), affecting high concentration levels in indoor environments [15,16]. The urea-formaldehyde foam for insulating (UFFI) the buildings, particularly diffused in the 1970s, was substituted, in recent years, by the urea-formaldehyde spray foam (UF) [14], that is dried to remove any volatile compounds, thus less formaldehyde would be expected to be released. A variety of products present in the home can be sources of formaldehydes release, among those more diffused are wood floor finishes, pressed-wood, and wood-based products containing UF resins, such as wallpaper, paints, cigarette smoke, cooking fumes, but also carpets or gypsum board. Due to their porosity, they absorb significant amounts of formaldehyde that could become trapped inside these materials and subsequently released over time in the indoor air. Despite the wide presence of formaldehyde in several materials, it has been classified as cytotoxic, a mutagen, and a human carcinogen by the International Agency for Research on Cancer [17–20]. For such reasons, it is very important to preventively note the risks for human health and the environment by evaluating the hazards in order to limit the exposure. The UF resins have been proven to be efficient, cost and time saving, materials for the inertization of OFMSW. In previous works [1–3], the pre-sterilized OFMSW is mixed with a given amount of UF and water for the production of a pourable slurry. The developed OFMSW-transformation process without any pressure application in the POIROT prototype machinery allows curing of the resin. This approach enables the resin to block the release of odors and percolates from the OFMSW, and at the same time produce low cost bricks or panels, which can be useful in different industrial and building applications.

On the other hand, the aforementioned issues associated with the use of UF-based systems suggest the possibility of replacing them, also in view of their poor water resistance, which can cause degradation of the properties and release of free formaldehyde.

Therefore, this work is aimed at studying the suitability of different formaldehyde systems (urea/formaldehyde and melamine/formaldehyde) for the inertization of the treated OFMSW. The choice of a proper matrix is mainly based on the durability of the produced panels, with particular emphasis on

the resistance towards the effect of water, which can be detrimental for the mechanical properties, and at the same time can promote hydrolysis of the matrix, and consequent release of free formaldehyde.

2. Materials and Methods

Three resins, with decreasing formaldehyde content, were used in this work, in order to allow the intertization of the OFMSW, by producing composite panels with different performances:

1. Urea formaldehyde powder polymer, commercialized by Sadepan as SADECOL P 100N (Sadepan Chimica S.r.l, Viadana, Italy). It is supplied as fine powder/granules with defined grain size and a viscosity from 60 to 130 mPa*s at 20 °C. The resin is characterized by a formaldehyde content lower than 1% [21]. This resin is labelled as HUF (urea-formaldehyde with higher content of free formaldehyde);
2. Urea-formaldehyde powder polymer, commercialized by Sadepan as SADECOL P 410 (Sadepan Chimica S.r.l, Viadana, Italy). The resin is characterized by a formaldehyde content lower than 0.1% [22]. This resin is labeled as LUF (urea-formaldehyde with lower content of free formaldehyde);
3. Melamine-formaldehyde powder polymer, commercialized by Sadepan as SADECOL P 656 (Sadepan Chimica S.r.l, Viadana, Italy), obtained by condensation between melamine and formaldehyde, modified by addition of fillers, additives, and hardeners. The resin is characterized by a formaldehyde content lower than 0.1% [23]. This resin is labelled as MF (melamine-formaldehyde).

An amount of 10 wt% of a proper catalyst was added (Fast sad SD 10, supplied by Sadepan Chimica S.r.l, Viadana, Italy), in order to reduce the time and temperature of the curing process.

The OFMSW used was unsorted food waste collected according to standard Italian regulation. In particular, OFMSW was collected from a local dining room, and apart from food wastes, it contained small amounts (less than 0.5% in weight) of different soft wastes, such as tissues or napkins.

The amount of resin was chosen as the lowest quantity able to reach a complete hardening after the cure (Table 1). Lower amounts involved a partial, or total, desegregation of the sample after the polymerization. Each sample is labelled according to the amount of the organic fraction of municipal solid waste (OFMSW), which is therefore, for three samples, equal to 80% (labelled as OF80), 70% (labelled as OF70) and 50% (labelled as OF50). However, it should be kept in mind that the OFMSW is actually made of about 70% by water, which, however, is removed by evaporation at the end of the curing process. Therefore, in Table 1, the amount of water and the amount of dry OFMSW are also reported. In addition, the composition of cured samples, in which water is completely removed, is reported. The three samples also differ by the type of matrix which was used. Sample OF80_HUF with 80% of wet OFMSW was obtained with the UF SADECOL P 100N matrix (above defined HUF resin) characterized by a higher free formaldehyde content, whereas sample OF70_LUF with 70% of wet OFMSW was obtained with the SADECOL P 410 matrix (above defined LUF resin) characterized by a lower content of free formaldehyde. Finally, the sample OF50_MF with 50% of wet OFMSW was obtained with the melamine-formaldehyde P 656 matrix (above defined MF resin).

Rheological analyses were carried out on a Rheometrics Ares rheometer (TA Instruments, New Castle, DE, USA) on the slurry produced with the different resins. Steady rate tests were carried out at 25 °C, varying the shear rate from 0.05 to 1 s⁻¹, in order to evaluate the possible changes in viscosity due to the use of the different resins. In addition, dynamic temperature ramp tests were performed on all of the mixtures produced, in order to analyze the curing process of the samples during a heating scan from 25 to 120 °C with a heating rate of 5 °C/min, on a parallel geometry plate with a gap of 0.3 mm, constant oscillatory amplitude (1%), and frequency (1 Hz).

Table 1. Composition of the blends: OF80_HUF sample is a blend with 80% of wet OFMSW inertized in 20% of HUF resin, OF70_LUF refers to blend with 70% of wet OFMSW and 30% of LUF resin, finally OF50_MF is a blend with 50% of wet OFMSW and 50% of MF resin.

Formulation	Composition of the Slurry (wt%)			Composition of Cured Samples (wt%)	
	Water	Resin	Dry OFMSW	Resin	Dry OFMSW
OF80_HUF	54.9	21.6	23.5	48	52
OF70_LUF	47.9	31.6	20.5	60	40
OF50_MF	33.6	52	14.4	78	22

Several panels with the different resins of Table 1 (some of them shown in Figure 1) were produced by using the POIROT prototype machinery [1,3]. The latter prototype, besides the possibility to carry out a mechanical and thermal process for the transformation and valorization of the OFMSW, allows us to perform an electronic control aimed to check the correct operation of the different transformation processes. Additionally, a continuous diagnostic is ensured by means of appropriate measurement systems of the physical-chemical parameters related to each transformation phase of the conferred organic waste and of the intermediate and final waste water [3].

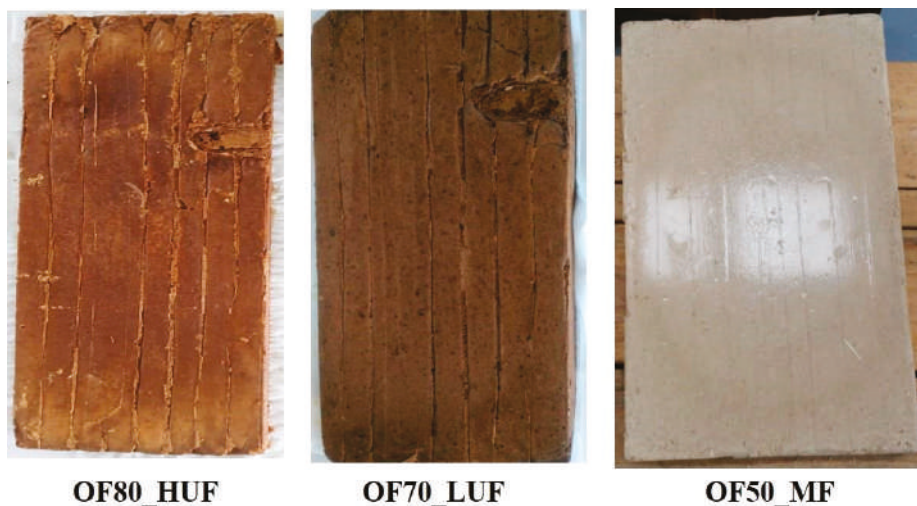


Figure 1. OFMSW-based panel production with different resins.

The dimensions of the produced panels are 400 mm × 200 mm × 30 mm, with an in-plane standard deviation of 3 mm and a through thickness standard deviation of 1 mm (Figure 1).

Compression, tensile, and flexural tests were performed according to, respectively, UNI EN 826 [24], UNI EN 319 [25], and UNI EN 310 [26] Italian standards that implement European directives on the cured panels for building applications. Before mechanical tests, all of the samples were weathered at RH 65%, 20 °C, up to constant weight. Referring to the standards, six samples were extracted from the panels with the following geometry:

UNI EN 826 (compression tests) [24]: sample dimensions equal to $t \times 50 \text{ mm} \times 50 \text{ mm}$, where t is the thickness of the panel (30 mm). Tests were carried out with a crosshead speed of 0.3 mm/min;

UNI EN 319 (tensile tests) [25]: sample dimensions equal to $L \times 50 \text{ mm} \times t$, where L is 200 mm, corresponding to half of the length of the panel and t is the thickness of the panel (30 mm). The crosshead speed was chosen as 5 mm/min, in order to obtain broken samples in 60 s;

UNI EN 310 (flexural tests) [26]: sample dimensions equal to $t \times 50 \text{ mm} \times 20t$, where t is the thickness of the panel (30 mm). The crosshead speed was chosen as 1.5 mm/min, in order to obtain broken samples in 60 s.

Afterwards, all the samples were subjected to cyclic boiling tests, in order to assess their resistance to water and humidity. In particular, according to UNI EN 321 [27], cyclic tests involved immersion in water for 70 h at 20 °C, followed by freezing at −18 °C for 24 h and heating at 70 °C for 70 h, and finally keeping them at room temperature for 4 h. The whole cycle is repeated three times. At the beginning and at the end of the test, the sample is weathered in a climatic chamber (at 20 °C and 65% RH) until constant weight is reached.

Samples exposed to cyclic tests were then subjected to compression tests, according to UNI EN 826 standard.

Also, boiling tests were performed on samples extracted from the panels, by following the UNI EN 1087-1 standard [28]. Tests consisted of immersion of the samples in neutral water at 20 °C, followed by heating in an oven at 110 °C. After water boiling, the sample is held in the oven for 120 min. After cooling, differently from the cyclic tests, the sample is not weathered.

After boiling, all the samples were subjected to compression, tensile and flexural tests with the procedures described above.

For each test, six repetitions were performed. The six samples were extracted from three different panels, in order to account also for the change of the properties due to different batches of OFMSW.

Finally, the formaldehyde emission for each panel was assessed, according to the UNI EN 717-2 standard [29]. Tests, performed in external laboratories, consisted of placing samples of 400 mm × 50 mm × board thickness in a 4-liter cylindrical chamber with controlled temperature (60 ± 0.5 °C), relative humidity ($\text{RH} \leq 3\%$), air flow (60 ± 3 L/h) and pressure. Air is continuously passed through the chamber at 1 L/min over the test piece, whose edge was sealed with self-adhesive aluminum tape before testing. The determinations were made in duplicate using two different pieces and the actual formaldehyde value is the average of the two pieces after 4 h expressed in mg-HCHO/m²·h. The formaldehyde amount in the water is then determined photometrically by acetyl acetone spectrophotometric analysis. The determination is based on the Hantzsch reaction, in which aqueous formaldehyde reacts with ammonium ions and acetyl acetone to yield dia-cetyldihydrolutidine (DDL) [30].

3. Results and Discussion

In Figure 2a, the steady state viscosity is reported as a function of shear rate for the different formulations reported in Table 1. In order to attain a low viscosity of the slurry, necessary to allow its pressure-free processing in the POIROT prototype, the matrices used in this work required different amounts of water. In the developed process, the required amount of water was supplied by the OFMSW, which was composed of about 70% water and the remaining fraction (about 30%) is made, above all, of different types of lipids, carbohydrates, and proteins. Reducing the amount of water necessary to attain the same viscosity has the distinct advantage of reducing the porosity of the panels, which in turn involves better mechanical properties [3].

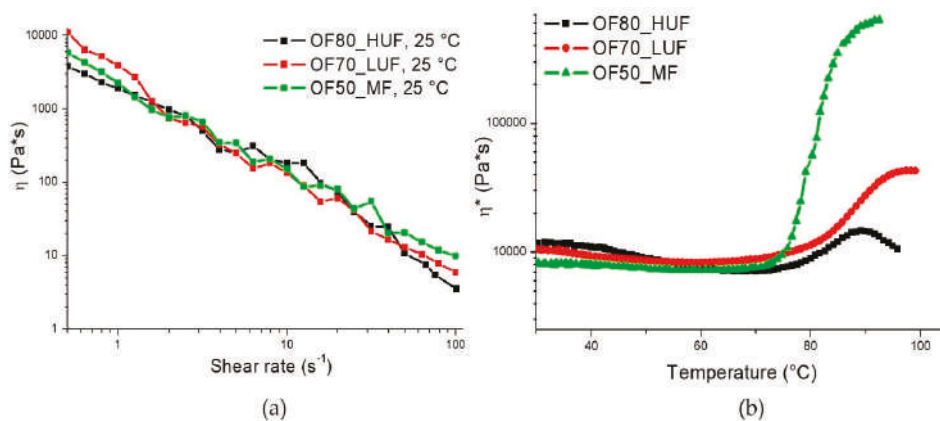


Figure 2. (a) Steady rate sweep tests at room temperature and (b) dynamic temperature ramp tests on OF80_HUF, OF70_LUF and OF50_MF samples.

The reactivity of the different mixtures was assessed through dynamic rheological analyses. Results, reported in Figure 2b, show that all of the tested formulations are characterized by similar onset temperatures of curing (T_0) (Table 2). On the other hand, as clearly shown in Figure 2b, the melamine/formaldehyde resin shows a much faster curing, as highlighted by the much higher slope of the curve (Table 2). Furthermore, the final viscosity (η_f) that is reached with this sample is much higher than those of the other two blends. This result is related to the lower water content of the mixture, which allows lower reaction times and higher final viscosity values.

Table 2. Rheological data obtained from the curves of Figure 2 (T_0 is the onset temperature of curing, η_f is the samples final viscosity).

Formulation	T_0 (°C)	Slope (Pa*s/°C)	η_f (Pa*s)
OF80_HUF	74.2	0.02688	1.47E4
OF70_LUF	71.5	0.04939	4.41E4
OF50_MF	70.7	0.20397	6.83E6

Typical stress-strain curves from compression, tensile, and flexural tests are reported in Figure 3a–c, respectively. The corresponding values for the strength (σ_R), strain at break (ϵ_R), and modulus (E) are reported in Table 3. The panels produced by the MF SADECOL P 656 resin are characterized by higher strength and elastic modulus in all of the loading conditions. This is due to the higher value of the density (ρ) of the panels, also reported in Table 3. In turn, the higher density is a direct consequence of the lower amount of water added in the slurry, which reduced the porosity of the panels. All of the samples show much better properties in compression than in tension. This is due to the brittle behavior of all of the panels and to the significant amount of porosity in each sample. As highlighted by the results of Table 3, all of the samples show, in flexural tests, an intermediate behavior between that measured in tension and in compression.

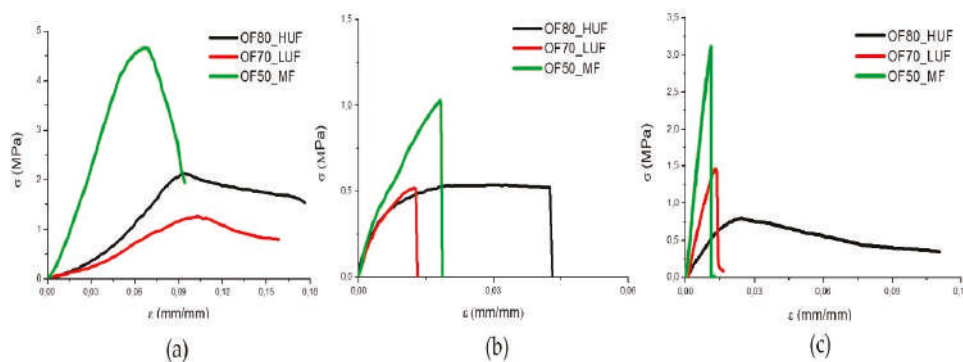


Figure 3. (a) Compression, (b) tensile, and (c) flexural tests on samples realized with different resins.

Table 3. Mechanical tests results (σ_R is the samples strength, ϵ_R the strain at break, E the modulus and ρ the density).

Formulation	σ_R (MPa)	ϵ_R (mm/mm)	E (MPa)	ρ (g/cm ³)
Compression Tests				
OF80_HUF	1.75 ± 0.36	0.16 ± 8.5E-02	40.79 ± 3.48	0.76 ± 0.02
OF70_LUF	1.98 ± 0.72	0.27 ± 6E-03	26.61 ± 6.16	0.75 ± 0.04
OF50_MF	5.17 ± 1.04	0.12 ± 1.3E-02	86.48 ± 10.69	0.86 ± 0.05
Tension Tests				
OF80_HUF	0.41 ± 0.13	0.07 ± 1.5E-02	79.14 ± 46.63	
OF70_LUF	0.44 ± 0.10	0.03 ± 1.4E-02	74.07 ± 20.84	
OF50_MF	1.02 ± 0.12	0.02 ± 3E-03	126.69 ± 15.87	
Flexural Tests				
OF80_HUF	0.76 ± 0.24	0.07 ± 0.02	75.87 ± 21.51	
OF70_LUF	1.21 ± 0.17	0.01 ± 2E-03	118.27 ± 17.10	
OF50_MF	2.79 ± 0.41	0.01 ± 2E-03	236.43 ± 41.61	

Compression tests were then carried after subjecting samples to cyclic humidity weathering according to UNI EN 321 standard. Only the OF80_HUF and OF50_MF samples were tested, since OF70_LUF ones were completely broken after the heating-cooling cycles, as detailed in Section 2. Results, reported in Figure 4, indicate, for both systems, a decrease of about 20% in compressive strength. On the other hand, the compressive modulus was strongly affected by the heating-cooling cycles, with a reduction of about 40% for OF50_MF system and a sharp decrease of about 70% for OF80_HUF samples. Therefore, in accordance with the results in Table 3. Mechanical tests results the analysis of the compressive behavior indicates better performances of OF50_MF samples even after cyclic tests.

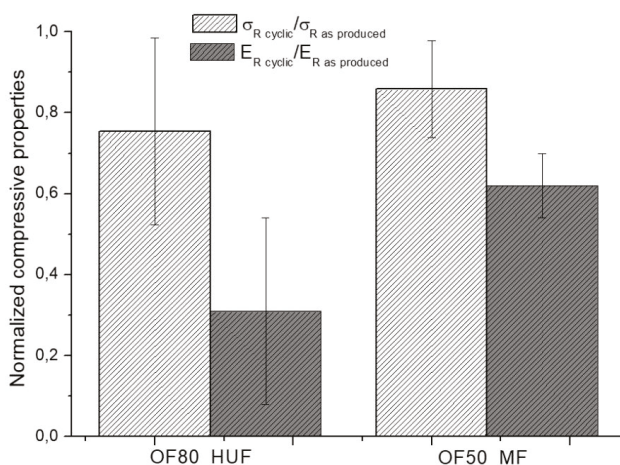


Figure 4. Normalized compressive tests after repeated heating-cooling cycles on OF80_HUF and OF50_MF samples.

Afterwards, all of the produced samples were subjected to boiling tests, according to UNI EN 1087-1. Once extracted, samples were tested in wet conditions with compressive, tensile, and flexural tests.

All of the measured properties showed a significant decrease after the boiling tests. In particular, referring to compressive tests, the results of Figure 5a,b show a reduction of about 30% and 90% respectively for the strength and modulus of the OF80_HUF samples. Referring to compressive properties, the ratio between the strength of the OF50_MF sample after and before the aging are comparable to that of OF70_LUF sample, whereas the ratio of modulus after and before the boiling tests of OF50_MF sample is much higher than that of OF70_LUF sample.

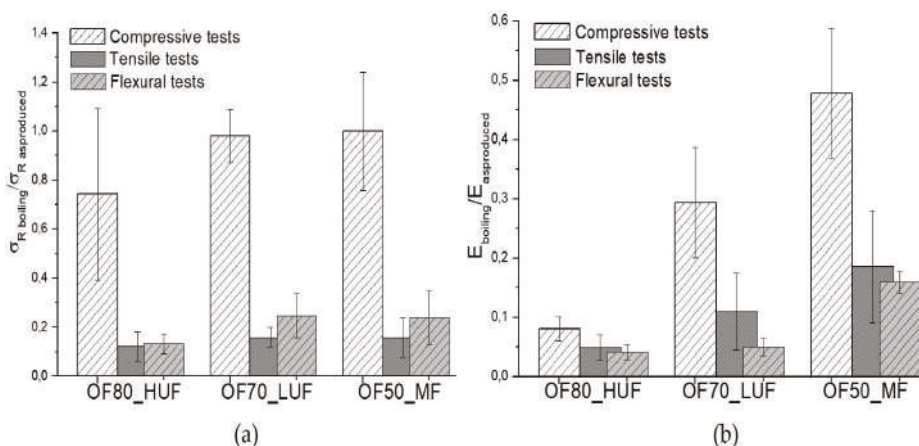


Figure 5. Mechanical response of OF80_HUF, OF70_LUF and OF50_MF samples after the boiling tests; ratio between strength of the samples after and before the boiling tests (a), ratio of samples' modulus after and before the boiling tests (b).

Tensile and flexural properties are, in general, much more affected by the boiling tests compared to compression properties. In particular, a reduction of about 90% for the strength was found relative

to the OF80_HUF sample, both in the flexural and tensile tests. The corresponding modulus decrease is about 95%. Therefore, even for boiling tests, the OF80_HUF sample showed the higher sensitivity.

The strength reduction for the OF70_LUF and OF50_MF samples are substantially equivalent both in tension and flexural tests. In both cases, a reduction of about 75–80% is found. However, the OF50_MF sample showed a better retention of the stiffness compared to the OF70_LUF sample, both in tension and flexural tests. Therefore, even in this case, better performances were reached with the OF50_MF composition.

Formaldehyde release was evaluated according to the UNI EN 717-2 standard, in order to assess whether the formaldehyde emission of the produced panels is lower than the standard limits for manufactured housing at the time of sale, thus allowing a possible commercialization of the realized products. Results in Figure 6 indicate that only OF50_MF samples show a formaldehyde release lower than the threshold limit value (TLV), thus confirming that these samples comply with the UNI EN 717-2 standard. On the other hand, both OF80_HUF and OF70_LUF panels showed a higher formaldehyde release than the TLV, with a higher gap for OF80_HUF samples. This result is attributable to a higher water content of the slurry before the curing process. Higher moisture and water content implies higher formaldehyde emissions, either due to retention of dissolved formaldehyde, less effective cure, or higher hydrolysis rate. Therefore, a lower release could be attained by decreasing the water content of the mixtures before the curing process.

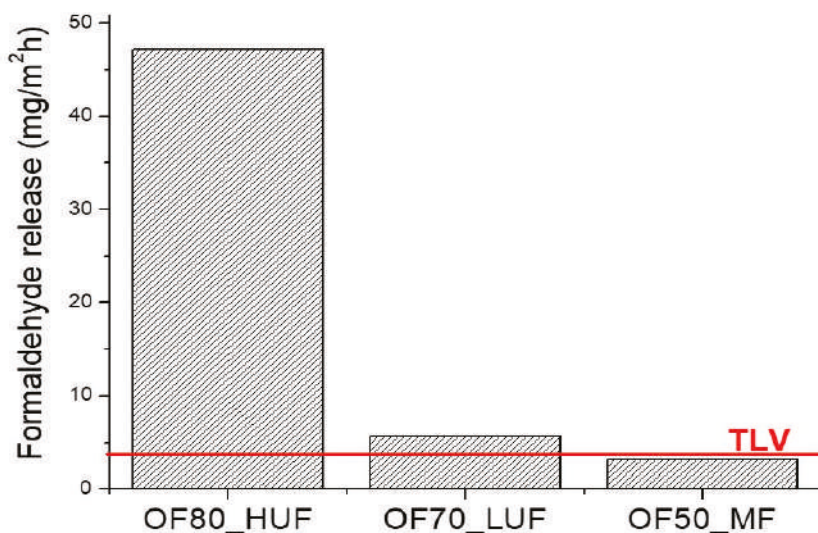


Figure 6. Formaldehyde release according to UNI EN 717-2 standard.

4. Conclusion

An innovative prototype machinery for the stabilization and valorization of the organic fraction of municipal solid waste (OFMSW) has been already assessed in the framework of the POIROT Project research activities, by using a urea–formaldehyde resin containing a formaldehyde content of less than 1 wt% [1,2]. In this paper, the possibility to substitute the previous resin with two different matrices containing a lower amount of free formaldehyde was evaluated. The composition of the blends between OFMSW and formaldehyde resins were, initially, optimized in order to improve the processability of the slurries. Attaining the same viscosity with the three different resins required different amounts of water, and therefore, different amounts of dry OFMWS. In particular, the melamine-formaldehyde SADECOL P 656 resin required the lower amount of water. The panels produced by the POIROT

platform showed a density which is strictly correlated to the initial amount of water of the slurry. A lower porosity was found for samples requiring lower amount of water.

As a consequence of this, the melamine–formaldehyde-based blend showed the best mechanical performances on the as-produced samples. However, even after artificial weathering cyclic heating–cooling or boiling tests, the melamine–formaldehyde based blend showed a better retention of the initial mechanical properties. In addition, the panels produced with melamine–formaldehyde showed the lowest values of formaldehyde release, evidencing the lowest hazard level. Starting from the results obtained in this work, the melamine–formaldehyde-based resin was selected as the more suitable matrix for the production of OFMSW-based composites with high mechanical and durability properties and low environmental impact, as achieved with the use of POIROT machinery.

Author Contributions: Investigation, F.F. and R.S.; supervision, C.E.C. and A.G. and P.V.; project administration, P.V.

Funding: This work is funded by the project POIROT with CUP code B89J17000370008 supported by the MISE (Ministry of Economic Development) of Italy within the European Union’s Horizon 2020 research and innovation program, in collaboration with Italian companies Medinok SpA (Volla, NA) and Arter Srl (Castello di Cisterna, NA).

Acknowledgments: The authors gratefully acknowledge SADEPAN CHIMICAL S.r.l. for supplying the Urea-Formaldehyde resin and for technical support.

Conflicts of Interest: The authors declare no conflict of interest.

References

- Esposito Corcione, C.; Ferrari, F.; Striani, R.; Minosi, S.; Pollini, M.; Paladini, F.; Panico, A.; Greco, A. An innovative green process for the stabilization and valorization of organic fraction of municipal solid waste (OFMSW) I part. *Appl. Sci.* **2019**, *9*, 4516. [CrossRef]
- Esposito Corcione, C.; Ferrari, F.; Striani, R.; Minosi, S.; Pollini, M.; Paladini, F.; Panico, A.; Greco, A. An innovative green process for the stabilization and valorization of organic fraction of municipal solid waste (OFMSW) II part: Optimization of the curing process. *Appl. Sci.* **2019**, *9*, 3702. [CrossRef]
- Ferrari, F.; Striani, R.; Minosi, S.; De Fazio, R.; Visconti, P.; Patrono, L.; Catarinucci, L.; Esposito Corcione, C. An innovative IoT-oriented prototype platform for the management and valorization of the organic fraction of municipal solid waste. *Submitt. J. Clean. Prod.*, under review.
- Conner, A.H. Urea-Formaldehyde Adhesive Resins. *Polym. Mater. Encycl.* **1996**, *128*, 8496–8501.
- Nowshad, F.; Islam, M.N.; Khan, M.S. Analysis of the Concentration and Formation Behavior of Naturally Occurring Formaldehyde Content in Food. *Int. J. Food Eng.* **2018**, *4*, 71–75. [CrossRef]
- European Food Safety Authority (EFSA). Scientific Opinion on the safety and efficacy of formaldehyde as a feed hygiene substance in feed for pigs and poultry. *EFSA J.* **2014**, *12*, 3790. [CrossRef]
- Adiveter, S.L. Scientific Opinion on the safety and efficacy of formaldehyde for all animal species. *EFSA J.* **2014**, *12*, 3562. Available online: <https://efsa.onlinelibrary.wiley.com/doi/abs/10.2903/j.efsa.2014.3562> (accessed on 30 October 2019).
- Regabl, B.V. Scientific opinion on the safety and efficacy of formaldehyde for all animal species based. *EFSA J.* **2014**, *12*, 3561. Available online: <https://efsa.onlinelibrary.wiley.com/doi/abs/10.2903/j.efsa.2014.3561> (accessed on 30 October 2019).
- Wahed, P.; Razzaq, M.A.; Dharmapuri, S.; Corrales, M. Determination of formaldehyde in food and feed by an in-house validated HPLC method. *Food Chem.* **2016**, *202*, 476–483. [CrossRef] [PubMed]
- Directorate, C. *Update of the Opinion of the Scientific Committee for Animal Nutrition on the Use of Formaldehyde as a Preserving Agent for Animal Feeding Stuffs of 11 June 1999 Scientific Opinions*; European Commission: Brussels, Belgium, 1999; pp. 1–19.
- United States Environmental Protection Agency (USEPA). *Toxicological Review of Formaldehyde-Inhalation Assessment USEPA*; USEPA: Washington, DC, USA, 2010.
- Liteplo, R.G.; Beauchamp, R.; Chénier, R.; Meek, M.E. *International Programme on Chemical Safety*; World Health Organization: Geneva, Switzerland, 2002.
- Salthammer, T.; Mentese, S.; Marutzky, R. Formaldehyde in the indoor environment. *Chem. Rev.* **2010**, *110*, 2536–2572. [CrossRef] [PubMed]

14. U.S. Consumer Product Safety Commission. *An Update on Formaldehyde*; U.S. Consumer Product Safety Commission: Bethesda, MD, USA, 2016. Available online: https://www.cpsc.gov/s3fs-public/An-Update-On-Formaldehyde-725_0.pdf (accessed on 30 October 2019).
15. Knudsen, H.N.; Kjaer, U.D.; Nielsen, P.A.; Wolkoff, W. Sensory and chemical characterization of VOC from emissions from building products: Impact of concentration and air velocity. *Atmos. Environ.* **1999**, *33*, 1217–1230. [CrossRef]
16. Calisti, R.; Isolani, L.; Rossano, M. Formaldehyde exposure patterns in a set of Italian indoor workplaces with and without specific emission sources—2011–2018. *Ital. J. Occup. Environ. Hyg.* **2018**, *9*, 165–175.
17. International Agency for Research on Cancer—IARC, Monographs on the Evaluation of Carcinogenic Risks to Humans—Internal report 14/002, France, 2014. Available online: <https://monographs.iarc.fr/wp-content/uploads/2018/08/14-002.pdf> (accessed on 30 October 2019).
18. Yu, P.H. Deamination of methylamine and angiopathy; toxicity of formaldehyde, oxidative stress and relevance to protein glycooxidation in diabetes. *J. Neural Transm.* **1998**, *52*, 201–216.
19. Feron, V.J.; Til, H.P.; de Vrijer, F.; Woutersen, R.A.; Cassee, F.R.; van Bladeren, P.J. Aldehydes: Occurrence, carcinogenic potential, mechanism of action and risk assessment. *Mutat. Res. Toxicol.* **1991**, *259*, 363–385. [CrossRef]
20. *World Health Organization—International Agency for Research on Cancer—IARC, Overall Evaluation of Carcinogenicity to Humans*; Formaldehyde—Monographs Series; Lyon, France, 2004.
21. Technical Data-Sheet, Sadepan SADECOL P 100N-Product Specifications. 2018. Available online: <https://www.sadepan.com/en/products/> (accessed on 30 October 2019).
22. Technical Data-Sheet, Sadepan SADECOL P 410-Product Specifications. 2018. Available online: <https://www.sadepan.com/en/products/> (accessed on 30 October 2019).
23. Technical Data-Sheet, Sadepan SADECOL P 656-Product Specifications. 2018. Available online: <https://www.sadepan.com/en/products/> (accessed on 30 October 2019).
24. Italian standardization institute, UNI EN 826:2013 Isolanti Termici per Edilizia—Determinazione del Comportamento a Compressione; 2013. Available online: <http://store.uni.com/catalogo/uni-en-826-2013>, (accessed on 30 October 2019).
25. Italian Standardization Institute. UNI EN 319:1994 Pannelli di Particelle di Legno e Pannelli di Fibra di Legno. Determinazione Della Resistenza a Trazione Perpendicolare al Piano del Pannello; 1994. Available online: <http://store.uni.com/catalogo/uni-en-319-1994> (accessed on 30 October 2019).
26. Italian Standardization Institute. UNI EN 310:1994 Pannelli a Base di Legno. Determinazione del Modulo di Elasticità a Flessione e Della Resistenza a Flessione; 1994. Available online: <http://store.uni.com/catalogo/index.php/uni-en-310-1994> (accessed on 30 October 2019).
27. Italian Standardization Institute. UNI EN 321:2002 Pannelli a Base di Legno—Determinazione Della Resistenza All Umidità Mediante Prove Cicliche; 2002. Available online: <http://store.uni.com/catalogo/index.php/uni-en-321-2002> (accessed on 30 October 2019).
28. Italian Standardization Institute. UNI EN 1087-1:1997 Pannelli di Particelle di Legno. Determinazione Della Resistenza All Umidità. Prova in Acqua Bollente; 1997. Available online: <http://store.uni.com/catalogo/uni-en-1087-1-1997> (accessed on 30 October 2019).
29. Italian Standardization Institute. UNI EN 717-2:1996 Pannelli a Base di Legno. Determinazione del Rilascio di Formaldeide. Rilascio di Formaldeide con il Metodo Dell’analisi del Gas; 1996. Available online: <http://store.uni.com/catalogo/index.php/uni-en-717-2-1996> (accessed on 30 October 2019).
30. Salem, M.Z.M.; Böhm, M.; Barčík, S.; Beránková, J. Formaldehyde Emission from Wood-Based Panels Bonded with Different Formaldehyde-Based, Resins. *Wood Ind. Drv. Ind.* **2011**, *62*, 177–183. [CrossRef]



© 2019 by the authors. Licensee MDPI, Basel, Switzerland. This article is an open access article distributed under the terms and conditions of the Creative Commons Attribution (CC BY) license (<http://creativecommons.org/licenses/by/4.0/>).

Review

A Review on the Flammability Properties of Carbon-Based Polymeric Composites: State-of-the-Art and Future Trends

Karthik Babu ¹, Gabriella Rendén ², Rhoda Afriyie Mensah ³, Nam Kyeun Kim ⁴, Lin Jiang ³, Qiang Xu ³, Ágoston Restás ⁵, Rasoul Esmaeely Neisiyany ⁶, Mikael S. Hedenqvist ^{2,*}, Michael Försth ⁷, Alexandra Byström ⁷ and Oisik Das ^{8,*}

¹ Center for Polymer Composites and Natural Fiber Research, Tamil Nadu 625005, India; karthikbabunitt@gmail.com

² Department of Fibre and Polymer Technology, Polymeric Materials Division, School of Engineering Sciences in Chemistry, Biotechnology and Health, KTH Royal Institute of Technology, 100 44 Stockholm, Sweden; grenden@kth.se

³ School of Mechanical Engineering, Nanjing University of Science and Technology, Nanjing 210094, China; ramensah@ymail.com (R.A.M.); ljiang@njust.edu.cn (L.J.); xuqiang@njust.edu.cn (Q.X.)

⁴ Centre for Advanced Composite Materials, Department of Mechanical Engineering, University of Auckland, Auckland 1142, New Zealand; nam.kim@auckland.ac.nz

⁵ Department of Fire Protection and Rescue Control, National University of Public Service, H-1011 Budapest, Hungary; Restas.Agoston@uni-nke.hu

⁶ Department of Materials and Polymer Engineering, Faculty of Engineering, Hakim Sabzevari University, Sabzevar 9617976487, Iran; r.esmaeely@hsu.ac.ir

⁷ Structural and Fire Engineering Division, Department of Civil, Environmental and Natural Resources Engineering, Luleå University of Technology, 97187 Luleå, Sweden; michael.forsth@ltu.se (M.F.); alexandra.bystrom@ltu.se (A.B.)

⁸ Department of Engineering Sciences and Mathematics, Luleå University of Technology, 97187 Luleå, Sweden

* Correspondence: mikaelhe@kth.se (M.S.H.); oisik.das@ltu.se (O.D.)

Received: 26 April 2020; Accepted: 1 June 2020; Published: 8 July 2020

Abstract: Carbon based fillers have attracted a great deal of interest in polymer composites because of their ability to beneficially alter properties at low filler concentration, good interfacial bonding with polymer, availability in different forms, etc. The property alteration of polymer composites makes them versatile for applications in various fields, such as constructions, microelectronics, biomedical, and so on. Devastations due to building fire stress the importance of flame-retardant polymer composites, since they are directly related to human life conservation and safety. Thus, in this review, the significance of carbon-based flame-retardants for polymers is introduced. The effects of a wide variety of carbon-based material addition (such as fullerene, CNTs, graphene, graphite, and so on) on reaction-to-fire of the polymer composites are reviewed and the focus is dedicated to biochar-based reinforcements for use in flame retardant polymer composites. Additionally, the most widely used flammability measuring techniques for polymeric composites are presented. Finally, the key factors and different methods that are used for property enhancement are concluded and the scope for future work is discussed.

Keywords: biochar; carbon fillers; nanocomposites; flame retardants; fire

1. Introduction

In the forwarded note of World Health Organization (WHO), it is mentioned that burns constitute a major public health problem, especially in low- and middle-income countries, where over 95% of all burn

deaths occur. Fire-related burns alone account for over 300,000 deaths per year [1]. The development of safer buildings and appliances is one of the reasons for low death rate in high-income countries. Nowadays, polymers and their composite products are ubiquitous in numerous fields in day-to-day life, such as microelectronics, construction, furniture, automotive, packaging, etc. However, an important limitation is that most polymers are easily flammable [2]. Initially, polymers start to degrade (pyrolyse) when a sufficient amount of heat and oxygen are present. Further, the release of combustible gases, which mixes with atmospheric air, together promote the vigorous burning of substrate and the consequent decomposition of materials. This burn initiation (ignition) depends on flash point and auto-ignition of the material. In brief, polymer decomposition mainly depends on its ignitability, fire spread, and heat release characteristics. The sufficient amount of heat, fuel, and oxygen supply are needed at each and every stage of combustion, and these sources may be ambient or self-induced (especially during material burn. the release of volatile gases and particulates act as a sources for further combustion and create a cyclic process). It is critical to improve the flame retardancy of the polymers and their composites in order to satisfy safety guidelines. Carbon-based materials have demonstrated exceptional thermal, chemical and mechanical properties along with their inherent resistance towards degradation by combustion. Therefore, the enhancement of the flame retardancy of polymer composites by utilizing the carbo-based nano-fillers, such as fullerene, CNTs, graphene, graphene nanosheets (GNSs), Graphene quantum dots (GQDs), graphite, etc., is currently being attempted by numerous researches. Thus, it is worthwhile to gain a holistic view on the effect of carbon-based nano-fillers on flammability characteristics of various multifunctional polymer composites. There are numerous tests that enable the determination of the fire behaviour of polymeric composite materials. For instance, the Limiting Oxygen Index (LOI) test can give information regarding the minimum amount of O₂ that is required by a material to sustain burning. Common polymers like polypropylene (PP) and polyethylene (PE) have LOI ranging between 17 to 19%. This means that the aforementioned materials require 17 to 19% of oxygen concentration for complete material combustion process in 3 min. [3]. In addition, one of the most potent technique to judge the reaction-to-fire properties of materials is cone calorimetry. The fire properties of polymers can be determined at various fire circumstances (Time to ignition/TTI: ignition stage, Heat release rate/HRR: fire developing stage, and Total heat release/THR: fully developed fire stage). The main purpose of the above outline is to emphasise the need for fire testing of polymeric composites and the widely used fire tests, such as LOI test, UL-94 vertical burning test, cone calorimetry, and micro- combustion calorimetry, are discussed in detail in this review. It is envisaged that this review will provide a summative information regarding the flammability properties of carbon-based polymeric composites, thus aiding researchers to gain insight into the efficacy of particular carbon-based additives.

2. Carbon Family Materials

Carbon and its family materials are employed in numerous applications owing to their inherent advantages, such as porosity, high strength and stiffness, conductivity, etc., and the family is comprised of carbon black (low cost), biochar (widely available and eco-friendly) or single and multi-walled carbon nanotubes (sophisticated), and so on. In the past two decades, a significant diversion and development in material science research were noticed when new members entered into the carbon family. This kind of revolutionary development in engineering primarily started with the discovery of fullerene [4]. Subsequently, such developments were propagated by the discovery of carbon nanotubes (CNTs) [5] and graphene [6]. The application of these carbon-based materials to address the issue of flammability in polymeric composites stems from the fact that conventional fire retardants (FRs) are detrimental for the mechanical properties. Additionally, some halogen-based FRs are pernicious towards the environment. Chen et al. used both nanoclays and CNTs FRs in epoxy composites and arrived at the following conclusions. The reduction in the flammability of the polymer composite is primarily due to the formation of network structure layer on the burning surface and, as compared to nanoclays FR, this layer is effectively formed while using CNTs [7]. For instance, Figure 1 shows the

importance and role of carbon-based filler addition in polymer. During polymer pyrolysis, a protective layer (Figure 1b) is formed on the polymer composites, which restricts the transfer of combustible gases and heat; thus, the further degradation of materials can be avoided.

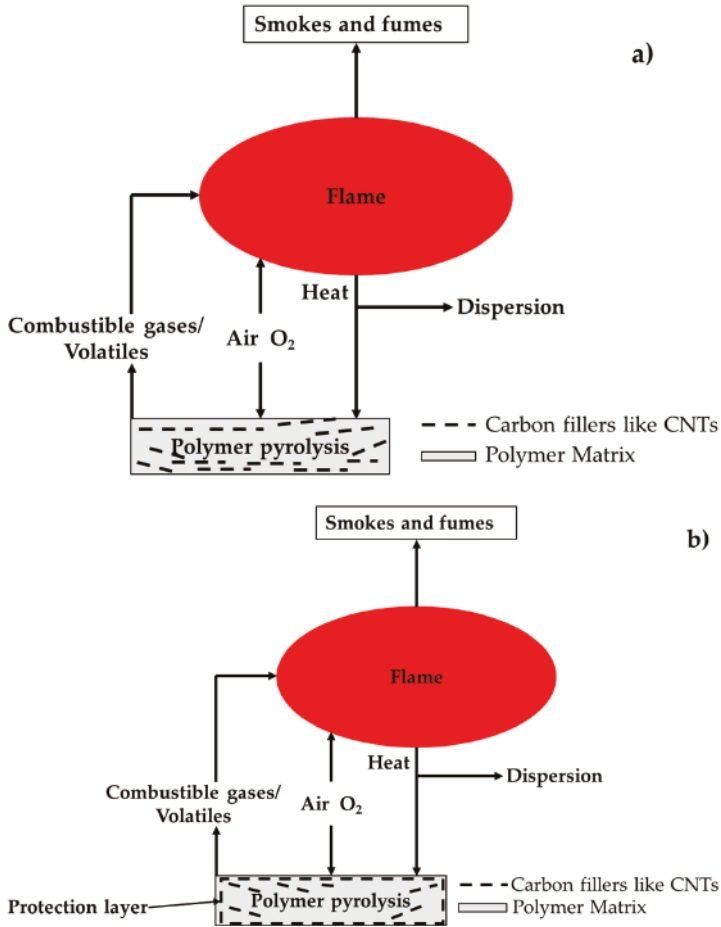


Figure 1. Polymer Combustion (a) at initial stage and (b) carbon fillers formed protection layer.

2.1. Effect of Various Carbon-Based Materials on Flammability of Polymer Composites

2.1.1. Fullerene

Fullerene, informally called buckyball, is an allotrope of carbon. The fullerene family contain C₆₀, C₇₀, C₇₈, C₈₂, C₈₄, C₉₀, C₉₆, and so on, and, among these, the most important and widely used member in polymer composites is C₆₀, which is spherically shaped carbonaceous nanomaterial having excellent medical benefits and it is also an antioxidant [8]. C₆₀ is called radical sponge i.e., C₆₀ shows high reactivity towards free radicals and can trap more than 34 free radicals during the combustion of polymer [9]. In the past decade, the influence of fullerene reinforcement on the mechanical strength of different polymer matrices has adequately been studied and presented [10–12]. However, there are limited studies available regarding the effect of fullerene on the enhancement of fire resistant properties of polymer matrix composites. For instance, Kausar analysed the effect of polyurethane (PU)

coating on various flame retardancy properties of poly (methyl methacrylate) (PMMA), in which the reinforcement used was C₆₀. The continuous reduction in peak heat release rate (pHRR) was recorded while incorporating C₆₀ in the PU coated PMMA matrix and compared to neat PU/PMMA, 0.5 wt% of C₆₀ added PU/PMMA displayed 61% of reduced pHRR. In addition, C₆₀ reinforced composites have showed prolonged time delay to ignition and reduced time to pHRR [13], and the reasons are subsequently explained. Song et al. have demonstrated the flammability behaviour of polypropylene (PP) nanocomposites, in which the reinforcement used was fullerene C₆₀. It was reported that, as compared to neat PP, different amounts of C₆₀ reinforced PP composites have showed significantly reduced flammability i.e., notable drop in pHRR and extended time to ignition [14]. Guo et al. prepared the surface functionalised C₆₀ using 9, 10-dihydro-9-oxa-10-phosphaphenanthrene-10-oxide in order to further promote the flame retardancy of PP composites. Compared to as received C₆₀ nano-fullerene, the reinforcement of 3 wt% surface functionalised filler had exhibited higher TTI and lower combustion duration [15]. The enhancement of flame retardancy of polymers while adding different carbon-based FRs can be perceived from Table 1. Various fire properties are quantitated and their improvement (in %) corresponding to neat polymer value are calculated.

In summary, the combustion mechanism of most of the polymer chains follow a free radical chain reaction via β -scission and the presence of fullerene in polymers might trap these free radicals produced due to thermal degradation of polymers. This process subsequently forms an in-situ crosslinked network and as a result of this network formation the thermal stability and fire-resistant properties are enhanced. Fullerene also shows good synergistic effect with inorganic metal flame retardant (mFR), intumescent flame retardants (iFRs), brominated flame retardants (bFRs), nanoclay, CNTs, graphene oxide (GO), and so on.

2.1.2. Nanotubes

There are generally three classes of carbon nanotubes, namely multi-walled carbon nanotube (MWCNT), double-walled carbon nanotube, and single walled carbon nanotubes (SWCNT). Amongst these, the first discovered MWCNT has two or more tubular shaped graphite fibres and these hollow nanotubes form a concentric cylindrical structure with a space between them that is near to that of the interlayer distance in graphite (0.34 nm) [7]. The MWCNT is a potent FR and its performance is more effective than the organoclays [16]. On the other hand, a single layer tube extending from end to end is called SWCNTs, which has uniform cross section of 0.7–3 nm and their size is close to fullerenes [17]. Both classes of CNTs are widely used as nanofillers in polymer nanocomposites because of their inherent and superior electrical and thermal conductivity and mechanical strength [18]. These varieties of fillers have been used in order to improve the flame retardancy of polymers since the discovery of CNTs in 1991. This is because of the effective formation of continuous thin protective layer on the surface of the polymer, acting as a thermal shield between the oncoming heat/O₂ and underneath virgin polymer. Most importantly, a considerable reduction in HRR might be accomplished with low filler concentrations [19]. P. Patel et al. applied both single and multi-walled CNTs separately in polyether ether ketones (PEEK) matrix and the flammability behaviour of prepared nanocomposites was investigated. The study revealed that the incorporation of small quantity of CNT (0.1 to 1 wt%) showed significant changes of thermal decomposition and flammability of PEEK. Notably, the optimum loading amount of SWCNT (1 wt%) in PEEK is twice than that of MWCNT (0.5 wt%), because the MWCNT showed better dispersion in PEEK than SWCNT [20]. The principal challenge in using nanofillers, like CNTs, is obtaining uniform dispersion and distribution. Since most of the polymers are viscous in nature, the possibility of agglomeration increases with an increasing concentration of nanofillers in the matrix. Kashiwagi et al. showed an impact of CNTs dispersion and concentration on the flammability of PMMA. The better fire resistance performance of the samples during the burning test was found when the dispersion of the SWCNTs is uniform and the filler concentration was between 0.2 to 1 wt%. The PMMA nanocomposites with less than 0.2 wt% of SWCNT showed large number of black discrete islands from which vigorous bubbling during burning occurred. On the other hand,

the samples having more than 0.2 wt% SWCNT exhibited reduced crack formation and the creation of an effective network on the nanocomposite surface during the burning test. The nanocomposites with good network layer and very low discrete islands showed significantly reduced pHRR. The pHRR of the nanocomposite that had good network structured layer is approximately 50% less than those that formed the islands [21]. Therefore, the dispersion of nano-fillers in a matrix can strongly influence the flammability behaviour of the composites and, to improve it further, the functionalization of CNT can also be performed [22]. Mostly, coupling agents were used to functionalize the surface of the CNTs, through which the uniform dispersion was accomplished [23]. For instance, epoxy composites with 9 wt% concentration of vinyltriethoxysilane functionalized CNTs showed 22 to 27% of increase in LOI and V-1 to V-0 rating progress in UL-94. Moreover, the glass transition temperature (T_g) was shifted from 118 to 160 °C and char yield at 750° was increased by 47% for the same level of reinforcement [24]. The uniform dispersion and distribution of CNTs have the main contribution in the formation of continuous barrier layer with the help of high quality char. This high-quality char plays a predominant role in the minimization of pHRR [25,26]. The other commonly used techniques are the use of surfactants [27], controlled sonication of fillers in various solvents [28], and ultra-speed mechanical stirring [29]. Besides, the combined effects of CNTs with other fillers are also demonstrated to enhance the flame retardancy of polymers. For instance, the hybrid filler reinforced composites formed a superior barrier char layer with reduced cracks during cone calorimeter test when compared to individual CNTs or organoclay reinforced composites [30]. In another study, Wen et al. demonstrated the effect of carbon black (CB) on thermal stability and flame retardancy of PP/CNTs ternary nanocomposites. When compared to neat PP and PP/CNTs nanocomposites, the carbon black added nanocomposites (PP/CNTs/CB) displayed improved thermal stability and exhibited lower pHRR and higher LOI. It was concluded that the improvement of flame retardancy was strongly dependent on the concentration of CB [31].

2.1.3. Graphene and Graphene Derivatives

Graphene has the unique structure of one atomically thick and two-dimensional (2D) monolayer composed of sp^2 hybridised carbon atoms. Graphene is the relatively younger member in the carbon family, which was discovered in the year 2004 by the exfoliation of graphite. Graphene has high specific surface area [32], excellent tensile modulus, high strength [33], and superior thermal conductivity [34]. Besides, graphene is an effective FR due to its layered and graphitized structure [35]. Because of these properties of graphene, it is used as a potential reinforcement to enhance the fire retardancy and thermal conductivity of polymer composites. In this section, the recent studies regarding the effect of graphene addition on flammability of various polymer composites are discussed.

Huang et al. prepared poly (vinyl alcohol) (PVA) nanocomposites, in which they have reinforced various amounts of graphene and compared their flammability behaviour with sodium montmorillonite (Na-MMT) and MWCNT reinforced PVA nanocomposites. The PVA filled with 3 wt% of graphene displayed 49% of reduced pHRR when compared to neat PVA. For the same level of filler concentration, the graphene/PVA composites exhibited superior flame retardancy as compared to Na-MMT/PVA and MWCNTs/PVA composites. When compared to neat PVA, the 2 wt% graphene reinforced PVA composites displayed 11 s delay in time to ignition (TTI) and 45% reduction of pHRR, whereas 5 wt% graphene reinforced PVA composites showed 27 s delay in time to ignition (TTI) and 64% reduction of pHRR. When compared to smooth surface of MWCNTs, the presence of oxygen and hydroxyl groups on graphene surface is the main reason for intimate graphene/PVA interactions, which led to the enhancement of flame retardancy of polymer [36]. Attia et al. synthesised graphene while using the ultrasonication process in which maleate diphosphate (MDP) was used as dispersant. Followed by synthesis, acrylonitrile-butadiene-styrene (ABS) composites were fabricated, in which the reinforcements were MDP, graphene-MDP, and graphene-MDP-TiO₂, and their flammability were determined. The TiO₂ nanoparticles decorated graphene reinforced ABS composite exhibited 49% of reduction in both pHRR and total heat release (THR). In addition, the average mass loss rate

and emission of CO₂ were significantly reduced by 50% and 37%, respectively. When compared to neat ABS, the nanocomposites exhibited a slow burning rate and the reduction in burning rate was recorded as 71% [37]. In addition, the possibility of using reduced graphene oxide (rGO) as an active synergist for iFR/PP composites was demonstrated by Yuan et al. The reduced heat and smoke release were observed at a lower content (between 0.5 to 1 wt%) of rGO addition in the iFR/PP composites and this was due to the improved char swelling and better insulation by the char. The high thermal conductivity of rGO leads to an increase in thermal conductivity of iFR/PI composites. This caused the enhancement of pHRR from 156 to 262 kW/m² while increasing the rGO concentration from 1 to 2 wt%, respectively. This shows that FR synergism is effective at a lower amount of graphene (less than 1 wt%) and higher loading of rGO exhibits antagonistic effect on the iFR. Li et al. prepared epoxy nanocomposites in which the reinforcement used was silane treated graphene oxide nanosheets (GON). The 2-(Diphenylphosphino)ethyltriethoxy silane (DPPES) was grafted onto the surface of the GON while using a condensation reaction, as a result of this synergistic phosphorus/silicon-contained GON FR was obtained. The effect of DPPES-GON addition on the flammability of epoxy was assessed using LOI and UL-94 tests. The 10 wt% of DPPES-GON incorporated epoxy composite displayed significantly enhanced flame retardancy. The LOI of neat and DPPES-GON 10 wt%/epoxy composite is 20% and 36%, respectively. In addition, the UL-94 results changed from no-rating to V-0 rating when 10 wt% of DPPES-GON was added with neat epoxy. The protective layer arrested the flammable gases and acted as a barrier between the heat and unburned epoxy. The synergism of phosphorus and silicon was increased by the effectiveness of the FR system. The presence of phosphorus in compounds formed H₃PO₄ during thermal decomposition and subsequently produced pyrophosphoric acid. The residue from the condensation of phosphoric acid played the major role in curbing combustion. Glass-like phosphorus-containing solid residue is formed due to the condensation of pyrophosphoric acid. This layer would limit the production of volatiles and inhibit the combustion process. Silicon also plays a vital role in this FR system. The low surface energy of silicon caused it to move towards the surface of the protective layer and the protective char layer was evidenced by the char that is obtained from the samples after the LOI test. As the sample was burned, the silicon oxidized into inorganic silicon dioxide due to high heat generation and it formed a thermally stable protective char layer [38]. Thus, the incorporation of low concentration of graphene into iFR/PP composites leads to the formation of closed chamber in the char residue and, consequently, an enhanced char swelling was accomplished that imparted flame retardancy [39].

GQD is zero-dimensional graphene nanofragments, which consists of one or a few layers of graphene and their lateral dimension is less than 100 nm [40]. GQDs exhibit different properties as compared to bulk graphene, like easy functionalization, good physical and chemical stability, high surface to mass ratio, and offer many benefits for energy storage applications [41]. More recently, GQDs have been used as a FR material in polymer composites. Mostly, the hydrothermal method was adopted to synthesise GQDs from nitrogen, nitrogen phosphorous, GO, etc., since this method is economical, sustainable, and the resultant FR will be effective [42–44]. Rahimi-Aghdam, et al. prepared two types of GQDs, in which the first one is nitrogen doped GQDs (NGQDs) and the other one is nitrogen and phosphorous co-doped GQDs (NPGQDs). They have used the hydrothermal method to perform the synthesis process. Subsequently, the polyacrylonitrile (PAN) nanocomposites were prepared with the two types of GQDs as additives and their flammability behaviours were recorded. PAN/NGQDs and PAN/NPGQDs nanocomposites both achieved V-0 rating in UL-94 test [42]. The same group of authors have synthesised ZnAl layered double hydroxide and mixed with NPGQDs. The resultant hybrid fillers were used as reinforcement in PAN nanocomposites and their flammability performance was assessed through cone calorimeter (Table 1) [43]. Khose et al. effectively synthesised functionalized FR GQDs while using GO and phosphorous source via a hydrothermal treatment and recommended for textile applications. It was reported that the transparency of prepared carbon-based GQDs FR retains the colour of the cloth. The flame test results showed that the FR GQDs coated cloth

initially emitted very low smoke and did not ignite for more than 300 s while retaining its shape. On the contrary, the normal cloth ignited in just in 5 s and it was completely burnt within 15 s [44].

In summary, graphene and newly found graphene derivatives, like GO, rGO, and GQDs, are potent FRs. These can be employed individually (graphene alone) and in hybrid form (graphene with conventional FRs or inorganic nanofillers) in order to enhance the flame retardancy of the polymer composites.

2.1.4. Graphite

Graphite, which is also known as plumbago or black lead, is an important allotrope of elemental carbon. It is a layered mineral set (can be natural or synthetic) that is made up of stacked GNSs, in which the carbon atoms in the layer forms hexagonal rings through covalent bonds and the successive carbon layers are connected together by weak Van der Waals forces. The usage of as received graphite as FRs in polymers is limited, since the infiltration of viscous polymer resins is very difficult in natural graphite. Therefore, the chemically treated natural graphite, known as expandable graphite (EG), has been extensively used as FR for a variety of polymers. Chemicals, such as sulfuric acid (H_2SO_4) or nitric acid (HNO_3), may be inserted between the graphite layers [45]. Hence, EG acting as an intumescent additive is also a graphite intercalation compound. When EG is exposed to a heat source, the decomposition of H_2SO_4 occurs, which is followed by a redox reaction process (Equation (1)) between H_2SO_4 and the graphite will produce the blowing gaseous products, such as CO_2 , SO_2 , and H_2O [46].



As stated above, the EG contains treated flake graphite with intercalation reagents, such as H_2SO_4 . When EG material is exposed to high heat, the H_2SO_4 starts to decompose and release gaseous products. This process leads to an increase in inter-graphene layer pressure and generates sufficient strong push, which keeps graphite layers apart. As a result of high heat and successive pressure development, the material starts to expand and the volume of the EG increases about 10 to 100 times the initial volume, known as the blowing effect. The expansion suffocates the flame, acts as a good smoke suppressant, and restricts mass transfer from the polymers, which prevents further degradation of the underneath virgin materials [47,48]. Therefore, when a material is exposed to high temperature, EG expands and produces a voluminous protective layer, thus providing FR performance to various polymeric matrices [49]. Lee et al. demonstrated the enhancement of flame retardancy and self-extinguishing properties of polyketone (PK) nanocomposites. The authors have reinforced hybrid fillers in PK matrix, which has EG and MWCNTs, in order to achieve superior flame retardancy. The addition of small quantity of MWCNTs (1 wt%) with EG led to better protection network formation in PK and, as a result, the thermal stability and LOI were significantly enhanced. This network that formed during combustion acted as a barrier and restricted the polymer degradation. From the experimental results, the LOI and pHRR for neat PK is 25% and 464.4 kW/m^2 , respectively. The reinforcement of 30 wt% of EG in PK displayed 35% of LOI and 182.7 kW/m^2 of pHRR. Further addition of 1 wt% of MWCNTs with 40 wt% of EG hybridisation showed the LOI of 45% and pHRR of 118.4 kW/m^2 . This tremendous enhancement of flame retardancy was due to the formation of bridging network by EG and MWCNTs. During combustion, the exfoliation of EG is restricted while adding 1 wt% of MWCNTs and degradation of underneath materials are also prevented [47]. Zhu et al. analysed the synergistic effect of adding EG and ammonium polyphosphate (APP) on flame retardancy of poly lactic acid (PLA)-based composites. The prepared PLA composites contained 15 wt% of APP/EG (1:3 ratio) that exhibited 36.5% of LOI and rated V-0 in UL-94 test. The PLA containing same combination of filler showed 38.3% reduced pHRR than neat PLA. The synergism between APP and EG was advantageous, since they together formed a stable and more dense char protective layer. This layer formation avoided the further combustion of underlying substrate [50].

In summary, EG is widely used as an effective FR in various polymeric materials. Compared to individual EG as FR, the synergistic effect of two fillers produced significant enhancement of flame retardancy in polymeric composites. Addition of small amount of CNTs with EG performed well during combustion.

2.1.5. Biochar (BC)

The limitations of inorganic carbon family based (fullerene, CNT, etc.) FRs are their high cost, since they need advanced synthesis techniques. There is a huge demand for green, sustainable, eco-friendly, and renewable alternative materials for composite applications due to the increased environmental awareness. Hence, carbon rich filler materials derived from the renewable source is an appropriate substitute for this issue and can be used as reinforcement in polymer composites preparation to enhance various physical, mechanical, and FR properties.

BC, or biocarbon, is a carbonaceous material that is made by heating virtually any biomass in a neutral environment. This carbon rich material has been recently used as the reinforcement in polymer composites and led the way for the production of eco-friendly composites with enhanced mechanical and FR properties [51,52]. Instead of using the organic wastes directly in the manufacturing of biocomposites, BC derived from various biomasses, such as Rice Husk [53], bamboo [54], paunch grass, pine wood saw dust, date palm [55], poultry litter, and sewage and dewatered sludge [56], are utilized as a reinforcement. Thermo-chemical conversion technology of slow pyrolysis is the main process that is used for the generation of high yield BC. The physical and chemical properties of the BC are highly dependent on the selected biomass and thermal processing conditions, such as pyrolysis temperature, residence time, heating rate, sweep gas flow rate, etc. [57,58]. These properties include density, surface area, microscopic changes, like pore growth (size and volume), hardness/modulus, and pulverisability [59]. The density of the selected biomass as a feedstock has strong influence on the density of BC. For instance, the high-density BC could be produced using high density biomass [60]. The BC has better thermal stability than the natural fibres [61]. The macro, meso, and micro-pores on its surface provide better physical bonding with matrix (Figure 2) [59]. Chemically treated and untreated BCs reveal different functional groups on their surfaces, which consist of carboxyl ($-\text{COOH}$) and hydroxyl ($-\text{OH}$) groups. These functionalities are sensitive to carbonisation temperature and, with the increase in temperature, they start to dwindle [62]. Better bonding and good compatibility between matrix and BC could be obtained while the surface area and pore volume are high. Typically, the BC surface has a porous honeycomb structure consisting of a high concentration of carbon. These porous honeycomb structures of BC filler allow for the infiltration of the molten polymer during processing and they create a physical bonding, which could result in an improvement of mechanical properties of the composites [63]. Liu et al. studied the combustion characteristics of bamboo-BCs at the heat flux of 35 kW/m^2 , which were produced at three different pyrolysis temperatures (200, 250, and $300 \text{ }^\circ\text{C}$) and at three different residence times (1, 1.5, and 2 h). For all temperatures, the TTI is shortened with an increase in residence time, while all of the bamboo-BCs (produced at different temperatures and residence time) displayed a shorter TTI when compared to bamboo materials. It was observed that with an increase in test time, bamboo-BCs exhibited random cracks on its surface due to the differential thermal stability of their compositions. With the help of these cracks, some volatile material is released and caused faster ignition. The pHRR of bamboo-BCs was lower when compared to bamboo materials, which indicated a lower content of moisture content and volatile matter [64]. Zhao et al. analysed the flammability of BC, which were produced from different feedstocks, namely, corn, wood, dairy manure with rice husk, and bull manure with sawdust at different pyrolysis temperatures and as a function of time post production. In general, BCs made at higher pyrolysis temperatures had lower flammability. All four BCs used in the study also displayed the highest surface area at high temperature. The study also confirmed that none of the tested biochar samples qualified as flammable substances, which extend its application in manufacturing FR polymer composites [65]. Das et al. fabricated BC/PP biocomposites and their mechanical, thermal stability, and flammability

behaviour were evaluated. The reinforced biocomposites showed increased thermal stability, reduced pHRR, and lower smoke release when compared to neat PP. The strong covalent bonding of carbon atoms makes them difficult to be separated during combustion, thereby increasing fire resistance. The BC had high thermal stability, as observed from TGA by the authors and, thus, their addition in composites also increased the thermal stability of the polymer due to the additive effect. It was concluded that both tensile and flexural modulus of the biocomposites were increased with an increase in concentration of BC. Additionally, the major reasons for this enhancement of mechanical properties are better compatibility and good physical bonding between the BC and the matrix, owing to the porous structure of the BC [66]. Elnour et al. used lignocellulosic biowaste from date palm, which were pyrolysed at different temperatures and their effect on physical structure and surface morphology was studied. The authors manufactured BC/PP composites and concluded that the reinforced PP showed better thermal stability and enhanced stiffness. In particular, as compared to neat PP, the BC added PP displayed reduced thermal decomposition and lower maximum degradation temperature. Moreover, the authors suggested surface functionalization of filler for the further enhancement of the mechanical, thermal, and flammability properties [67]. Ikram et al. studied the mechanical and flammability characteristics of wood/pine wood BC/PP biocomposites and demonstrated the properties with respect to neat PP and maleated anhydride polypropylene. It was concluded that the addition of MAPP coupling agent and wood particles have significantly enhanced the tensile and flexural properties, but the pHRR remained unaffected [68]. Elsewhere, the hybridisation technique was followed by Das et al., where the authors used a mixture of BC and wool. Biocomposites with hybrid fillers significantly minimised the pHRR and smoke release when compared to neat PP. The char layer limited the heat and fuel transfer between the ambient air and underneath polymer. The LOI value was enhanced because of the hybridisation with wool [69]. When BC is made at high temperature, all of the volatiles escape from its surface, leaving behind a carbon skeleton. The absence of these flammable volatiles does not provide the fuel for combustion to occur [67,70]. Two batches of wood dust (WD)/BC/PP composites were fabricated, in which two types of conventional FRs such as APP and magnesium hydroxide $Mg(OH)_2$, were individually added and their reaction-to-fire properties were assessed through cone calorimeter test by Das et al. The TTI and pHRR of neat PP was found as 29 s and 1054 kW/m^2 , respectively. Whereas, adding 20 wt% of APP and $Mg(OH)_2$ with WD (10 wt%)/BC (24 wt%)/PP composites significantly reduced the pHRR to 376.2 kW/m^2 and 333.3 kW/m^2 , respectively. In both cases, the PP composite, which has higher BC concentration and less WD, actively reduced the pHRR. The carbonaceous layer that formed by the thermally stable BC with other constituents have restricted the transport of fuel and O_2 , which led to improved fire properties, such as LOI, pHRR, and THR. In addition, the tensile strength was unaffected, whereas other mechanical properties, such as tensile modulus, flexural strengths, and flexural modulus, were considerably improved when compared to neat PP. However, some of the FR particles got trapped inside the biochar pores, thereby somewhat reducing their efficiencies. APP was more affected, because it relies on condensed phase reaction requiring contact with the polymer [71]. In summary, enhanced flame retardancy of polymer composites using BC reinforcement is one of the best techniques, since both environmental sustainability and low-cost are considered. The BC that is derived from wood, grasses and agricultural wastes using any suitable thermo-chemical conversion technique can be effectively used in biocomposites fabrication, which significantly reduces the landfilling of agro wastes and also provides a new platform for the development of new materials [72,73].

Table 1. Cone calorimetry and Limiting Oxygen Index (LOI) test data for various neat polymers and its nanocomposites.

Type of Composites	TTI (s)	% of Ignition Time Delay from Neat Polymer Increased (↑) or Decreased (↓)	pHRR (kW/m ²)	% of pHRR Increased (↑) or Decreased (↓) wr. to Neat Polymer	Time to pHRR (s)	THR (MJ/m ²)	LOI (%)	Ref.
PU/PMMA	70	—	343	—	189	—	—	[13]
PU/PMMA/FluI-C ₆₀ 0.5	101	44% (↑)	131	61.8% (↓)	150	—	—	[13]
Neat PP	29	—	1054	—	—	97	—	[63]
TCP 900 *	20	31% (↓)	473.68	55% (↓)	—	86.95	—	[63]
Neat PP	29 ± 2	—	1054 ± 120	—	120 ± 18	97 ± 14	18 ± 0.1	[69]
BC + PP + APP	14 ± 0	51.7% (↓)	277.82 ± 2.4	73.6% (↓)	120 ± 29.6	88.75 ± 0.7	22.08 ± 0.1	[69]
Neat PP	30	—	1261	—	335	208	18	[31]
PP + 3wt% CB	20	33.3% (↓)	584	53.6% (↓)	355	192	22.6	[31]
PP + 3wt% CNT + 5wt% CB	25	16.6% (↓)	314	75.1% (↓)	70	180	27.6	[31]
Neat PVA	18 ± 2	—	373 ± 6	—	—	58 ± 0.6	—	[36]
PVA + 3wt% Na-MMT	20 ± 2	11.1% (↑)	263 ± 7	29.4% (↓)	—	58 ± 0.4	—	[36]
PVA + 3wt% MWCNT	24 ± 2	33.3% (↑)	241 ± 8	35.3% (↓)	—	52 ± 0.4	—	[36]
PVA + 3wt% GNS	33 ± 2	83.3% (↑)	190 ± 6	49% (↓)	—	45 ± 0.3	—	[36]
PVA + 5wt% GNS	45 ± 3	150% (↑)	133 ± 5	64.3% (↓)	—	38 ± 0.5	—	[36]
Neat ABS	43 ± 1.5	—	1385 ± 92	—	—	145 ± 11	—	[37]
ABS-MDP	32 ± 1.5	25.5% (↓)	821 ± 55	40.7% (↓)	—	97 ± 9	—	[37]
ABS-GRP-MDP	18 ± 1	58.1% (↓)	81.2 ± 54	41.3% (↓)	—	91 ± 6	—	[37]
ABS-GRP-MDP-TiO ₂ NP-5	35 ± 1.2	18.6% (↓)	720 ± 48	48% (↓)	—	75 ± 6	—	[37]
Neat PAN	10	—	609	—	25	9.1	—	[42]
PAN/NGQDs	15	50% (↑)	565	7.2% (↓)	30	8.5	—	[42]
PAN/NPGQDs	20	100% (↑)	515	15.4% (↓)	35	7.7	—	[42]
Neat PAN	10	—	609	—	25	9.1	—	[43]
PAN/ZnAl LDH	20	100% (↑)	462	24.1% (↓)	40	7.9	—	[43]
PAN/ZnAl LDH-NPGQD	25	150% (↑)	435	28.5% (↓)	45	7.4	—	[43]

* pine wood-based BC were produced at pyrolysis temperatures of 900 °C. Note: The expansion for all used abbreviations is available in the running text.

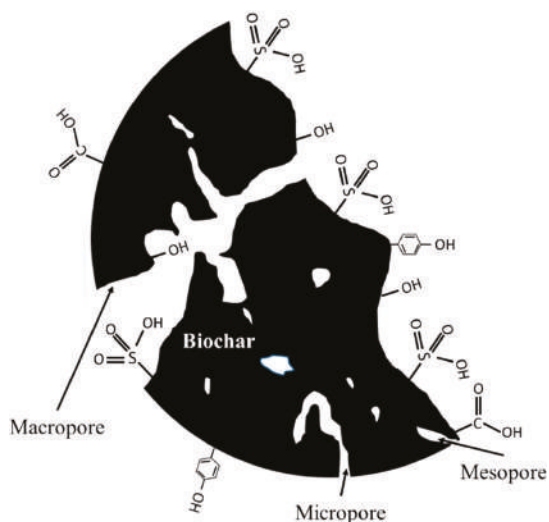


Figure 2. Schematic of biochar (BC) with different functional groups and pores. Adapted with permission from Ref. [59].

2.1.6. Other Carbon-Based Materials

Apart from all of the aforementioned fillers, nanosized carbon black (CB) is a low cost, abundantly available, electrically conductive, and low-density reinforcement that has been widely used to enhance properties of polymer composites. A few studies reported its effect on the flammability of various polymeric matrices (Table 1). Studies revealed that the CB filled composites not only exhibited good flame retardancy, but also the thermal stability was improved [74–76]. Yang et al. studied the effect of CB incorporation on flame retardancy and thermal decomposition of PP/carbon fibre (CF) composites. The authors confirmed the uniform dispersion of CB fillers in PP/carbon fibre composites while using morphological analysis. LOI of neat PP was 18.2% and the individual effect of 3 wt% of CF and 5 wt% of CB reinforced PP composites on LOI was 19.9% and 24.6%, respectively. The hybrid form of CF and CB fillers showed significant beneficial effect on the flammability of PP composites when compared to individual CF and CB reinforcement. LOI of 3 wt% CF and 5 wt% CB reinforced PP composites was recorded as 25.7%. Importantly, the pHRR assessed from cone calorimeter for neat PP and hybrid fillers reinforced composites is 1212 kW/m² and 361 kW/m², respectively. This synergistic effect of hybrid form of CB and CF have shown better flame retardancy in the PP matrix as compared to the individual performance of CB and CF. The one-dimensional (1-D) CF and zero-dimensional (0-D) CB together formed a strong three-dimensional (3-D) network in PP matrix. The developed network had significant role in the formation of compact carbonaceous protection layer during pyrolysis. As a result, as compared to neat PP, PP/CF, and PP/CB composites, a significant enhancement of flame retardancy of PP/CF/CB composites was obtained [75].

3. Flammability Measuring Techniques

Experiments for measuring material flammability and fire behaviour are classified into small, bench, and large scales, depending on the sample size required [77]. However, these tests involve a great deal of expertise in their operation. Hence, standard protocols, like ASTM and ISO, have been provided for easy application. The following sections briefly reports some commonly used small-scale and bench-scale experiments for flammability analysis.

3.1. LOI Test

The LOI test (Figure 3a) is a laboratory scale test process that provides a measure of the lowest amount of oxygen needed to ignite a vertically positioned sample of size $80 \times 10 \times 4 \text{ mm}^3$ in an oxygen and nitrogen mixed environment [78,79]. The test procedure and calibrations can be found in ASTM D2863, ISO 4589-2, and NES 714. According to the standards, the gas stream flows in an upward direction to the vertically oriented sample in a chimney, whilst a propane gas flame ignites the upper part of the material. Thus, the sample's burning length and time are determined for flammability analysis. LOI can be calculated by following mathematical expression:

$$\text{LOI} = \left(\frac{[\text{O}_2]}{([\text{O}_2] + [\text{N}_2])} \right) \times 100$$

where, $[\text{O}_2]$ and $[\text{N}_2]$ are the flow rate of oxygen and nitrogen in L/min. respectively.

Therefore, a material, which demands more oxygen, will display higher LOI. In addition, a higher index indicates that the material is more flame resistant. Given that atmospheric air has 21% of O_2 , the risk of burning of polymer materials is high, whose LOI value is less than 21; however, materials with an LOI above 21 are categorized as self-extinguishing because their combustion cannot be retained at standard atmosphere without the support of an external source [80].

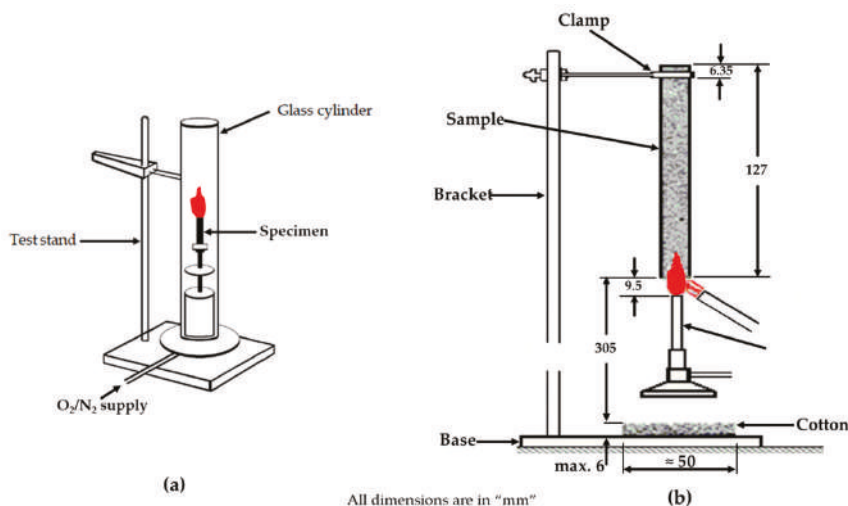


Figure 3. Experimental set-up: (a) LOI and (b) UL-94 vertical burn tests. Adapted with permission from Ref. [81].

In summary, LOI is a common characterisation method and it has been used in numerous studies. The main objective of most of the studies is fabricating polymer composites with increased flame retardancy, so that it will demand higher oxygen percentage in order to combust.

3.2. Vertical Burn Test (UL 94)

This test has been developed by Underwriters Laboratory Inc. for testing the flammability of plastics. In practice, the UL 94 vertical burning test is common technique (Figure 3b), which provides the rating for the test specimens based on its ignition and flame spread of materials exposed to a small flame [82]. The test protocol is designated in ASTM D3801. The procedure involves the preparation and exposure of the said sample of size $127 \times 13 \times 3 \text{ mm}^3$ to a carefully controlled flame for 10 s. Any burning action after the removal of the flame is monitored and recorded. If the specimen

self-extinguishes. the flame is then reapplied for another 10 s, and then removed. For improved accuracy and reliability, at least five samples are tested for each material combination. The burning time for flame exposures and afterglow are recorded. The qualitative ranks for evaluating the test results of the experiment are no-rating, V-0, V-1, and V-2, as shown in the test protocol. Materials are classified into these three categories, depending on satisfaction of the conditions that are mentioned in Table 2. If the sample continue to burn upon initial flame application, it is given no rating.

Table 2. Conditions for UL-94 classifications [83].

Specific Flaming Characteristics	Rating		
	V-0	V-1	V-2
Total flaming combustion time (in seconds)			
• for each specimen	≤10	≤30	≤30
• for all five specimens of any set	≤50	≤250	≤250
Flaming and glowing combustion for each specimen after second burner flame application	≤30	≤60	≤60
Cotton ignited by flaming drips from any specimen	No	No	Yes
Glowing or flaming combustion of any specimen to holding clamp	No	No	No

3.3. Micro-Scale Combustion Calorimetry (MCC)

MCC is used to characterize the fire behaviour of materials. It uniquely measures the heat release capacity (HRC), which is a combination of thermal stability and combustion properties of materials that can be used to categorise the flammability [77,84]. The HRC is also described as a rate-independent flammability parameter and, from thermodynamics point of view, it is an intensive property and can be measured from chemical structure of a material [84]. The HRC (in $\text{J g}^{-1} \text{K}^{-1}$) is defined as the maximum HRR per unit mass in the test (in W g^{-1}) divided by the average heating rate over the measurement range (K s^{-1}), and this is the single best measure of the fire hazard of a material [85].

The test apparatus has two separate stages. the pyrolysis and combustion phases. In ASTM D7309-19. the experimental procedure consists of two selectable pyrolysis modes, namely Method-A and Method-B, which are used for controlled thermal and thermal oxidative decomposition, respectively. Samples of mass 0.5–50 mg are pyrolysed in inert gas and the volatile effluent is mixed with excess oxygen prior to combustion in Method-A, while pyrolysis in Method-B occurs in a mixture of oxygen and inert gas [86]. The heat release rate from the test is obtained from oxygen consumption calorimetry. Other derived parameters are the total heat release rate, time, and temperature at pHRR. MCC curves are represented by plots of heat release rate against temperature or time.

3.4. Cone Calorimetry

Cone calorimetry is the most widely applied bench-scale fire experiment. The test method measures the heat release rate, ignition time, mass loss rate, combustion or extinction time, smoke production, soot yield, and quantities of CO and CO₂. The sample size for the test is within $0.1 \times 0.1 \times 0.001\text{--}0.05 \text{ m}^3$ and the applicable heat flux ranges from 10 to 100 kW/m^2 . The prepared samples are wrapped in aluminium foils and positioned horizontally or vertically under the cone-shaped heater, according to the designated standards (ASTM E1354, ISO 5660). A load cell measures the weight change and the pyrolysate is ignited by an electric pilot spark igniter. The smoke is collected in the hood of the equipment for further analysis. The cone calorimeter operates on the principles of oxygen consumption calorimetry. Extrinsic factors, such as geometry and orientation of the sample, sample thickness, ignition source, ventilation, and temperature, affect the measurement accuracy [77,87].

1. TTI or t_{ig} in s: describes the ease of ignition of the polymeric material by measuring how fast the flaming combustion occurs when the polymeric material is exposed to incident heat flux (in kW/m^2) and in oxygen-controlled ambient environment. Hence, polymeric material with a high TTI indicates material that is difficult to be ignited. In the case of flame-retarding polymer composites, sometimes the addition of FRs lead to advance decomposition and, thereby, the reduction of TTI (Table 1). Thus, the shorter TTI is not an indication of worsening flame retardancy of a material.
2. HRR in kW/m^2 : is known as the heat release per unit time and unit surface area during the cone calorimetry test. Mainly, the amount of peak HRR (pHRR) and time taken to reach the pHRR are used to measure the fire performance of polymeric materials.
3. Total heat release (THR in kJ/m^2): is the total quantity of calorific value released per unit area after the combustion of materials, and this can be determined according to the integration of the HRR vs. time.
4. Fire growth rate (FGR in $\text{KW}/(\text{s.m}^2)$): FGR is mathematically calculated as $\text{FGR} = \text{pHRR}/(\text{pHRR})_{t_i}$ [81], $(\text{pHRR})_{t_i}$ is the time taken to reach the pHRR. The faster FGR indicates the shorter the time that is taken to notice the fire [88].
5. Mass loss rate (MLR in g/s): is the amount of mass loss of polymeric material per unit time during combustion.

4. Conclusions and Scope for Future Research

In summary, carbon and its family materials are potential FR reinforcement in polymer composites and these reinforcements are attractive alternatives for conventional FRs. The carbon-based fillers actively reduce the flammability of the polymer composites by (1) the formation of protective char layer and (2) absorbing free radicals. In the first case, the contact of atmosphere and flame with underlying materials is reduced, since the char layer acts as a shield between them. The second is the internal process, which minimise the reaction rate and, as a result, the combustion is disrupted. In addition, carbon-based filler reinforcements are able to improve thermal stability, mechanical properties, and thermal conductivity of the polymers. Chemicals, like silane, can be grafted onto the surface of the carbon-based fillers and analysing their performance on flame retardancy in polymers without compromising the mechanical strength still has scope for further research.

The high purity nanofillers are cost intensive; therefore, achieving the flame retardancy at lowest filler concentration is desired. This could be achieved by using carbon based nanofillers (like CNTs, Fullerene, graphene sheets, etc.). Either one of following methods was followed in order to obtain further enhancement of flame retardancy in polymer composites: surface functionalization, coupling agents, and hybridisation of fillers. In most of the cases, the best FR synergism with iFRs can be achieved at less than 1 wt% of CNTs or graphene concentration and further loading of carbon-based fillers exhibits adverse effects. Recently, there is a huge scope for the enhancement of fire safety of polymers using GQDs based FRs and limited studies are available in this field.

Most importantly, eco-composites that were produced with BC reinforcement exhibited acceptable FR effect and this BC could be derived from various biomasses (feedstock is agro and forestry wastes) by the pyrolysis process, which also reduces the landfilling of agro wastes. However, scientific studies are required to understand the synergistic effect of BC with other fillers (it might be a carbon-based filler or inorganic particle in hybrid form) on FR properties of polymer composites. BC is merely a fire-resistant additive that indicates further research is needed to make them fire retarding. Furthermore, BC could be used in conjunction with other FRs. In addition, the incorporation of FRs reduces the mechanical properties, such as tensile and flexural strength of composites, and the use of BC with conventional FRs could conserve the strength and enhance fire resistance. However, the application of BC in the field of FR polymer composites is mainly at the stage of laboratory experiments or at infant stages in some industrial application. However, in the future, such a situation might be entirely changed, since BC could be produced in large quantity at a low cost.

Author Contributions: Conceptualization, O.D.; data curation, K.B., G.R., R.A.M., N.K.K., R.E.N.; writing—original draft preparation, K.B., G.R., R.A.M., R.E.N., O.D., N.K.K.; writing—review and editing, O.D., M.F., M.S.H., Á.R., L.J., Q.X., A.B.; supervision, O.D., M.S.H., M.F.; All authors have read and agreed to the published version of the manuscript.

Funding: The funders had no role in the design of the study; in the collection, analyses, or interpretation of data; in the writing of the manuscript, or in the decision to publish the results.

Acknowledgments: The authors express their gratitude towards STINT/NFSC grant (CH2018-7733).

Conflicts of Interest: The authors declare no conflict of interest.

References

1. World Health Organization. *A WHO Plan for Burn Prevention and Care*; World Health Organization: Geneva, Switzerland, 2008.
2. Younis, A. Flammability properties of polypropylene containing montmorillonite and some of silicon compounds. *Egypt. J. Pet.* **2017**, *26*, 1–7. [[CrossRef](#)]
3. Fang, L.; Lu, X.; Zeng, J.; Chen, Y.; Tang, Q. Investigation of the Flame-Retardant and Mechanical Properties of Bamboo Fiber-Reinforced Polypropylene Composites with Melamine Pyrophosphate and Aluminum Hypophosphite Addition. *Materials* **2020**, *13*, 479. [[CrossRef](#)] [[PubMed](#)]
4. Kroto, H.W.; Heath, J.R.; O'Brien, S.C.; Curl, R.F.; Smalley, R.E. C₆₀: Buckminsterfullerene. *Nature* **1985**, *318*, 162–163. [[CrossRef](#)]
5. Ribeiro, B.; Botelho, E.C.; Costa, M.L.; Bandeira, C.F. Carbon nanotube buckypaper reinforced polymer composites: A review. *Polimeros* **2017**, *27*, 247–255. [[CrossRef](#)]
6. Novoselov, K.; Geim, A.K.; Morozov, S.; Jiang, D.; Zhang, Y.; Dubonos, S.V.; Grigorieva, I.V.; Firsov, A.A. Electric Field Effect in Atomically Thin Carbon Films. *Science* **2004**, *306*, 666–669. [[CrossRef](#)]
7. Gürünlü, B.; Yücedağ, Ç.T.; Bayramoğlu, M.R. Green Synthesis of Graphene from Graphite in Molten Salt Medium. *J. Nanomater.* **2020**, *2020*, 1–12. [[CrossRef](#)]
8. Pan, Y.; Guo, Z.; Ran, S.; Fang, Z. Influence of fullerenes on the thermal and flame-retardant properties of polymeric materials. *J. Appl. Polym. Sci.* **2019**, *137*, 47538. [[CrossRef](#)]
9. Krusic, P.J.; Wasserman, E.; Keizer, P.N.; Morton, J.R. Radical reactions of C₆₀. *Science* **1991**, *254*, 1183–1185. [[CrossRef](#)]
10. Zuev, V.V. Polymer Nanocomposites Containing Fullerene C₆₀ Nanofillers. *Macromol. Symp.* **2011**, *301*, 157–161. [[CrossRef](#)]
11. Zuev, V.V.; Kostromin, S.; Shlykov, A.V. The effect of fullerene fillers on the mechanical properties of polymer nanocomposites. *Mech. Compos. Mater.* **2010**, *46*, 147–154. [[CrossRef](#)]
12. Ogasawara, T.; Ishida, Y.; Kasai, T. Mechanical properties of carbon fiber/fullerene-dispersed epoxy composites. *Compos. Sci. Technol.* **2009**, *69*, 2002–2007. [[CrossRef](#)]
13. Kausar, A. Adhesion, morphology, and heat resistance properties of polyurethane coated poly (methyl methacrylate)/fullerene-C₆₀ composite films. *Compos. Interface* **2017**, *24*, 649–662. [[CrossRef](#)]
14. Song, P.; Zhu, Y.; Tong, L.; Fang, Z. C₆₀ reduces the flammability of polypropylene nanocomposites by in situ forming a gelled-ball network. *Nanotechnology* **2008**, *19*, 225707. [[CrossRef](#)] [[PubMed](#)]
15. Guo, Z.; Wang, Z.; Fang, Z. Fabrication of 9,10-dihydro-9-oxa-10-phosphaphenanthrene-10-oxide-decorated fullerene to improve the anti-oxidative and flame-retardant properties of polypropylene. *Compos. Part B Eng.* **2020**, *183*, 107672. [[CrossRef](#)]
16. Beyer, G. Short communication: Carbon nanotubes as flame retardants for polymers. *Fire Mater.* **2002**, *26*, 291–293. [[CrossRef](#)]
17. Ajayan, P.M. Nanotubes from Carbon. *Chem. Rev.* **1999**, *99*, 1787–1800. [[CrossRef](#)]
18. Al Sheheri, S.Z.; Al-Amshany, Z.M.; Al Sulami, Q.A.; Tashkandi, N.Y.; Hussein, M.A.; El-Shishtawy, R.M. The preparation of carbon nanofillers and their role on the performance of variable polymer nanocomposites. *Des. Monomers Polym.* **2019**, *22*, 8–53. [[CrossRef](#)]
19. Kausar, A.; Rafique, I.; Anwar, Z.; Muhammad, B. Recent Developments in Different Types of Flame Retardant and Effect on Fire Retardancy of Epoxy Composite. *Polym. Technol. Eng.* **2016**, *55*, 1512–1535. [[CrossRef](#)]
20. Patel, P.; A Stec, A.; Hull, R.; Naffakh, M.; Diez-Pascual, A.M.; Ellis, G.; Safronava, N.; Lyon, R.E. Flammability properties of PEEK and carbon nanotube composites. *Polym. Degrad. Stab.* **2012**, *97*, 2492–2502. [[CrossRef](#)]

21. Kashiwagi, T.; Du, F.; Winey, K.I.; Groth, K.; Shields, J.R.; Bellayer, S.P.; Kim, H.; Douglas, J.F. Flammability properties of polymer nanocomposites with single-walled carbon nanotubes: Effects of nanotube dispersion and concentration. *Polymer* **2005**, *46*, 471–481. [[CrossRef](#)]
22. Wang, X.; Kalali, E.N.; Wan, J.-T.; Wang, D.-Y. Carbon-family materials for flame retardant polymeric materials. *Prog. Polym. Sci.* **2017**, *69*, 22–46. [[CrossRef](#)]
23. Guadagno, L.; De Vivo, B.; Di Bartolomeo, A.; Lamberti, P.; Sorrentino, A.; Tucci, V.; Vertuccio, L.; Vittoria, V. Effect of functionalization on the thermo-mechanical and electrical behavior of multi-wall carbon nanotube/epoxy composites. *Carbon* **2011**, *49*, 1919–1930. [[CrossRef](#)]
24. Kuan, C.-F.; Chen, W.J.; Li, Y.-L.; Chen, C.-H.; Kuan, H.; Chiang, C.-L. Flame retardance and thermal stability of carbon nanotube epoxy composite prepared from sol–gel method. *J. Phys. Chem. Solids* **2010**, *71*, 539–543. [[CrossRef](#)]
25. Gao, F.; Beyer, G.; Yuan, Q. A mechanistic study of fire retardancy of carbon nanotube/ethylene vinyl acetate copolymers and their clay composites. *Polym. Degrad. Stab.* **2005**, *89*, 559–564. [[CrossRef](#)]
26. Ma, H.; Tong, L.; Xu, Z.; Fang, Z. Synergistic effect of carbon nanotube and clay for improving the flame retardancy of ABS resin. *Nanotechnology* **2007**, *18*, 375602. [[CrossRef](#)]
27. Vaisman, L.; Marom, G.; Wagner, H.D. Dispersions of Surface-Modified Carbon Nanotubes in Water-Soluble and Water-Insoluble Polymers. *Adv. Funct. Mater.* **2006**, *16*, 357–363. [[CrossRef](#)]
28. Schaefer, D.W.; Zhao, J.; Brown, J.M.; Anderson, D.P.; Tomlin, D.W. Morphology of dispersed carbon single-walled nanotubes. *Chem. Phys. Lett.* **2003**, *375*, 369–375. [[CrossRef](#)]
29. Martin, C.; Sandler, J.; Shaffer, M.S.P.; Schwarz, M.-K.; Bauhofer, W.; Schulte, K.; Windle, A. Formation of percolating networks in multi-wall carbon-nanotube–epoxy composites. *Compos. Sci. Technol.* **2004**, *64*, 2309–2316. [[CrossRef](#)]
30. Beyer, G. Carbon Nanotubes—A New Class of Flame Retardants for Polymers. *Int. Polym. Sci. Technol.* **2003**, *30*, 1–6. [[CrossRef](#)]
31. Wen, X.; Tian, N.; Gong, J.; Chen, Q.; Qi, Y.; Liu, Z.; Liu, J.; Jiang, Z.; Chen, X.; Tang, T. Effect of nanosized carbon black on thermal stability and flame retardancy of polypropylene/carbon nanotubes nanocomposites. *Polym. Adv. Technol.* **2013**, *24*, 971–977. [[CrossRef](#)]
32. Dai, J.F.; Wang, G.J.; Ma, L.; Wu, C.K. Surface properties of graphene: Relationship to graphene-polymer composites. *Rev. Adv. Mater. Sci.* **2015**, *40*, 60–71.
33. Lee, J.-U.; Yoon, D.; Cheong, H. Estimation of Young’s Modulus of Graphene by Raman Spectroscopy. *Nano Lett.* **2012**, *12*, 4444–4448. [[CrossRef](#)] [[PubMed](#)]
34. Ghosh, S.; Calizo, I.; Teweldebrhan, D.; Pokatilov, E.P.; Nika, D.L.; Balandin, A.A.; Bao, W.; Miao, F.; Lau, C.N. Extremely high thermal conductivity of graphene: Prospects for thermal management applications in nanoelectronic circuits. *Appl. Phys. Lett.* **2008**, *92*, 151911. [[CrossRef](#)]
35. Szeluga, U.; Pusz, S.; Kumanek, B.; Olszowska, K.; Kobyluk, A.; Trzebiecka, B. Effect of graphene filler structure on electrical, thermal, mechanical, and fire retardant properties of epoxy-graphene nanocomposites—A review. *Crit. Rev. Solid State Mater. Sci.* **2020**, 1–36. [[CrossRef](#)]
36. Huang, G.; Gao, J.; Wang, X.; Liang, H.; Ge, C. How can graphene reduce the flammability of polymer nanocomposites? *Mater. Lett.* **2012**, *66*, 187–189. [[CrossRef](#)]
37. Attia, N.F.; El-Aal, N.A.; Hassan, M. Facile synthesis of graphene sheets decorated nanoparticles and flammability of their polymer nanocomposites. *Polym. Degrad. Stab.* **2016**, *126*, 65–74. [[CrossRef](#)]
38. Li, K.-Y.; Kuan, C.-F.; Chen, H.; Chen, C.-H.; Shen, M.-Y.; Yang, J.-M.; Chiang, C.-L. Preparation and properties of novel epoxy/graphene oxide nanosheets (GON) composites functionalized with flame retardant containing phosphorus and silicon. *Mater. Chem. Phys.* **2014**, *146*, 354–362. [[CrossRef](#)]
39. Yuan, B.; Fan, A.; Yang, M.; Chen, X.; Hu, Y.; Bao, C.; Jiang, S.; Niu, Y.; Zhang, Y.; He, S.; et al. The effects of graphene on the flammability and fire behavior of intumescent flame retardant polypropylene composites at different flame scenarios. *Polym. Degrad. Stab.* **2017**, *143*, 42–56. [[CrossRef](#)]
40. Smith, A.T.; Lachance, A.M.; Zeng, S.; Liu, B.; Sun, L. Synthesis, properties, and applications of graphene oxide/reduced graphene oxide and their nanocomposites. *Nano Mater. Sci.* **2019**, *1*, 31–47. [[CrossRef](#)]
41. Tian, P.; Tang, L.; Teng, K.S.; Lau, S.P. Graphene quantum dots from chemistry to applications. *Mater. Today Chem.* **2018**, *10*, 221–258. [[CrossRef](#)]

42. Rahimi-Aghdam, T.; Shariatinia, Z.; Hakkarainen, M.; Haddadi-Asl, V. Nitrogen and phosphorous doped graphene quantum dots: Excellent flame retardants and smoke suppressants for polyacrylonitrile nanocomposites. *J. Hazard. Mater.* **2019**, *381*, 121013. [[CrossRef](#)] [[PubMed](#)]
43. Rahimi-Aghdam, T.; Shariatinia, Z.; Hakkarainen, M.; Haddadi-Asl, V. Polyacrylonitrile/N,P co-doped graphene quantum dots-layered double hydroxide nanocomposite: Flame retardant property, thermal stability and fire hazard. *Eur. Polym. J.* **2019**, *120*, 109256. [[CrossRef](#)]
44. Khose, R.V.; Pethsangave, D.A.; Wadekar, P.H.; Ray, A.K.; Some, S. Novel approach towards the synthesis of carbon-based transparent highly effective flame retardant. *Carbon* **2018**, *139*, 205–209. [[CrossRef](#)]
45. Wang, G.; Yang, J. Influences of expandable graphite modified by polyethylene glycol on fire protection of waterborne intumescent fire resistive coating. *Surf. Coat. Technol.* **2010**, *204*, 3599–3605. [[CrossRef](#)]
46. Ye, L.; Meng, X.-Y.; Ji, X.; Li, Z.-M.; Tang, J.-H. Synthesis and characterization of expandable graphite–poly(methyl methacrylate) composite particles and their application to flame retardation of rigid polyurethane foams. *Polym. Degrad. Stab.* **2009**, *94*, 971–979. [[CrossRef](#)]
47. Lee, S.; Kim, H.M.; Seong, D.G.; Lee, D. Synergistic improvement of flame retardant properties of expandable graphite and multi-walled carbon nanotube reinforced intumescent polyketone nanocomposites. *Carbon* **2019**, *143*, 650–659. [[CrossRef](#)]
48. Hong, L.; Hu, X. Mechanical and Flame Retardant Properties and Microstructure of Expandable Graphite/Silicone Rubber Composites. *J. Macromol. Sci. Part B* **2016**, *55*, 175–187. [[CrossRef](#)]
49. Guo, C.; Zhou, L.; Lv, J. Effects of Expandable Graphite and Modified Ammonium Polyphosphate on the Flame-Retardant and Mechanical Properties of Wood Flour-Polypropylene Composites. *Polym. Polym. Compos.* **2013**, *21*, 449–456. [[CrossRef](#)]
50. Zhu, H.; Zhu, Q.; Li, J.; Tao, K.; Xue, L.; Yan, Q. Synergistic effect between expandable graphite and ammonium polyphosphate on flame retarded polylactide. *Polym. Degrad. Stab.* **2011**, *96*, 183–189. [[CrossRef](#)]
51. Savi, P.; Jose, S.P.; Khan, A.A.; Giorcelli, M.; Tagliaferro, A. Biochar and carbon nanotubes as fillers in polymers: A comparison. In Proceedings of the 2017 IEEE MTT-S International Microwave Workshop Series on Advanced Materials and Processes for RF and THz Applications (IMWS-AMP), Pavia, Italy, 20–22 September 2017; pp. 1–3. [[CrossRef](#)]
52. Das, O.; Sarmah, A.K.; Bhattacharyya, D. A novel approach in organic waste utilization through biochar addition in wood/polypropylene composites. *Waste Manag.* **2015**, *38*, 132–140. [[CrossRef](#)]
53. Zhang, Q.; Yi, W.; Li, Z.; Wang, L.; Cai, H. Mechanical Properties of Rice Husk Biochar Reinforced High Density Polyethylene Composites. *Polymer* **2018**, *10*, 286. [[CrossRef](#)] [[PubMed](#)]
54. You, Z.; Li, D. Highly filled bamboo charcoal powder reinforced ultra-high molecular weight polyethylene. *Mater. Lett.* **2014**, *122*, 121–124. [[CrossRef](#)]
55. Poulouse, A.M.; Elnour, A.Y.; Anis, A.; Shaikh, H.; Al-Zahrani, S.; George, J.; Al-Wabel, M.I.; Usman, A.R.; Ok, Y.S.; Tsang, D.C.; et al. Date palm biochar-polymer composites: An investigation of electrical, mechanical, thermal and rheological characteristics. *Sci. Total. Environ.* **2017**, *619*, 311–318. [[CrossRef](#)]
56. Srinivasan, P.; Sarmah, A.K.; Smernik, R.; Das, O.; Farid, M.; Gao, W.; Smernik, R. A feasibility study of agricultural and sewage biomass as biochar, bioenergy and biocomposite feedstock: Production, characterization and potential applications. *Sci. Total. Environ.* **2015**, *512*, 495–505. [[CrossRef](#)] [[PubMed](#)]
57. Das, O.; Sarmah, A.K. Mechanism of waste biomass pyrolysis: Effect of physical and chemical pre-treatments. *Sci. Total. Environ.* **2015**, *537*, 323–334. [[CrossRef](#)]
58. Das, O.; Sarmah, A.K. Value added liquid products from waste biomass pyrolysis using pretreatments. *Sci. Total Environ.* **2015**, *538*, 145–151. [[CrossRef](#)]
59. Lee, J.; Kim, K.-H.; Kwon, E.E. Biochar as a Catalyst. *Renew. Sustain. Energy Rev.* **2017**, *77*, 70–79. [[CrossRef](#)]
60. Byrne, C.; Nagle, D. Carbonization of wood for advanced materials applications. *Carbon* **1997**, *35*, 259–266. [[CrossRef](#)]
61. Das, O.; Capezza, J.A.; Mårtensson, J.; Dong, Y.; Neisiany, E.R.; Pelcastre, L.; Jiang, L.; Xu, Q.; Olsson, T.R.; Hedenqvist, S.M. The Effect of Carbon Black on the Properties of Plasticised Wheat Gluten Biopolymer. *Molecules* **2020**, *25*, 2279. [[CrossRef](#)]
62. Netravali, A.N.; Mittal, K.L. *Interface/Interphase in Polymer Nanocomposites*; John Wiley & Sons: Hoboken, NJ, USA, 2016.
63. Das, O.; Sarmah, A.K.; Bhattacharyya, D. Biocomposites from waste derived biochars: Mechanical, thermal, chemical, and morphological properties. *Waste Manag.* **2016**, *49*, 560–570. [[CrossRef](#)] [[PubMed](#)]

64. Liu, Z.; Fei, B.; Jiang, Z.; Yang, X. Combustion characteristics of bamboo-biochars. *Bioresour. Technol.* **2014**, *167*, 94–99. [[CrossRef](#)]
65. Zhao, M.Y.; Enders, A.; Lehmann, J. Short- and long-term flammability of biochars. *Biomass Bioenergy* **2014**, *69*, 183–191. [[CrossRef](#)]
66. Das, O.; Bhattacharyya, D.; Hui, D.; Lau, K.T. Mechanical and flammability characterisations of biochar/polypropylene biocomposites. *Compos. Part B Eng.* **2016**, *106*, 120–128. [[CrossRef](#)]
67. Elnour, A.Y.; Alghyamah, A.A.; Shaikh, H.M.; Poulouse, A.M.; Al-Zahrani, S.M.; Anis, A.; Al-Wabel, M.I. Effect of Pyrolysis Temperature on Biochar Microstructural Evolution, Physicochemical Characteristics, and Its Influence on Biochar/Polypropylene Composites. *Appl. Sci.* **2019**, *9*, 1149. [[CrossRef](#)]
68. Ikram, S.; Das, O.; Bhattacharyya, D. A parametric study of mechanical and flammability properties of biochar reinforced polypropylene composites. *Compos. Part A Appl. Sci. Manuf.* **2016**, *91*, 177–188. [[CrossRef](#)]
69. Das, O.; Kim, N.K.; Sarmah, A.K.; Bhattacharyya, D. Development of waste based biochar/wool hybrid biocomposites: Flammability characteristics and mechanical properties. *J. Clean. Prod.* **2017**, *144*, 79–89. [[CrossRef](#)]
70. Zhang, Q.; Khan, M.U.; Lin, X.; Cai, H.; Lei, H. Temperature varied biochar as a reinforcing filler for high-density polyethylene composites. *Compos. Part B Eng.* **2019**, *175*, 107151. [[CrossRef](#)]
71. Das, O.; Kim, N.K.; Kalamkarov, A.L.; Sarmah, A.K.; Bhattacharyya, D. Biochar to the rescue: Balancing the fire performance and mechanical properties of polypropylene composites. *Polym. Degrad. Stab.* **2017**, *144*, 485–496. [[CrossRef](#)]
72. Behazin, E.; Misra, M.; Mohanty, A.K. Sustainable biocarbon from pyrolyzed perennial grasses and their effects on impact modified polypropylene biocomposites. *Compos. Part B Eng.* **2017**, *118*, 116–124. [[CrossRef](#)]
73. Zhang, Q.; Zhang, D.; Xu, H.; Lu, W.; Ren, X.; Cai, H.; Lei, H.; Huo, E.; Zhao, Y.; Qian, M.; et al. Biochar filled high-density polyethylene composites with excellent properties: Towards maximizing the utilization of agricultural wastes. *Ind. Crop. Prod.* **2020**, *146*, 112185. [[CrossRef](#)]
74. Wen, X.; Wang, Y.; Gong, J.; Liu, J.; Tian, N.; Wang, Y.; Jiang, Z.; Qiu, J.; Tang, T. Thermal and flammability properties of polypropylene/carbon black nanocomposites. *Polym. Degrad. Stab.* **2012**, *97*, 793–801. [[CrossRef](#)]
75. Yang, H.; Gong, J.; Wen, X.; Xue, J.; Chen, Q.; Jiang, Z.; Tian, N.; Tang, T. Effect of carbon black on improving thermal stability, flame retardancy and electrical conductivity of polypropylene/carbon fiber composites. *Compos. Sci. Technol.* **2015**, *113*, 31–37. [[CrossRef](#)]
76. Liu, Z.; Li, Z.; Yang, Y.-X.; Zhang, Y.-L.; Wen, X.; Li, N.; Fu, C.; Jian, R.-K.; Li, L.; Wang, D.-Y. A Geometry Effect of Carbon Nanomaterials on Flame Retardancy and Mechanical Properties of Ethylene-Vinyl Acetate/Magnesium Hydroxide Composites. *Polymer* **2018**, *10*, 1028. [[CrossRef](#)]
77. Mensah, R.A.; Xu, Q.; Asante-Okyere, S.; Jin, C.; Bentum-Micah, G. Correlation analysis of cone calorimetry and microscale combustion calorimetry experiments. *J. Therm. Anal. Calorim.* **2018**, *136*, 589–599. [[CrossRef](#)]
78. Van Krevelen, D.W.; Te Nijenhuis, K. *Properties of Polymers: Their Correlation with Chemical Structure; Their Numerical Estimation and Prediction from Additive Group Contributions*; Elsevier: Amsterdam, The Netherlands, 2009.
79. Shrivastava, A. *Introduction to Plastics Engineering*; William Andrew: Cambridge, MA, USA, 2018; pp. 1–16.
80. Papaspyrides, C.D.; Kiliaris, P. *Polymer Green Flame Retardants*; Newnes: Waltham, MA, USA, 2014.
81. Laoutid, F.; Bonnaud, L.; Alexandre, M.; Lopez-Cuesta, J.-M.; Dubois, P. New prospects in flame retardant polymer materials: From fundamentals to nanocomposites. *Mater. Sci. Eng. R Rep.* **2009**, *63*, 100–125. [[CrossRef](#)]
82. Hsinjin, E.Y. *Quantitative Microscale Assessment of Polymer Flammability*; Plastics Research: Gansu, China, 2015.
83. Wan, L.; Deng, C.; Zhao, Z.-Y.; Chen, H.; Wang, Y.-Z. Flame Retardation of Natural Rubber: Strategy and Recent Progress. *Polymer* **2020**, *12*, 429. [[CrossRef](#)]
84. Xu, Q.; Jin, C.; Majlingova, A.; Restas, A. Discuss the heat release capacity of polymer derived from microscale combustion calorimeter. *J. Therm. Anal. Calorim.* **2017**, *133*, 649–657. [[CrossRef](#)]
85. Xu, Q.; Jin, C.; Majlingova, A.; Zachar, M.; Restas, A. Evaluate the flammability of a PU foam with double-scale analysis. *J. Therm. Anal. Calorim.* **2019**, *135*, 3329–3337. [[CrossRef](#)]
86. *Standard Test Method for Determining Flammability Characteristics of Plastics and Other Solid Materials Using Microscale Combustion Calorimetry*; ASTM D7309; American Society for Testing and Materials: West Conshohocken, PA, USA, 2019.

87. Babrauskas, V. Development of the cone calorimeter? A bench-scale heat release rate apparatus based on oxygen consumption. *Fire Mater.* **1984**, *8*, 81–95. [[CrossRef](#)]
88. Holborn, P.; Nolan, P.; Golt, J. An analysis of fire sizes, fire growth rates and times between events using data from fire investigations. *Fire Saf. J.* **2004**, *39*, 481–524. [[CrossRef](#)]



© 2020 by the authors. Licensee MDPI, Basel, Switzerland. This article is an open access article distributed under the terms and conditions of the Creative Commons Attribution (CC BY) license (<http://creativecommons.org/licenses/by/4.0/>).

Review

A Review on Barrier Properties of Poly(Lactic Acid)/Clay Nanocomposites

Shuvra Singha * and Mikael S. Hedenqvist *

KTH Royal Institute of Technology, School of Engineering Sciences in Chemistry, Biotechnology and Health, Department of Fibre and Polymer Technology, SE-100 44 Stockholm, Sweden

* Correspondence: shuvras@kth.se (S.S.); mikaelhe@kth.se (M.S.H.)

Received: 30 March 2020; Accepted: 1 May 2020; Published: 11 May 2020

Abstract: Poly(lactic acid) (PLA) is considered to be among the best biopolymer substitutes for the existing petroleum-based polymers in the field of food packaging owing to its renewability, biodegradability, non-toxicity and mechanical properties. However, PLA displays only moderate barrier properties to gases, vapors and organic compounds, which can limit its application as a packaging material. Hence, it becomes essential to understand the mass transport properties of PLA and address the transport challenges. Significant improvements in the barrier properties can be achieved by incorporating two-dimensional clay nanofillers, the planes of which create tortuosity to the diffusing molecules, thereby increasing the effective length of the diffusion path. This article reviews the literature on barrier properties of PLA/clay nanocomposites. The important PLA/clay nanocomposite preparation techniques, such as solution intercalation, melt processing and in situ polymerization, are outlined followed by an extensive account of barrier performance of nanocomposites drawn from the literature. Fundamentals of mass transport phenomena and the factors affecting mass transport are also presented. Furthermore, mathematical models that have been proposed/used to predict the permeability in polymer/clay nanocomposites are reviewed and the extent to which the models are validated in PLA/clay composites is discussed.

Keywords: barrier properties; poly(lactic acid); clay; nanocomposite; permeability

1. Introduction

Amid the growing environmental concern about the decreasing fossil resources and the increasing plastic footprint, biopolymers obtained from renewable resources such as agricultural products represent a promising alternative to the non-degradable petroleum-based polymers for short-life range applications, for example food packaging [1–5]. Poly (lactic acid) (PLA) has emerged as the frontrunner among the many biopolymers in this regard owing to its many eco-friendly attributes such as low energy consumption during production, availability and low cost of the raw material, biodegradability in soil and water and being non-toxic to the environment [6–12]. Although the most successful application of PLA is in the containers and food packaging industry, other applications include biodegradable scaffolds for tissues, bioresorbable implants, surgical equipment, intravenous administration of antivirals, cardiovascular stents and controlled drug delivery. PLA is also used for making fibers in the textile industry and mulching materials for agriculture. The important properties which make PLA a promising candidate for food packaging is that it possesses sufficient thermal stability, i.e., the onset degradation temperature lies in the range of 330–350 °C [13,14] and good mechanical properties: tensile strength of ca. 50–70 MPa, Young's modulus of ca. 3 GPa, elongation at break of ca. 4% and impact strength of around 2.5 kJ/m², making it a useable substitute for single-use plastics such as PE, PP and PET [10,15].

PLA is derived from renewable agro-resources such as corn, cassava, potato, cane molasses and sugar beet, and hence is considered as an eco-friendly thermoplastic. The polymer is produced from

the monomer of lactic acid (LA), the simplest hydroxy acid, which is obtained either biologically by the fermentation of carbohydrates by lactic bacteria belonging to the *Lactobacillus* genus or by chemical synthesis [16–18]. PLA is produced through two important routes—(a) direct polycondensation (DP) of LA and (b) ring opening polymerization (ROP) of the cyclic dimer of LA, i.e., lactide (Figure 1B). The DP route is an equilibrium reaction which demands high temperature, long reaction times and continuous removal of water from the reaction vessel, often leading to low molecular weight PLA [19]. Hence, ring opening polymerization (ROP) of lactide (cyclic dimer of LA) in the presence of a robust catalyst–initiator, tin(II)bis(2-ethylhexanoate) ($\text{Sn}(\text{Oct})_2$) and alcohol, is the preferred synthesis route in industry, which can result in high molecular weight PLA [7,20,21].

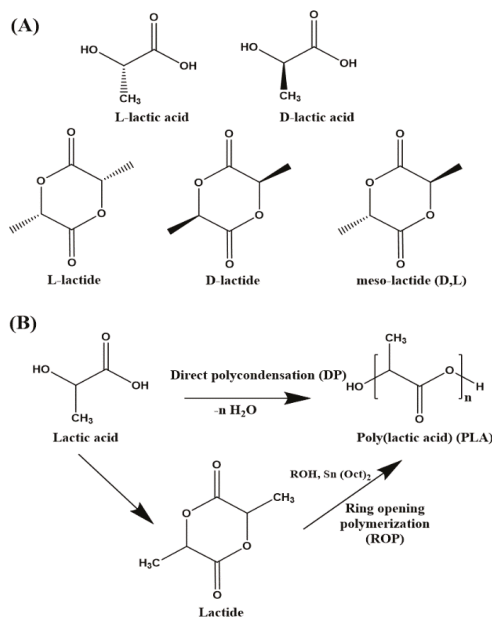


Figure 1. (A) Chemical structures of L-lactic acid, D-lactic acid, L-lactide, D-lactide and mesolactide, (B) Schematic representation of direct polycondensation (DP) of lactic acid and ring opening polymerization (ROP) of lactide.

LA is a chiral molecule and exists in two stereo-isomeric forms (optical isomers) L-lactic acid (L-LA) and D-lactic acid (D-LA). Two optically inactive forms are also available which are the meso-LA and racemic mixture (50:50) of L-LA and D-LA (Figure 1A) [16]. PLAs formed from the isotactic sequence of L-LA and D-LA are referred to as PLLA and PDLA, respectively. PLA prepared from a racemic mixture of both the enantiomers and from meso-LA is referred to as PDLLA [22]. The final properties of PLA largely depend on the ratio and distribution of the LA enantiomers in the polymer chains. A high L-isomer in the chains results in a crystalline matrix, whereas a high D-isomer (>15%) results in an amorphous matrix. The meso-form (atactic PDLLA) is also amorphous. The polymer chain orientation and packing affect the crystallinity, crystal thickness, spherulite size and morphology [12]. These are important factors which influence two important physical properties, i.e., mechanical and barrier performance [23–25]. Although PLA is among the best biodegradable and nontoxic polymers with high thermal stability and good mechanical stability (although with low extensibility without a plasticizer), its limiting property is its permeability to low molecular weight gases, vapors and organic molecules [26]. Permeation of oxygen and water vapor through polymer films can drastically decrease the service performance of a packaging material, thereby making it difficult to maintain food quality throughout its shelf life [27,28]. Research on mass transfer in polymers is, therefore, of high

importance. Inclusion of two-dimensional (2D) platelets or disk-shaped nanoparticles in the polymer matrix has proven to be a good strategy to significantly decrease gas/liquid permeation in polymers. The 2D inclusions act as physical obstacles in the diffusion path of the permeant molecule creating a tortuosity effect. This helps to enhance the barrier performance of the polymer and increases the food shelf-life [29–32]. Nanoclays such as mica, saponite, montmorillonite and kaolinite are widely used 2D nanoparticles for improving the barrier properties in many polymers [33]. Thousands of publications can be found on PLA/Clay nanocomposites which have largely focused on improving the thermal [34–36], mechanical [37–39] and optical properties [40,41] and biodegradability [42,43]. However, only a meagre number of publications have been devoted to the study of mass transfer in PLA, and just a handful on PLA/clay nanocomposites. This encourages further review so as to update the trends, accomplishments and recurring challenges in this field. This review intends to highlight the usefulness of clay platelets for improving the barrier properties of PLA. First, the current methods of fabrication of PLA/clay nanocomposites are summarized, and then the barrier performance of the nanocomposites is reviewed. A brief introduction to the theory, mechanism and factors affecting mass transport in polymers is presented followed by a description of some of the important mathematical models that have been proposed to predict permeability in polymer/clay nanocomposites. The validation of some of the models in PLA/clay nanocomposites is reviewed.

2. PLA/Layered Silicate Nanocomposites

The 2D layered inorganic nanofillers like clays and silicates, owing to their abundance, low cost, high aspect ratio, rich intercalation chemistry, high strength and stiffness and thermal stability, provide favorable synergetic effects that help to significantly improve many polymer properties, especially mechanical and barrier properties [44–47]. However, the extent of dispersion of the clay layers and the morphology thus achieved in the polymer matrix (intercalation, exfoliation, mixed intercalation and exfoliation, aggregation, etc.) greatly affect the gas barrier properties. To achieve a high level of exfoliation and desired orientation of the platelets has remained a challenging task [48–51]. Good dispersion can be realized by increasing the affinity between the clay layers and the polymer through organic modification of the interlayer galleries with organic ammonium, sulfonium or phosphonium cations. A detailed and extensive list of common organic modifiers has been reported by Nordqvist and Hedenqvist [33]. The common routes to achieve dispersion of the organo-modified layered silicates in a PLA matrix are solution intercalation, melt processing and in situ polymerization (Figure 2) [52].

2.1. Solution Intercalation

Solution intercalation is one of the easiest techniques on a laboratory scale to prepare nanocomposites. In this technique, clay platelets are first exfoliated in a solvent in which the polymer is also soluble. The polymer solution is then mixed with the clay suspension, where the polymer chains intercalate/are adsorbed on the surface of the platelets and form a clay–polymer complex. The solvent is later removed by evaporation. This method is considered environmentally unfriendly because of the use of organic solvents [51]. Maharana et al. [12] demonstrated the preparation of PLA/clay nanocomposites using a solution intercalation method and showed improved mechanical and barrier properties of the nanocomposites. The effect of the structure of different organic modifiers of clay nanoparticles, Cloisite-15A, -25A and -30B modified with dimethyl dihydrogenated tallow quaternary ammonium, dimethyl hydrogenated tallow-2-ethylhexyl ammonium and methyl tallow-bis-2-hydroxyethyl quaternary ammonium, respectively, was studied by Pochan and Krikorian [53] to determine the extent of exfoliation of the nanoclay in a PLA matrix by solvent intercalation. Cloisite is a montmorillonite (MMT) clay: the term ‘Cloisite’ followed by an alphanumeric sequence refers to the commercially available clay, whereas the organically modified MMT (OMMT) refers to the tailor-made clay prepared by individual research groups. Cloisite 30B containing an organic diol in the inter-galleries established favorable interactions with the carbonyl functionality of PLA, leading to significant intercalation of

PLA chains into the clay spacing. Hence, PLA/Cloisite 30B formed the best nanocomposites in terms of maximum intercalation.

2.2. Melt Intercalation

This is a widely used technique to fabricate PLA/clay nanocomposites. The method involves mixing organo-modified nanoclay and the polymer and heating the mixture above the melting temperature of the polymer, either under shear or no shear. Due to the high temperatures and mechanical forces used, polymer chains are forced to diffuse into the clay galleries, giving rise to either intercalated or exfoliated nanostructures depending on the amount of polymer chains diffused into the silicate layers [32]. The main advantage of the technique is the specificity for the polymer intercalation into the clays as there is no solvent in the system that can give rise to competing clay–solvent or polymer–solvent interactions [54]. Most of the PLA/clay systems prepared by melt processing have resulted in intercalated structures. To achieve further exfoliation, Sabet and Katbab [55] investigated the role of oligo(ϵ -caprolactone) as compatibilizer. Although the effort did not result in complete exfoliation, it did result in flocculation of the clay layers due to hydroxylated edge-edge interactions and, therefore, better parallel stacking of the layers. However, fully exfoliated nanostructures were achieved by Chen et al. [56] who performed a second time functionalization of Cloisite 25A using an epoxy containing organic modifier—(glycidoxypropyl)trimethoxysilane. Melt processing of the nanoclay with PLA yielded fully exfoliated nanostructures when the epoxy content in the clay was high (about 0.36 mmol/g). PLA nanocomposites with epoxy containing Cloisite 25A showed better mechanical properties than those of the unmodified Cloisite composites. Melt blending of PLA in the presence of nanoclay with other polymers have been reported by several authors [57–59].

2.3. In Situ Polymerization

This technique is the most effective to obtain well exfoliated clay platelets in the polymer matrix. First, the clay is swollen in a suitable monomer melt or monomer solution. Then, polymerization is carried out induced by heat or radiation or by pre-intercalated initiators or catalyst. During the polymerization reaction, polymeric chains are formed inside the clay galleries which force delamination of the platelets in the matrix. Melt intercalation of LA monomer in the clay galleries followed by in situ ROP of PLA was found to be an efficient route to prepare high molecular weight PLA composites. Here, the silicate inter-galleries are considered as “nano-reactors” yielding high molecular weight PLA. Cloisite- Na^+ , Cloisite 20A, Cloisite 30B and organo-modified montmorillonite (abbr. as OMMT) (modified with hexadecyltrimethyl ammonium bromide and dioctadecyldimethyl ammonium bromide) nanoclays were used to first form the LA monomer–clay intercalated mixture. The mixture was subjected to ROP using $\text{Sn}(\text{Oct})_2$ as the catalyst for 2 h at 120–180 °C. High molecular weight PLA composite, ca. 126,000 g/mol, was obtained [60]. Katiyar and Nanavati [61] demonstrated a novel solid-state polymerization route to prepare high molecular weight PLA using a two-step in situ ROP process. The PLA prepolymer was first synthesized via ROP inside the clay layers followed by solid-state polymerization at 150–160 °C. Another innovative approach using in situ coordination insertion polymerization was reported by Paul et al. [62], referred to as the “grafting-from” approach. In this method, aluminum oxide reactive species was first formed in situ by reacting triethylaluminum with hydroxyl groups of the ammonium cation (organic modifier) of Cloisite 30B. ROP of the intercalated monomer was then carried out at the site of active species in the presence of initiator and catalyst.

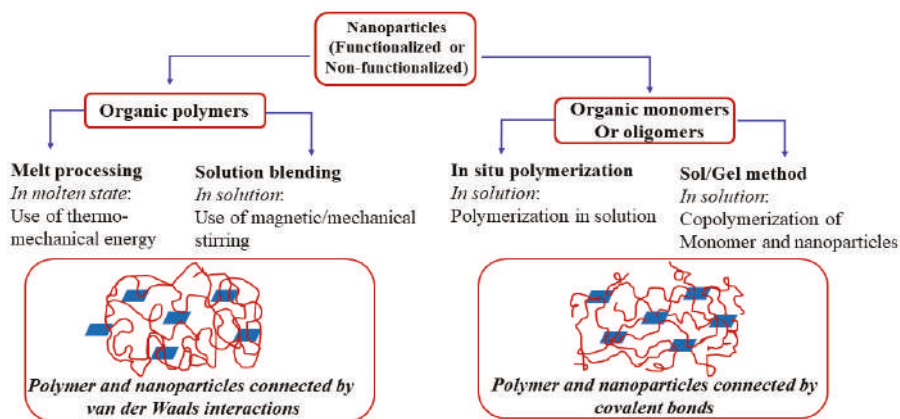


Figure 2. Outline of polymer nanocomposite preparation techniques.

3. Barrier Performance

The effects of the type of organo-modifier used, clay volume fraction, aspect ratio and dispersion on the barrier properties of PLA/organo-clay nanocomposite films have been investigated. The nanocomposite films demonstrated improved barrier properties compared to the neat PLA film. Gorrasi et al. [63] prepared PLA nanocomposites with Cloisite 30B by the melt blending method where PLA, clay and polyethylene glycol (PEG) as plasticizer and stabilizer were mixed together in a counter rotating mixer. Films were then produced by compression molding the blend. These authors also prepared nanocomposite by in situ polymerization of PLA from the monomer-swollen clay. Fully exfoliated nanostructures were obtained from the in situ process that had significantly lower water solubility and diffusivity than the melt processed composite. It was also observed that the water vapor zero concentration diffusivity measured at 30 °C was decreased in the case of in situ blends by about two orders of magnitude compared to that of the melt-processed blend and neat PLA films.

The oxygen permeability of PLA nanocomposites prepared with different clay modifications (Cloisite 25A, OMMT modified with dodecyltrimethyl ammonium cation and OMMT modified with hexadecylamine) was investigated by Chang et al. [64]. The permeability of all the composites was found to be less than that of pure PLA films and, at a clay content of 10 wt%, the permeability decreased to less than half the value of the neat PLA film. The barrier performance was determined from the barrier improvement factor (BIF) which is the ratio of transmission through the neat film to the transmission through the composite film. The BIF values are tabulated in Table 1. Maiti et al. [65] studied the effect of chain length of organic modifier in different types of clay, smectite, mica and OMMT. The clays were modified with a phosphonium ion containing three butyl branches and an alkyl chain the length of which was varied from 1–16 carbon atoms. The composite containing the C16 modifier was only evaluated for oxygen permeability. Smectite clays showed better dispersion than other clays and, therefore, showed better barrier properties than the mica and MMT loaded films (BIF for the highest clay loading of 4 wt% is shown in Table 1). The mica system with stacked clay layers exhibited poor barrier performance and low modulus.

Ray et al. [66–70] measured the oxygen permeability of PLA/organo-modified clays in a series of papers where the nanocomposites were prepared by melt extrusion in a twin-screw extruder followed by compression molding the granulated material. In Ref [66], three different clays with three different organic modifiers were used to assess the PLA nanocomposite properties. MMT was modified with octadecyl ammonium and octadecyltrimethyl ammonium cations, saponite was modified with hexadecyltributyl phosphonium cation, and synthetic fluorine mica (SFM) was modified with dipolyoxyethylene alkyl(coco) methyl ammonium cation. Although the saponite system showed the best dispersion, higher barrier properties were obtained with the mica system. Synthetic

fluorine mica modified with hydroxy functional ammonium cations was dispersed in the PLA matrix, resulting in intercalated stacks and a fairly large number of exfoliated layers being revealed in TEM micrographs. The highest barrier performance in terms of oxygen permeability was seen at 10 wt% mica content [67]. OMMT modified with octadecyltrimethyl ammonium cation [68] and also with the linear analog (octadecyl ammonium cation) [69], was blended with PLA. Interestingly, the linear surfactant-containing composite displayed higher barrier properties at 7 wt% clay than with the trimethyl functional surfactant.

Investigation of the effect of different processing parameters and techniques such as compounding and blown-film processing using a co-rotating twin screw extruder, were carried out by Thellen et al. [71]. The nanocomposite films showed 48% improvement in oxygen barrier and 50% improvement in water vapor barrier properties compared to the neat PLA film. Their results indicated that barrier property enhancements can be achieved by conventional processing techniques.

Lagaron et al. [72] used food contact approved nanoclays and amorphous polylactic acid (aPLA) to fabricate aPLA/organoclay nanocomposites. The organoclays used were Nanoter C1 (kaolinite) and AE21 (MMT) from nano-biomatters S.L. (Spain) (organo-modifiers not disclosed). TEM analyses revealed a mixed morphology of exfoliation and agglomeration of the clay platelets in the OM-kaolinite/aPLA matrix. The oxygen permeability BIF was higher (1.8) for the kaolinite system at 40% RH and 21 °C, whereas for the MMT system BIF was 1.1 (Table 1). The nanocomposites displayed very little swelling in water compared to the neat unfilled aPLA.

The solvent casting method was used to prepare nanocomposite films of PLA with Cloisite Na⁺, Cloisite 30B and Cloisite 20A nanoclays by Rhim et al. [73]. Among the clays used, Cloisite 20A showed the highest water vapor barrier performance with a BIF of 1.5 measured at 99% RH, but the tensile properties were sacrificed. The BIF values for the Cloisite Na⁺ and Cloisite 30B systems were 0.8 and 1.05, respectively. Zenkiewicz and Richert [74] used Cloisite 30B and Nanofil 2 nanoclays, poly(methyl methacrylate) (PMMA) and ethylene–vinyl alcohol copolymer as modifiers and polycaprolactone and poly(ethylene glycol) (PEG) as compatibilizers to fabricate a series of 27 PLA nanocomposite samples, and studied the effect on oxygen, water vapor and carbon dioxide permeability. Cloisite 30B samples improved the barrier properties much more than Nanofil clay—water vapor, oxygen and CO₂ permeability decreased by 60%, 55% and 90%, respectively, at 5 wt% clay content. All the modifiers and compatibilizers decreased the CO₂ transmission rate, whereas the oxygen and water vapor transmission rates were reduced only with the modifiers and not with the compatibilizers. The same group also studied the effect of blow molding ratio of PLA/MMT nanocomposite films containing (i) MMT, (ii) MMT with PMMA as modifier and (iii) MMT and PEG as plasticizer on water vapor, oxygen and CO₂ transmission. Among them, the MMT system showed the highest barrier performance with reduction in the transmission rates of water vapor, oxygen and CO₂ by 40%, 40% and 80%, respectively. A further decrease by 10% to 27% was achieved by extrusion blow molding. The least permeable films were obtained at a blow molding ratio of 4 [75].

Koh et al. [76] prepared PLA nanocomposites with Cloisite 15A, Cloisite 20A and Cloisite 30B clays using the solution intercalation method. The Cloisite 30B system revealed exfoliated morphology in the TEM analysis and, consequently, outstanding gas (O₂, CO₂ and N₂) barrier properties were obtained compared to the other clay systems and neat PLA. It was also found that the gas permeability decreased with decreasing kinetic diameter of the molecule: CO₂ (3.3 Å) > O₂ (3.46 Å) > N₂ (3.64 Å), i.e., the films showed highest permeability for CO₂ owing to its comparatively small size. The BIF values are shown in Table 1. Nanocomposites of aPLA and aPLA/polycaprolactone blends with organo-modified kaolinite (OM-kaolinite) were reported by Cabedo et al. [77]. Addition of OM-kaolinite drastically decreased the O₂ permeability of aPLA (BIF 1.8, Table 1). The BIF of aPLA/PCL was 0.44 and the addition of OM-kaolinite was not as effective as in a neat aPLA matrix because of the effect of the interfaces in blend systems which provide a path for permeation. Trifol et al. [78] explored the synergistic effect of Cloisite 30B and cellulose nanofibers (CNF) on PLA barrier properties. A combination of 5 wt% Cloisite 30B and 5 wt% CNF showed a reduction of 90% in oxygen transmission rate and 76% in water vapor

transmission rate compared to the neat PLA film. Even at a low filler content, 1 wt% of both materials, significant reductions in oxygen transmission rate, OTR (74%) and water vapor transmission rate, WVTR (57%), were achieved. However, in another study [79] 1 wt% Cloisite 30B in PLA showed only a 26% decrease in OTR and 43% in WVTR. Many groups have used Cloisite 30B as filler material in PLA matrix and demonstrated improved barrier properties, and the BIF values are shown in Table 1 [80–84]. Darie et al. [85] used nanoclays (Cloisite 93A modified with methyl dihydrogenated tallow quaternary ammonium and Dellite HPS, a hydrophilic smectite clay) varying in their degree of hydrophilicity to prepare PLA nanocomposites by melt processing. The O₂ and CO₂ transmission rates reduced by half in the Cloisite 93A matrix, and an even more drastic reduction occurred in the hydrophilic Dellite HPS matrix. Rhim [86] performed lamination of PLA films by using agar/κ-carrageenan modified Cloisite-Na⁺. The double layer and multilayer nanocomposite films showed a large decrease in OTR. Jalalvandi et al. [87] prepared nanocomposites of PLA/starch blend using unmodified MMT. The barrier properties of the nanocomposites were studied in terms of water uptake of the films. Neat starch films showed an uptake of 38%, whereas the nanocomposite with the highest clay loading of 7 wt% showed only 2% uptake. Othman et al. [88] varied the MMT clay content from 1 wt% to 9 wt% in the PLA matrix and obtained the best barrier performance at 3 wt% (BIF 1.5). In a similar study, Mohsen and Ali [89] varied the clay content and achieved best barrier properties at 4 wt%–6 wt% of nanoclay in a PLA matrix. A novel silver based organo-modified MMT (Bactiblock[®] from Nanobiomatters, Spain) was used by Busolo et al. [90] to prepare antimicrobial PLA nanocomposite coating for food packaging. However, a reduction in the permeability of water vapor by only 20% was achieved at a clay loading as high as 10 wt%. Sengül et al. [91] used MMT clay modified with different organic modifiers (Table 1) and investigated the effect of clay modification and ratio on the barrier properties of PLA nanocomposites. The oxygen permeability decreased by 22% to 49% and the water vapor permeation by 46% to 80%. Chowdhury [92] investigated the effect of clay aspect ratio and the degree of dispersion on the barrier properties of PLA nanocomposites. Three different clays modified with the same organic modifier were used in the study. The trend in permeability depended on the aspect ratio, dispersion and the degree of disorder of the clays in the matrix. Jorda-Beneyto et al. [93] prepared PLA/MMT nanocomposite bottles by injection stretch blow molding and obtained decreased oxygen and water vapor permeability compared to the neat PLA bottle.

The best improvement in O₂ permeability of a PLA/clay system to date was achieved with layer-by-layer (LbL) technique. Svagan et al. [94] prepared transparent films of PLA/MMT nanocomposites using LbL techniques that showed tunable O₂ barrier properties (Figure 3). Very thin laminar multilayer structures of chitosan and MMT were constructed by an LbL process (driven by electrostatic interactions) on extruded PLA films. Light transmittance analysis revealed high optical clarity for the coated PLA films, and TEM images showed well-ordered laminar structures of the bilayers. When 70 bilayers were used, the oxygen permeability coefficient of the coated PLA reduced by 99% and 96% at 20% and 50% RH, respectively. The data correspond to better oxygen barrier properties than PET at these humidity levels. Federico et al. [95] developed quadlayers (QL) and hexalayers (HL) of alternating branched poly(ethylene imine), Nafion and MMT on PLA thin film by LbL technique. The oxygen permeability reduced by 98% and 97% in dry and humid conditions, respectively for 10 HL and QL layers, whereas the water vapor transmission reduced by 78%. HL films displayed efficient barrier properties than the QL films.

Table 1. Barrier improvement factors (BIFs) for PLA/clay nanocomposites.

Matrix	Nanoclay	Name and Formula of Organic Modifier	Penetrant	Clay Content	BIF	Ref
PLA	MMT	Dodecyltrimethyl ammonium, (Me) ₃ (C ₁₂ H ₂₅)N ⁺	O ₂	10 wt%	2.3	[64]
	MMT	Hexadecyl ammonium, (C ₁₆ H ₃₃)NH ₃ ⁺	O ₂	10 wt%	2.4	
	Cloisite 25A	Dimethyloctyl tallow amine (Me) ₂ (C ₈ H ₁₇)TN ⁺	O ₂	10 wt%	2.3	
PLA	Smectite	Hexadecyltributyl phosphonium (C ₄ H ₉) ₃ (C ₁₆ H ₃₃)P ⁺	O ₂	4 wt%	1.7	[65]
PLA	MMT	Octadecyl ammonium C ₁₈ H ₃₇ NH ₃ ⁺	O ₂	4 wt%	1.2	[66]
	MMT	Octadecyltrimethyl ammonium (Me) ₃ (C ₁₈ H ₃₇)N ⁺	O ₂	4 wt%	1.1	
PLA	Saponite	Hexadecyltributyl phosphonium (C ₄ H ₉) ₃ (C ₁₆ H ₃₃)P ⁺	O ₂	4 wt%	1.7	
	Synthetic fluorine mica (SFM)	Dipolyoxyethylene alkyl (coco) methyl ammonium (CH ₂ CH ₂ O) _x H(CH ₂ CH ₂ O) _y H(Me)R(coco)N ⁺	O ₂	4 wt%	2.8	
	SFM	N-(cocoalkyl)-N,N-[bis(2-hydroxyethyl)]-N-methyl ammonium (Me)(EtOH) ₂ R(cocoalkyl)N ⁺	O ₂	10 wt%	5.5	[67]
PLA	MMT	Octadecyltrimethyl ammonium (Me) ₃ (C ₁₈ H ₃₇)N ⁺	O ₂	7 wt%	1.2	[68]
PLA	MMT	Octadecyl ammonium C ₁₈ H ₃₇ NH ₃ ⁺	O ₂	7 wt%	1.5	[69]
PLA	SFM	N-(cocoalkyl)-N,N-[bis(2-hydroxyethyl)]-N-methyl ammonium (Me)(EtOH) ₂ R(cocoalkyl)N ⁺	O ₂	4 wt%	2.8	[70]
PLA	Cloisite 25A	Dimethyl hydrogenated tallow-2-ethylhexyl ammonium (Me) ₂ (C ₈ H ₁₇)(HT)N ⁺	O ₂	5 wt%	1.7	[71]
			H ₂ O	5 wt%	2.7	
aPLA	Kaolinite	Not disclosed	O ₂	4 wt%	1.8	[72]
	MMT	Not disclosed	O ₂	4 wt%	1.1	
PLA	Cloisite 20A	Dimethyl dihydrogenated tallow quaternary ammonium (Me) ₂ (HT) ₂ N ⁺	H ₂ O	5 pph	1.5	[73]
	Cloisite 30B	Methyltallow-bis-2-hydroxyethyl quaternary ammonium (Me)(CH ₂ CH ₂ OH) ₂ (T)N ⁺	H ₂ O	5 pph	1.0	
	Cloisite Na ⁺	Unmodified	H ₂ O	5 pph	0.8	
PLA	Cloisite 15A	Dimethyl dihydrogenated tallow quaternary ammonium (Me) ₂ (HT) ₂ N ⁺	CO ₂	0.8 wt%	2.0	[76]
			O ₂	0.8 wt%	1.4	
			N ₂	0.8 wt%	1.5	
PLA	Cloisite 20A	Dimethyl dihydrogenated tallow quaternary ammonium (Me) ₂ (HT) ₂ N ⁺	CO ₂	0.8 wt%	1.4	
			O ₂	0.8 wt%	1.1	
			N ₂	0.8 wt%	1.5	
PLA	Cloisite 30B	Methyl tallow-bis-2-hydroxyethyl quaternary ammonium (Me)(CH ₂ CH ₂ OH) ₂ (T)N ⁺	CO ₂	0.8 wt%	2.0	
			O ₂	0.8 wt%	1.3	
			N ₂	0.8 wt%	2.0	
aPLA	Kaolinite	Not disclosed	O ₂	4 wt%	1.8	[77]

Table 1. Cont.

Matrix	Nanoclay	Name and Formula of Organic Modifier	Penetrant	Clay Content	BIF	Ref		
PLA	Cloisite 30B	Methyl tallow-bis-2-hydroxyethyl quaternary ammonium (Me)(CH ₂ CH ₂ OH) ₂ (T)N ⁺	O ₂	5 wt%	1.6	[78]		
			H ₂ O	5 wt%	2.1			
PLA	Cloisite 30B	Methyl tallow-bis-2-hydroxyethyl quaternary ammonium (Me)(CH ₂ CH ₂ OH) ₂ (T)N ⁺	O ₂	3 phr	1.5	[80]		
PLA	Cloisite 30B	Methyl tallow-bis-2-hydroxyethyl quaternary ammonium (Me)(CH ₂ CH ₂ OH) ₂ (T)N ⁺	O ₂	1 wt%	187.0	[81]		
			H ₂ O	1 wt%	1.25			
PLA	Cloisite 30B	Methyl tallow-bis-2-hydroxyethyl quaternary ammonium (Me)(CH ₂ CH ₂ OH) ₂ (T)N ⁺	O ₂	2 wt%	1.6	[82]		
			H ₂ O	1 wt%	1.2			
PLA	Cloisite 30B	Methyl tallow-bis-2-hydroxyethyl quaternary ammonium (Me)(CH ₂ CH ₂ OH) ₂ (T)N ⁺	H ₂ O	5 wt%	2.8	[83]		
PLA	Cloisite 30B	Methyl tallow-bis-2-hydroxyethyl quaternary ammonium (Me)(CH ₂ CH ₂ OH) ₂ (T)N ⁺	O ₂	3 wt%	1.3	[84]		
PLA	Cloisite 93A	Methyl dihydrogenated tallow quaternary ammonium (Me)(HT) ₂ NH ⁺	O ₂	3 wt%	2.0	[85]		
			CO ₂	3 wt%	3.45			
			O ₂	3 wt%	18.4			
	Dellite HPS	Not disclosed	CO ₂	3 wt%	30.2			
PLA	Cloisite-Na ⁺	Agar/κ-carrageenan	O ₂	5 wt%	516.0	[86]		
PLA	MMT	unmodified	H ₂ O	7 wt%	19.0	[87]		
PLA	MMT	Not disclosed	O ₂	3 wt%	1.5	[88]		
PLA	Clay name not mentioned	Not disclosed	O ₂	4 wt%	2.6	[89]		
			H ₂ O	6 wt%	3.1			
PLA	Ag-based MMT	Not disclosed	H ₂ O	10 wt%	1.2	[90]		
PLA	MMT	Dimethyldialkyl ammonium (Me) ₂ (R) ₂ N ⁺	O ₂	10 wt%	2.0	[91]		
			H ₂ O	10 wt%	4.8			
			Aminopropyltriethoxysilane (CH ₃ CH ₂ O) ₃ Si(C ₃ H ₆)NH ₂	O ₂	10 wt%	1.5		
			H ₂ O	10 wt%	2.7			
			Distearyldimethyl ammonium (C ₁₈ H ₃₇) ₂ (Me) ₂ N ⁺	O ₂	10 wt%	1.9		
			H ₂ O	10 wt%	5.0			
			Hydrogenated tallow quaternary ammonium (HT) ₄ N ⁺	O ₂	10 wt%	1.7		
			H ₂ O	10 wt%	2.3			
			MMT (Southern clay)	Octadecyl ammonium C ₁₈ H ₃₇ NH ₃ ⁺	O ₂	5 wt%	1.8	[92]
			MMT (Nanocor)	Octadecyl ammonium C ₁₈ H ₃₇ NH ₃ ⁺	O ₂	5 wt%	1.3	
SFM	Octadecyl ammonium C ₁₈ H ₃₇ NH ₃ ⁺	O ₂	5 wt%	2.1				
PLA	MMT	Hexadecyltrimethyl ammonium (Me) ₃ (C ₁₆ H ₃₃)N ⁺	H ₂ O	4 wt%	1.6	[93]		
			O ₂	4 wt%	1.7			

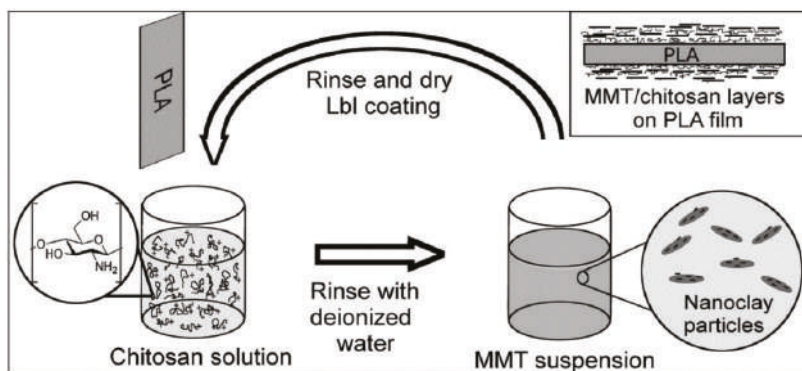


Figure 3. Schematic representation of layer-by-layer (LbL) deposition of chitosan and montmorillonite (MMT) on extruded poly(lactic acid) (PLA) film. Reprinted with permission from Ref [94]. Copyright (2012) American Chemical Society.

4. Mass Transfer in Polymers

Small molecules, such as O₂, CO₂, H₂O, N₂, permeate through a polymer membrane due to a gas chemical potential gradient through the membrane. The chemical potential difference acts as the driving force for the molecules to permeate from the high chemical potential side to the side of low chemical potential. The phenomenon of permeant transport in polymers is described using the solution–diffusion model. According to this model, the permeation in polymers consists of three steps, as depicted in Figure 4: (a) sorption of the permeant from the high concentration side onto the membrane/film surface, (b) diffusion of the permeant along the concentration gradient through the membrane and (c) desorption through evaporation from the low concentration surface of the membrane. Deviations from a gradient with a straight line can be observed when the permeating molecule interacts with the polymer and is categorized as non-Fickian diffusion, which is described by the diffusion–relaxation model [96,97].

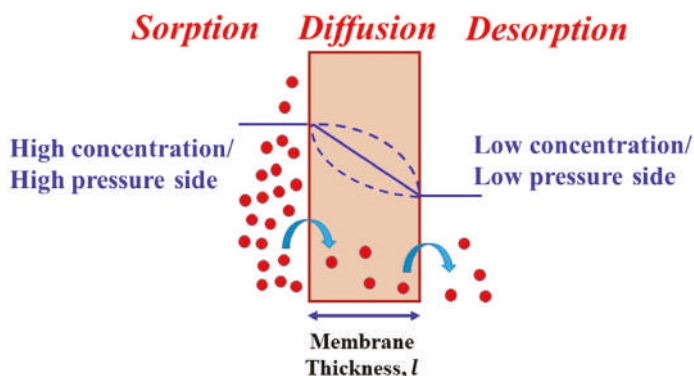


Figure 4. Schematic illustration of the solution diffusion model.

Based on the assumption that the diffusion takes place in the *x*-direction of a flat membrane/film, the process is described by Fick’s first law of diffusion that gives the relationship between flux (*F*) and the concentration gradient (*dc/dx*) [96]:

$$F = -D \frac{dc}{dx} \tag{1}$$

where D is the diffusion coefficient, c is the concentration and x is the direction of the moving permeant. This equation is used in steady-state conditions, i.e., when the permeant concentration does not change with time. The flux at steady state is defined as the amount of the permeant (no. of moles or weight) passing through a surface of unit area (perpendicular to the flow direction) per unit time:

$$F = \frac{q}{At} \quad (2)$$

where q is the amount of the permeant, A is the membrane area and t is the time. At steady state, the permeant concentration is constant on both sides (just inside the material), c_1 and c_2 for high and low concentration, respectively, of the film. Therefore, Equation (1) can be integrated across the total thickness (L) of the membrane which gives:

$$F = D \frac{(c_1 - c_2)}{L} \quad (3)$$

Equations (2) and (3) can be equated to get q :

$$q = D \frac{(c_1 - c_2)At}{L} \quad (4)$$

For gases, it is convenient to measure the partial pressure (p) of the gas that is in equilibrium with the polymer rather than the concentration. Henry's law is applied [96] at sufficiently low concentration and, when the interaction between the permeating molecule and the polymer is small:

$$c = Sp \quad (5)$$

where S is the solubility coefficient of the permeant in the polymer. Hence, assuming there is no interaction between the permeant and the polymer, Equation (4) can be expressed as:

$$q = DS \frac{(p_1 - p_2)At}{L} \quad (6)$$

which, can be rearranged as:

$$DS = \frac{qL}{(p_1 - p_2)At} \quad (7)$$

Equation (7) is nothing, but the permeability, P , of the permeant at steady state:

$$P = \frac{qL}{At\Delta p} \quad (8)$$

Therefore, from Equations (7) and (8) permeability can be expressed as the product of the diffusion coefficient D and the solubility coefficient S :

$$P = DS \quad (9)$$

D is the kinetic term (from Equation (1)) describing the mass flux of permeant through the film in response to a concentration gradient and S is the thermodynamic factor arising due to the interactions between the polymer and permeant molecules, which, is the ratio of equilibrium permeant concentration at the high concentration side of the film to the permeant partial pressure [98]:

$$S = \frac{c}{p} \quad (10)$$

Equations (7) and (8) are very simplistic and can be applied to penetrants in rubbery polymers which typically exhibit Fickian behavior at low concentrations. For glassy polymers, deviation from

Fickian behavior can be observed due to the restricted chain mobility, leading to slow polymer chain reorganization in comparison to permeant-induced swelling [99]. As a consequence, a dual-mode sorption model is used to describe gas sorption in polymers at temperature below the glass transition temperature (T_g) [100].

The unsteady state portion of the mass transfer permeation process is described by Fick's second law, given by [101]:

$$\frac{dc}{dt} = \frac{d}{dx} \left(D \frac{dc}{dx} \right) \quad (11)$$

When D is position-, concentration- and time-independent, Equation (11) is expressed as:

$$\frac{dc}{dt} = D \frac{d^2c}{dx^2} \quad (12)$$

When there is a strong interaction between the polymer and the permeant, D becomes dependent on time, position and concentration and Equation (11) is solved using numerical methods [102].

4.1. Measurement of Mass Transport Properties

Two basic methods are used to determine the permeability of gases or vapors in polymer films: (a) isostatic and (b) quasi-isostatic methods [103]. In the isostatic method (continuous flow method), one side of the film is exposed to a constant concentration of the permeant and zero concentration is maintained on the other side. On the zero-concentration side, inert gas is purged to carry the permeant to the detector for quantification. In the quasi-isostatic method (lag-time method) constant permeant concentration is maintained on one side and the permeant is allowed to accumulate on the other side to a very low concentration of <5 wt% of the concentration on the feed side. The permeant from the accumulated side is removed at regular time intervals and quantified to generate a plot of permeant quantity vs time. By applying specified initial conditions (concentration throughout the film to be equal to zero) and specified boundary conditions with constant permeant concentration on the feed side and zero permeant concentration on the permeate side, a mathematical expression can be derived to describe the situation [104]:

$$q = \frac{Dc_1}{L} \left(t - \frac{L^2}{6D} \right) - \frac{2Lc_1}{\pi^2} \sum_{n=1}^{\infty} \frac{(-1)^n}{n^2} \exp\left(\frac{-Dn^2\pi^2t}{L^2} \right) \quad (13)$$

When steady state is reached, t becomes sufficiently large, i.e., $t \rightarrow \infty$, then the exponential term in Equation (13) becomes negligibly small and hence the Equation reduces to:

$$q = \frac{Dc_1}{L} \left(t - \frac{L^2}{6D} \right) \quad (14)$$

A plot of q vs t gives a straight line with an intercept on the time-axis. The slope of the straight-line curve is the steady state flux ($F = DC/L$, from Equation (1)) and the intercept is the time-lag (t_{lag}) (the intercept is an extrapolation from the straight-line curve to the time-axis, thus it is a shorter time to reach the steady state):

$$t_{lag} = \frac{L^2}{6D} \quad (15)$$

The diffusion coefficient D can then be calculated from the above Equation as:

$$D = \frac{L^2}{6t_{lag}} \quad (16)$$

This is a simple time-lag analysis and may result in errors when measuring diffusion coefficient in concentration-dependent cases where t_{lag} may vary with pressure differences across the membrane. In

this case, a concentration-averaged diffusion coefficient can be estimated from the plot of normalized permeant flux, i.e., ratio of the flux at time t to the flux at equilibrium (steady state) as a function of time. The diffusion coefficient can then be estimated using the relationship [105]:

$$D = \frac{L^2}{7.199t_{1/2}} \quad (17)$$

where $t_{1/2}$ is the time required to reach half of the steady state value. The permeability coefficient can be calculated using Equations (7) and (8). There is also another method to determine D , whereby the equation:

$$\frac{Q}{Q_\infty} = \frac{4}{\sqrt{\pi}} \sqrt{\frac{l^2}{4Dt}} \exp\left(\frac{-l^2}{4Dt}\right) \quad (18)$$

is fitted to Q/Q_∞ vs t curve using a simplex search algorithm [106]. Q is the flow rate at time t and Q_∞ is the steady-state flow rate. Equation (18) can be obtained from dynamic flow rate permeation experiments [107,108]. Assuming Henry's law is valid, the solubility, S , can be calculated using:

$$S = \frac{Q_\infty l}{Dp} \quad (19)$$

It is also possible to obtain D and S and then P from a gravimetric method, but it is not considered here [109].

4.2. Factors Affecting Mass Transport

One important factor affecting the mass transfer in polymers is the free volume of the polymer. Free volume holes are created due to Brownian motion and thermal perturbations of the polymer chains. During the sorption process, the permeant molecule occupies a free volume hole and then diffuses by short "jumps" into neighboring holes. It can also occur through gradual motion into a new hole that develops next to the first hole due to Brownian motion. The latter process is not really thermally activated since there is no barrier in energy to get across. Thus, the transport depends on the static free volume (number and size of the holes) and dynamic free volume (frequency of jumps). The static free volume is independent of the thermal motions of the polymer chains and is related to the permeant solubility, S , whereas the dynamic free volume is due to the segmental motions of the chains and is related to permeant diffusivity, D . The solubility coefficient S is related to specific free volume by [110]:

$$v_{sp} = v - v_0 = \frac{S}{\rho_{gas}} \quad (20)$$

where v_{sp} is the specific free volume, v is the specific volume, v_0 is the occupied specific volume and ρ_{gas} is the density of the gas. The fractional free volume, v_f , is given by:

$$v_f = \frac{v_{sp}}{v} \quad (21)$$

Assuming that the holes are identical spheres arranged in a cubic lattice with lattice constant ' a ', the average radius of the holes, R can be calculated by:

$$R = a \sqrt[3]{\frac{3v_f}{4\pi}} \quad (22)$$

The gas diffusivity depends on the dynamic free volume of the matrix, size of the gas molecules (molecular diameter, d') and the velocity of the gas molecules (u) by [111]:

$$D = g d' u \exp\left(-\frac{\gamma v_0}{v_{sp}}\right) \quad (23)$$

where, g is a geometric factor and γ is the overlap free volume factor, i.e., the degree to which more than one molecule can access the same free volume site. Therefore, after regrouping, the constants in Equation (23) become:

$$D = A \exp\left(-\frac{B}{v_f}\right) \quad (24)$$

The higher the fractional free volume, the larger will be the diffusivity. The dependence of solubility on v_f is weaker than the diffusivity. Thus, permeability often follows a similar dependence on free volume as the gas diffusivity.

The effect of temperature on permeability, diffusivity and solubility is modeled using the Arrhenius equation [104]:

$$P = P_0 \exp\left(\frac{-E_p}{RT}\right) \quad (25)$$

$$D = D_0 \exp\left(\frac{-E_D}{RT}\right) \quad (26)$$

$$S = S_0 \exp\left(\frac{-\Delta H_s}{RT}\right) \quad (27)$$

where P_0 , D_0 and S_0 are the pre-exponential factors, E_p and E_D are the activation energies for permeation and diffusion, respectively and ΔH_s is the heat of dissolution of the permeant molecule in the polymer. Based on Equation (9), E_p can be given as:

$$E_p = E_D + \Delta H_s \quad (28)$$

E_D is always positive, ΔH_s can be positive for light gases like H_2 , O_2 and N_2 and negative for condensable vapors like water, C_3H_8 and C_4H_{10} .

Other factors which affect the transport phenomenon include polymer chain structure (flexibility, polarity), crystallinity, chain orientation and packing, permeant solubility and humidity [28,104]

5. Modeling of Permeability of Polymer/Clay Nanocomposites

The mass transport mechanism in polymers containing platelet fillers (like nanoclays, graphene, etc.) is similar to that in semi-crystalline polymers. In semi-crystalline polymers, the content, shape and size of the crystals and the superstructure they form (spherulites, axialites) affect the transport properties. Thus, the crystals are considered as the gas-impermeable phase in an otherwise permeable amorphous matrix. There is, however, an important difference between the effects of crystals and impermeable platelets. It is only in special cases that the crystals are randomly dispersed in the amorphous matrix, e.g., in ultra-high molar mass polyethylene. Normally, the spherulitic structure gives rise to “dead-ends” at points where the crystals splay, and all amorphous parts are not necessarily reachable by the permeant [112,113]. The gas sorption in amorphous polymers at low to moderate uptake is given by Equation (10) (Henry’s law) and for semi-crystalline polymers it is given, assuming that all the amorphous parts are accessible by the permeant, by [114]:

$$S = S_0(1 - \phi_c) \quad (29)$$

where S_0 is the solubility coefficient of the amorphous phase and ϕ_c is the volume fraction of the crystalline phase. For a “theoretically” 100% crystalline polymer, $S = 0$. In nanocomposites, the clay platelets are the non-permeable phase dispersed in the permeable polymer phase. The three main factors that influence the transport properties in clay/polymer nanocomposites are (a) the volume fraction of the nanoparticles (ϕ), (b) aspect ratio (l/w) of the platelets and (c) platelet orientation with

respect to the direction of diffusion [45,51]. Incorporation of nano-platelets results in a decrease in the permeability of the polymer due to the permeant having to circumvent the platelets (leading to a tortuous diffusion path, or, in other words, a labyrinth effect) and this reduced permeability, represented as the ratio of composite permeability to the neat matrix permeability (P/P_0) or the ‘relative permeability,’ is plotted as a function of the filler volume fraction (ϕ) to describe the transport properties in several models. A typical plot displays the nonlinear decay in (P/P_0) with increasing filler volume fraction [33]. The volume fraction, which is the main input parameter in all mathematical models, can be calculated with [49]:

$$\phi = \frac{\frac{w_{np}}{\rho_{np}}}{\frac{w_{np}}{\rho_{np}} + \frac{1 - w_{polymer}}{\rho_{polymer}}} \tag{30}$$

where w_{np} and ρ_{np} are, respectively, the weight fraction and density of the nanoparticles and $w_{polymer}$ and $\rho_{polymer}$ are the weight fraction and density of the polymer matrix. The main assumptions in most of the models are that the platelets have a regular geometry (thin rectangular or circular shaped platelets) and form an ordered array in space arranged either parallel to each other or display a distribution of orientation [45]. The average orientation is assumed to be at a particular angle to the direction of diffusion of the permeant molecules. Some of the important and common models can be grouped into three categories of spatial arrangement (i) parallel arrangement, (ii) random positioning and (iii) arrangements at an angle $\theta \neq 90^\circ$ and these are discussed below.

5.1. Periodic Arrangement of Parallel Nanoplatelets

A simple permeability model was proposed by Nielsen [115]. In this model the platelets are considered to have a rectangular shape with a finite length (l) and thickness (w) and are dispersed evenly in the polymer matrix with orientation perpendicular to the diffusion direction. The basic theory of the model is that the presence of impermeable platelets forces the permeant molecules to follow a longer diffusion path by traversing around the platelets. Therefore, this is also called the ‘tortuous path’ model, as shown in Figure 5.

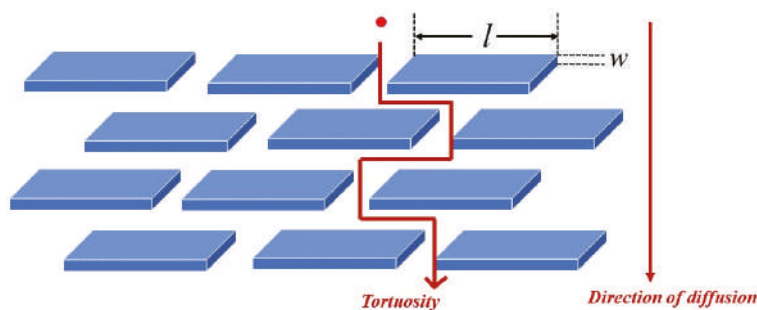


Figure 5. Schematic illustration of the tortuous path model.

The solubility coefficient, S , of this clay/polymer composite can be arrived at, from Equation (29) as:

$$S = S_0(1 - \phi) \tag{31}$$

where S_0 is the solubility coefficient of the neat polymer and ϕ is the volume fraction of the clay nano-filler. The diffusion coefficient, being influenced by the tortuous path, is given by:

$$D = \frac{D_0}{\tau} \tag{32}$$

where D_0 is the diffusion coefficient of the neat polymer and τ is the tortuosity factor that depends on the platelet shape, aspect ratio and its orientation in the matrix. It is defined as:

$$\tau = \frac{d'}{L} \tag{33}$$

where, d' is the distance that the permeant molecules must travel through the film in the presence of platelets and L is the actual distance the molecule would have traveled in the absence of platelets, i.e., thickness of the membrane. From Equations (9) and (31), we have;

$$\frac{P}{P_0} = \frac{1 - \phi}{\tau} \tag{34}$$

If $\langle N \rangle$ is the average number of platelets that the permeant molecule encounters during diffusion and if each platelet enhances the diffusion length by $l/2$ on average, then the tortuous path length (prolonged diffusion length) is given by:

$$d' = L + \langle N \rangle \frac{l}{2} \tag{35}$$

Since, $\langle N \rangle = \frac{L\phi}{w}$, the tortuosity factor, τ becomes:

$$\tau = 1 + \frac{l}{2w}\phi \tag{36}$$

Combining Equations (34) and (36) gives:

$$\frac{P}{P_0} = \frac{1 - \phi}{1 + \frac{\alpha}{2}\phi} \tag{37}$$

where $\alpha = l/w$ is the aspect ratio of the clay platelets. This is Nielsen’s equation which shows that the relative permeability decreases with increase in α and ϕ in the nanocomposite membrane [115]. However, it can be used as a rough estimate only up to a threshold limit in filler content, $\phi \leq 10\%$, beyond which the particles may aggregate leading to increased permeation. The Nielsen equation was remarkably successful in validating the permeability reduction in many polymer systems. Figure 6 shows the predicted permeability decay curves for Nielsen’s model at different aspect ratios. However, it should be highlighted that incomplete exfoliation or orientation of the platelets and the occurrence of voids will result in systems deviating from the Nielsen model [115].

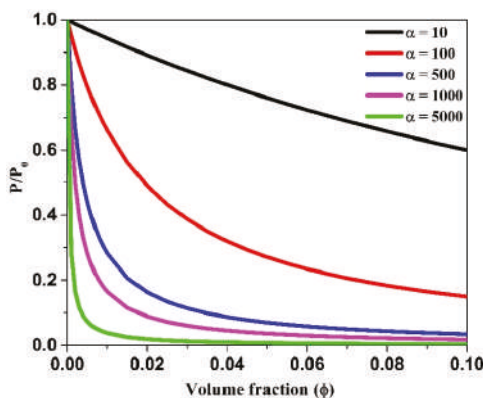


Figure 6. Prediction plot of Nielsen’s model at different aspect ratios.

A second model where the resistance to diffusion arising from the tendency of the permeant molecule to get constricted in the slits (distance between two adjacent platelets) along with the contribution from the platelet length is given by Cussler et al. [116]. In this model, platelets are considered to be arranged parallel in multiple layers with a narrow-slit separation (s) between the platelets in each layer. In this case the following equation was derived:

$$\frac{P}{P_0} = \left(1 + \frac{da}{s(a+b)} + \frac{d^2}{b(a+b)} + \frac{2b}{L} \ln \left(\frac{d}{2s} \right) \right)^{-1} \tag{38}$$

where L is the film thickness and other parameters are as defined in Figure 7.

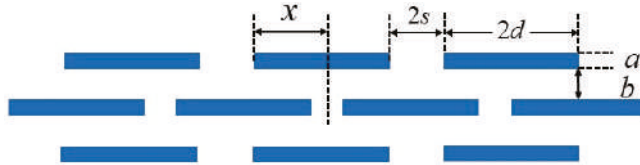


Figure 7. Ribbon arrangement of platelets.

Here, the volume fraction and aspect ratio are given by:

$$\phi = \frac{da}{(d+s)(a+b)}, \quad \alpha = \frac{d}{a} \tag{39}$$

In this model, d is half the platelet length, and hence the aspect ratio is half that of the Nielsen model. Since the slit is considered to be very narrow, the second term was neglected, and the simplified expression of the relative permeability is given as:

$$\frac{P}{P_0} = \left(1 + \frac{\alpha^2 \phi^2}{1-\phi} \right)^{-1} \tag{40}$$

This model predicts a rapid reduction in relative permeability at low volume fraction, as opposed to Nielsen’s model which requires high volume fraction or aspect ratio to achieve the same reduction in permeability.

5.2. Random Arrangement of Parallel Nanoplatelets

Brydges et al. [117] described the relative permeability considering random positioning of the parallel platelets in each layer and used a stacking parameter $\gamma' = x/2d$ to account for the deviation from periodicity, i.e., it defines the horizontal offset of each ribbon layer with respect to the platelet layer beneath it. A case of $\gamma' = 1/2$ is when the platelets in one ribbon layer are positioned at the center of the slit gaps of the layer underneath, and thus gives the lowest permeability. For very high aspect ratio, $\alpha > 100$, this model gives:

$$\frac{P}{P_0} = \left(1 + \frac{\alpha^2 \phi^2}{1-\phi} \gamma' (1-\gamma') \right)^{-1} \tag{41}$$

In another case, Lape et al. [118] also considered platelets of the same aspect ratio arranged in a random fashion in the parallel ribbons. The reduced permeability is given by the product of reduced area and increased diffusion path length:

$$\frac{P}{P_0} = \left(\frac{A}{A_0} \right) \left(\frac{d'}{L} \right) \tag{42}$$

The distance that the permeant has to diffuse through the nanocomposite films is given by:

$$d' = L + \langle N \rangle \langle n \rangle \tag{43}$$

This equation is similar to Equation (35) except that $l/2$ is replaced by $\langle n \rangle$, which is the average distance the permeant travels to reach the platelet edge. Using statistical considerations, d' is estimated to be:

$$d' = \left(1 + \frac{1}{3}\alpha\phi\right)L \tag{44}$$

The area available for diffusion is calculated by dividing the volume available for diffusion by the distance traversed to cross the membrane:

$$\frac{A}{A_0} = \frac{(V_{tot} - V_{np})/d'}{V_{tot}/L} \tag{45}$$

where V_{tot} is the total volume of the membrane and V_{np} is the volume of the nanoplatelets. Using Equation (44), the relative permeability is then given by:

$$\frac{P}{P_0} = \frac{1 - \phi}{\left(1 + \frac{1}{3}\alpha\phi\right)^2} \tag{46}$$

Fredrickson and Bicerano [119] modeled the case of circular shaped nanoplatelets with length $2R$ and thickness w having an aspect ratio $\alpha = R/w$. Two situations were considered, as shown in Figure 8, (a) when the average distance between the platelets exceeds R due to low volume fraction and aspect ratio ($\alpha\phi \ll 1$), i.e., in the dilute regime, the relative diffusivity is given by:

$$\frac{D}{D_0} = \frac{1}{1 + \kappa\alpha\phi} \tag{47}$$

where $\kappa = \pi/ln \alpha$ and (b) in the semi-dilute regime when the circular disks overlap due to higher aspect ratios ($\alpha\phi \gg 1$), the relation is given by:

$$\frac{D}{D_0} = \frac{1}{1 + \mu\alpha^2\phi^2} \tag{48}$$

where μ is a geometric factor.

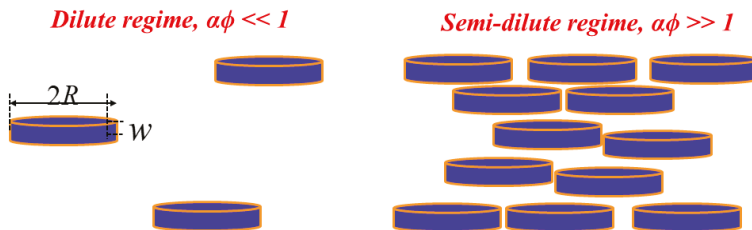


Figure 8. Schematic illustration of the dilute and the semi-dilute regimes of the oriented disk-shaped platelets.

Gusev and Lusti [120] developed periodic three-dimensional computer models containing a random dispersion of disk platelets in an isotropic matrix and solved the Laplace’s equation for the

local chemical potential μ , ($\nabla P(r) \cdot \nabla u = 0$). The expression developed for the relative permeability is given as:

$$\frac{P}{P_0} = \exp\left[-\left(\frac{\alpha\phi}{x_0}\right)^\beta\right] \tag{49}$$

The values of β and x_0 are 0.71 and 3.47, respectively [98].

In Figure 9, prediction curves for Nielsen, Cussler, Fredrickson and Bicerano and Gusev and Lusti models are compared for three different aspect ratios, $\alpha = 10, 100$ and 1000 .

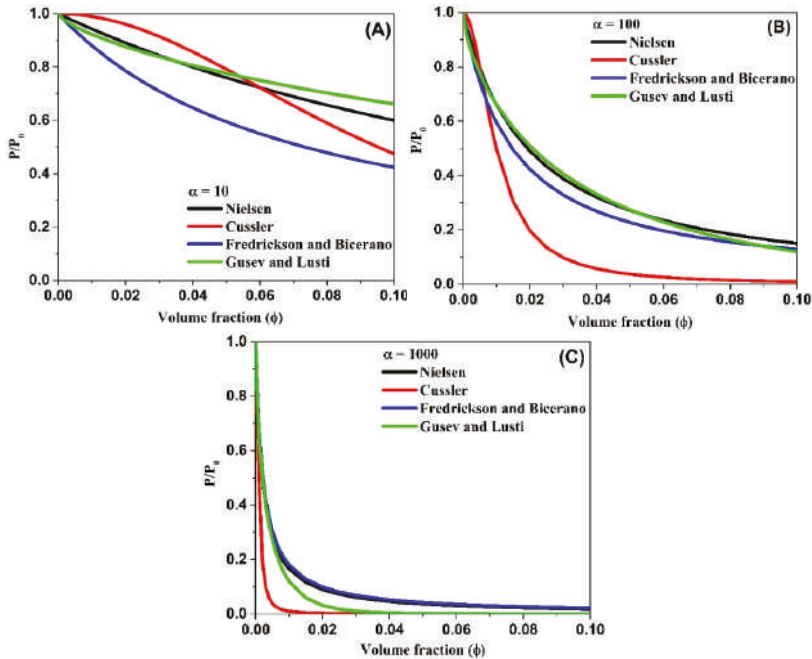


Figure 9. Prediction plots of relative permeability for different models at a fixed aspect ratio, (A) $\alpha = 10$, (B) $\alpha = 100$ and (C) $\alpha = 1000$.

It is observed that the predictions for the decrease in relative permeability is different for different models, particularly in the region of low ϕ values. To avoid this anomaly, P/P_0 vs $\alpha\phi$ can be plotted [46]. Cussler and Gusev’s models predict dramatic decrease in P/P_0 to almost zero permeability for $\phi \geq 0.02$ at very high aspect ratios. The plots also show that, at low aspect ratios, the models predict the need for a large volume fraction to achieve a significant decrease in permeability.

5.3. Platelet Arrangement at an Angle $\theta \neq 90^\circ$ to the Diffusion Direction

The main assumption in all the models discussed above is that the platelets are aligned perpendicular to the diffusion direction and hence the tortuosity is the highest. However, Bharadwaj [121] described the case where the platelets can be oriented at different angles ($\neq 90^\circ$) with respect to the direction of diffusion. For describing this nonuniformity in alignment, Nielsen’s model was modified accordingly by introducing an order parameter which gives the degree of orientation of the platelets to the diffusion direction:

$$S' = \frac{1}{2}(3 \cos^2 \theta - 1) \tag{50}$$

where θ is the angle between direction of diffusion and the unit vector normal to the nanoplatelets' large surface. When the platelets are oriented perpendicular to the direction of diffusion (i.e., $\theta = 0$), then $S' = 1$, whereas when platelets are oriented parallel to the diffusion direction (i.e., $\theta = \pi/2$, then $S' = -1/2$. For a random degree of orientation, $S' = 0$. The modified Nielsen's equation is then given by:

$$\frac{P}{P_0} = \frac{1 - \phi}{1 + \frac{\alpha\phi}{2} \left(S' + \frac{1}{2} \right)} \quad (51)$$

The case of $S' = 1$ presents maximum tortuosity, and hence, the greatest reduction in relative permeability can be observed. The values of the order parameter for the different orientations are shown in Figure 10.

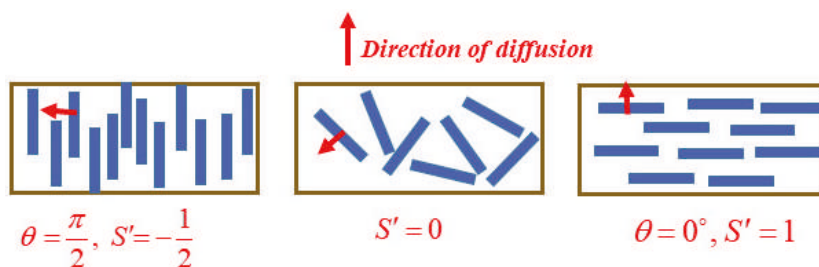


Figure 10. Different orientations of the platelets with the corresponding order parameter.

6. Model Validation for PLA/Clay Nanocomposites

Although a large body of literature is available describing the effects of two-dimensional clay sheets on reducing the water vapor permeability and gas permeability in PLA/clay nanocomposites, only a handful is available where the mathematical models have been successfully validated to account for the experimental results. Ray et al. [67] prepared PLA nanocomposites with organically modified (N-(coco alkyl)-N,N-[bis(2-hydroxyethyl)]-N-methyl ammonium cation) synthetic fluorine mica by melt extrusion using a twin-screw extruder. Films were prepared by compression molding at 190 °C. The WAXD and TEM analysis revealed intercalation of the clay platelets. However, the reduction in oxygen permeability with increasing clay concentration could not be explained by an intercalated nano-structure. Nevertheless, HRTEM revealed the co-existence of mixed intercalated and exfoliated structures that were found to be responsible for the improved oxygen barrier. Nielsen's tortuosity model was found to match the experimental results well, which confirmed the presence of exfoliated mica sheets in large amounts in the matrix, with negligible role of the intercalated structures in the observed gas barrier properties.

Guo et al. [122] used two different modifications of Cloisite- Na^+ ; (i) Cloisite 30B modified with bis(2-hydroxyethyl) methyl hydrogenated tallow quaternary ammonium cation and (ii) Cloisite- RDP modified with resorcinol di (phenyl phosphate) (RDP) and studied the oxygen barrier properties of the organically modified clay composites and compared them with those of the unmodified clay composite. The O_2 barrier performance was explained using the work of adhesion (W_a) parameter obtained from contact angle measurements. W_a essentially describes the strength of affinity between PLA and the clay sheets. Higher W_a values, indicating strong affinity, were obtained for PLA/Cloisite 30B, and the lowest value was observed for the PLA/Cloisite- Na^+ . The bulky tallow molecule in Cloisite 30B helped in forming exfoliated nanostructures in the PLA matrix that, in turn, demonstrated the best barrier performance of the three clays. On the other hand, the PLA/Cloisite- Na^+ , with less interfacial interactions, was shown to be a poor barrier film. The authors obtained best fit of the experimental permeability data with Nielsen's model. The aspect ratios calculated from curve fitting of the Nielsen model were smaller than that observed by TEM, and the difference was attributed to the tilt angle (angle between platelet and the direction of diffusion).

Picard et al. [123] investigated the role of clay platelets (Nanofil 804; MMT modified with a dihydroxy methyl tallow quaternary ammonium cation) on the PLA crystallization, as well as the gas (O_2 and He) permeability and established a crystallization-permeability relationship in PLA/clay nanocomposites for the first time. Melt compounding of PLA and OMMT was carried out using a mini-extruder to prepare the nanocomposites, followed by compression molding to make 100 μm thick films. The nanocomposites showed improved gas barrier properties at two different filler concentrations. A ca. 15% to 25% reduction in permeability/diffusivity was observed—a change that was higher than that reported by Ray et al. [66–70] for several PLA/OMMT systems. Nielsen's tortuosity model was used to provide an accurate description of the experimental results for relative permeability and diffusivity of the nanocomposites. A mean clay aspect ratio of 24 calculated from the model curve was found to be in good agreement with that obtained from TEM micrographs. The presence of the OMMT platelets increased the crystallinity of the PLA by 46%, which decreased the O_2 permeability in the annealed nanocomposite films. This permeability decrease induced by the increase in crystallinity was described well by the Maxwell equation [122].

Li et al. [124] prepared PLA/OMMT nanocomposites by solution intercalation and, later, coagulation in water. The coagulated solid was dried, and compression molded to form films. Experimental results of relative permeability of CO_2 were found to follow the Nielsen model well at low clay loadings, but the model underestimated the permeability at higher clay content; the model predicted 60% reduction in the permeability of the clay-free material at a clay content of 3 wt%, whereas the corresponding experimental value was only 40%. This is because the model describes the system better in the dilute regime but is inaccurate in the semi-dilute regime. In their study, composites with >3 wt% OMMT loading belonged to the semi-dilute regime, and the theoretical permeability matched well with the measured permeability at 1 wt% and 3 wt% of clay loading. Nevertheless, the Cussler model still overestimated the permeability at higher clay loading of 7 wt% (theoretical permeability = 9% and measured permeability = 19%). The reason is the aggregation of silicate layers at higher clay concentrations leading to nonuniform dispersion of the layers/platelets and a decreased "effective" aspect ratio. According to Equation (40), a decrease in α will substantially increase the relative permeability. However, the Cussler model was found to give a better prediction of the system compared to other models. The Bharadwaj model fitting for $S' = 0$ was unsuitable at all clay loadings and was attributed to the uneven orientation of the silicate layers, corroborating with the observations from the TEM micrographs. The use of $S' = 1$ (platelets perpendicular to the diffusion direction) yielded the same description of the system as the Nielsen model.

PLA/poly(butylene succinate)/clay nanocomposites prepared by Bhatia et al. [125] by melt extrusion showed improved O_2 barrier property with increasing clay content. However, the formation of clay stacks and nonuniform dispersion at high clay loading (>3 wt%) led to reduced tortuosity, and further improvement in barrier properties was negligible. Nanocomposite films prepared by compression molding could be described by the Bharadwaj model only up to 3 wt% clay, beyond which deviations from the model occurred because of the aforementioned clay agglomerates/nonuniform clay dispersion.

Tenn et al. [126] investigated the effect of the clay platelet hydration on the barrier properties of PLA/OMMT nanocomposites. The relative water and oxygen permeability results were fitted to the Bharadwaj model. However, the fitting for the water permeability was quite unsuitable. It was concluded that, apart from the aspect ratio and orientation of the clays, other parameters, such as interaction between silicate layers and water molecules, rigidity of the polymer chains in the vicinity of the clay layers, degree of crystallinity and percolation effects at the clay-polymer interface can interfere with the tortuosity concept, and thus make the tortuosity models less useable for prediction purposes. Nevertheless, the Nielsen-Bharadwaj model was found to be the best model to fit for the relative oxygen permeability experimental data of the PLA/OMMT nanocomposites. It was suggested that the tortuosity concept can be applied in a straightforward way to a gas-polymer system when there is no interaction between the diffusing gas molecules and the polymer matrix, whereas in the case

of water or organic species, in addition to the tortuosity, different physical phenomena and chemical interactions can play a large role during the course of permeation, which can result in significant deviation from the expected tortuosity-based results.

7. Conclusions

Two-dimensional platelet/disk-shaped fillers (e.g., nanoclays) have been identified as the most effective nano-filler for increasing the gas barrier properties of polymers. These nanoparticles not only improve barrier properties of the polymer, but also improve mechanical properties and, often, the thermal stability owing to interfacial interactions with the polymer matrix. In this article, the commonly followed preparation methods for PLA/organoclay nanocomposites were elaborated which are solution intercalation, melt processing and in situ polymerization. The melt processing method is the most preferred route because of ease of implementation in industry. The barrier performance of PLA/clay nanocomposites with different kinds of nanoclay and with a vast variety of modifiers were reviewed to highlight the structure-property relationship, which varied from case to case. In general, the extent of exfoliation and stacking orientation of the nanoclays was found to be the most important factor affecting the barrier properties of PLA, where improvement by one or two orders of magnitude can be observed for fully exfoliated platelets. The individual clay platelets act as blockages and create tortuosity to the diffusing permeant molecules, and thus extend the diffusion path length and time. In many cases, they also reduce the solubility of the permeating gas molecules. Best barrier performance was found to be obtained through the Lbl technique. Although it is successful on the laboratory scale, the future success of this technique will depend on industrial implementation. The ability of the Lbl prepared clays to impart delayed diffusion is most useful in packaging and coating applications.

Some important mathematical models for estimating the relative permeability of polymer/organoclay nanocomposites have been described. The commonality among the models is the dependence of relative permeability on three factors: clay aspect ratio, volume fraction and the clay platelet orientation with respect to the direction of diffusion. Experimental validation of the models on PLA/clay systems has been studied only by a few groups and the results were reviewed in this article. Most of the models, Nielsen's model in particular, were found to fit the data well at lower clay content. However, the models cannot be compared as the aspect ratios are different: some authors define aspect ratio as the width to thickness ratio while others define it as half width to thickness ratio. It can become more complicated because the degree of interaction between the polymer and the clay particles and the degree of delamination can be expected to vary. Nevertheless, with known aspect ratios of the clay, the simplest model proposed by Nielsen has proven to predict the relative permeability reasonably well. Another model which describes the tortuosity in polymer nanocomposites is the Fricke model that has been applied successfully in several composite systems, but has not so far been applied to PLA systems, although there is scope for in future studies [127].

Author Contributions: Conceptualization, M.S.H. and S.S.; writing—original draft preparation, S.S.; writing—review and editing, M.S.H. and S.S.; funding acquisition, M.S.H. All authors have read and agreed to the published version of the manuscript.

Funding: Knut och Alice Wallenbergs Stiftelse: 63235.

Acknowledgments: Knut and Alice Wallenberg foundation, through the Wallenberg Wood Science Center at KTH Royal Institute of Technology, is acknowledged for the financial support.

Conflicts of Interest: The authors declare no conflict of interest.

References

1. Jenck, J.F.; Agterberg, F.; Droescher, M.J. Products and processes for a sustainable chemical industry: A review of achievements and prospects. *Green Chem.* **2004**, *6*, 544–556. [[CrossRef](#)]
2. Kaplan, D.L. *Biopolymers from Renewable Resources*; Springer: Berlin, Germany, 1998.

3. Mekonnen, T.; Mussone, P.; Khalil, H.; Bressler, D. Progress in bio-based plastics and plasticizing modifications. *J. Mater. Chem. A* **2013**, *1*, 13379–13398. [[CrossRef](#)]
4. Kabir, E.; Kaur, R.; Lee, J.; Kim, K.-H.; Kwon, E.E. Prospects of biopolymer technology as an alternative option for non-degradable plastics and sustainable management of plastic wastes. *J. Clean. Prod.* **2020**, *258*, 120536. [[CrossRef](#)]
5. Stefani, R.; Vinhal, G.L.R.R.B.; do Nascimento, D.V.; Pereira, M.C.S.; Pertuzatti, P.B.; da Silva Chaves, K. Smart Biopolymers in Food Industry. In *Industrial Applications for Intelligent Polymers and Coatings*; Hosseini, M., Makhoulouf, A.S.H., Eds.; Springer International Publishing AG: Cham, Switzerland, 2016.
6. Catalá, R.; López-Carballo, G.; Hernández-Muñoz, P.; Gavara, R. PLA and Active Packaging. In *Poly(lactic acid) Science and Technology: Processing, Properties, Additives and Applications*; Jiménez, A., Peltzer, M., Ruseckaite, R., Eds.; The Royal Society of Chemistry: Cambridge, UK, 2015.
7. Fiori, S. Industrial uses of PLA. *RSC Polym. Chem. Ser.* **2015**, *2015*, 317–333.
8. Lim, L.T.; Auras, R.; Rubino, M. Processing technologies for poly(lactic acid). *Prog. Polym. Sci.* **2008**, *33*, 820–852. [[CrossRef](#)]
9. Castro-Aguirre, E.; Iñiguez-Franco, F.; Samsudin, H.; Fang, X.; Auras, R. Poly(lactic acid)—Mass production, processing, industrial applications, and end of life. *Adv. Drug Deliv. Rev.* **2016**, *107*, 333–366. [[CrossRef](#)] [[PubMed](#)]
10. Farah, S.; Anderson, D.G.; Langer, R. Physical and mechanical properties of PLA, and their functions in widespread applications—A comprehensive review. *Adv. Drug Deliv. Rev.* **2016**, *107*, 367–392. [[CrossRef](#)]
11. Armentano, I.; Bitinis, N.; Fortunati, E.; Mattioli, S.; Rescignano, N.; Verdejo, R.; Lopez-Manchado, M.A.; Kenny, J.M. Multifunctional nanostructured PLA materials for packaging and tissue engineering. *Prog. Polym. Sci.* **2013**, *38*, 1720–1747. [[CrossRef](#)]
12. Maharana, T.; Mohanty, B.; Negi, Y.S. Melt-solid polycondensation of lactic acid and its biodegradability. *Prog. Polym. Sci.* **2009**, *34*, 99–124. [[CrossRef](#)]
13. Kang, H.; Li, Y.; Gong, M.; Guo, Y.; Guo, Z.; Fang, Q.; Li, X. An environmentally sustainable plasticizer toughened polylactide. *RSC Adv.* **2018**, *8*, 11643–11651. [[CrossRef](#)]
14. Mofokeng, J.P.; Luyt, A.S.; Tábi, T.; Kovács, J. Comparison of injection moulded, natural fibre-reinforced composites with PP and PLA as matrices. *J. Thermoplast. Compos. Mater.* **2012**, *25*, 927–948. [[CrossRef](#)]
15. Anderson, K.S.; Schreck, K.M.; Hillmyer, M.A. Toughening polylactide. *Polym. Rev.* **2008**, *48*, 85–108. [[CrossRef](#)]
16. Garlotta, D. A Literature Review of Poly(Lactic Acid). *J. Polym. Environ.* **2001**, *9*, 63–84. [[CrossRef](#)]
17. Avérous, L. Polylactic acid: Synthesis, properties and applications. In *Monomer, Polymer and Composites from Renewable Resources*; Belgacem, M.N., Gandini, A., Eds.; Elsevier: London, UK, 2008.
18. Wee, Y.J.; Kim, J.N.; Ryu, H.W. Biotechnological production of lactic acid and its recent applications. *Food Technol. Biotechnol.* **2006**, *44*, 163–172.
19. Carothers, W.H.; Borough, G.L.; Natta, F.J. Studies of polymerization and ring formation. X. The reversible polymerization of six-membered cyclic esters. *J. Am. Chem. Soc.* **1932**, *54*, 761–772. [[CrossRef](#)]
20. Albertsson, A.C.; Varma, I.K. Aliphatic polyesters: Synthesis, properties and applications. *Adv. Polym. Sci.* **2002**, *157*, 1–40.
21. Okada, M. Chemical syntheses of biodegradable polymers. *Prog. Polym. Sci.* **2002**, *27*, 87–133. [[CrossRef](#)]
22. Madhavan Nampoothiri, K.; Nair, N.R.; John, R.P. An overview of the recent developments in polylactide (PLA) research. *Bioresour. Technol.* **2010**, *101*, 8493–8501. [[CrossRef](#)]
23. Guinault, A.; Menary, G.H.; Courgneau, C.; Griffith, D.; Ducruet, V.; Miri, V.; Sollogoub, C. The effect of the stretching of PLA extruded films on their crystallinity and gas barrier properties. *AIP Conf. Proc.* **2011**, *1353*, 826–831.
24. Driessens, M.; Peeters, R.; Mullens, J.; Franco, D.; Lemstra, P.J.; Hristova-Bogaerds, D.G. Structure versus properties relationship of poly(lactic acid). I. Effect of crystallinity on barrier properties. *J. Polym. Sci. Part B Polym. Phys.* **2009**, *47*, 2247–2258. [[CrossRef](#)]
25. Guinault, A.; Sollogoub, C.; Domenek, S.; Grandmontagne, A.; Ducruet, V.J. Influence of crystallinity on gas barrier and mechanical properties of PLA food packaging films. *Int. J. Mater. Form.* **2010**, *3*, 603–606. [[CrossRef](#)]
26. Sonchaeng, U.; Iñiguez-Franco, F.; Auras, R.; Selke, S.; Rubino, M.; Lim, L.T. Poly(lactic acid) mass transfer properties. *Prog. Polym. Sci.* **2018**, *86*, 85–121. [[CrossRef](#)]

27. Koros, W.J. Barrier Polymers and Structures. *Anal. Chem.* **1990**, *62*, 737A.
28. Hedenqvist, M.S. Barrier packaging materials. In *Handbook of Environmental Degradation of Materials*, 3rd ed.; Kutz, M., Ed.; Elsevier Inc.: Cambridge, MA, USA, 2018.
29. Majeed, K.; Jawaid, M.; Hassan, A.; Abu Bakar, A.; Abdul Khalil, H.P.S.; Salema, A.A.; Inuwa, I. Potential materials for food packaging from nanoclay/natural fibres filled hybrid composites. *Mater. Des.* **2013**, *46*, 391–410. [[CrossRef](#)]
30. Bee, S.L.; Abdullah, M.A.A.; Bee, S.T.; Sin, L.T.; Rahmat, A.R. Polymer nanocomposites based on silylated-montmorillonite: A review. *Prog. Polym. Sci.* **2018**, *85*, 57–82. [[CrossRef](#)]
31. Silvestre, C.; Duraccio, D.; Cimmino, S. Food packaging based on polymer nanomaterials. *Prog. Polym. Sci.* **2011**, *36*, 1766–1782. [[CrossRef](#)]
32. Sinha Ray, S.; Okamoto, M. Polymer/layered silicate nanocomposites: A review from preparation to processing. *Prog. Polym. Sci.* **2003**, *28*, 1539–1641. [[CrossRef](#)]
33. Nordqvist, D.; Hedenqvist, M.S. Transport Properties of Nanocomposites Based on Polymers and Layered Inorganic Fillers. In *Packaging Nanotechnology*; Mohanty, A.K., Misra, M., Eds.; American Scientific Publishers: Valencia, CA, USA, 2009.
34. Wokadala, O.C.; Ray, S.S.; Bandyopadhyay, J.; Wesley-Smith, J.; Emmambux, N.M. Morphology, thermal properties and crystallization kinetics of ternary blends of the polylactide and starch biopolymers and nanoclay: The role of nanoclay hydrophobicity. *Polymer* **2015**, *71*, 82–92. [[CrossRef](#)]
35. Hoidy, W.H.; Al-Mulla, E.A.J.; Al-Janabi, K.W. Mechanical and Thermal Properties of PLLA/PCL Modified Clay Nanocomposites. *J. Polym. Environ.* **2010**, *18*, 608–616. [[CrossRef](#)]
36. Ibrahim, N.; Jollands, M.; Parthasarathy, R. Mechanical and thermal properties of melt processed PLA/organoclay nanocomposites. *IOP Conf. Ser. Mater. Sci. Eng.* **2017**, *191*, 012005. [[CrossRef](#)]
37. Krishnamachari, P.; Zhang, J.; Lou, J.; Yan, J.; Uitenham, L. Biodegradable poly(Lactic Acid)/clay nanocomposites by melt intercalation: A study of morphological, thermal, and mechanical properties. *Int. J. Polym. Anal. Charact.* **2009**, *14*, 336–350. [[CrossRef](#)]
38. Hasook, A.; Tanoue, S.; Iemoto, Y.; Unryu, T. Characterization and mechanical properties of poly(lactic acid)/poly(ϵ -caprolactone)/organoclay nanocomposites prepared by melt compounding. *Polym. Eng. Sci.* **2006**, *46*, 1001–1007. [[CrossRef](#)]
39. Lai, S.M.; Wu, S.H.; Lin, G.G.; Don, T.M. Unusual mechanical properties of melt-blended poly(lactic acid) (PLA)/clay nanocomposites. *Eur. Polym. J.* **2014**, *52*, 193–206. [[CrossRef](#)]
40. Tabatabaei, S.H.; Aji, A. Orientation, mechanical, and optical properties of poly (lactic acid) nanoclay composite films. *Polym. Eng. Sci.* **2011**, *51*, 2151–2158. [[CrossRef](#)]
41. Cele, H.M.; Ojijo, V.; Chen, H.; Kumar, S.; Land, K.; Joubert, T.; De Villiers, M.F.R.; Ray, S.S. Effect of nanoclay on optical properties of PLA/clay composite films. *Polym. Test.* **2014**, *36*, 24–31. [[CrossRef](#)]
42. Stloukal, P.; Pekařová, S.; Kalendova, A.; Mattausch, H.; Laske, S.; Holzer, C.; Chitu, L.; Bodner, S.; Maier, G.; Slouf, M.; et al. Kinetics and mechanism of the biodegradation of PLA/clay nanocomposites during thermophilic phase of composting process. *Waste Manag.* **2015**, *42*, 31–40. [[CrossRef](#)]
43. Castro-Aguirre, E.; Auras, R.; Selke, S.; Rubino, M.; Marsh, T. Impact of nanoclays on the biodegradation of poly(lactic acid) nanocomposites. *Polymers* **2018**, *10*, 202. [[CrossRef](#)]
44. Rovera, C.; Ghaani, M.; Farris, S. Nano-inspired oxygen barrier coatings for food packaging applications: An overview. *Trends Food Sci. Technol.* **2020**, *97*, 210–220. [[CrossRef](#)]
45. Choudalakis, G.; Gotsis, A.D. Permeability of polymer/clay nanocomposites: A review. *Eur. Polym. J.* **2009**, *45*, 967–984. [[CrossRef](#)]
46. Kotal, M.; Bhowmick, A.K. Polymer nanocomposites from modified clays: Recent advances and challenges. *Prog. Polym. Sci.* **2015**, *51*, 127–187. [[CrossRef](#)]
47. Zhu, T.T.; Zhou, C.H.; Kabwe, F.B.; Wu, Q.Q.; Li, C.S.; Zhang, J.R. Exfoliation of montmorillonite and related properties of clay/polymer nanocomposites. *Appl. Clay Sci.* **2019**, *169*, 48–66. [[CrossRef](#)]
48. Tan, B.; Thomas, N.L. A review of the water barrier properties of polymer/clay and polymer/graphene nanocomposites. *J. Memb. Sci.* **2016**, *514*, 595–612. [[CrossRef](#)]
49. Wolf, C.; Angellier-Coussy, H.; Gontard, N.; Doghieri, F.; Guillard, V. How the shape of fillers affects the barrier properties of polymer/non-porous particles nanocomposites: A review. *J. Memb. Sci.* **2018**, *556*, 393–418. [[CrossRef](#)]

50. Kalendova, A.; Merinska, D.; Gerard, J.F.; Slouf, M. Polymer/clay nanocomposites and their gas barrier properties. *Polym. Compos.* **2013**, *34*, 1418–1424. [[CrossRef](#)]
51. Cui, Y.; Kumar, S.; Rao Kona, B.; Van Houcke, D. Gas barrier properties of polymer/clay nanocomposites. *RSC Adv.* **2015**, *5*, 63669–63690. [[CrossRef](#)]
52. Raquez, J.M.; Habibi, Y.; Murariu, M.; Dubois, P. Polylactide (PLA)-based nanocomposites. *Prog. Polym. Sci.* **2013**, *38*, 1504–1542. [[CrossRef](#)]
53. Krikorian, V.; Pochan, D.J. Poly (l-Lactic Acid)/Layered Silicate Nanocomposite: Fabrication, Characterization, and Properties. *Chem. Mater.* **2003**, *15*, 4317–4324. [[CrossRef](#)]
54. Pavlidou, S.; Papaspyrides, C.D. A review on polymer-layered silicate nanocomposites. *Prog. Polym. Sci.* **2008**, *33*, 1119–1198. [[CrossRef](#)]
55. Yang, Z.; Peng, H.; Wang, W.; Liu, T. Crystallization behavior of poly(ϵ -caprolactone)/layered double hydroxide nanocomposites. *J. Appl. Polym. Sci.* **2010**, *116*, 2658–2667. [[CrossRef](#)]
56. Chen, G.X.; Kim, H.S.; Shim, J.H.; Yoon, J.S. Role of epoxy groups on clay surface in the improvement of morphology of poly(L-lactide)/clay composites. *Macromolecules* **2005**, *38*, 3738–3744. [[CrossRef](#)]
57. Jiang, L.; Liu, B.; Zhang, J. Properties of poly(lactic acid)/poly(butylene adipate-co-terephthalate)/nanoparticle ternary composites. *Ind. Eng. Chem. Res.* **2009**, *48*, 7594–7602. [[CrossRef](#)]
58. Ozkoc, G.; Kemaloglu, S.; Quaedflieg, M. Production of poly(lactic acid)/organoclay nanocomposite scaffolds by microcompounding and polymer/particle leaching. *Polym. Compos.* **2010**, *31*, 674–683. [[CrossRef](#)]
59. Hasook, A.; Muramatsu, H.; Tanoue, S.; Iemoto, Y.; Unryu, T. Preparation of nanocomposites by melt compounding polylactic acid/polyamide 12/organoclay at different screw rotating speeds using a twin screw extruder. *Polym. Compos.* **2008**, *29*, 1–8. [[CrossRef](#)]
60. Katiyar, V.; Nanavati, H. In situ synthesis of high molecular weight poly(L-lactic acid) clay nanocomposites. *Polym. Eng. Sci.* **2011**, *51*, 2066–2077. [[CrossRef](#)]
61. Katiyar, V.; Nanavati, H. High molecular weight poly (L-lactic acid) clay nanocomposites via solid-state polymerization. *Polym. Compos.* **2011**, *32*, 497–509. [[CrossRef](#)]
62. Paul, M.A.; Delcourt, C.; Alexandre, M.; Degée, P.; Monteverde, F.; Rulmont, A.; Dubois, P. (Plasticized) polylactide/(organo-)clay nanocomposites by in situ intercalative polymerization. *Macromol. Chem. Phys.* **2005**, *206*, 484–498. [[CrossRef](#)]
63. Gorrasi, G.; Tammara, L.; Vittoria, V.; Paul, M.A.; Alexandre, M.; Dubois, P. Transport properties of water vapor in polylactide/montmorillonite nanocomposites. *J. Macromol. Sci. Phys. Part B* **2004**, *43*, 565–575. [[CrossRef](#)]
64. Chang, J.H.; An, Y.U. Nanocomposites of polyurethane with various organoclays: Thermomechanical properties, morphology, and gas permeability. *J. Polym. Sci. Part B Polym. Phys.* **2002**, *40*, 670–677. [[CrossRef](#)]
65. Maiti, P.; Yamada, K.; Okamoto, M.; Ueda, K.; Okamoto, K. New polylactide/layered silicate nanocomposites: Role of organoclays. *Chem. Mater.* **2002**, *14*, 4654–4661. [[CrossRef](#)]
66. Ray, S.S.; Yamada, K.; Okamoto, M.; Fujimoto, Y.; Ogami, A.; Ueda, K. New polylactide/layered silicate nanocomposites. 5. Designing of materials with desired properties. *Polymer* **2003**, *44*, 6633–6646.
67. Sinha Ray, S.; Yamada, K.; Okamoto, M.; Ogami, A.; Ueda, K. New polylactide/layered silicate nanocomposites. 3. High-performance biodegradable materials. *Chem. Mater.* **2003**, *15*, 1456–1465. [[CrossRef](#)]
68. Sinha Ray, S.; Yamada, K.; Okamoto, M.; Ueda, K. New polylactide-layered silicate nanocomposites. 2. Concurrent improvements of material properties, biodegradability and melt rheology. *Polymer* **2002**, *44*, 857–866. [[CrossRef](#)]
69. Ray, S.S.; Yamada, K.; Okamoto, M.; Ogami, A.; Ueda, K. New polylactide/layered silicate nanocomposites, 4. Structure, properties and biodegradability. *Compos. Interfaces* **2003**, *10*, 435–450. [[CrossRef](#)]
70. Ray, S.S.; Yamada, K.; Ogami, A.; Okamoto, M.; Ueda, K. New polylactide/layered silicate nanocomposite: Nanoscale control over multiple properties. *Macromol. Rapid Commun.* **2002**, *23*, 943–947. [[CrossRef](#)]
71. Thellen, C.; Orroth, C.; Froio, D.; Ziegler, D.; Lucciarini, J.; Farrell, R.; D'Souza, N.A.; Ratto, J.A. Influence of montmorillonite layered silicate on plasticized poly(l-lactide) blown films. *Polymer* **2005**, *46*, 11716–11727. [[CrossRef](#)]
72. Lagarón, J.M.; Cabedo, L.; Cava, D.; Feijoo, J.L.; Gavara, R.; Gimenez, E. Improving packaged food quality and safety. Part 2: Nanocomposites. *Food Addit. Contam.* **2005**, *22*, 994–998. [[CrossRef](#)]
73. Rhim, J.W.; Hong, S.I.; Ha, C.S. Tensile, water vapor barrier and antimicrobial properties of PLA/nanoclay composite films. *LWT Food Sci. Technol.* **2009**, *42*, 612–617. [[CrossRef](#)]

74. Zenkiewicz, M.; Richert, J. Permeability of polylactide nanocomposite films for water vapour, oxygen and carbon dioxide. *Polym. Test.* **2008**, *27*, 835–840. [[CrossRef](#)]
75. Zenkiewicz, M.; Richert, J.; Rózański, A. Effect of blow moulding ratio on barrier properties of polylactide nanocomposite films. *Polym. Test.* **2010**, *29*, 251–257. [[CrossRef](#)]
76. Koh, H.C.; Park, J.S.; Jeong, M.A.; Hwang, H.Y.; Hong, Y.T.; Ha, S.Y.; Nam, S.Y. Preparation and gas permeation properties of biodegradable polymer/layered silicate nanocomposite membranes. *Desalination* **2008**, *233*, 201–209. [[CrossRef](#)]
77. Cabedo, L.; Feijoo, J.L.; Villanueva, M.P.; Lagarón, J.M.; Giménez, E. Optimization of biodegradable nanocomposites based on aPLA/PCL blends for food packaging applications. *Macromol. Symp.* **2006**, *233*, 191–197. [[CrossRef](#)]
78. Trifol, J.; Plackett, D.; Sillard, C.; Szabo, P.; Bras, J.; Daugaard, A.E. Hybrid poly(lactic acid)/nanocellulose/nanoclay composites with synergistically enhanced barrier properties and improved thermomechanical resistance. *Polym. Int.* **2016**, *65*, 988–995. [[CrossRef](#)]
79. Trifol, J.; Plackett, D.; Sillard, C.; Hassager, O.; Daugaard, A.E.; Bras, J.; Szabo, P. A comparison of partially acetylated nanocellulose, nanocrystalline cellulose, and nanoclay as fillers for high-performance polylactide nanocomposites. *J. Appl. Polym. Sci.* **2016**, *133*, 43257. [[CrossRef](#)]
80. Singh, S.; Gupta, R.K.; Ghosh, A.K.; Maiti, S.N.; Bhattacharya, S.N. Poly(L-lactic acid)/layered silicate nanocomposite blown film for packaging application: Thermal, mechanical and barrier properties. *J. Polym. Eng.* **2010**, *30*, 361–375. [[CrossRef](#)]
81. Park, S.H.; Lee, H.S.; Choi, J.H.; Jeong, C.M.; Sung, M.H.; Park, H.J. Improvements in barrier properties of poly(lactic acid) films coated with chitosan or chitosan/clay nanocomposite. *J. Appl. Polym. Sci.* **2012**, *125*, E675–E680. [[CrossRef](#)]
82. Kim, H.K.; Kim, S.J.; Lee, H.S.; Choi, J.H.; Jeong, C.M.; Sung, M.H.; Park, S.H.; Park, H.J. Mechanical and barrier properties of poly(lactic acid) films coated by nanoclay-ink composition. *J. Appl. Polym. Sci.* **2013**, *127*, 3823–3829. [[CrossRef](#)]
83. Farmahini-Farahani, M.; Xiao, H.; Zhao, Y. Poly lactic acid nanocomposites containing modified nanoclay with synergistic barrier to water vapor for coated paper. *J. Appl. Polym. Sci.* **2014**, *131*, 40952. [[CrossRef](#)]
84. Zheng, W.; Beeler, M.; Claus, J.; Xu, X. Poly(lactic acid)/montmorillonite blown films: Crystallization, mechanics, and permeation. *J. Appl. Polym. Sci.* **2017**, *134*, 45260. [[CrossRef](#)]
85. Darie, R.N.; Păslaru, E.; Sdrobis, A.; Pricope, G.M.; Hitruc, G.E.; Poiată, A.; Baklavaridis, A.; Vasile, C. Effect of nanoclay hydrophilicity on the poly(lactic acid)/clay nanocomposites properties. *Ind. Eng. Chem. Res.* **2014**, *53*, 7877–7890. [[CrossRef](#)]
86. Rhim, J.W. Effect of PLA lamination on performance characteristics of agar/κ-carrageenan/clay bio-nanocomposite film. *Food Res. Int.* **2013**, *51*, 714–722. [[CrossRef](#)]
87. Jalalvandi, E.; Majid, R.A.; Ghanbari, T.; Ilbeygi, H. Effects of montmorillonite (MMT) on morphological, tensile, physical barrier properties and biodegradability of polylactic acid/starch/MMT nanocomposites. *J. Thermoplast. Compos. Mater.* **2015**, *28*, 496–509. [[CrossRef](#)]
88. Othman, S.H.; Ling, H.N.; Talib, R.A.; Naim, M.N.; Risyon, N.P.; Saifullah, M. PLA/MMT and PLA/halloysite bio-nanocomposite films: Mechanical, barrier, and transparency. *J. Nano Res.* **2019**, *59*, 77–93. [[CrossRef](#)]
89. Mohsen, A.H.; Ali, N.A. Mechanical, Color and Barrier, Properties of Biodegradable Nanocomposites Poly(lactic Acid)/Nanoclay. *J. Bioremediat. Biodegrad.* **2018**, *9*, 455. [[CrossRef](#)]
90. Busolo, M.A.; Fernandez, P.; Ocio, M.J.; Lagaron, J.M. Novel silver-based nanoclay as an antimicrobial in polylactic acid food packaging coatings. *Food Addit. Contam. Part A Chem. Anal. Control Expo. Risk Assess.* **2010**, *27*, 1617–1626. [[CrossRef](#)] [[PubMed](#)]
91. Şengül, B.; El-abassy, R.M.A.; Materny, A.; Dilsiz, N. Poly(lactic acid)/Organo-Montmorillonite Nanocomposites: Synthesis, Structures, Permeation Properties and Applications. *Polym. Sci. Ser. A* **2017**, *59*, 891–901. [[CrossRef](#)]
92. Chowdhury, S.R. Some important aspects in designing high molecular weight poly(L-lactic acid)-clay nanocomposites with desired properties. *Polym. Int.* **2008**, *57*, 1326–1332. [[CrossRef](#)]
93. Jorda-Beneyto, M.; Ortuño, N.; Devis, A.; Aucejo, S.; Puerto, M.; Gutiérrez-Praena, D.; Houtman, J.; Pichardo, S.; Maisanaba, S.; Jos, A. Use of nanoclay platelets in food packaging materials: Technical and cytotoxicity approach. *Food Addit. Contam. Part A Chem. Anal. Control Expo. Risk Assess.* **2014**, *31*, 354–363. [[CrossRef](#)]

94. Svagan, A.J.; Åkesson, A.; Cárdenas, M.; Bulut, S.; Knudsen, J.C.; Risbo, J.; Plackett, D. Transparent films based on PLA and montmorillonite with tunable oxygen barrier properties. *Biomacromolecules* **2012**, *13*, 397–405. [[CrossRef](#)]
95. Carosio, F.; Colonna, S.; Fina, A.; Rydzek, G.; Hemmerlé, J.; Jierry, L.; Schaaf, P.; Boulmedais, F. Efficient gas and water vapor barrier properties of thin poly(lactic acid) packaging films: Functionalization with moisture resistant Nafion and clay multilayers. *Chem. Mater.* **2014**, *26*, 5459–5466. [[CrossRef](#)]
96. Crank, J.; Crank, E.P.J. *The Mathematics of Diffusion*; Oxford University Press: Oxford, UK, 1979.
97. Wijmans, J.G.; Baker, R.W. The solution-diffusion model: A review. *J. Memb. Sci.* **1995**, *107*, 1–21. [[CrossRef](#)]
98. Crank, J. A theoretical investigation of the influence of molecular relaxation and internal stress on diffusion in polymers. *J. Polym. Sci.* **1953**, *11*, 151–168. [[CrossRef](#)]
99. Crank, J.; Park, G.S. *Diffusion in Polymers*; Academic Press: London, UK; New York, NY, USA, 1968.
100. Barrer, R.M. Diffusivities in glassy polymers for the dual mode sorption model. *J. Memb. Sci.* **1984**, *18*, 25–35. [[CrossRef](#)]
101. Meares, P. Transient permeation of organic vapors through polymer membranes. *J. Appl. Polym. Sci.* **1965**, *9*, 917–932. [[CrossRef](#)]
102. Hedenqvist, M.S.; Gedde, U.W. Parameters affecting the determination of transport kinetics data in highly swelling polymers above T(g). *Polymer* **1999**, *40*, 2381–2393. [[CrossRef](#)]
103. Vieth, W.R. *Diffusion in and Through Polymers: Principles and Applications*; Hanser Publications: Cincinnati, OH, USA, 1991.
104. Dhoot, S.N.; Freeman, B.D.; Stewart, M.E. Barrier Polymers. In *Encyclopedia of Polymer Science and Technology*; John Wiley and Sons Inc.: New York, NY, USA, 2002.
105. Ziegel, K.D.; Frensdorff, H.K.; Blair, D. Measurement of Hydrogen Isotope Transport in Poly(Vinyl Fluoride) Films By Permeation-Rate Method. *J. Polym. Sci. Phys.* **1969**, *7*, 809–819. [[CrossRef](#)]
106. Hedenqvist, M.; Angelstok, A.; Edsberg, L.; Larsson, P.T.; Gedde, U.W. Diffusion of small-molecule penetrants in polyethylene: Free volume and morphology. *Polymer* **1996**, *37*, 2887–2902. [[CrossRef](#)]
107. Webb, J.A.; Bower, D.L.; Ward, I.M.; Cardew, P.T. The effect of drawing on the transport of gases through polyethylene. *J. Polym. Sci. Part B Polym. Phys.* **1993**, *31*, 743–757. [[CrossRef](#)]
108. Paternak, R.; Schimscheimer, J.F.; Heller, J. Dynamic Approach To Diffusion and Permeation Measurements. *J. Polym. Sci. Part A 2 Polym. Phys.* **1970**, *8*, 467–479. [[CrossRef](#)]
109. Hedenqvist, M.S.; Ritums, J.E.; Condé-Brana, M.; Bergman, G. Sorption and desorption of tetrachloroethylene in fluoropolymers: Effects of the chemical structure and crystallinity. *J. Appl. Polym. Sci.* **2003**, *87*, 1474–1483. [[CrossRef](#)]
110. Hiltner, A.; Liu, R.Y.F.; Hu, Y.S.; Baer, E. Oxygen transport as a solid-state structure probe for polymeric materials: A review. *J. Polym. Sci. Part B Polym. Phys.* **2005**, *43*, 1047–1063. [[CrossRef](#)]
111. Cohen, M.H.; Turnbull, D. Molecular transport in liquids and glasses. *J. Chem. Phys.* **1959**, *31*, 1164–1169. [[CrossRef](#)]
112. Nilsson, F.; Hedenqvist, M.S.; Gedde, U.W. Small-molecule diffusion in semicrystalline polymers as revealed by experimental and simulation studies. *Macromol. Symp.* **2010**, *298*, 108–115. [[CrossRef](#)]
113. Nilsson, F.; Gedde, U.W.; Hedenqvist, M.S. Penetrant diffusion in polyethylene spherulites assessed by a novel off-lattice Monte-Carlo technique. *Eur. Polym. J.* **2009**, *45*, 3409–3417. [[CrossRef](#)]
114. Mogri, Z.; Paul, D.R. Gas sorption and transport in side-chain crystalline and molten poly(octadecyl acrylate). *Polymer* **2001**, *42*, 2531–2542. [[CrossRef](#)]
115. Nielsen, L.E. Models for the Permeability of Filled Polymer Systems. *J. Macromol. Sci. Part A Chem.* **1967**, *1*, 929–942. [[CrossRef](#)]
116. Cussler, E.L.; Hughes, S.E.; Ward, W.J.; Aris, R. Barrier membranes. *J. Memb. Sci.* **1988**, *38*, 161–174. [[CrossRef](#)]
117. Brydges, W.T.; Gulati, S.T.; Baum, G. Permeability of glass ribbon-reinforced composites. *J. Mater. Sci.* **1975**, *10*, 2044–2049. [[CrossRef](#)]
118. Lape, N.K.; Nuxoll, E.E.; Cussler, E.L. Polydisperse flakes in barrier films. *J. Memb. Sci.* **2004**, *236*, 29–37. [[CrossRef](#)]
119. Fredrickson, G.H.; Bicerano, J. Barrier properties of oriented disk composites. *J. Chem. Phys.* **1999**, *110*, 2181–2188. [[CrossRef](#)]
120. Gusev, A.A.; Lusti, H.R. Rational design of nanocomposites for barrier applications. *Adv. Mater.* **2001**, *13*, 1641–1643. [[CrossRef](#)]

121. Bharadwaj, R.K. Modeling the barrier properties of polymer-layered silicate nanocomposites. *Macromolecules* **2001**, *34*, 9189–9192. [[CrossRef](#)]
122. Guo, Y.; Yang, K.; Zuo, X.; Xue, Y.; Marmorat, C.; Liu, Y.; Chang, C.C.; Rafailovich, M.H. Effects of clay platelets and natural nanotubes on mechanical properties and gas permeability of Poly (lactic acid) nanocomposites. *Polymer* **2016**, *83*, 246–259. [[CrossRef](#)]
123. Picard, E.; Espuche, E.; Fulchiron, R. Effect of an organo-modified montmorillonite on PLA crystallization and gas barrier properties. *Appl. Clay Sci.* **2011**, *53*, 58–65. [[CrossRef](#)]
124. Li, Y.; Ren, P.; Zhang, Q.; Shen, T.; Ci, J.; Fang, C. Properties of Poly(lactic acid)/Organo-Montmorillonite Nanocomposites Prepared by Solution Intercalation. *J. Macromol. Sci. Part B Phys.* **2013**, *52*, 1041–1055. [[CrossRef](#)]
125. Bhatia, A.; Gupta, R.K.; Bhattacharya, S.N.; Choi, H.J. Analysis of Gas Permeability Characteristics of Poly(Lactic Acid)/Poly (Butylene Succinate) Nanocomposites. *J. Nanomater.* **2012**, *2012*, 249094. [[CrossRef](#)]
126. Tenn, N.; Follain, N.; Soulestin, J.; Crétois, R.; Bourbigot, S.; Marais, S. Effect of Nanoclay Hydration on Barrier Properties of PLA/Montmorillonite Based Nanocomposites. *J. Phys. Chem. C* **2013**, *117*, 12117–12135. [[CrossRef](#)]
127. Hedenqvist, M.; Gedde, U.W. Diffusion of small-molecule penetrants in semicrystalline polymers. *Prog. Polym. Sci.* **1996**, *21*, 299–333. [[CrossRef](#)]



© 2020 by the authors. Licensee MDPI, Basel, Switzerland. This article is an open access article distributed under the terms and conditions of the Creative Commons Attribution (CC BY) license (<http://creativecommons.org/licenses/by/4.0/>).

MDPI
St. Alban-Anlage 66
4052 Basel
Switzerland
Tel. +41 61 683 77 34
Fax +41 61 302 89 18
www.mdpi.com

Polymers Editorial Office
E-mail: polymers@mdpi.com
www.mdpi.com/journal/polymers



MDPI
St. Alban-Anlage 66
4052 Basel
Switzerland

Tel: +41 61 683 77 34
Fax: +41 61 302 89 18

www.mdpi.com



ISBN 978-3-0365-0313-4